UNIVERSIDADE ESTADUAL PAULISTA "JÚLIO DE MESQUITA FILHO"

Programa: Ciência e Tecnologia de Materiais

Tsegaye Gashaw Getnet

ATMOSPHERIC PLASMA TREATMENT OF BIOMATERIALS WITH EUGENOL AND CARVACROL THIN FILMS FOR INHIBITING BACTERIAL ADHESION AND PROLIFERATION

SOROCABA

2020

Tsegaye Gashaw Getnet

ATMOSPHERIC PLASMA TREATMENT OF BIOMATERIALS WITH EUGENOL AND CARVACROL THIN FILMS FOR INHIBITING BACTERIAL ADHESION AND PROLIFERATION

Tese apresentada como requisito à obtenção do título de Doutor à Universidade Estadual Paulista "Júlio de Mesquita Filho" - Programa de Pós-Graduação em Ciência e Tecnologia de Materiais, área de concentração Materiais, sob a orientação do Prof. Dr. Nilson C. da Cruz.

Sorocaba

2020

G394a

Getnet, Tsegaye Gashaw
Atmospheric plasma treatment of biomaterials with eugenol and carvacrol thin films for inhibiting bacterial adhesion and proliferation / Tsegaye Gashaw Getnet. -- Sorocaba, 2020
159 p. : il.

Tese (doutorado) - Universidade Estadual Paulista (Unesp), Instituto de Ciência e Tecnologia, Sorocaba
Orientador: Nilson C. da Cruz

1. Diagnóstico de plasma. 2. Polimerização em plasma. 3. Descarga de barreira dielétrica. I. Título.

Sistema de geração automática de fichas catalográficas da Unesp. Biblioteca do Instituto de Ciência e Tecnologia, Sorocaba. Dados fornecidos pelo autor(a).

UNIVERSIDADE ESTADUAL PAULISTA

Câmpus de Bauru

ATA DA DEFESA PÚBLICA DA TESE DE DOUTORADO DE TSEGAYE GASHAW GETNET, DISCENTE DO PROGRAMA DE PÓS-GRADUAÇÃO EM CIÊNCIA E TECNOLOGIA DE MATERIAIS, DA FACULDADE DE CIÊNCIAS - CÂMPUS DE BAURU.

Aos 16 dias do mês de outubro do ano de 2020, às 13:30 horas, no(a) por videoconferência, reuniu-se a Comissão Examinadora da Defesa Pública, composta pelos seguintes membros: Prof. Dr. NILSON CRISTINO DA CRUZ - Orientador(a) do(a) Curso de Engenharia de Controle e Automação / Instituto de Ciência e Tecnologia/ UNESP/ Sorocaba, Prof. Dr. CLODOMIRO ALVES JUNIOR do(a) Departamento de Física Teórica e Experimental / UNIVERSIDADE FEDERAL DO RIO GRANDE DO NORTE, Prof. Dr. FRANCISCO TRIVINHO STRIXINO do(a) Departamento de Física, Química e Matemática / Universidade Federal de São Carlos - Centro de Ciências e Tecnologias para a Sustentabilidade, Prof. Dr. MILTON EIJI KAYAMA do(a) Departamento de Física e Química / Faculdade de Engenharia de Guaratinguetá, Prof. Dr. STEVEN FREDERICK DURRANT do(a) Departamento de Engenharia de Controle e Automação / ICT - Unesp / Sorocaba, sob a presidência do primeiro, a fim de proceder a arguição pública da TESE DE DOUTORADO de TSEGAYE GASHAW GETNET, intitulada **Atmospheric Plasma Treatment of Biomaterials with Eugenol and Carvacrol Thin Films for Inhibiting Bacterial Adhesion and Proliferation**. Após a exposição, o discente foi arguido oralmente pelos membros da Comissão Examinadora, tendo recebido o conceito final:_ _ _ _ _ APROVADO _ . Nada mais havendo, foi lavrada a presente ata, que após lida e aprovada, foi assinada pelos membros da Comissão Examinadora.

Prof. Dr. NILSON CRISTINO DA CRUZ

Prof. Dr. CLODOMIRO ALVES JUNIOR Participação por videoconferência

Prof. Dr. FRANCISCO TRIVINHO STRIXINO Participação por videoconferência

Prof. Dr. MILTON EIJI KAYAMA Participação por videoconferência

Prof. Dr. STEVEN FREDERICK DURRANT Participação por videoconferência

Acknowledgments

Above all, thanks to the Almighty God with His Mother Virgin Mary, for His help in passing me through the difficult times I faced in pursuing my study (from high school to university) and for His help and encouragement throughout my life.

I would like to express my deepest gratitude to my advisor, Prof. Nilson C. da Cruz for his unreserved cooperation, excellent guidance, and timely advice, close follow up and supervision, continuous encouragement and patience, and giving me valuable comments throughout my Ph.D. study period. And I am very grateful to him for providing me an opportunity to learn at Sao Paulo State University, Brazil.

I would like to express my deep and sincere gratitude to Prof. Milton E. Kayama for his constant encouragement and patience throughout this dissertation, without his support and knowledge this dissertation would not have been completed.

I would like to thank Prof. Iolanda S. Duarte, Federal University of Sao Carlos, UFSCar, Environmental Microbiology Laboratory, Sorocaba, Brazil, for working collaboration and several scientific discussions.

My sincere thanks to Dr. Bruno, Federal Institute of Education, Science and Technology of São Paulo, IFSP, Brazil, for providing AFM measurement.

I thank Prof. Elidiane, Dr. Rita, Dr. Isaias, Miss Lilian, Mr. Sandro, and Mr. Rafael for their kind help during my stay in Sorocaba, Brazil.

It is my great pleasure to thank everyone at the UNESP community here in Sorocaba, Brazil. I'd especially like to thank all of our former and present Laboratory of Technological Plasmas, LaPTec, technicians, Miss Larissa, Mr. Luan, and Mr. Lucas for their timely help during my experiments. I would also like to thank Miss Gabriela from UFSCar for her help during biofilm assay experiments.

I would like to thank my family members and all of my friends for their inspiration, invaluable advice, and support.

Last but not the least, it is my great pleasure in acknowledging the CNPq-TWAS postgraduate fellowship for providing financial support throughout my Ph.D. study period.

Atmospheric Plasma Treatment of Biomaterials with Eugenol and Carvacrol Thin Films for Inhibiting Bacterial Adhesion and Proliferation.

Abstract

Owing to their ability to repair and substitute damaged tissue or organs, the use of implantable medical devices (IMD) is rising in modern medicine and healthcare. However, attention must be paid when choosing the materials to be used in IMD´s to assure the best performance of the device when in a biological environment. In addition to good biocompatibility and chemical stability, in several situations, the ideal material must also be able to inhibit implant bacterial colonization. Although bacterial infections may be treated with antibiotics, the overuse of such drugs has led to the development of antibiotic-resistant microorganisms. Furthermore, when adhered to a surface, bacteria can form biofilms, i.e. an agglomeration of cells that shields them from external agents. In this context, the modification of biomaterial surfaces with natural antimicrobial compounds has the potential to address these common implant-related inconveniences. In this scenario, we have examined the deposition and characterization of polymeric thin films produced from natural carvacrol and eugenol monomers in a Dielectric Barrier Discharge (DBD) plasma reactor. The electrical discharge characteristics were diagnosed by measuring the drop of voltage on a resistor and capacitor, and its applied voltage was measured by a voltage divider. The maximum applied voltage was 14.4 kV peak-to-peak and the power around 1.2 W. The study also included the analysis of the film structure using infrared reflectance spectroscopy, scanning electron and atomic force microscopies, profilometry, and contact angle measurements. Uniform, smooth, and dense films having chemical similarity to the corresponding monomer have been obtained. Inhibition of biofilms of Staphylococcus aureus, Pseudomonas aeruginosa, Escherichia coli*, and* Candida albicans *on stainless steel was evaluated. While it has been observed the formation of biofilm of all the microbes on the untreated samples, the coatings derived from carvacrol completely inhibited the adhesion of* E. coli *and reduced by 90% the proliferation of* S. aureus*. The coating has also inhibited the adhesion of* P. aeruginosa *and* C. albicans *in up to 44% and 60%, respectively. Similarly, films produced in plasmas containing eugenol inhibited by more than 75% and 65% the adhesion* of E. coli *and* S. aureus*, respectively, and the adhesion of* P. aeruginosa *and* C. albicans *by more than 30% and 40%, respectively. Electrochemical impedance spectroscopy and the potentiodynamic results revealed that both carvacrol- and eugenol-derived films have increased by at least 10 times the corrosion resistance of stainless steel in NaCl solution.*

Tratamento por plasma atmosférico de biomateriais com filmes finos de Eugenol e Carvacrol para inibir a adesão e proliferação bacteriana.

RESUMO

Um dispositivo médico implantado (IMD) é qualquer material inserido ou enxertado no corpo para fins protéticos, diagnósticos, terapêuticos ou experimentais. O uso dos IMD´s tem crescido significativamente em todas as áreas da medicina devido à sua capacidade de reparar ou substituir tecidos e órgãos danificados. No entanto, deve-se atentar para a escolha dos materiais a serem utilizados nos IMD´s para garantir o melhor desempenho do dispositivo quando em ambiente biológico. Além de boa biocompatibilidade e estabilidade química, em diversas situações o material também deve ser capaz de inibir a colonização bacteriana do implante. Embora infecções bacterianas possam ser tratadas com antibióticos, o uso excessivo de tais drogas levou ao desenvolvimento de microrganismos resistentes aos antibióticos. Além disso, quando aderidas a uma superfície, as bactérias podem formar biofilmes, ou seja, uma aglomeração de células que as protege de agentes externos. Nesse contexto, a modificação de superfícies de biomateriais com compostos antimicrobianos naturais apresenta grande potencial para resolver muitos dos inconvenientes relacionados ao uso de implantes. Nesse cenário, neste trabalho foi investigada a deposição e caracterização de filmes finos produzidos a partir de monômeros naturais de carvacrol e eugenol empregaudo plasmas de Descargas de Barreiras Dielétricas (DBD). As características elétricas das descargas foram avaliadas medindo-se a queda de tensão em um resistor e capacitor, respectivamente, e a tensão aplicada foi medida com um divisor de tensão. A tensão máxima aplicada foi de 14,4 kV pico a pico e a potência em torno de 1,2 W. O estudo também compreendeu a avaliação das propriedades físicas e químicas dos filmes por espectroscopia de reflexão-absorção no infravermelho, microscopias eletrônica de varredura e de força atômica, perfilometria e medidas de ângulo de contato. Avaliou-se ainda o efeito dos revestimentos sobre a formação de biofilmes de Staphylococcus aureus, Pseudomonas aeruginosa, Escherichia coli *e* Candida *albicans sobre substratos de aço inoxidável. Filmes uniformes, densos e quimicamente semelhantes aos respectivos monômeros foram obtidos. Os resultados de espectroscopia de impedância eletroquímica revelaram que os revestimentos aumentaram em mais de 10 vezes a resistência à corrosão dos substratos quando imersos em soluções de NaCl. Embora tenha sido observada a formação de biofilmes de todos os micróbios sobre as amostras não tratadas, os filmes derivados do carvacrol inibiram completamente a adesão de* E. coli *e reduziram em 90% a proliferação de* S. aureus*. O revestimento também inibiu a adesão de* P. aeruginosa *e* C. albicans *em mais de 40%. Da mesma forma, filmes*

produzidos em plasmas contendo eugenol inibiram em mais de 65% a adesão de E. coli *e* S. aureus *e em mais de 30% a adesão de* P. aeruginosa *e* C. albicans.

Table of Contents

List of Figures

Abbreviations

AFM	Atomic Force Microscopy
BAI	Biomaterial-associated infection
CDF	Carvacrol-derived film
CFU	Colony-forming unit
DBD	Dielectric barrier discharge
E_{corr}	Corrosion Potential
EDF	Eugenol-derived film
EDS	Energy Dispersive X-ray Spectroscopy
HAI	Hospital-Acquired Infections
ICB	Initial Colonies of Bacteria
IMD	Implant Medical Device
IRRAS	Infrared Reflectance Absorbance Spectroscopy
j_{corr}	Current density
LTE	Local Thermodynamic Equilibrium
PP-PSMs	Plasma polymers of plant secondary metabolites
R_{MS}	Root Mean Square (Roughness)
R_p	Polarization resistance
R_p	Polarization resistance
SEM	Scanning Electron Microscopy
SS	Stainless Steel
TSA	Tryptic Soy Agar
TSB	Tryptic Soy Broth
UV-VIS	Ultraviolet-visible Spectroscopy
β_a	Tafel slope of the anodic polarization curve
β_c	Tafel slope of the cathodic polarization curve

1 Introduction

Owing to their ability to repair and substitute damaged tissue or organs (SUCI DHARMAYANTI *et al*., 2020; HOGAN *et al*., 2019), the use of implantable medical devices (IMD) is rising in modern medicine and healthcare. Despite their biocompatibility with living tissue, implants can lead to uncontrolled biological responses, such as immune system activation, protein adsorption, inflammatory reactions, and cellular adhesion (VELNAR *et al*., 2016). This consists of a series of complex reactions involving various cell types, proteins, platelets, and many chemical mediator pathogens (ACHINGER; AYUS, 2019). In addition, high corrosion rates of some metallic biomaterials promote cracks and releasing of particles and ions in surrounding tissues, which may limit their clinical application. For instance, magnesium (BORNAPOUR *et al*., 2013; LI *et al*., 2012), titanium and their alloys (CORDEIRO *et al*., 2018), are susceptible to degradation in body fluids.

At the same time, the susceptibility of the implant surface to bacterial colonization is another barrier for the long-term use of implants (ÇAKMAK *et al*., 2019). For instance, in the United States, hospital-acquired infections alone cause between 60,000 and 100,000 deaths, amounting to an economic burden of $17 to $30 billion annually (GOMEZ *et al*., 2018). It is estimated that as many as 80% of those infections arise from bacterial biofilms (EDMISTON *et al*., 2015). Once the biofilm is established, it is quite difficult to eradicate it as microbes develop a shell that protects them from external agents, such as antibiotics (TAN *et al*., 2018; WOLFMEIER *et al*., 2018). The only solution to extirpate the colonization of biofilm-forming bacteria is to surgically remove the infected implant, which in turn causes high economic costs and extra risks of morbidity and mortality to the patients. In addition to medical problems, biofilm on ship hulls and heat exchangers, for instance, causes an increase in energy consumption and equipment damage, resulting in heavy economic losses (SONG, 2016). Moreover, many industries suffer the ill-effects of biofilm growth of one type or another, which can result in extra maintenance costs (TARIFA; LOZANO; BRUGNONI, 2018).

To overcome such problems, great attention has been devoted to developing a biomaterial for prolonged use or with controlled release of therapeutic molecules, such as antibiotics, antitumor, anti-inflammatory, antiseptics, and biocides (MONZILLO *et al*., 2012). However, some protection against implant infection is, generally, only obtained in the first week with antibiotic coated devices while drug release by the biomaterial surface is poorly controlled (AL-

JUMAILI *et al*., 2017; BAZAKA *et al*., 2011a). Additionally, the use of antibiotics leads to undesired consequences, including the spread of antibiotic-resistant bacteria (FAN *et al*., 2020). For example, 60% of *Staphylococcus aureus* strains isolated from intensive care units were resistant to methicillin (RAMRITU *et al*., 2008; LAXMINARAYAN *et al*., 2013). The use of silver is also problematic, as silver resistance has been observed in bacteria, notably *Pseudomonas aeruginosa* (SILVER; PHUNG; SILVER, 2006). Thereby, antimicrobial non-antibiotics compounds, like essential oils, that do not contribute to the development of resistant genes are highly desirable. In this regard, plasma-assisted chemical vapor deposition gained considerable interest in the conversion of bio-renewable resources into diverse structures from simple polymers to advanced carbon nanostructures (AL-JUMAILI *et al*., 2017b). Plasma-enhanced technology is also an attractive method to modify the surface properties of biomaterials while preserving their bulk characteristics (SANTOS *et al*., 2016a; LEE *et al*., 2016).

Plasma polymers are a particular class of thin films that can present highly cross-linked and biochemically inert structures (KYLIAN *et al*., 2017; AGRAWAL *et al*., 2019). The properties of such films can be altered by varying the deposition condition, such as pressure, applied voltage, monomer flow rate, and polymerization time. By employing this technique, it is possible to deposit coatings from a wide array of organic and synthetic materials, including those that do not normally polymerize via conventional pathways (MANAKHOV *et al*., 2016; MACGREGOR *et al*., 2019). Also, plasma polymers are manufactured in a dry environment without the production of significant amounts of toxic byproducts (ZILLE; SOUTO; OLIVEIRA, 2019). Owing to this, plasma deposited coatings have been used in many different applications, for instance, as electrode insulation (PETER *et al*., 2018; WANG *et al*., 2017; REICHEL *et al*., 2018), diffusion barriers (HOFFMANN *et al*., 2017), corrosion protection (SANTOS *et al*., 2017b; RANGEL *et al*., 2019; RANGEL; CRUZ; RANGEL, 2020), sensor devices and antimicrobial coatings (ALEMÁN *et al*., 2018; GAO; HANG; CHU, 2017). In theory, it is, therefore, possible to engineer a biocompatible material through plasma coating with inherent antimicrobial functional groups of natural agents, like essential oils (BAZAKA *et al*., 2017).

Several studies (QIAN *et al*., 2020; RIBES *et al*., 2019; CHANG; MCLANDSBOROUGH; MCCLEMENTS, 2013) have demonstrated the biocidal activity of carvacrol and eugenol against free-standing micro-organisms. Also, their use has been approved

by the European Parliament and Council and by the U.S. Food and Drug administration (BAMPIDIS *et al*., 2019; EAFUS, 2006). However, the feasibility of stable thin film formation, biofilm inhibition, and corrosion protection activities of both oregano and cloves oil, either independently or in combination with another monomer, has not been conducted yet as far as we know, in both low- and atmospheric pressure plasma. In this context, the present study has focused on the development of a novel organic thin film coating on stainless steel (SS) substrates by Dielectric Barrier Discharge (DBD) plasmas from eugenol and carvacrol monomers, whose chemical structures are depicted in figure 1, aiming inhibiting bacterial adhesion and proliferation, as well as corrosion protection.

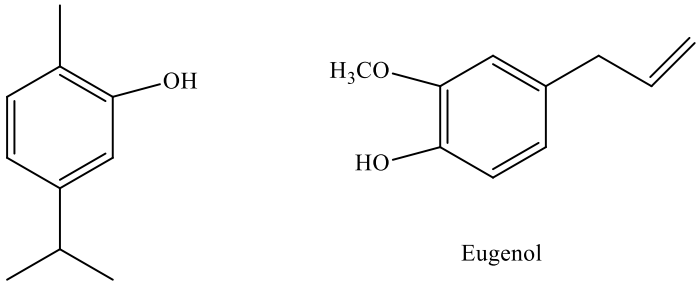

Figure 1. Chemical structure of carvacrol and eugenol.

2 General and Specific Objectives

General Objective

The general objective of this work was to deposit a thin film from essential oils, carvacrol and eugenol, on stainless steel surfaces aiming at the suppression of microbial adherence and proliferation. And also, the deposited film application for corrosion protection of stainless steel was evaluated using electrochemical impedance spectroscopy.

Specific Objectives

- ✓ To deposit plasma polymerized thin films from carvacrol and eugenol on a biomaterial surface.
- ✓ To diagnose both electronic and optical properties of the dielectric barrier discharge plasma applied for the film deposition.
- ✓ To characterize the thin film properties, such as chemical structure, wettability, topography and morphology, thickness and roughness, aging, and thermal stability.
- ✓ To test the effect of coating on the suppression of microbial biofilm formation.
- ✓ To test the anti-corrosion protection of the films in NaCl solution.

3 Literature Review

3.1. Biomaterials and their use

A biomaterial is “any substance (other than a drug) or combination of substances, that may be natural or synthetic in origin, for any period of time which can be used, as a part or as a whole of a system which treats, augments, or replaces any tissue, organ, or function of the body" (PATEL; GOHIL, 2012). Meanwhile, other definitions of the term “Biomaterials” can be any material whether from the natural or synthetic origin, that comprises whole or part of living structures or biomedical devices that performs, augments, or replace a natural function (IGE; UMORU; ARIBO, 2012). The use of biomaterials has vigorously increased in the last decades. For instance, in the United State alone every year 13 million medical devices are used (BOSE *et al*., 2018). According to a market survey report, the global bio-implant market was expected to grow up to $115.8 billion by 2020 with a compound annual growth rate of 10.3% during the estimated period (2014–2020) (KUMAR *et al*., 2020). The most common classes of biomaterials are metals pure or as alloys, polymers, ceramics, and composites (YAQUB KHAN; MOHD YAQUB; MIN-HUA, 2019).

Nowadays, several metallic biomaterials, such as titanium and its alloys (KULKARNI *et al*., 2014; KHORASANI *et al*., 2015; ZHANG; CHEN, 2019), cobalt-chromium alloys (AHERWAR; SINGH; PATNAIK, 2016; HASSIM *et al*., 2019; SINGH; SINGH; SIDHU, 2019), nickel-chromium alloy (FIROUZI-NERBIN; NASIRPOURI; MOSLEHIFARD, 2020; MOSLEHIFARD *et al*., 2019) and stainless steel (HASSAN; ABDEL GHANY, 2017; LONGHI *et al*., 2019) have been used as orthopedic and dental implants, and surgical instruments, because of their excellent biocompatibility, low elastic modulus, high yield strength, and corrosion resistance (LIU *et al*., 2016; ZHOU *et al*., 2005). Among them, stainless steel (SS) is frequently used for various orthopedic and surgical applications, due to good ductility and fatigue behaviour, excellent corrosion resistance, good formability, and low cost of production in comparison with other metallic biomaterials (VAHIDGOLPAYEGANI *et al*., 2017; NASERI *et al*., 2018; POLYAKOV *et al*., 2018).

Despite their excellent strength and mechanical properties of metallic biomaterials, mostly, they have been chosen to be used as a substitute for hard-tissue replacement, such as artificial hip joints. However, they do not receive long-term maintenance and satisfaction of patients for a high quality of life due to tissue-related problems such as swelling and lack of biocompatibility

between the interface of the biomaterials and living tissue. Also, their high corrosion rate in the aggressive microenvironment may lead to material degradation, and the associated release of unwanted metallic ions, which may induce local tissue damage and inflammatory reactions, such as gradual osteolysis of adjacent tissues, as well as systemic damage, such as metal hypersensitivity. The osteolysis may undermine the fixation and ultimately the loading and force transfer of the implant, leading to implant failure, corrective surgeries, or post-surgery complications (MEARS; KATES, 2015; PRASAD *et al*., 2017; SU *et al*., 2018; BARRÈRE *et al*., 2008) Therefore, it is important to understand such metallic biomaterial limitations before applying them to increase patient satisfaction and reduce the risk of death and disease. In line with this, surface modification of biomaterials with the bioactive compound is of paramount importance to overcome these limitations and make the bioactive surface. Besides, polymer surface modification is required to enhance the bio-functionalization process, like the creation of biomaterials with the harmonization of metals, ceramics, and polymers is desired (BAZAKA *et al.*, 2010; VAITHILINGAM *et al*., 2015).

3.2. **Medical Implants and their Challenges**

3.2.1. **Bacterial biofilm**

The most common biofilm-forming bacteria are *Enterococcus faecalis*, *Staphylococcus aureus*, *Staphylococcus epidermidis*, *Streptococcus viridans*, *Escherichia coli*, *Klebsiella pneumonia*, *Proteus mirabilis*, and *Pseudomonas aeruginosa (*KHALID *et al*., 2017; HOGAN *et al*., 2019; SURYALETHA *et al*., 2019; LIU *et al*., 2020; SAMAD *et al*., 2019; TORZEWSKA; BEDNARSKA; RÓŻALSKI, 2019). *S. aureus* and *S. epidermidis* cause about 50% of prosthetic heart valve infections, 70% of catheter biofilm infections (AGARWAL; SINGH; JAIN, 2010; PAHARIK; HORSWILL, 2016). Similarly, several investigators (BREZNICKY; NOVAK, 2019; MORAN *et al*., 2007; WOUTHUYZEN-BAKKER *et al*., 2019) reported that 65% to 80% of the prosthetic joint replacement infections are caused by *S. aureus* and coagulase-negative staphylococci. Also, TORNERO *et al*., (2012) have evaluated the specific characteristics, outcome, and predictors of failure of prosthetic joint infections due to *S. aureus* and *coagulase-negative staphylococci* treated with open debridement and retention of the implant for 10 consecutive years. They conclude that prosthetic joint infections due to *S. aureus* were mainly in primary arthroplasties; presented higher inflammatory response, and the strains were more

susceptible to fluoroquinolones and methicillin than *coagulase-negative staphylococci* infections. *S. aureus* infections had also led to a higher implant failure rate than *coagulase-negative staphylococci* infections, however, the difference was not statistically significant. Besides, around 19% of the knee or hip joint arthroplasty infections are caused by *S. aureus* (BERRÍOS-TORRES *et al*., 2014). Moreover, approximately 87% of bloodstream infections were caused by *staphylococci* (AGARWAL; SINGH; JAIN, 2010). *P. aeruginosa* bacterial biofilm is also a common source of about 12% of urinary tract infections (SAMAD *et al*., 2019; TUMBARELLO *et al*., 2020; SUETENS *et al*., 2018; FERREIRO *et al*., 2017) and 10% of bloodstream infections (THADEN *et al*., 2017). A study published by KANG *et al*., (2003) has presented a set of 136 patients with *P. aeruginosa* bacteremia, of which 20% received inadequate definitive antimicrobial therapy, with a 75% mortality rate at 30 days of those with inappropriate therapies compared with the mortality of 29% of those treated with appropriate antibiotics (KANG *et al*., 2003).

Biofilm formation is a dynamic process including attachment, micro-colony formation, maturation, and dispersion (SONG, 2016**)**. Among these steps, initial attachment plays an important role in biofilm formation and is known to be influenced by many factors such as surface chemistry, hydrophobicity, stiffness, roughness, topography, and charge. Once the initial attachment of bacteria reached the maturation stage, the synthesis of extracellular polymers matrices and exchange of genetic information between one cell to another is enhanced, increasing their resistance against antimicrobials, ultraviolet light, and secondary metabolic products (SINGH *et al*., 2017; CHENG *et al*., 2016; MARTINS *et al*., 2019). Thereby, biocompatible and antimicrobial surface treatments before the implantation of the biomaterials are supposed to prevent the initial attachment of bacterial colony (DAS GHATAK *et al*., 2018; GOMEZ-CARRETERO; NYBOM; RICHTER-DAHLFORS, 2017). In this regard, one promising strategy has been inspired by the inherent bioactivity of plant secondary metabolites (PSMs), such as essential oils and herb extracts, which have relatively powerful broad-spectrum antibacterial activities (WANG *et al*., 2014; BELIBEL *et al*., 2016). Indeed, plant secondary metabolites (PSMs) are a relatively low-cost renewable resource available in commercial quantities, with limited toxicity. However, using PSMs for surface functionalization through immobilization or synthesis of coatings without loss of functionality is challenging, in part due to solubility and volatility issues.

In this scenario, plasma-assisted techniques are potentially interesting as they allow the fabrication of thin-film coatings from renewable precursors with control of their chemical functionality (AL-JUMAILI *et al*., 2017; ÇAKMAK *et al*., 2019, GOMEZ *et al*., 2018). Under appropriate deposition conditions, plasma-synthesis is able to preserve the inherent antimicrobial functionality of PSMs in the solid film. Moreover, plasma polymers of plant secondary metabolites (pp-PSMs) have several advantages including low cytotoxicity, long-term stability, and a reduced risk of developing microbial resistance (BAZAKA *et al*., 2011b). These advantageous properties render PP-PSMs a suitable candidate for bioactive coating applications.

3.2.2. **Fungal biofilm**

Like bacteria, fungal biofilm formation on medical devices is a very serious clinical problem (BERMAN; KRYSAN, 2020; SULEYMAN; ALANGADEN, 2016; KHAN; BAIG; MEHBOOB, 2017). The most common sites for fungal infections associated with biofilms are the oral cavity, lungs, burn wounds, the lower reproductive tract, the gastrointestinal tract, skin, and the insertion site of urinary catheters (IÑIGO; DEL POZO, 2018). Fungal biofilms also damaged the vascular endothelium of native heart valves in patients with pre-existing cardiac disease (DOUGLAS, 2003). Among the many fungal species, *Candida* species, most notably *C. albicans*, cause many infections ranging from superficial to invasive infections as they reside in a commensal manner in the oral cavity, bloodstream, gastrointestinal tract, etc. (PATHAK, 2019). Also, MARRA *et al*., (2011) studied a surveillance study of nosocomial bloodstream infections of more than 2,563 patients in 16 Brazilian hospitals over 4 years (2007-2010), 6.1% were caused by *Candida* species. *Candida* infections have been also associated with various invasive IMD, including central venous catheters, joint prostheses, dialysis access, cardiovascular devices (NOBILE; JOHNSON, 2015; TSUI; KONG; JABRA-RIZK, 2016), as well as with superficial devices like dentures (OTERO REY *et al*., 2015). In addition to this, *Candida albicans* biofilms are highly resistant to some of the antifungal drugs, such as nystatin, chlorhexidine, fluconazole, and amphotericin B (RODRÍGUEZ-CERDEIRA *et al*., 2019).

It is not clear the exact mechanism of drug resistance of fungal biofilm, due to their genetic and biochemical alteration of fungal cells or the production of extracellular material (VAN ACKER; VAN DIJCK; COENYE, 2014). Some researchers proposed that the antifungal resistance of biofilm-producing fungus was due to the metabolic quiescence of fungal cells

(TANWAR *et al*., 2014). They observed that biofilm formation by *C. albicans* occurred more on latex-polyvinyl chloride or silicone elastomer and less on polyurethane or pure latex. Similarly, RAMAGE *et al*., (2004) have used scanning electron microscopy to assess the etiology of denture stomatitis and have shown that *Candida* biofilms could be visualized on samples obtained from patients with stomatitis. Clinical isolates of *C. albicans* were also able to form biofilms in vitro, although the amount of biofilm formed was diverse for different isolates recovered from the same patient. However, susceptibility tests indicated that the resulting biofilms presented increased resistance to antifungal treatment (CÓRDOVA-ALCÁNTARA *et al*., 2019). These implant-associated infections are inherently difficult to resolve and may require both long-term antifungal therapy and the physical removal of the implant to control the infection (VAN ACKER; VAN DIJCK; COENYE, 2014). Other non-*albicans Candida* species associated with biofilm formation and catheter-related bloodstream or device-related infections are *C. glabrata*, *C. parapsilosis, C. dubliniensis, C. krusei,* and *C. tropicalis* (RAMAGE; MARTÍNEZ; LÓPEZ-RIBOT, 2006; TUMBARELLO *et al*., 2007).

3.2.3. **Corrosion Protection from Natural Extract**

Corrosion of metallic biomaterials can cause the loss of their structural integrity and surface functionality (MANAM *et al*., 2017). Also, it causes alterations in the environment of biomaterials, such as a change in pH, chemical components, and a decrease of dissolved oxygen. Moreover, the release of metal ions during corrosion, even in very small amounts, may cause allergic response and carcinogenesis in the human body (ELTIT; WANG; WANG, 2019; ASRI *et al*., 2017; ELIAZ, 2019). Owing to these problems, the number of metals that can be used as biomaterials is much smaller than that for structural and industrial applications. Thus, understanding the influence of corrosion processes of metallic biomaterials on the tissue response and accurate evaluation of the corrosion behaviour of metallic biomaterials is essential (HIROMOTO, 2010; REVIE; UHLIG, 2008; ASRI *et al*., 2017).

Despite the alloying elements added to improve its corrosion resistance, SS is still subject to being corroded in an aggressive environment, such as a medium containing chloride ions like body fluids, for instance, contributing to biomaterial-associated infection (BAI). Therefore, it is of paramount importance to the improvement of the corrosion resistance in this medium (ZHANG *et al*., 2016; SHINTANI *et al*., 2008; KOŽUHA *et al*., 2016; MURUVE *et al*., 2016).

There are various methods for the protection of metals against corrosion, but the most used are corrosion inhibitors (CHANG *et al.*, 2018). Amongst the variety of corrosion inhibitors, organic compounds are widely used for preventing corrosion in most metal surfaces (VERMA *et al.*, 2018; FOUDA; DIAB; FATHY, 2017; UMOREN; SOLOMON, 2017). They provide a barrier against various corrosive species present in the environment, due to their high resistance to oxygen, water, and ions transport (HARB *et al.*, 2020; O. KOLAWOLE *et al.*, 2019). Also, they work by adsorption of ions or molecules on the steel surface and block active sites, thus decreasing the corrosion rate of the metals (AL-AMIERY *et al.*, 2011). Particularly, organic additives prevent the adsorption of chloride ions and promote the formation of more resistant oxide films on the metal surface (MUSA *et al.*, 2009).

Although numerous organic compounds such as azoles and their derivatives are tested as corrosion inhibitors, many of these compounds are hazardous to the environment (ANTONIJEVIĆ *et al.*, 2005; TASIC *et al.*, 2016; BARRETO *et al.*, 2017). In this regard, the green corrosion inhibitors extracted from plants have attracted the attention of numerous researchers since they are biodegradable, inexpensive, non-toxic, environmentally acceptable, readily available, and renewable (MAKHLOUF; HERRERA; MUÑOZ, 2018; RAJA *et al.*, 2014; PETROVIĆ MIHAJLOVIĆ *et al.*, 2017). Moreover, they do not contain heavy metals or other toxic compounds (OSTOVARI *et al.*, 2009). It has been reported that the successful use of many of those natural products, for instance, green tea and mango leaves extracts (ALSABAGH *et al.*, 2015; RAMEZANZADEH *et al.*, 2019), effectively diminishes the corrosion rate of carbon steel in HCl and H_2SO_4. *Hyoscyamus muticus* extract is effectively used for a copper corrosion inhibitor in HNO_3 (FOUDA *et al.*, 2015) and leaf extracts of *Chromolaena odorata* are reduced aluminum corrosion in 2 M HCl solution (OBOT; OBI-EGBEDI, 2010).

3.3. Essential Oil and its use for Biofilm Eradication

Owing to their unique characteristics, natural substances, such as essential oils and their constituents, have found wide application in pharmaceutical, agricultural, fragrance, cosmetic, and food industries along with dentistry and medicine (BAZAKA *et al.*, 2015a; CASTRO *et al.*, 2016; ESSID *et al.*, 2019). Essential oils are also widely used to alleviate stomach disorders, arthritis, headaches, as well as anesthetic and antiseptic in dentistry (ELIAZ, 2019). Some of these attributes are based on the coexistence of both hydrophilic and hydrophobic moieties in the

molecule. These activities have been reported in many studies and some of them were reviewed by (KAMATOU; VERMAAK; VILJOEN, 2012; JAGANATHAN; SUPRIYANTO, 2012).

Essential oils are extracted from different parts of plants such as bark, stems, buds, flowers, fruits, leaves, seeds, and roots, by various methods (FALEIRO M.L., 2011; MANION; WIDDER, 2017). The extraction mainly depends on the rate of diffusion of the oil through the plant tissues to an exposed surface from where the oil can be removed by several processes. However, different methods are available depending upon the stability of the oil and the plant materials. Steam distillation and hydrodistillation are still in use nowadays as the most important process for obtaining essential oils from each medicinal plant (SOKOVIĆ; VAN GRIENSVEN, 2006). Other methods also employed for the isolation of essential oils include the use of liquid carbon dioxide or microwaves, and low or high-pressure distillation using boiling water or hot steam (DONELIAN *et al*., 2009).

Several researchers (CAZZOLA *et al*., 2019; CELLS, 2019; SAHAL *et al*., 2020) have also worked on the reduction of biofilms adhesion and proliferation on different surfaces by the direct coating of essential oils, either independently or in combination with another antibiotic. The coating of essential oil of *Ocimum basilicum L.* (OB) on surfaces of polymethylmethacrylate and polystyrene to prevent bacterial colonization and biofilm formation has been investigated by RAJARAMAN; JAINU; DHAKSHINAMOORTHY, (2016). In this study, gram-positive bacteria, including *Staphylococcus aureus* and *Staphylococcus epidermidis*, and gram-negative bacteria, including *Escherichia coli* and *Pseudomonas aeruginosa* were allowed to adhere and grow for 1, 3, and 24 h on the direct coated polymethylmethacrylate and polystyrene substrates, and resulted that the number of bacteria adhering on the coated surfaces was significantly less in comparison to uncoated surfaces, in the investigated periods. Their work has also revealed the potent bacteriostatic effects of OB essential oil on both gram-positive and gram-negative bacteria. Thus, OB essential oil may be considered as a promising coating material to prevent bacterial adhesion and biofilm growth.

Additionally, the anti-biofilm activity of five different plant essential oils, such as garlic, eucalyptus, neem, tulsi, and cloves were tested against *Bacillus cereus*, *Staphylococcus aureus*, *Pseudomonas aeruginosa*, *Escherichia coli*, *Acinetobacter baumannii,* and *Klebsiella pneumonia*, on the abiotic surface like a urinary catheter and others (MOHAMMADI *et al*., 2019; RUBINI *et al*., 2018). They found that the five tested essential oils possess a considerable

reduction in biofilm formation as follow: eucalyptus oil showed maximum inhibition of biofilm almost (82%), followed by tulsi oil (48.7%), garlic oil (44.3%), and neem oil (34.2%) and finally, cloves oil showed the least inhibition (31.4%). The other investigator MILADI *et al*., (2017) were tested the antibiofilm activities of five essential oils, such as eugenol, carvacrol, thymol, p-cymene and g-terpinene, independently or in combination with tetracycline, against *S. aureus*. They found that a reduction of biofilm rate ranged from 2 to 8-fold. And they conclude that the tested essential oils may be considered as a potential natural source with a resistance modifying activity and may be applied to eradicate bacterial biofilm. Besides, SAHAL *et al*., (2020) investigated the antifungal and biofilm inhibitory effects of *Cymbopogon citratus* oil coating of different biomaterials against clinical isolated *C. tropicalis* fungal strain. They found that *C. citratus* oil coating on silicone rubber had a 45 to76% reduction in biofilm formation in *all C. tropicalis* strains. And they conclude that *Cymbopogon citratus* oil has good potential to be used as an antifungal and anti-biofilm agent on silicone rubber prostheses and medical devices on which *C. tropicalis* biofilms pose a serious risk for skin infections and may cause a shorter lifespan of the prosthesis. In the later, DÍAZ DE RIENZO *et al*., (2016) reported the novel approach of *rhamnolipids* and a combination of *rhamnolipids* essential oil and caprylic acid against *P. aeruginosa* biofilm. They found that *rhamnolipids* may interfere with cell-to-cell interactions and cell-substratum interactions as well. The highest impact on mature biofilm was observed for the mixture of *rhamnolipids* and caprylic acid (its biofilm reduction over 60%).

3.3.1. **Antimicrobial Activity of Eugenol**

Eugenol (4-allyl-2-methoxy phenol), is a naturally occurring aromatic compound, which has a pleasant odor and taste (PRAMOD; ANSARI; ALI, 2010). It is a high volatile phenolic compound with low chemical stability, being sensitive to oxidation and chemical interactions (MARCHESE *et al*., 2017). It can be extracted up to 90% from buds and leaves of cloves (*Syzygium aromaticum*) and cinnamon (*Cinnamomum zeylanicum*) plants (MITTAL *et al*., 2014; RAO; GAN, 2014; ZAIDI *et al*., 2015). The oils extracted from such plants are used to treat many diseases including acne, asthma, rheumatoid arthritis, scarring, warts, and various allergies, due to their higher constituents of eugenol. Also, it is used as a dental analgesic, perfuming, cosmetics, as food flavoring agents, mouthwashes, antispasmodic, and a general

antiseptic in medical dental practice (MARCHESE *et al*., 2017; SHAO *et al*., 2018; KHALIL *et al*., 2017).

Eugenol has also shown excellent antioxidant, anti-inflammatory, and antimicrobial activity against fungi and a wide range of gram-negative and gram-positive bacteria, such as *Escherichia coli*, *Staphylococcus aureus*, and *Pseudomonas aeruginosa* (LV *et al*., 2011; QIAN *et al*., 2020; RIBES *et al*., 2019; WANG *et al*., 2010). The antibacterial action of eugenol is mostly ascribed to the presence of a free hydroxyl group in its molecular structure (NAZZARO *et al*., 2013). Its hydrophobic nature enables the penetration in the lipopolysaccharide of the bacterial cell membrane and alters the cell structure, which subsequently results in the leakage of intracellular constituents (BURT, 2004; ESSID *et al*., 2019; MAJEED *et al*., 2016). Also, its phenolic groups disrupt the cytoplasmic membrane, which increases its nonspecific permeability and affects the transport of ions and Adenosine Triphosphate (ATP) (DEVI *et al*., 2010). For instance, it altered the cell membrane permeability of *Salmonella typhi* followed by leakage of ions and extensive loss of other cellular contents (DEVI *et al*., 2010) and increased the K^+ ion permeability of *L. monocytogenes* cells (FILGUEIRAS; VANETTI, 2006).

Other shreds of evidence reveal that the hydroxyl group on eugenol is thought to bind to proteins and prevent enzyme action (BURT, 2004; BI *et al*., 2012). In 2015, PERUGINI BIASI-GARBIN *et al*., studied the morphological and ultrastructural alterations in eugenol treated *Streptococcus agalactiae* planktonic cells and they have observed that after 5 h of incubation with an inhibitory concentration of eugenol, the planktonic cell of *S. agalactiae* displayed various alterations, such as changes in cell morphology and disruption of the cell wall. Moreover, eugenol modified the fatty acid profile of the cell membrane of different bacteria. For instance, DI PASQUA *et al*., (2007) have measured changes in the principal fatty acid composition of *Escherichia coli*, *S. typhimurium*, *Pseudomonas fluorescens*, and *Staphylococcus aureus*. In all tested strains, it has been observed large increases in concentrations of low molecular weight fatty acids. DAS *et al*., (2016) have also confirmed that eugenol was able to trigger cell cytotoxicity of several *S. aureus* bacteria, includes vancomycin-resistant *S. aureus*, due to the production of intracellular reactive oxygen species (ROS) which induces the inhibition of the growth of the cell, disruption of the cell membrane and DNA damage resulting in cell decomposition and death. In general, the major mechanisms/actions of essential oils and, in particular, eugenol against bacteria and fungi are summarized in Fig. 2.

The action mechanisms of eugenol against fungi have also been investigated by (MARCHESE *et al.*, 2017), they have found that eugenol changes the membrane of fatty acid and cell morphology, affecting the transport of ions and ATP of fungi, as shown in Fig. 2. In particular, BRAGA *et al.*, (2007) and BENNIS *et al.*, (2004) have sown, respectively, that eugenol induced morphological alterations in the envelope of *S. cerevisiae* and *C. albicans*. According to this study, eugenol at up to 500 µg/mL minimum inhibitory concentration (MIC) has reduced significantly the number of normal yeast colonies and increased the number of damaged cells with rough and wrinkled surfaces. Because of its lipophilic nature, eugenol can enter between the fatty acyl chains of the membrane lipid bilayer, disturbing its fluidity and permeability. The authors have also highlighted that the interference with the morphology of the envelope of *C. albicans* is very relevant to the pathogenicity of these microorganisms because it can compromise the adhesion to host cells and morphological transition to hyphal form, thus reducing the ability of the fungus to colonize and infect host tissues. Another researcher, AHMAD *et al.*, (2010) have shown that ion transport of the yeast is affected by eugenol. It also inhibits the H^+-ATPase and glucose-stimulated H^+- extrusion activity of *Candida spp* at a concentration of 500 µg/mL MIC.

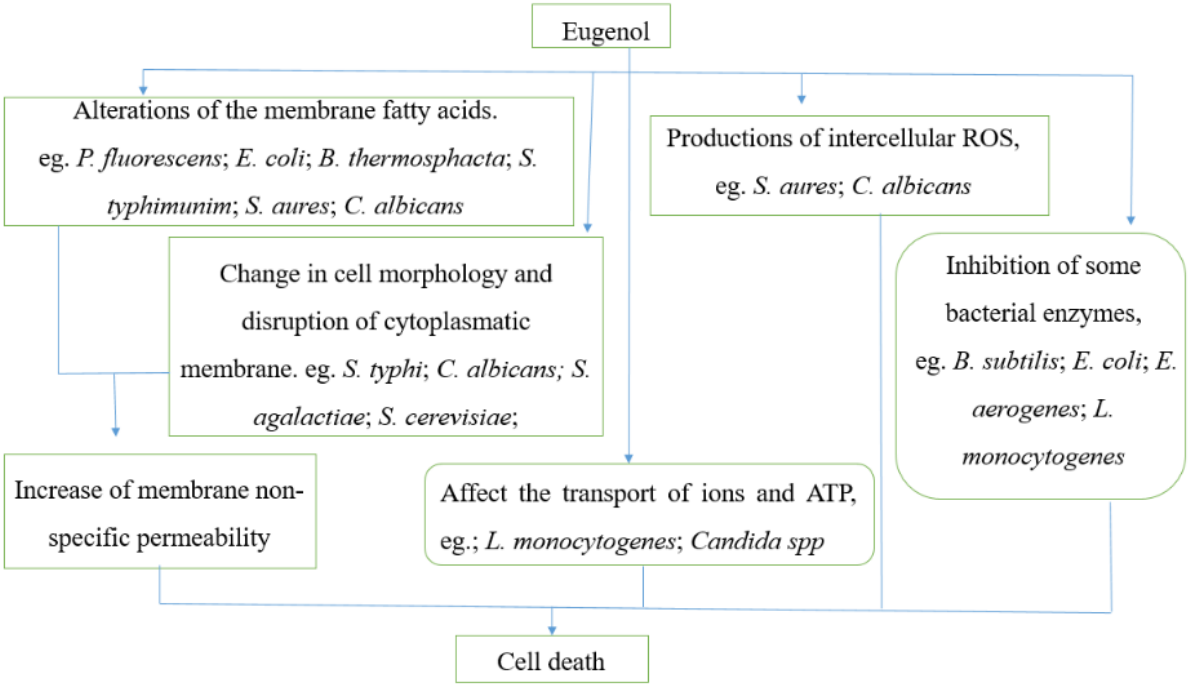

Figure 2. Effect of eugenol against bacteria and fungi.

3.3.2. Antimicrobial Activity of Carvacrol

Like eugenol, carvacrol (5-Isopropyl-2-methyl phenol) is another naturally occurring monoterpene phenolic compound. It can be extracted from commonly used traditional medicine plants of the *Labiatae* family, including *Origanum*, *Satureja*, *Thymbra*, *Thymus,* and *Corydothymus* species (ANTONIA NOSTRO; TERESA PAPALIA, 2012; SHARIFI-RAD *et al*., 2018). It can be used as a flavoring agent in several products and possesses anti-inflammatory, antioxidant, antitumor, analgesic, antihepatotoxic, and insecticidal properties (SUNTRES; COCCIMIGLIO; ALIPOUR, 2015). Besides those properties, several studies have demonstrated that carvacrol has a wide-spectrum antimicrobial activity against many bacterial and fungal, extended to food spoilage or pathogenic microorganisms, including drug-resistant and biofilm-forming microorganisms (MEMAR *et al*., 2017; VINCIGUERRA *et al*., 2019).

Similar to eugenol, the antimicrobial activity of carvacrol has been attributed to the presence of phenol groups (NOSTRO *et al*., 2004; SHARIFI-RAD *et al*., 2018). The inhibitory action of phenolic compounds is, in most cases, related to the hydrophobicity, which is directly correlated to the partition in the cytoplasmic microbial membranes (LANCIOTTI *et al*., 2003; SIKKEMA; DE BONT; POOLMAN, 1995; WEBER; DE BONT, 1996). Also, due to its hydrophobic nature, carvacrol interacts with the lipid bilayer of the cytoplasmic membrane and aligns itself between the fatty acid chains causing the expansion and destabilization of the membrane structure and increasing its fluidity and permeability of microbes (BAJPAI; SHARMA; BAEK, 2014; CRISTANI *et al*., 2007). Moreover, carvacrol causes a rapid depletion of the intracellular ATP pool of bacteria, either by reduction of the intracellular ATP synthesis or increase of ATP hydrolysis (SHARIFI-RAD *et al*., 2018).

Other researchers have investigated the relationship between the chemical structure and the antimicrobial activity of carvacrol in comparison with eugenol, menthol and two synthesized carvacrol derivative compounds, namely, carvacrol methyl ether and carvacrol acetate, ether and ester group, respectively, instead of the hydroxyl group of carvacrol, against *Escherichia coli*, *Pseudomonas fluorescens*, *Staphylococcus aureus*, *Lactobacillus plantarum* and *Bacillus subtilis* bacteria, *Saccharomyces cerevisiae,* and *Botrytis cinerea* fungi. Carvacrol, being the most hydrophobic compound, has shown stronger antibacterial activity than eugenol and menthol. The two synthesized compounds, carvacrol acetate and carvacrol methyl ether were not effective (BEN ARFA *et al*., 2006; ANTONIA NOSTRO; TERESA PAPALIA, 2012), suggesting that the

specific structural features of the carvacrol molecule are key features to its bioactivity and the presence of a free phenolic hydroxyl group coupled with its hydrophobicity is essential for antimicrobial activity (GALLUCCI *et al*., 2009). Besides, ULTEE; BENNIK; MOEZELAAR, (2002) has hypothesized that the hydroxyl group and the presence of a system of delocalized electrons are important for the antimicrobial activity of phenolic compounds, such as carvacrol and thymol. The importance of a delocalized electron system is to allow the release of protons from the hydroxyl group, which is supported by the higher antimicrobial effect of carvacrol and eugenol compared with menthol (BEN ARFA *et al*., 2006). In contrast, the delocalized electron system present in carvacrol acetate and carvacrol methyl ether implied that they are proton acceptors, but they are not able to release a proton through the ester or the ether group. Moreover, the weaker antimicrobial effect of eugenol is attributed to its low hydrophobicity and the presence of a methoxy group in the ortho position, which prevents the OH group to easily release its proton.

3.4. **Plasma and Plasma Polymerization**

3.4.1. **Plasma**

The word plasma comes from the Greek which means something molded. It is considered as the fourth state of matter and constitutes more than 99% of the visible universe (MACGREGOR; VASILEV, 2019; ZILLE; SOUTO; OLIVEIRA, 2019). The word plasma was applied for the first time by Tonks and Langmuir, in 1928 (LANGMUIR, 1928), to describe the inner and remote region of a glowing ionized gas produced by electric discharge in the boundaries of a glass tube. It is obvious that as temperature increases, molecules become more energetic and transform in the sequence: solid, liquid, gas, and plasma (JARAFAR *et al*., 2019). In the latter stages, molecules in the gas dissociate to form a gas of atoms and then a gas of freely moving charged particles, electrons, and positive ions. This state is called the plasma state. Like gas, plasma does not have a definite shape or a definite volume unless enclosed in a container. Unlike gas, under the influence of a magnetic field, it may form structures such as filaments, beams, and double layers (THESIS; AKTER, 2017).

From the commonly accepted definitions, plasma can be defined as a ´mixture´ of partially or fully ionized gas that contains charged and neutral species such as electrons, positive ions, negative ions, radicals, atoms, and molecules that express collective behavior (ZILLE; SOUTO;

OLIVEIRA, 2019). In this way, the plasma becomes a highly reactive medium (GONÇALVES, 2012). In nature, we can find plasmas in the forms of lightning, flames, stars, the solar wind, auroras, interstellar space, and among others (THESIS; AKTER, 2017; MACGREGOR; VASILEV, 2019). Artificially, humans produce plasmas using a variety of energy sources including strong magnetic fields, lasers, and electric fields (MACGREGOR; VASILEV, 2019).

In the laboratory, plasma can be created by supplying energy to a gas or a mixture of gases or vapors (SIMENI *et al*., 2017; CHNG *et al*., 2019). Man-made plasmas are nowadays seen everywhere from commodities such as TV screens, toys, and low energy lighting to nuclear reactors and spacecraft propulsion turbines. Currently, plasmas have been widely applied in many fields of research, technology, and industry, for the treatment of wastes, and, more recently, in medical applications, for the conversion of bio-renewable ethanol, and hydrogen production (ZHOU *et al*., 2020; LYTLE *et al*., 2019; AL-JUMAILI *et al*., 2019; KULAWIK; KUMAR TIWARI, 2019; CAO *et al*., 2016; PARK; CHA; UHM, 2018; LEE *et al*., 2016; CHEN *et al*., 2019).

When plasma species come in contact with solids, such as metal, plastic, or any other material, they can cause important changes on the material surface properties without changing their bulk properties (MACGREGOR; VASILEV, 2019). In this way, it is possible to use plasma-assisted processes to modify surface energy, wettability, chemistry, and even topography, to suit the requirements of a variety of applications, without affecting the bulk properties of the material (BAZAKA *et al*., 2011a; BAZAKA *et al*., 2015b). Several researchers (BOSE; ROBERTSON; BANDYOPADHYAY, 2018; MINATI *et al*., 2017; GAN; BERNDT, 2015) have described some detail of plasma-assisted surface modifications for the specific case of metallic biomaterials surface, such as, (1) chemically or physically altering the surface at the atomic or molecular scale, and (2) coating a surface with a material of the different composition. Generally, modification techniques can be classified into three categories, depending on the characteristics of the surface transformation: (1) removal of materials, such as plasma etching and sputtering; (2) chemical and structural modifications of materials, such as plasma immersion ion implantation; and (3) addition of materials, such as plasma polymerization and plasma immersion ion implantation and deposition (SABOOHI *et al*., 2017; BORMASHENKO *et al*., 2015).

Plasma sputtering is the removal of materials from the surface of the solid substrate through momentum transfer via bombardment by ions of inert gas, typically argon. The ions are generated by a glow discharge that is initiated and maintained with an applied electric potential between an anode and a cathode (SZABO *et al*., 2018). Sputtering is often used as a pretreatment to remove contaminants, such as oxides, for subsequent implantation, and as deposition processes as well (GAN; BERNDT, 2015). On the other hand, plasma etching, another process that causes material removal, occurs when chemical reactions between species in the discharge and on the surfaces exposed to the plasmas result in volatile byproducts (DONNELLY; KORNBLIT, 2013; PULIYALIL; CVELBAR, 2016). In plasma etching, reactive particles from the plasma adsorb on the material exposed to the discharge forming chemical bonds with atoms at the surface. Depending on the chemical reactions involving plasma and surface species, the produced molecule may subsequently be desorbed from the surface transferring material from the surface to the gas phase. Plasma etching is commonly used to pattern microelectromechanical devices (HU *et al*., 2012; SONG *et al*., 2014), but it has also been applied to biomaterials to improve the surface topography and bio-functionality (PULIYALIL; CVELBAR, 2016; VALIEV; PARFENOV; PARFENOVA, 2019; GANJIAN *et al*., 2019). The combination of processes has also been reported where anisotropic chemical etching is accelerated by ion sputtering (VON KEUDELL; CORBELLA, 2017). In biomaterials engineering, plasma is generally used for surface cleaning and sterilization, but at its extreme, plasma etching can also be used for surface roughening and nanopatterning, and even generating novel nanostructures (ALVES; ALBANO; DE OLIVEIRA, 2017; MESA *et al*., 2019).

Plasma ion implantation introduces elements in the surfaces through the collision of high-energy ions. The ions are accelerated by voltages typically between 0.5 and 20 kV towards the sample surface. This process operates in a vacuum environment and has a relatively shallow treatment depth since the ions are only able to penetrate solid materials up to several nanometers (CUI; LUO, 1999; LU; QIAO; LIU, 2012). At last, is plasma polymerization, which involves the formation of high-molecular-weight solid material organic compounds through activation mainly by collisions of energetic plasma electrons. The plasma is used to induce the formation of radicals at solid surfaces or in the gas phase, which are then randomly recombined to form a material commonly referred to as plasma polymer. It differs from the other plasma-assisted surface modification by the fact that a thin coating is formed on the surface of the original

material. Therefore, surfaces with properties completely different from those of the bulk can be generated via plasma deposition (SABOOHI *et al*., 2017).

3. 4.2. **Types and Generation of Plasma**

Plasma can be classified in various ways, such as atmospheric- and low-pressure plasma based on the gas pressure, hot and cold plasma based on the temperature of electron and ions, and electropositive and electronegative gas plasma depending on the gas electron affinity (PIAVIS; TURN; ALI MOUSAVI, 2015; CONRADS; CHNG *et al*., 2019; HERTWIG; MENESES; MATHYS, 2018).

In atmospheric-pressure plasmas, the collision rate is much higher than in low-pressure plasmas and the kinetic energy transfer from electrons to heavy ions and natural particles becomes more efficient. Therefore, under such conditions, the charged species within the plasma achieve thermal equilibrium, which includes kinetic equilibrium ($T_e \approx T_h$ where T_e = electron temperature and T_h = heavy particle temperature). In contrast, in low-pressure plasmas, the gas density is low and, consequently, the collision rate is not high enough to increase the gas temperature. In this circumstance, electrons, neutral species, and ions achieve their equilibrium independently, with the former at a faster rate (FRIEDRICH, 2012; WANG *et al*., 2018). That is, the electrons remain highly energetic, with average temperatures ranging from 10^4 to 10^5 K, while the heavy particles are near the ambient temperature.

Additionally, atmospheric-pressure plasmas fall into two distinct categories, thermal plasmas, such as the electric arcs, and non-thermal atmospheric plasma, such as DBD (TANAKA *et al*., 2017; KÜHN *et al*., 2010). The latter has a very high electron temperature, T_e, but the ion and gas temperatures remain close to ambient temperature ($T_e >> T_{ion} \approx T_{gas}$). It has also a high density of reactive species, such as free radicals and atoms in excited states. Thus, DBD discharges contain a significant amount of species able to change surface properties of a substrate, even those made from normally inert materials such as ceramics and polymer (MOKHTAR, 2018; ARJUNAN; SHARMA; PTASINSKA, 2015).

Atmospheric pressure plasmas are generated by the application of high voltages to a gas leading to a self-sustained discharge maintained by the applied electric field. As described fully by CASTELL; IGLESIAS; RUIZ-CAMACHO, (2004), during the applying of a potential difference, a subsequent electric field pulls the bound electrons toward the anode while the

cathode pulls the ion. As the voltage increases farther, the current stresses the material by electric polarization beyond its dielectric limit into a stage of electrical breakdown, marked by an electric spark, where the material transforms from being an insulator into a conductor.

3.4.3. **Dielectric Barrier Discharge**

Low-pressure (LP) plasmas are the most common type of gas discharge mainly due to their simple experimental setup and versatility (DURRANT, 2018; THIRY *et al*., 2016). However, the large-scale application of low-pressure plasmas is mainly limited by the high cost of vacuum systems and also by the impossibility of using high vapor pressure materials, such as living tissues, for instance (FIEBRANDT; LACKMANN; STAPELMANN, 2018). As a result, several alternative atmospheric or sub-atmospheric pressure plasma techniques, such as corona plasma, micro hollow cathode discharges, plasma torch, and dielectric barrier discharges (KAYAMA *et al*., 2017), have emerged to overcome the limitations of LP plasmas. Among the various types of plasma, the dielectric barrier discharges have drawn much attention due to peculiarities, such as low instrumental costs and easy handling and operation (LAROUSSI; LU; KEIDAR, 2017; STRYCZEWSKA *et al*., 2013).

Atmospheric pressure DBD can produce diffuse and relatively homogenous non-thermal plasma (SUBLET *et al*., 2006), which can be applied in various fields. For instance, DBDs have been used for the production of nitric acid and ammonia (BARBOUN; C. HICKS, 2020; MALIK *et al*., 2016), and in various medical and biological applications, including wound healing, tissue regeneration, blood coagulation, tooth bleaching, and cancer treatment (KIM; CHUNG, 2016; YANG *et al*., 2015; HAERTEL *et al*., 2014; FRIDMAN *et al*., 2008; KIM *et al*., 2010; IRANI *et al*., 2015). DBD´s have also been used in agriculture as treatment of seeds to enhance the germination rate, plant growth, and crop yield, and for controlling plant disease (KYZEK *et al*., 2019; AMBRICO *et al*., 2020; ZAHORANOVÁ *et al*., 2018; SAJIB *et al*., 2020). Furthermore, DBDs have many applications including sterilization (DORIA *et al*., 2016; MACKINDER *et al*., 2020), for clean fuel production (LIU *et al*., 2014a; SASUJIT; DUSSADEE; TIPPAYAWONG, 2019), bacteria inactivation (BOURKE *et al*., 2017; SARANGAPANI *et al*., 2018; HAN *et al*., 2016), for surface treatment and modification of biomaterial (BORMASHENKO *et al*., 2015; TREJBAL *et al*., 2018), thin-film deposition (LEE *et al*., 2016; KAKIUCHI; OHMI;

YASUTAKE, 2014), and decontamination of waste-water (RYAN; STALDER; WOLOSZKO, 2013).

The dielectric barrier discharge is a non-thermal atmospheric plasma discharge, in which at least one of the two flat/cylindrical metal electrodes are covered with a non-conducting dielectric material such as glass, quartz, ceramics, and polymers, to avoid conduction current and the transition of the plasma discharge into an arc discharge (KOGELHEIDE *et al.*, 2019). The current in the gap is due to the variation of the electric field with time (displacement current = (ε_0 dE/dt)X area of electrodes, where ε_o is the vacuum permittivity)). Typically, they are operated with sinusoidal wave current, square wave current, or pulse waveforms with frequency in the range of 60 Hz to 13.5 MHz. The discharge produces highly non-equilibrium plasmas in a controllable way at moderate gas temperature. It can be classified as surface and volume plasma discharge (YU *et al.*, 2019; BRANDENBURG, 2017; HONG *et al.*, 2014). Surface discharge is arranged in such a way discharge will develop on the surface of a dielectric, with two electrodes placed on each side of a sheet, apart from each other (GALMIZ *et al.*, 2015). The volume discharge is arranged with two electrodes, one of them covered by a dielectric, and the discharge evolving in the gap of the electrodes (CHIRUMAMILLA *et al.*, 2016; TANG *et al.*, 2019). This method can be configured either in planar or cylindrical configurations (Fig. 3).

The DBD has great flexibility concerning its geometrical shape, working gas mixture composition, and operating parameters (e.g. power input, frequency of feeding voltage, pressure, and gas flow) (WANG *et al.*, 2012; NIU *et al.*, 2015; CHIRUMAMILLA *et al.*, 2016). In many cases, when these parameters have been optimized before in small laboratory devices, there are no problems in scaling up the conditions to larger (industrial) dimensions. Moreover, the plasma consists of electrons, positive and negative ions, free radicals, and excited or non-excited molecules and atoms, it also generates ultraviolet (UV) photons. In combination, these particles can break covalent bonds and initiate various chemical reactions. The ability to treat or coat surfaces at low gas temperatures and pressures close to the atmosphere is an important advantage for any application, as described above (KIM; LEE; MIN, 2014; ABDI *et al.*, 2019).

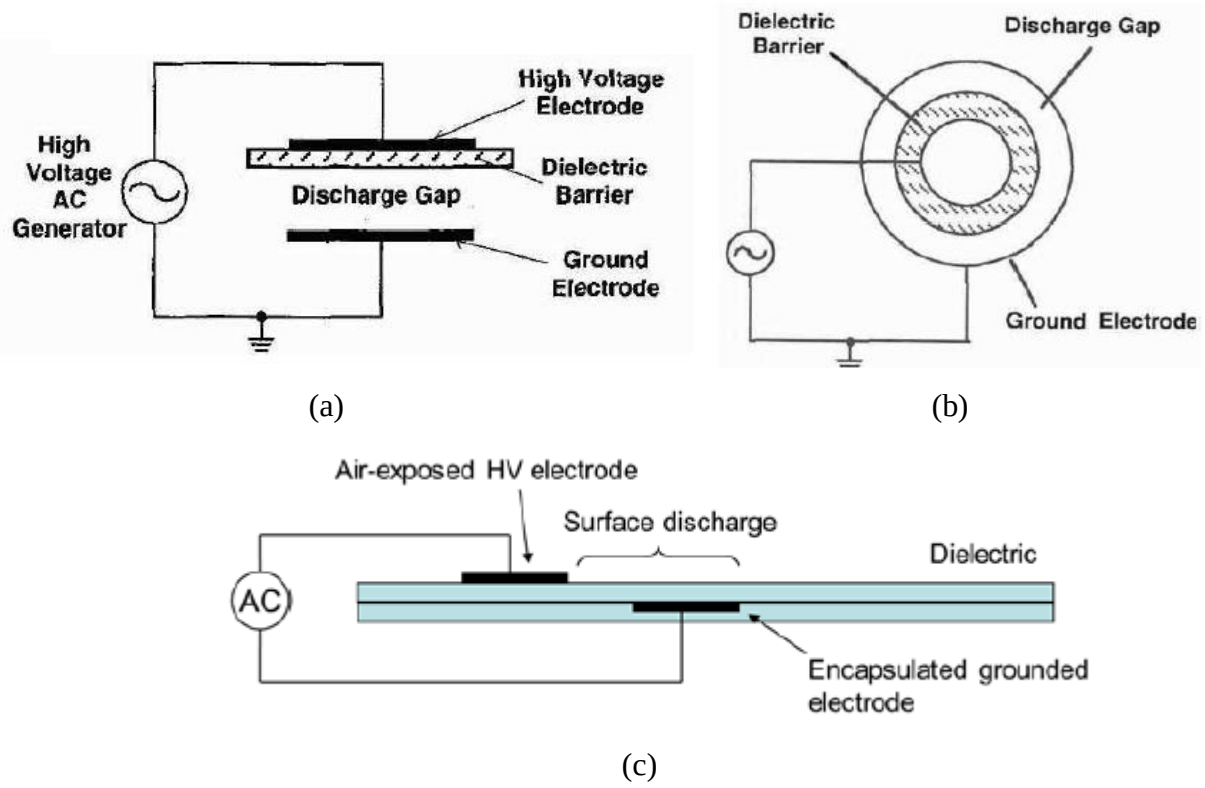

Figure 3. Schematic of the different configurations of volume DBD (a) planar and (b) cylindrical and (c) surface.

Adopted from (BRANDENBURG, 2017)

3.4.4. **Plasma Polymerization**

Polymerization is a process to form a polymer by the combination of repeating functional units, called monomers. It can be classified as conventional polymerization and plasma polymerization (VANDENBOSSCHE; HEGEMANN, 2018). In conventional polymerization reactions, only monomers with active double bonds or reactive functional groups will polymerize. It can be polymerized either in condensation or addition mechanisms. But, every organic molecule is not possible to be polymerized with these two methods, which have low reactivity and also are not biodegradable. The other way to polymerize organic molecules is the "Plasma Polymerization" technique. Plasma polymerization involves the formation of a high-molecular-weight polymer from its monomers through activation by an energetic plasma species (YURTCAN; KHANGHAH, 2019; MACGREGOR; VASILEV, 2019; VANDENBOSSCHE;

HEGEMANN, 2018). It increases the degree of crosslinking of the polymer, so its structure compared to the conventional polymer is different (LIGOT *et al.*, 2015).

It is important to stress that the deposition process of any organic material using plasmas is commonly referred to as "plasma polymerization" and, consequently, the material so produced is known as "plasma polymer", even when the film does not have any repetitive unity (FRIEDRICH, 2011; VANDENBOSSCHE; HEGEMANN, 2018). The structural difference between conventional polymer and plasma polymer is shown in Fig. 4. Finally, plasma polymerization is low-cost and environmentally friendly, has the versatile technique for fabricating organic thin films from a wide array of organic and synthetic materials, including those that do not normally polymerize via conventional pathways (LIU *et al.*, 2014b).

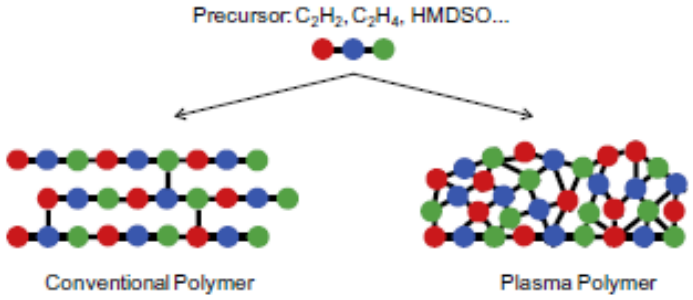

Figure 4. Comparison of a conventional polymer (left) consisting of repeating units with a plasma polymer (right) showing a branched, cross-linked network, here derived from equivalent precursors (monomers).
Adopted from VANDENBOSSCHE; HEGEMANN, (2018).

Plasma-enhanced chemical vapor deposition (PECVD) is one of the most common plasma polymerization techniques. Such plasma-assisted deposition is one of the coating techniques used to form thin polymer-like films on surfaces of solid substrate either by low pressure or atmospheric pressure plasma reactor (HEGEMANN *et al.*, 2016). At a low-pressure regime, the monomer precursors in the vapor are inserted in the discharge giving rise to a wide range of mechanisms including fragmentation, oligomerization, rearrangement, and polymerization (YASUDA; IRIYAMA, 1989). After igniting plasma, a large number of species that exist in the discharge (e.g. ions, electrons, stable molecules, radicals, and photons) can react with each other forming chains and finally adsorb onto a substrate surface depending on their sticking probabilities (MICHELMORE *et al.*, 2016). The properties of the polymeric film are not only determined by precursors but also by the deposition parameters (WALTON; GREENE, 2010;

MICHELMORE *et al*., 2016). The fragmentation is initiated by active electrons rather than thermal excitation or chemical reaction, creating a unique mixture of chemically-diverse species (e.g. unsaturated bonds, ions, neutrals, free radicals), which may not be reachable under other conditions (KUMAR *et al*., 2018). These free radicals and excited molecules condense and polymerize on the substrate to form high cross-linked films. Moreover, during plasma treatment, a constant bombardment of energetic particles (ions and fast neutrals) as well as a constant ultraviolet (UV) irradiation allows the restructuring of the growing plasma polymer film (more details regarding plasma deposition mechanisms have already been described in several excellent reviews (THIRY *et al*., 2016; KHELIFA *et al*., 2016; CORBELLA; GROSSE-KREUL; VON KEUDELL, 2015).

Regarding the film growth mechanisms of plasma polymerization of most organic compounds, many of which are not considered monomers of conventional polymerization reactions, are completely different from those of conventional polymerizations. For the first time, the plasma polymerization growth of such a type of polymer was explained by (YASUDA; WANG, 1985) as follows. Yasuda proposed the bicyclic rapid step-growth polymerization as shown schematically in Fig. 5, in which the reactive species are represented by free radicals; however, any other reactive species can contribute to each step. The same charged ions cannot react to each other and an equal number of positive and negative charge ions are needed in the growing mechanisms of the film. Therefore, the role of the ion can be excluded. The single reactive species or divalent reactive species can be polymerized with monomer by shifting the radical center and leaving it open for more polymerization process. Cycle I in the figure consists of activation reaction products from single reactive site species, and cycle II is propagated by divalent reactive species.

The reactions numbers 1 and 4, in Fig.5 show the addition of reactive species to the monomer or other reactive species which is the same as observed during the initiation and propagation reaction in the chain growth free radical polymerization. Reaction 2 shows the formation of the oligomer (the combination of a few monomer units) by losing its radical center, which is the same as the termination reaction in the chain growth free radical polymerization. Moreover, reaction 3 combines single reactive species with divalent reactive species by the cross-cycle reaction and the presence of a radical center shows the continuity of polymerization reaction. Reaction number 5 in the figure shows divalent reactive species that can react with

other divalent species to form a new bond while leaving additional reactive sites for further polymerization. When repeating these steps, the size of the gaseous species increases, and the saturation vapor pressure of the species decreases, which forces the species to be deposited on the substrate in the form of the polymer. The cycle may repeat or propagate through the formation of radicals on the already-deposited polymer.

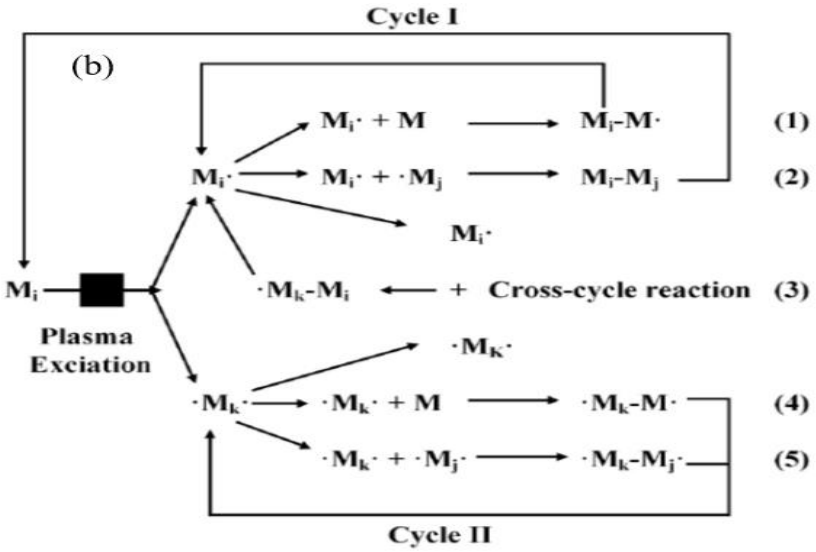

Figure 5. Growth and deposition mechanism of plasma polymerization.
Adopted from YASUDA; WANG, (1985).

4 General Experimental Procedures

4.1. **Sample Preparation**

Before depositions, 1 cm × 1 cm SS samples were cut using a metal cutter from a 1 mm thick SS sheet. Subsequently, the samples were mirror-polished by different grades of waterproof sandpapers that were in the sequence 600, 1000, and 1200 (HUACHO *et al*., 2017) and then cleaned in ultrasonic baths using detergent, distilled water, and isopropyl alcohol. Finally, the samples were dried with a hot air gun and stored in Petri dishes until use (MANCINI *et al*., 2013).

4.2. Description of the experiment

The dielectric barrier discharge plasma reactor used for the deposition of carvacrol- and eugenol-derived films is shown schematically in Fig. 6. It consists of cylindrical brass (2 cm in diameter) and aluminum disk (5.6 cm in diameter) electrodes, a polyester (mylar) sheet between them, and a 15 kV@220V transformer. The electrodes were assembled axially with a 3 mm gap and held by circular polyacetal (Delrin) flanges. Operating in the vertical position, the voltage was applied on the upper cylindrical brass electrode with the lower aluminum disk grounded. The discharge volume in the gap was protected from the environment by a 3 mm high, 40 mm diameter cylindrical, transparent polyethylene terephthalate (PET) disk with apertures for the exit of the injected gas or mixture. The output of a neon lamp transformer with 20 kV peak-to-peak voltage with the primary circuit controlled by a variac, at 60 Hz frequency, was applied to the upper electrode.

An atomizer with controlled temperature and gas flow rate was used to admixture the argon gas (99.9% purity) with the vapor of the monomer. This mixture was injected through an axial hole at the center of the upper electrode.

The applied voltage was measured with a voltage divider made with an array of 24 x330 kΩ resistors and an 8.1 kΩ load resistor, all connected in series. The discharge current $i(t) = v_r(t)/R$ and discharge charge $q(t) = Cv_c(t)$ were determined by measuring the voltage drop, $v_r(t)$ and $v_c(t)$, on a resistor with resistance R=57 Ω and a capacitor with capacitance C =10 nF, respectively. They are connected in series with the discharge with the ground. The signals were displayed and recorded using a 30 MHz and 500 MS/s sampling rate of two-channel digital storage oscilloscope Tektronix TDS1001C-30EDU.

The power P of the discharge was calculated using:

$$P = \frac{1}{T}\int_0^Q v_A dq \qquad , v_A \gg v_C \qquad (1)$$

where v_A is the applied voltage, v_C the voltage on the capacitor, T the period, Q the charge in one period, and q the instantaneous charge.

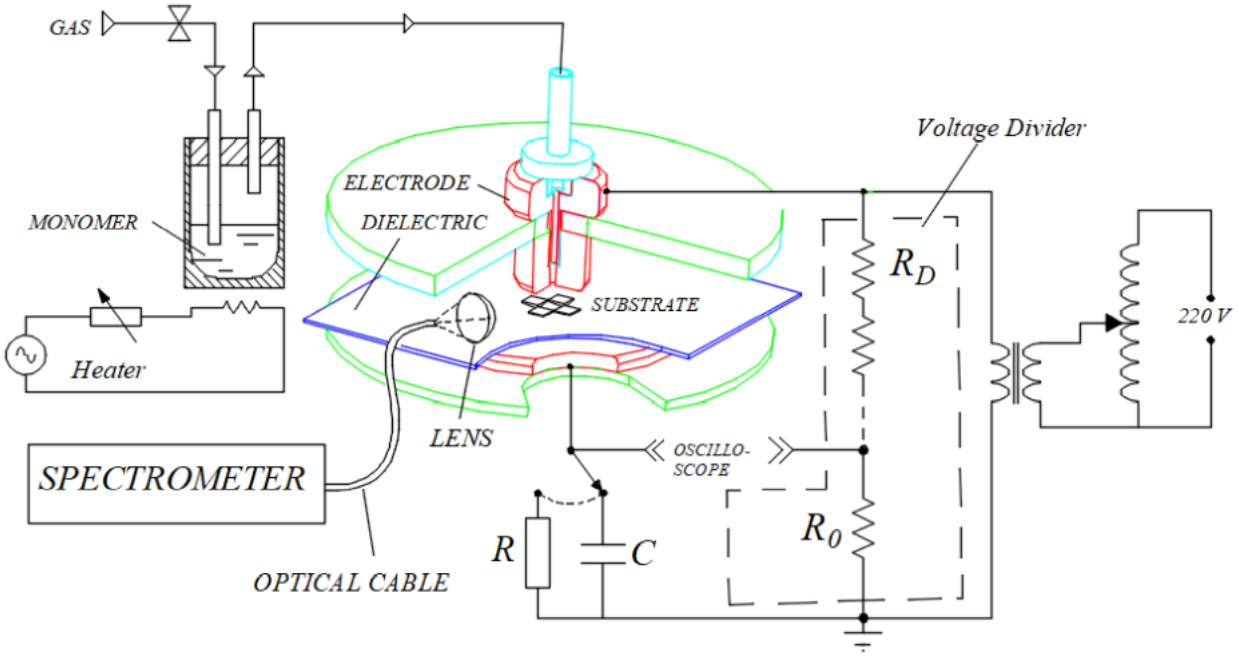

Figure 6. Schematic representation of the experimental setup used for film deposition and discharge characterization

The optical emission was measured by using an Ocean Optics spectrometer USB4000 connected to a computer. The spectrometer was connected to an optical cable and the light was collected by a collimating lens located 3 mm from the edge of the electrode as shown in Fig. 6. Electron temperature T_e was estimated using the Boltzmann plot method assuming local thermodynamic equilibrium (LTE) (KUO *et al*., 2006; JIN *et al*., 2013).

Film chemical structure, aging, and degradation were characterized by infrared reflectance absorbance spectroscopy (IRRAS), using a Jasco FTIR 410 spectrometer with 128 scans in the resolution of 4 cm^{-1}. The surface morphology of the film was inspected by scanning electron microscopy (SEM) Jeol JSM-6010LA, at 3 kV of an acceleration voltage of the electron beam corresponding to a beam diameter and working distance of 3.5 nm and 11 mm, respectively. The technique of energy-dispersive x-ray spectroscopy (EDS) was performed with a Dry SD Hyper

detector EX-94410T1L11, coupled with a scanning electron microscope, to characterize the chemical composition of the films. The energy-dispersive spectra were also acquired with 5 and 10 kV electron beam energy, which corresponds to a beam diameter and working distance of 6 nm and 10 mm, respectively. To avoid charging effects during the SEM inspections, samples were coated with a thin conducting layer of a golden-palladium produced by Ar-sputtering at 30 mA, 7 Pa gas pressure, and 60 s deposition time, in a Denton Vacuum HP Desk V system. Surface topography of the thin film was also evaluated by atomic force microscopy, Shimadzu SPM 9600, in non-contact mode operating with a stereomicroscope Zeiss lens of 100X magnification systems. The 3D and 2D images were acquired in the projection area of 10 μm x 10 μm within 512 scan points in each direction. The thicknesses and the roughness of the films were also determined with a surface profilometer, Veeco DEKTAK 150. To perform the measurements, the films were deposited on a partially covered stainless steel slide with a 3M-5413 Kapton tape mask, to protect half of its surface. The height of the step after removing the tape was measured with the aid of the profilometer and corresponds to the thickness of the film. For each sample, thickness and roughness were measured at least 10 times in different locations of the step. The wettability and surface energy of the films were analyzed using droplets of deionized water and diiodomethane in a goniometer Ramé-HART 100 and RHI 2001 image program. Finally, the film applicability was performed for corrosion-resistant with 3.5 wt.% NaCl corrosion solution and biofilm suppuration assay against *S. aureus, P. aeruginosa, and E. Coli* bacteria, and *C. albicans* fungus.

Article 1

Lecture Notes of the Institute for Computer Sciences, Social Informatics and Telecommunications Engineering, vol 308, pp. 716–725, 2020.
https://doi.org/10.1007/978-3-030-43690-2_55

5 Plasma Polymer Deposition of Neutral Agent Carvacrol on a Metallic Surface by Using Dielectric Barrier Discharge Plasma in Ambient Air

Tsegaye Gashaw Getnet[1,2], Nilson C. da Cruz[1], Milton E. Kayama[3], and Elidiane C. Rangel[1]
[1]Technological Plasmas Laboratory, São Paulo State University, Experimental Campus of Sorocaba, Sorocaba, SP, Brazil, [2]Department of Chemistry, College of Science, Bahir Dar University, Bahir Dar, Ethiopia, [3]Laboratory of Plasma and Applications, Sao Paulo State University, at Guaratinguetá Campus, Guaratinguetá, SP, Brazil.

Abstract: *This experiment was conducted by a newly designed home-made planar type dielectric barrier discharge plasma generator in ambient, with industrial argon as the primary plasma-forming and a monomer carrier gas. Natural agent carvacrol monomer was used as a precursor to depositing plasma polymeric thin film on the surface of metallic material. The discharge characteristics including, the effective power, the discharge voltage, and current were diagnosed. The applied voltage was measured by using a voltage divider and the current and the discharge-charge were measured by using the drop of voltage on a resistor and capacitor, respectively. The characteristics of the thin film deposited were presented by varying discharge conditions. The structures of the film, aging, and adhesion were characterized by infrared reflectance spectroscopy and its thicknesses and roughness by profilometry. The obtained film was exhibited smooth, dense, uniform, and having chemical similarity to that of the carvacrol. The obtained film also exhibited a high thermal resistivity, crosslink with good adhesion to the metallic surface. In general, the film produced in the present methods can be used for practical application as the surface of a biomaterial.*

Keywords: Dielectric barrier discharge, Plasma diagnostics, Plasma polymer.

1. Introduction

Research in the field of low-pressure plasma has gained emphasis, mainly due to its versatility and the various results obtained in the modification of material physical and chemical properties (ALVES *et al*., 2005). However, the large-scale application of low-pressure plasma is mainly limited to the high cost of vacuum installations, and also on the restriction to not be used

in high vapor pressure materials such as living tissues (KANAZAWA *et al*., 1989; YOKOYAMA *et al*., 1990). As a result, several alternative atmospheric or sub-atmospheric pressure plasma techniques, such as corona plasma, and micro hollow cathode discharge, plasma torch, and dielectric barrier discharge (DBD) (NAPARTOVICH, 2001; KAYAMA *et al*., 2017), are available nowadays to overcome these limitations since they do not require vacuum systems. Among those various types of plasma sources, atmospheric pressure DBD plasma sources have drawn more attention due to their many advantages, such as low-cost and easy handling and operation (LAROUSSI; LU; KEIDAR, 2017). In atmospheric pressure, DBD's can produce diffuse and relatively homogenous non-thermal plasma (KANAZAWA *et al*., 1988; MASSINES *et al*., 1998; YOKOYAMA *et al*., 1990). However, there is a need to improve the stability and repeatability of the discharge for practical and industrial applications. In addition to this, as far as our knowledge, there is no study of the atmospheric pressure plasma discharge of volatile natural agents to produce polymeric films. In this context, the present study was to investigate the use of carvacrol DBD plasma to produce films on the stainless steel (SS) surface. This work also deals with the diagnosis of the argon discharge in the presence and absence of carvacrol. We choose SS as a substrate due to its extensive use in many technological and biomedical applications and consumer products.

2. **Experimental Device and Operations**

2.1. Plasma Diagnosis

In this present study, the DBD equipment was designed and built at the Laboratory of Technological Plasma (LaPTec) of São Paulo State University, Sorocaba, Brazil. It consists of cylindrical brass with 2 cm in diameter and aluminum disk upper and lower electrodes, respectively. The electrodes were assembled axially with a 3 mm gap and held by circular polyacetal (Delrin) flanges (Fig. 1). The outer surface of the lower electrode was covered by a 0.1 mm thick polyester (Mylar) dielectric sheet and served as a sample holder. An atomizer with controlled temperature and gas flow rate was used to admixture the gas and the monomer that was injected through an axial hole in the upper electrode. Argon gas was used because with ambient air in the gap it was not possible to produce filamentary discharge. The output of a neon lamp transformer with 20 kV peak-to-peak voltage with the primary controller by a variac, at 60 Hz frequency, was applied on the upper brass electrode, while the lower one was grounded. The

voltage was measured with a voltage divider made with an array of 24×330 kΩ resistors and an 8.1 kΩ load resistor, all connected in series. The current *i(t)* of the discharge was measured through the voltage drop on a resistor with resistance R = 57 Ω connected between the lower electrode and the ground. The resistor was replaced by the capacitor C = 10 nF to measure the charge produced by the discharge. The signals were displayed and recorded using a 30 MHz and 500 MS/s resolution of two-channel digital storage oscilloscope Tektronix TDS 1001C-30EDU to calculate the effective plasma power as follows:

$$P_R = \frac{1}{T}\int_t^{t+T} v_A i dt \quad , v_A \gg v_R \qquad (1)$$

$$P_C = \frac{1}{T}\int_0^{Q} v_A dq \quad , v_A \gg v_C \qquad (2)$$

where v_A is the applied voltage, v_R the voltage on the resistor, v_C the voltage on the capacitor, T the period, Q the charge in one period in the capacitor, and q its instantaneous charge.

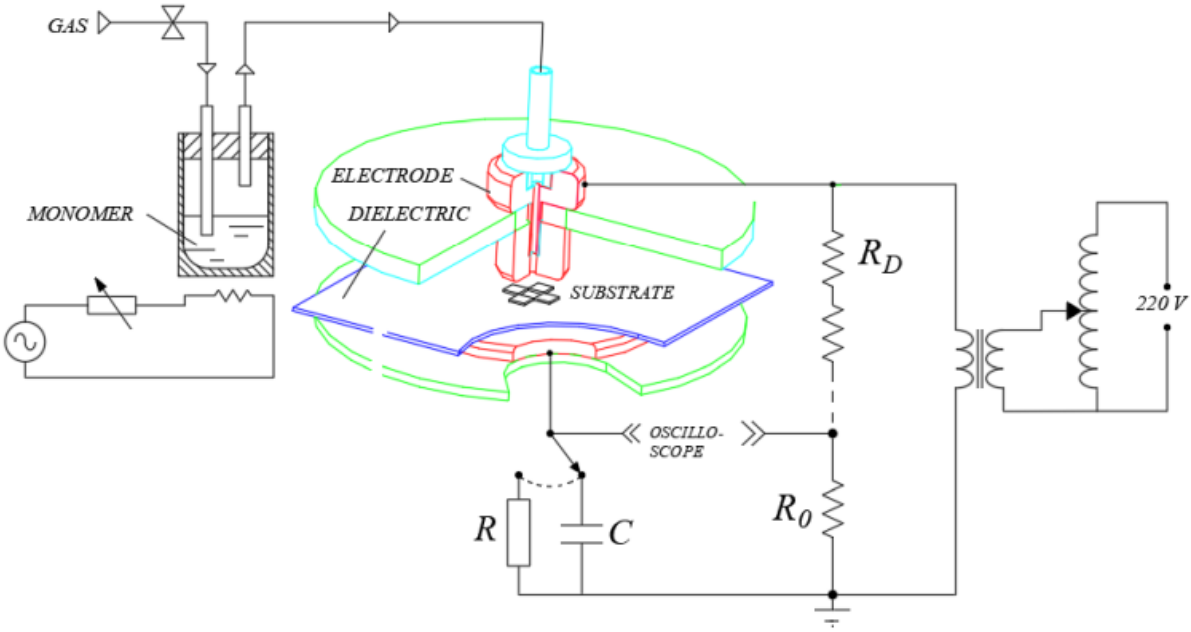

Figure 1. Schematic representation of the experimental setup.

The chemical structure, aging, adhesion, and thermal resistivity of the films were evaluated by infrared reflectance absorbance spectroscopy (IRRAS), using a Jasco FTIR 410 spectrometer and co-adding 128 spectra with a resolution of 4 cm^{-1}. The thicknesses and roughness of the films were determined with a Veeco Dektak 150 surface profilometer.

2.2. Numerical Program

The block diagrams for the numerical calculations of the Eqs. (1) and (2) are shown in Fig. 2, codes named POWER-VI and LISSA, respectively. They were written to process the digitalized even with a high signal to noise ratio. The calculation during one period is repeated as many times as possible on the recorded data. POWER-VI uses a smoothing algorithm for the applied voltage signals maintaining the original current signal. In LISSA, both signals, the applied voltage, and the capacitor voltage are smoothed by different methods. Power is calculated only on well-defined Lissajous figures. Noisy or ambiguous figures are disregarded.

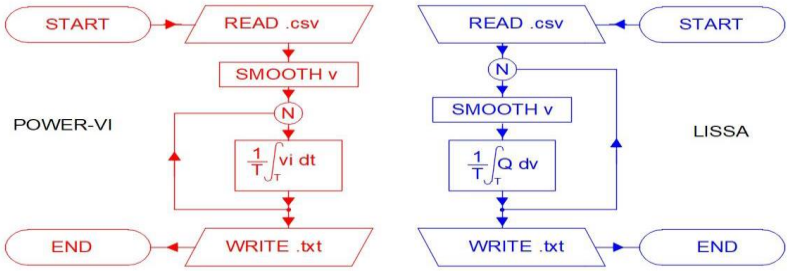

Figure 2. Block diagrams of the numerical programs

3**. Result and Discussion**

3.1. Electrical Characteristics

3.1.1. Voltage and Current Waveforms

The electrical behavior of the DBD plasma was characterized by the measurement of the applied voltage of the discharge, on the capacitor and resistor (XIAO *et al*., 2014; NI *et al*., 2008, KAYAMA et al., 2017). In this work, the applied voltage was gradually increased by a variac at the primary of the transformer. When the applied voltage reached the breakdown voltage of argon gas, the discharge was ignited with discrete filaments in the gap between the upper electrode and the dielectric. Figures 3(a) and 3(b), respectively, show a typical of the waveform of the current and applied voltage of the discharge of argon without and with carvacrol plasma at the peak-to-peak voltage of 10.0 *kV* and 5 L/min gas flow rate. According to these results, the discharge current curve shows several peaks with a very short time duration per each half cycle of the applied voltage, which indicates the filamentary mode of the discharge (GHERARDI *et al*., 2000; ZHOU *et al*., 2019). This is in agreement with the photographic image of the discharge as shown in Figs. 4(a) and 4(b), in the same discharge condition. These images also illustrate that

the filamentary discharge covers the entire surface of the electrode and is uniform to the human eyes.

When we compare the discharge of pure Ar and Ar with monomer, there was no significant variation on the images, only a slightly brighter image was observed when the monomer is present in the discharge, because of the monomer fragmentation into the discharge. It is interesting to point out that the discharge regime of the argon DBD plasma was not altered by the addition of a carvacrol monomer and works well for polymer deposition. However, the uniformity and intensity of the discharge are highly affected as we change the amplitude of the applied voltage, the gap of the electrodes, and the flow rate of the gas. That is when we increase the applied voltage keeping constant flow rate and gap distance, the intensity, and uniformity of the filamentary discharge increase in the gap between the upper electrode and dielectric, as a consequence of the increase in the electric field and electron density (QIAN *et al*., 2010). Similar phenomena were also observed for the increment of the flow rate of the gas. When we increased the gap, the more powerful filamentary discharge was produced from the center of the upper electrode. On the other hand, when we place the metallic substrate in the gap, as we can see in the image of the DBD plasma discharge in Fig. 4(c), the discharge concentrates around the substrate. This is due to the distortion of electric field lines promoted by the sharp borders of the substrate. These results are similar to the previously reported helium DBD plasma (GULATI *et al*., 2012).

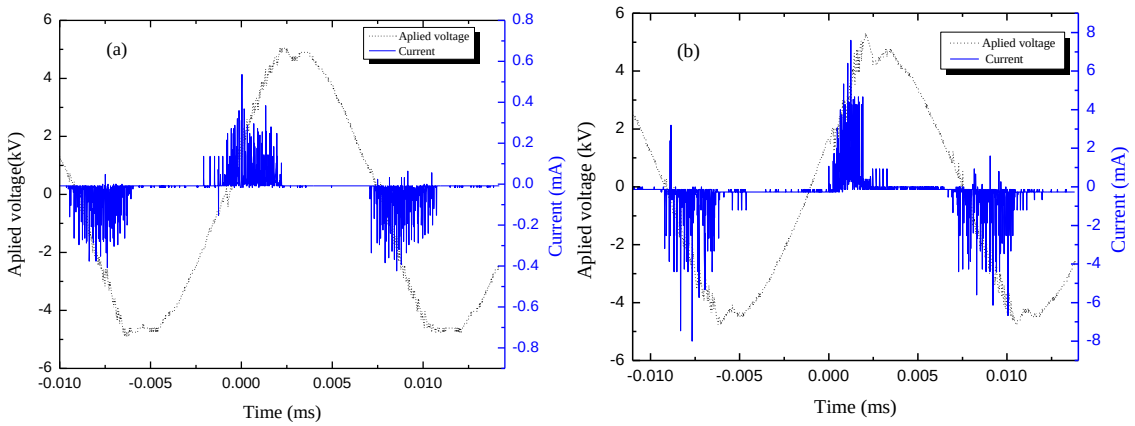

Figure 3. Voltage and current waveforms of dielectric barrier discharge plasma measured at 10.0 *kV* peak-to-peak voltage and 5 L/min gas flow rate of (a) argon only, (b) an admixture of argon and carvacrol.

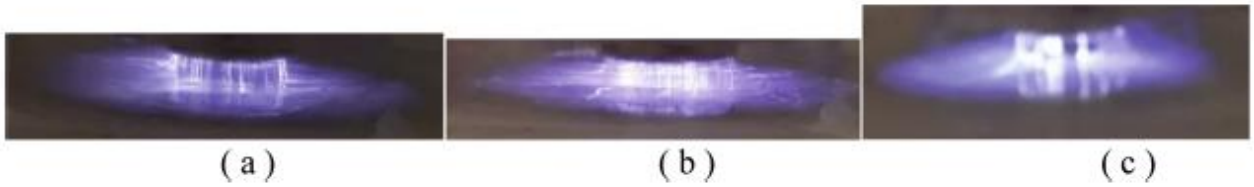

Figure 4. Images of a DBD plasma produced at 10.0 kV peak-to-peak voltage and 5 L/min gas flow rate of (a) argon only, (b) an admixture of argon and carvacrol, and (c) an admixture of argon and carvacrol in the presence of SS substrate.

3.1.2. Lissajous Figures

To further analysis of the electrical characteristics, the *Q-V* plots or the Lissajous figure were studied, as illustrated in Fig. 5. To generate the Lissajous figure, the x-axis is the applied voltage in the DBD electrodes, and at the y-axis is the charge in the capacitor $q(t) = CvC(t)$. Regarding the shape of a Lissajous figure, it looks like a parallelogram as shown in Fig. 5(a). In the Lissajous figure, the lines AB and CD represent the phase when no plasma is ignited, while lines DA and BC the phase when the plasma is formed in the gap. The slope of these lines indicates the approximate value of effective capacitance (GHERARDI *et al.*, 2000; GULATI *et al.*, 2012). As we can see in the Lissajous figures, the area of the discharge increases when we place the metallic substrate in the gap, keeping the same remaining discharge condition. It indicates an increase in the mean plasma power because of the distortion of electric field lines promoted by the sharp borders of the substrate (WANG *et al.*, 2016a).

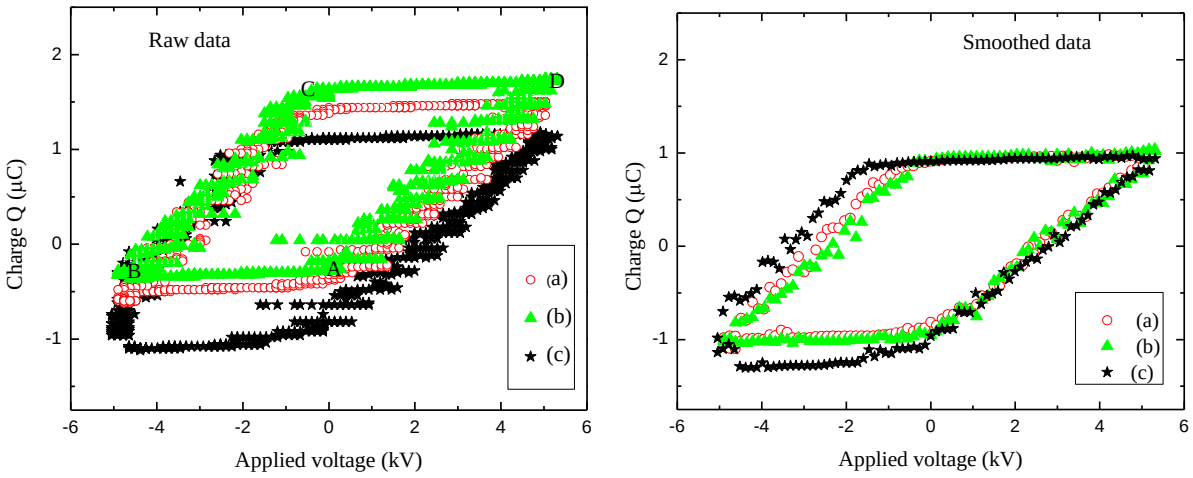

Figure 5. A Lissajous figure of, (a) argon only, (b) an admixture of argon and carvacrol, and (c) admixture of argon and carvacrol in the presence of a substrate in the gap of electrodes, measured at 10.0 kV peak-to-peak voltage and 5 L/min gas flow rate**.**

The effective power of the discharge in one cycle can be calculated from the area of the Lissajous figure (ASHPIS; LAUN; GRIEBELER, 2012; LIU *et al*., 2018). However, in our case, the raw data does not give the exact value of the discharge power, due to the noise in the signal (Fig. 5(a)). Therefore, a smoothing algorithm was used to obtain the *Q*-*V* plots, accordingly, the numerical block diagram (Fig. 2). A typical result of the smoothing process is shown in Fig. 5(b). This reduced data was used to calculate the power according to Eq. 2. Figure 6 shows the variation of the discharge power of argon only as a function of the applied voltage. The power increases from 0.4 to 1.4 W, with the peak-to-peak voltage in the range 8.0 to 13.5 kV. This result is in agreement with the literature reported previously (HAO *et al*., 2012; JUN-FENG *et al*., 2009; ZHOU *et al*., 2019), which means an increase in the effective power of the discharge with the applied voltage.

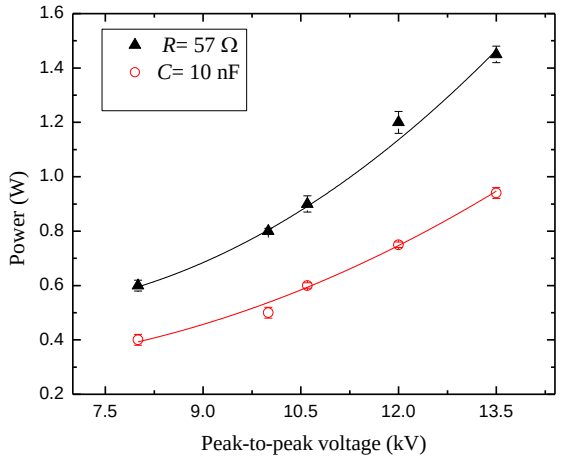

Figure 6. Mean power as a function of applied voltage in argon only DBD plasma at 5 L/min flow rate.

Figures 7(a) and 7(b) shows the variation of discharge power for, an admixture of argon and carvacrol in the presence and absence of a substrate in the gap, as a function of applied voltage, respectively. However, the power increases almost linearly with the applied voltage like that of argon only discharge. It is observed that the addition of monomers leads to a decrease of the effective power in comparison with the pure argon discharge, this can be related to a decrease in conduction current. The decrease in current is rationally expected and could be clarified by the

interactions between the highly energetic species, more specifically the electrons, and the injected monomer (MERTENS *et al.*, 2019). Also, it is interesting to mention that the power calculated by the R = 57 Ω is higher than that calculated by C = 10 nF. This is due to the fact that the higher impedance values of the discharge for the case of a later, it is 2.5X10^5 Ω.

The previous researchers (GRUNDMANN; TROPEA, 2009; BORCIA; ANDERSON; BROWN, 2003), had also calculated the effective power of DBD plasma by determining the operating voltage and either the current I or the charge Q through a probe resistor or capacitor, similar to this study. They conclude that the capacitor method is the more convenient choice since the capacitor integrates the current passing through the DBD actuator in time and thus captures all occurring micro-discharge pulses with an appropriate probe capacitor, which leads to a better signal-to-noise ratio compared to the resistor measurements. Furthermore, the measured probe voltage *Vp* across the probe capacitor *Cp* is proportional to the charge crossing the electrodes independent of the bandwidth of single discharge events and the capacitance is simply a proportionality factor.

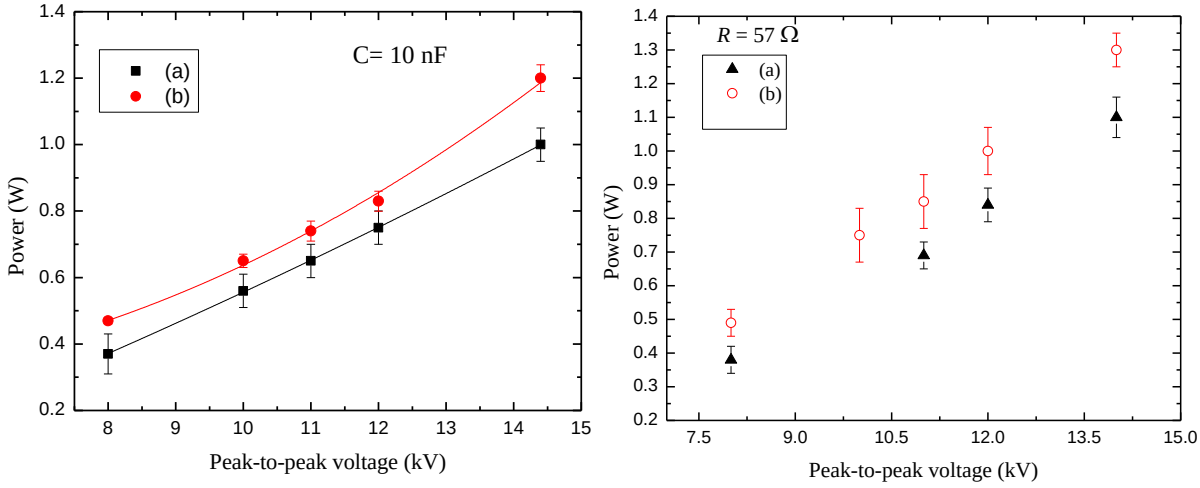

Figure 7. Mean power as a function of the applied voltage measured at 5 L/min gas flow rate of, (a) an admixture of argon and carvacrol and (b) admixture of argon and carvacrol in presence of a substrate in the gap.

3.2. Thickness and Rate of Deposition

Polymer thin films were successfully fabricated from carvacrol monomer on a SS surface. Figure 8 shows the variation of film thickness h with applied voltage. The h of the film increases from 0.85 to 2.25 µm, when we increase the peak-to-peak voltage from 7.5 to 12.0 kV.

After that, it declines to about 1.62 µm for further increases in the voltage up to 14.0 kV. Such decrement of thickness at higher voltage is due to the plasma ablation with competitive polymerization, and increasing substrate temperature. The deposition rate, defined as *h/t*, was followed in the same trends of *h* with voltage since the deposition time *t* is kept constant (15 min).

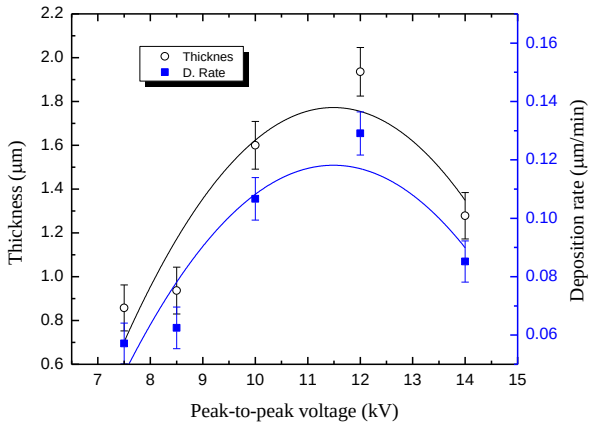

Figure 8. Thickness and deposition rate of the carvacrol-derived film, deposited for 15 min and at 5 L/min gas flow rate, as a function of the applied voltage.

3.3. Roughness

The average roughness, R_a, of CDF coated SS surface under different discharge conditions was determined by profilometry. The obtained R_a of CDF, deposited for 10 and 30 min at a 5 L/min gas flow rate, as a function of power is shown in Figure 9. As can be noted from this figure, all the films are rougher than the steel substrate exposed to the monomer with the plasma off, whose roughness is indicated by point P = 0. Also, the R_a of the film increases with power. However, the deviation of film roughness rises with power, particularly at a longer deposition time. This greater slope of the curves might be due to the rising number of filaments as a consequence of excess plasma power together with the longer deposition time, which increases the number of holes and valleys in the film (KUO *et al.*, 2010). This is clearly confirmed in the secondary electron micrographs of the thin film, we can see it in the next article 2 (Fig. 2).

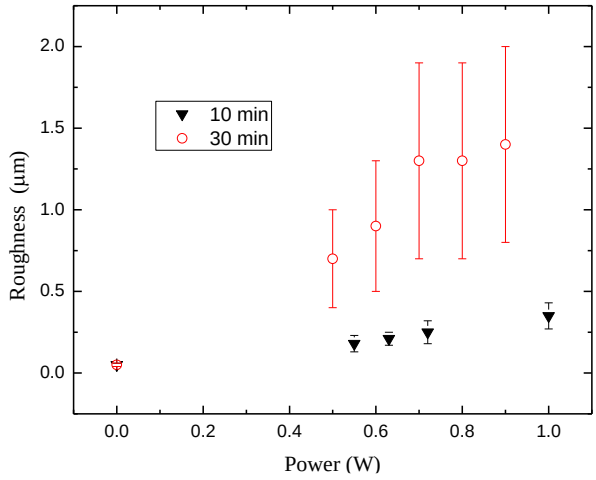

Figure 9. The roughness of the films, deposited at a 5 L/min gas flow rate, as a function of power. The values indicated at $P = 0$ correspond to results measured with the substrates exposed to the monomer with the plasma off

3.4. Chemical Structure

To complete the structure characterization, FTIR spectra analysis of the monomer (carvacrol) was also carried out in addition to the plasma polymerized carvacrol thin films, deposited under different discharge power, as shown in Fig. 10.

Considering first the spectrum of monomer, a broad peak centered at 3412 cm^{-1} and strong peaks at 1058 and 1112 cm^{-1} showed the O-H and C-O stretching vibration of phenol, respectively. The shorter and strong signals which appeared in the region 3057-3017 cm^{-1} and 1519-1620 cm^{-1} showed the presence of aromatic C-H and C=C stretching vibration, respectively. The peaks at 991 and 936 cm^{-1} also indicated the symmetric in-plane bending of the aromatic C-H group (overlapping with the OH bending vibration) and its asymmetric in-plane bending is 1418 cm^{-1}. Weak bands in the region 862–808 cm^{-1} and 752-640 cm^{-1} were due to out of plane bending vibration of adjacent and isolated CH of 1, 2, 4-substituted benzenoid compound. On the other hand, a strong absorbance peak in the region of 2959-2868 cm^{-1} indicates the C-H stretch of branched isopropyl groups (BOUGHENDJIOUA; DJEDDI; SERIDI, 2017; KREPKER *et al.*, 2018; BIZUNEH ADINEW, 2014).

When we compare the FTIR spectrum of the carvacrol-derived film and the monomer, the spectrum of the film was found to be notably similar to the one of the monomer, without the reduction of peak intensity upon plasma polymerization, particularly in the fingerprint region below 1500 cm^{-1}. This reduction in the peak intensities and disappearance of some peaks in the

film can be interpreted as the precursor molecules being partially dissociated as a result of being subjected to the plasma (AL-JUMAILI; BAZAKA; JACOB, 2017). On the other hand, a peak at 1705 cm^{-1} associated with ketone appeared in the film that was not seen in the spectrum of the monomer. This might be due to the post oxidation of the trapped free radicals confined during the formation of the film (MATIN; BHUIYAN, 2013; AHMAD; BAZAKA; JACOB, 2014; JACOB *et al.*, 2014).

Figure 10 also shows the effect of discharge power at a constant gas flow rate, deposition time, and gap distance. It clearly shows that the peak intensities of the spectra of the film increase with power up to 0.72 W. After that, the peak intensity of the spectra of the film was diminished, particularly in the fingerprint region. This reduction in intensity caused by the reduction of the thickness of the film, in turn, caused an increase in substrate temperature at higher power.

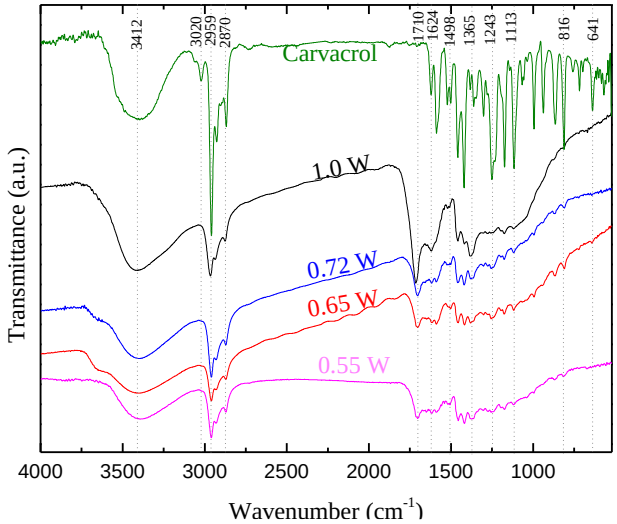

Figure 10. FTIR spectra of the carvacrol monomer and carvacrol-derived films deposited by varying plasma discharge powers from 0.55 to 1.0 W at 10 min deposition time and 4 L/min gas flow rate.

3.5. Aging and Adhesion of the Film

The thin film aging, deposited under different deposition times, was examined by using infrared spectroscopy after exposing the film in ambient air and the results are presented in Fig. 11(a). As can note from this figure, the FTIR spectra of the films were not changed after exposure to atmospheric air for 60, 90, and 120 days. It confirmed that the obtained films are

cross-linked to each other and durable to the surface of the substrate for a long period. The film, deposited at 0.54 W and 5 L/min for 45 min, adhesion is also tested by immersing the film in a clean Tryptic Soy Broth (TSB) medium. Since the initial attachment of bacteria assay was carried out in the TSB solution, it is worth seeing the physical and chemical stability of the film in this medium (CHAN *et al*., 2016). Figure 11(b) shows the FTIR spectra of TSB solution before and after the immersing of the film. It is clearly shown that the IR spectra of the solution have no significant change after immersing the film for 45 min. This indicates that the film exhibited good stability on the surface of the substrate and did not degrade in this medium.

Moreover, the film thermal stability and degradability were determined by using FTIR spectra change measurement after exposing the film to high thermal UV-lamp (at 65 ^{o}C) nearby 3 cm distance and the results are present in figure 12. As can see in Fig. 12(b), the carvacrol-derived film is fully unaffected after exposure to high thermal UV-lamp for 1 h. While the IR spectra of direct coating of carvacrol monomers degraded after 20 min when exposed to the same UV-lamp (Fig. 12(a)). It is also confirmed that the film, those obtained in the present work, thermally stable and cross-linked with good adhesion on the surface of the substrate.

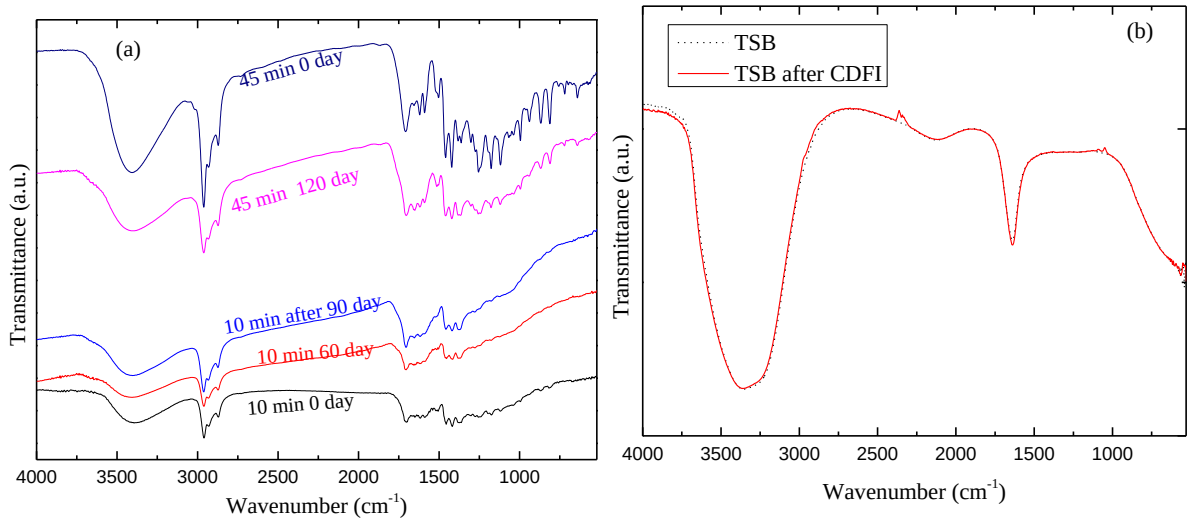

Figure 11. FTIR spectra of, (a) the film deposited at 0.54 ± 0.04 W and 5 L/min gas flow rate after exposing the atmospheric air, and (b) TSB before and after immersion the film. CDFI is carvacrol-derived film immersion.

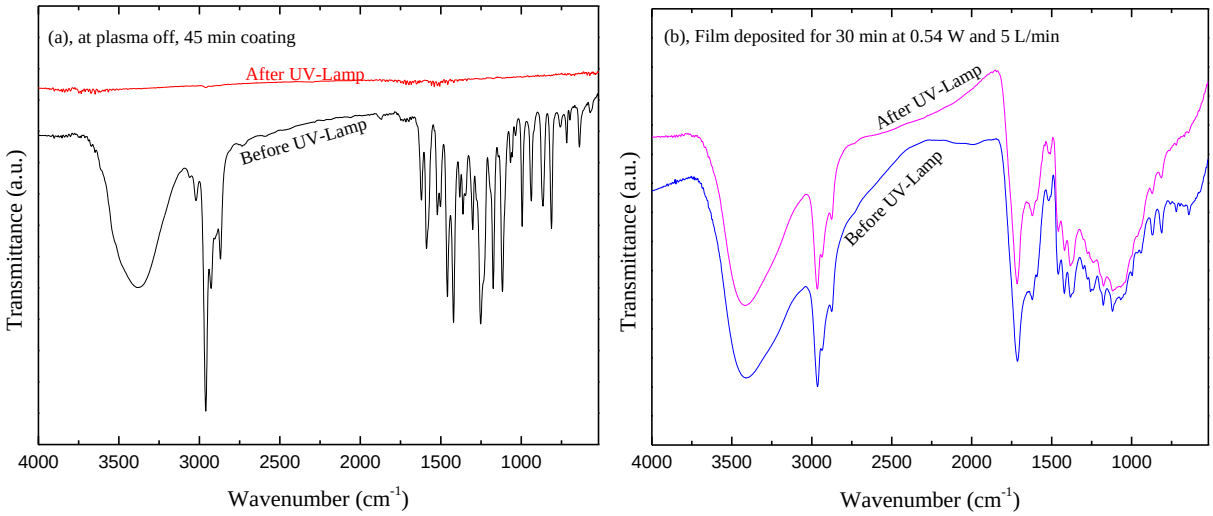

Figure 12**.** FTIR spectra of, (a) the direct carvacrol- and (b) the film carvacrol-coated SS substrate, before and after exposure to high thermal UV-lamp.

4. Conclusions

PolyCarvacrol thin film polymerization was successfully deposited by a filamentary dielectric barrier discharge on the metallic surface under different plasma discharge conditions. The surface property of the stainless steel surface was changed after treatment with carvacrol plasma polymeric thin films. The obtained film is thick up to 2,000 nm thickness with structural similarity to that of the monomer. The aging and thermal stability result also showed that the carvacrol-derived film has good adhesion to the surface of a substrate, and cannot be aged and degraded when exposed to atmospheric air for long periods and high thermal UV-lamp. In general, the current result encourages further investigation of carvacrol-derived film coating for practical application, like a bio-functional coating for food packaging and biomaterials.

Materials **2020**, 13, 3166; Doi: 10.3390/ma13143166

6 Atmospheric Pressure Plasma Chemical Vapor Deposition of Carvacrol Thin Films on Stainless Steel to Reduce the Formation of *Escherichia Coli* and *Staphylococcus Aureus* Biofilms

Tsegaye Gashaw Getnet [1,2], Gabriela F. da Silva[3], Iolanda S. Duarte[3], Milton E. Kayama[4], Elidiane C. Rangel[1,] and Nilson C. Cruz[1,*]

[1]Laboratory of Technological Plasmas, São Paulo State University, Sorocaba 18087-180, SP, Brazil; [2]Department of Chemistry, Bahir Dar University, Bahir Dar 79, Ethiopia; [3]Laboratory of Environmental Microbiology, Federal University of Sao Carlos, Sorocaba 18052-780, SP, Brazil; [4]Laboratory of Plasmas and Applications, São Paulo State University, Guaratinguetá 12516-410, SP, Brazil.

***** Correspondence: nilson.cruz@unesp.br or nilson@sorocaba.unesp.br; Tel.: +55-15-3238-3455

Abstract: *In this paper, we have investigated the deposition of thin films from natural carvacrol extract using dielectric barrier discharge (DBD) plasma polymerization, aiming at the inhibition of bacterial adhesion and proliferation. The films deposited on stainless steel samples have been characterized by scanning electron microscopy, infrared reflectance-absorbance spectroscopy, profilometry, and contact angle measurements. Films with thicknesses ranging from 1.5 µm to 3.0 µm presented a chemical structure similar to that of carvacrol. While the formation of biofilm was observed on untreated samples, the coating completely inhibited the adhesion of* E. coli *and reduced the adhesion of* S. aureus *biofilm by more than 90%.*

Keywords: dielectric barrier discharge; carvacrol plasma polymerization; biofilm inhibition.

1. Introduction

The excellent physical and chemical properties of metals make them very suitable for biomedical applications in medical devices, implants, and tissue engineering. Particularly in underdeveloped countries, stainless steel (SS) is widely used as implants and prosthesis in orthopedic surgeries for being cheaper than titanium and other more inert alloys. In spite of the relatively good clinical results, the bacterial colonization of such material is still a subject demanding attention. As is well known, many bacteria are able to attach and form complex colonies, known as biofilms, on various materials, including stainless steel (GOULTER; GENTLE; DYKES, 2009). Once established, the eradication of biofilms is quite difficult as they

present resistance to antibiotics that can be up to 10^3 times higher than that of planktonic bacteria (VASILEV *et al.*, 2009; BARTLETT, 2004; HOFFMAN *et al.*, 2005). Frequently, the only solution to extirpate the bacterial colonization is to surgically remove the infected implant, which, in addition to high economic costs, results in extra risks of morbidity and mortality to the patients. Thereby, methods of controlling harmful pathogenic biofilms are urgently required. In this regard, antimicrobial active coatings on biomaterials have gained significant interest over the past decade (MUÑOZ-BONILLA; FERNÁNDEZ-GARCÍA, 2012; WANG *et al.*, 2016b; RAVENSDALE; COOREY; DYKES, 2018; SANTOS *et al.*, 2016b; PENG *et al.*, 2019). However, potential health and safety risks associated with the release of synthetic antimicrobials could limit the application of such materials (PENG *et al.*, 2019). In this context, the well-known hazardous effects of most synthetic biocidal compounds and the need to develop cheap and eco-friendly coating processes have stimulated studies focusing on the use of natural bacterial inhibitors. Numerous studies have highlighted the immense potential of natural compounds as antimicrobial products in food packaging, pharmaceuticals, and hygiene (RIBEIRO-SANTOS *et al.*, 2017; JACOB *et al.*, 2013; BASSOLÉ; JULIANI, 2012). Furthermore, natural products have been considered as promising precursors for plasma polymerization. As an illustration, coatings produced from plasmas containing essential oils such as terpineol, linalyl acetate, and γ-terpinene have been demonstrated to be useful in different applications such as insulating and encapsulation layers in organic electronics, and biocompatible coatings for implants (OSTRIKOV, 2005).

Several studies (VALERO; FRANCÉS, 2006; LAMBERT *et al.*, 2001; MASTELIĆ *et al.*, 2008; CHANG; MCLANDSBOROUGH; MCCLEMENTS, 2013; U *et al.*, 2008) have demonstrated the biocidal activity of carvacrol, a natural oil extracted from oregano, against free-standing micro-organisms. In addition, its use has been approved by the European Parliament and Council and by the U.S. Food and Drug Administration (HYLDGAARD; MYGIND; MEYER, 2012; BAMPIDIS *et al.*, 2019). However, its activity, especially when immobilized on a surface, in inhibiting biofilm formation is still a subject under investigation. To fill this gap, in this work, to the best of our knowledge, for the first time, the feasibility of the deposition of carvacrol thin films by dielectric barrier discharge (DBD) plasmas to avoid biofilm formation on stainless steel samples has been evaluated.

2. Materials and Methods

2.1. Sample Preparation

Before depositions, 1 cm × 1 cm SS samples were mirror polished and then cleaned in ultrasonic baths using detergent, distilled water, and isopropyl alcohol. Subsequently, the samples were dried with a hot air gun and stored in Petri dishes until use.

2.2. Plasma Polymerization of Essential Oil

Film deposition was performed in an especially designed dielectric barrier discharge reactor depicted in Figure 1. It consists of two parallel circular brass electrodes, 3 mm apart from each other, fitted axially in two parallel PolyTetraFluoroEthylene (PTFE) discs. A polyester sheet on the grounded lower electrode served as a dielectric barrier, while sinusoidal AC pulses (60 Hz, 10 kV maximum amplitude) were applied to the upper electrode. Carvacrol (5-Isopropyl-2-methyl phenol, $(CH_3)_2CHC_6H_3(CH_3)OH$), at least 98% pure, was kept in a temperature-controlled-stainless steel bottle. Argon, at a flow of 5 L/min, was used as a monomer carrier gas as well as to help in plasma ignition. A 1000× voltage divider and a Tektronix TDS1001C, Tektronix China Co. Ltd., Shangai, China, (30 MHz, 500 MS/s) oscilloscope were used to measure the applied voltage v_A and the voltage drop *vc* through a 10 nF-capacitor. Such values were recorded and used to calculate the plasma excitation power as follows:

$$P = \frac{1}{T} \int_0^Q v_A \, dq \quad (1)$$

where T is the period of the voltage pulse, Q is the charge stored in the capacitor during one period, and q is the instantaneous charge. According to such calculations, the average power delivered during the depositions was 0.54 ± 0.04 W.

The deposition time ranged from 15 to 45 minutes and the chemical structure and stability of the films were characterized by infrared reflectance absorbance spectroscopy (IRRAS), using a model FT/IR-410 (Fourier-transform infrared spectrometer, Jasco Corp., Tokyo, Japan), co-adding 128 scans with a resolution of 4 cm^{-1}. The surface morphology of the samples was also inspected by scanning electron microscopy (SEM) (JSM-6010LA, JEOL Ltd., Peabody, MA, USA), at 3 kV acceleration voltage and beam diameter and the working distance of 3.5 nm and 10 mm, respectively. X-ray energy dispersive spectroscopy (EDS) was performed with a Dry SD Hyper EX-94410T1L11 detector (JEOL Ltd., Peabody, MA, USA), coupled to the SEM

microscope, to characterize the chemical composition of the films. The EDS spectra were acquired with 5 and 10 kV electron beam energy with a beam diameter and a working distance of 6 nm and 10 mm, respectively. To avoid charging effects during the SEM inspections, samples were coated with a thin conducting layer of a golden-palladium. The roughness of the films was determined with a surface profilometer model Veeco D150 (Veeco Metrology, Tucson, AZ, USA). To evaluate the thickness, the films were deposited on a stainless steel substrate partially masked with Kapton tape and the height of the step formed after removing the tape was also measured with the profilometer. Thickness and roughness were measured at least 10 times in different locations on each sample. Wettability and surface energy of the films were evaluated from contact angle measurements with deionized water and diiodomethane as probe liquids in a goniometer Ramé-Hart 100-00 (Ramè-hart Instrument Co., Succasunna, NJ, USA). Surface energy was calculated using the harmonic mean method proposed by Owens-Wendt (OWENS; WENDT, 1969), which has been considered the most universal procedure for such evaluation.

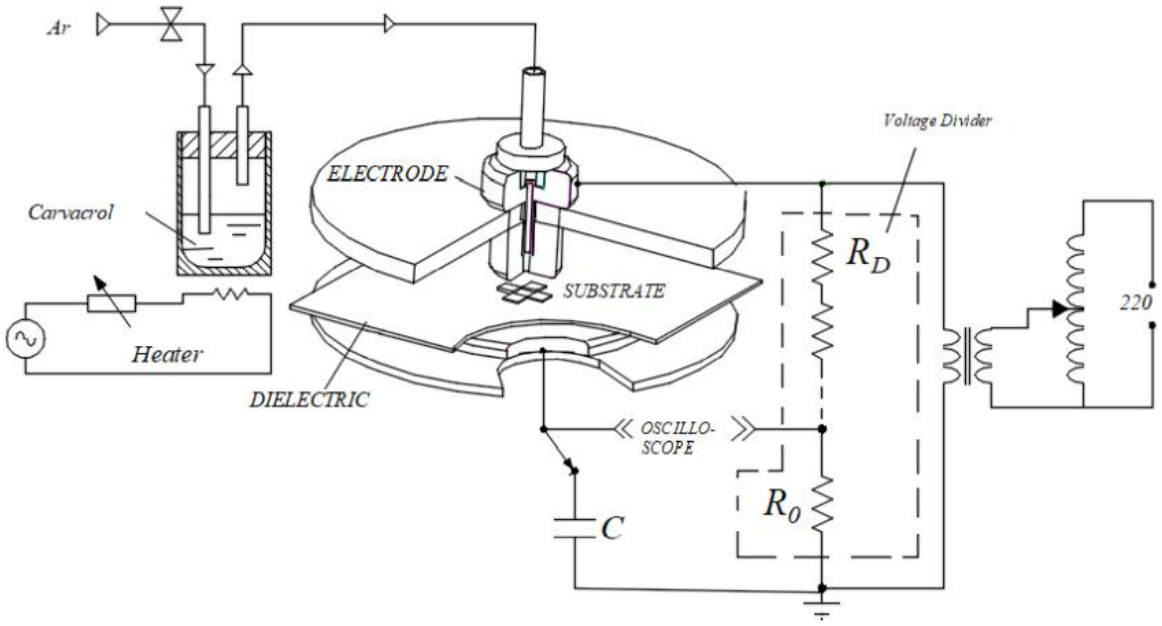

Figure 1. Schematic representation of the experimental setup.

2.3. Biofilm Assay

Escherichia coli (ATCC®11229, Campinas, SP, Brazil) and *Staphylococcus aureus* (ATCC® 6538) strains were used for biofilm assay. Initially, each stock strain was spread on Tryptic Soy Agar (TSA) medium, separately and incubated at 37 °C for 48 h (GIAOURIS; NYCHAS, 2006;

KOSTAKI *et al.*, 2012). Three samples produced with each treatment time were introduced separately in test tubes containing 5 mL of Tryptone Soy Broth (TSB) with a standardized inoculum concentration of 3.6-5.0 × 10^8 colony-forming unit (CFU)/mL. Then, the tubes were incubated for 3 h in a static oven at 36.5 °C for the adhesion phase. After this phase, the samples were withdrawn and washed two times with 3 mL of saline solution (0.85%) and transferred to sterile test tubes containing 5 mL of TSB culture medium, followed by incubation in a static oven at 36.5 °C for 24 h for biofilm formation. Afterward, the samples were transferred to a new test tube containing 10 mL of saline solution and then sonicated for 30 minutes to release the biofilms. From such tubes, dilutions of 10^{-1} up to 10^{-6} in saline were made, and then 100 μL aliquots of each dilution were seeded in TSA medium in sterile Petri dishes and incubated for 48 h. Untreated and carvacrol coated stainless steel slides were used as a positive and negative control, respectively. Finally, bacteria viability was expressed as the log of CFU/cm^2, by the following Equation (2):

$$CFU/cm^2 = \text{number of colonies} \times \text{dilution} \times \text{sample area} \quad (2)$$

For visualization of the bacterial cells attached to the sample surfaces, two samples on each treatment condition were fixed for three hours in Karnovsky solution (2.5% glutaraldehyde, 2% formaldehyde, 0.1 M sodium phosphate buffer; pH 7.2), followed by rinsing with phosphate buffer for 5 min, dehydration in a series of ethanol soaking (60%, 70% and 80% solution for 5 min and 100% for 10 min), and aseptically air-dried. Afterward, the samples were coated by a thin gold-palladium film for SEM analysis, which was performed in a JEOL JSM-6010LA at an acceleration voltage of 3 kV.

3. Result and Discussion

3.1. Morphology

Typical scanning electron microscope (SEM) images were carried out to determine the morphology of the prepared films. Figure 2 presents SEM micrographs of SS as-received (a) and coated with carvacrol-plasma derived film under different deposition conditions (b to d). As one can note in the SEM images, the obtained film grown under different discharge conditions showed similar morphological features, and the substrate was covered by round structures uniformly distributed over the whole area. It indicates that no significant morphological differences upon film deposited under different discharge conditions. However, under higher

magnification, X900, it is possible to observe that such structures are, in fact, holes surrounded by particle clusters of diverse sizes. To understand such a morphology, it is worthy to make clear that, under our experimental setup, the discharges used to deposit the coatings are filamentary (RAJASEKARAN *et al*., 2010) rather than homogeneously distributed over the whole substrate. Consequently, the holes are formed through the ablation of the coating by the intense and localized discharges. On the other hand, the clusters result from monomer polymerization driven by reactive species surrounding the filaments. It is clearly confirmed by EDS mapping shown in Fig. 3.

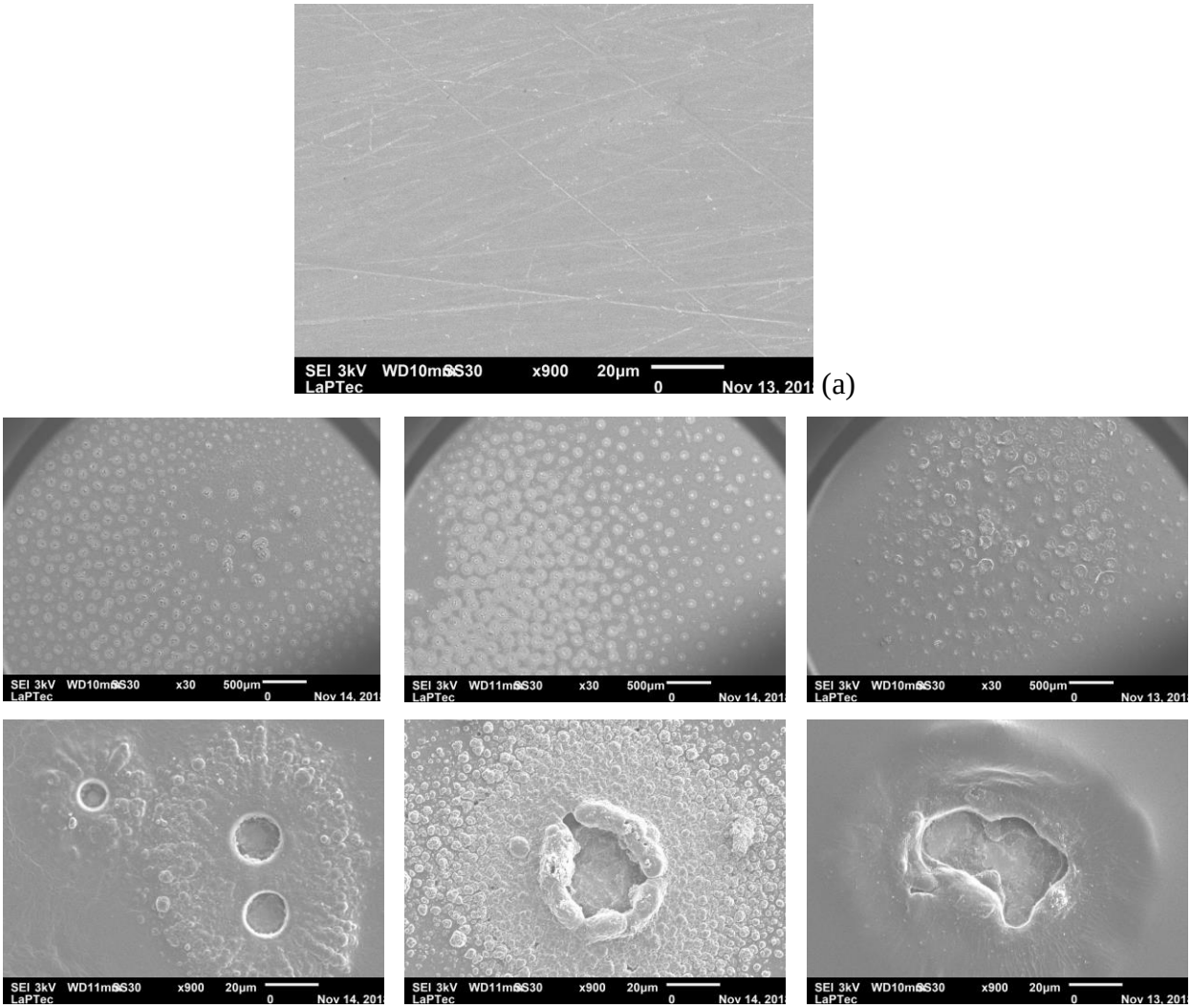

Figure 2. Scanning electron microscopy (SEM) micrographs at X30 and X900 resolution of stainless steel as-received (a), and of the carvacrol-derived film deposited for 45 min

deposition time and 5 L/min gas flow rate at 0. 54 W (b), for 30 min deposition time at 3 L/min gas flow rate and at, (c) 0.86 W, and (d), 0.37 W.

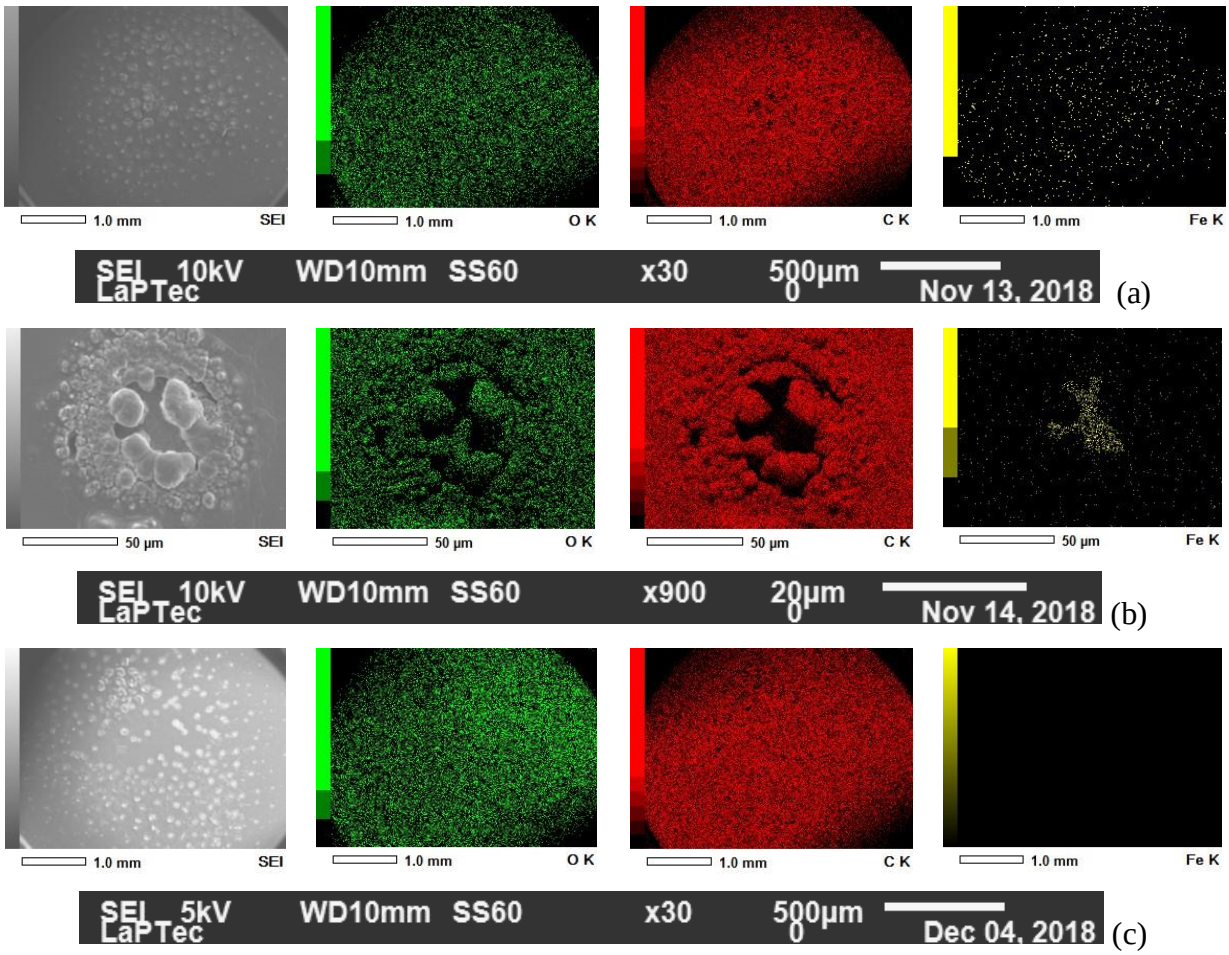

Figure 3. Elemental mapping images of Fe, C, and O_2 of carvacrol-derived film-coated SS surface performed by EDS. The film deposited for 45 min and 5 L/min gas flow rate at 0.54 W (a), and for 30 min deposition time at 3 L/min gas flow rate and at (b) 0.86 W, and (c) 0.37 W.

Table 1 shows the atomic proportions of carbon, oxygen, iron, and chromium in the SS substrate as received and CDF coated, obtained from the EDS spectra at 10 kV. As one can note from this table, the pure SS shows 76.9% iron, 18.0% chromium, and 5.2% carbons. The film-coated SS under different discharge conditions shows carbon and oxygen in a high proportion and iron to the smallest extent up to 1.92%. Such a small amount of iron present in all film is caused by the penetration of the beam to depths greater than the film thickness, particularly at the location of holes in the film, as confirmed by the EDS mapping in Fig. 3(b). Furthermore, it is confirmed that no iron was present when we operated the

microscope at 5 kV as shown by the EDS map in Fig. 3 (c). The remaining chromium is no longer visible in the film, except for the pure SS substrate. In general, the obtained EDS data and elemental mapping also confirmed that the whole area of the substrate was covered by the film.

Table 1 Elemental concentration of SS as-received (a), and coated by CDF for 45 min deposition time and 5 L/min gas flow rate at 0.54 W (b), for 30 min deposition time at 3 L/min gas flow rate and (c) at 0.37 W, and (d) at 0.86 W.

Sample	Elemental concentration (%)			
	C	Fe	O_2	Cr
(a)	5.2	76.8	Not detected	18.0
(b)	86.7	1.8	11.5	Not detected
(c)	86.1	1.5	12.5	Not detected
(d)	83.1	1.9	14.9	Not detected

3.2. Roughness

Figure 4 shows the average R_a roughness of the films as a function of the deposition time, *t*. As can be noted, all the films are rougher than the steel substrate exposed to the monomer with the plasma off, whose roughness is indicated by the point at $t = 0$. The observed increase of R_a as the deposition time was increased is the result of the overexposure of the films to the discharge filaments for longer periods, causing the degradation of the surfaces, as evidenced by SEM micrographs presented in Figure 2.

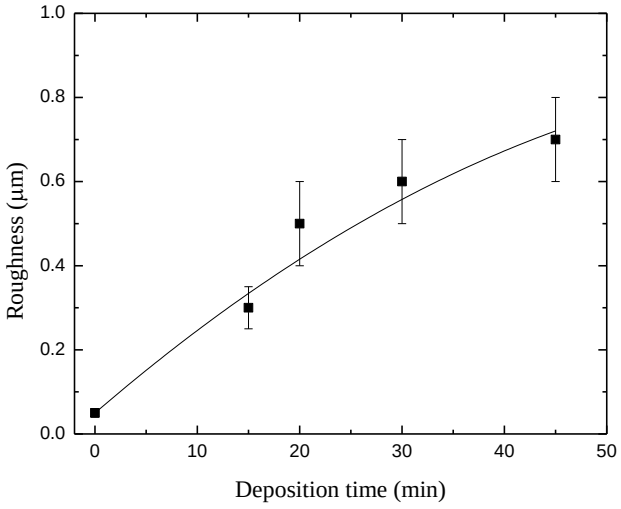

Figure 4. The roughness of the plasma polymerized carvacrol films as a function of deposition time. The value at $t = 0$ corresponds to the roughness of the substrate exposed to the monomer with the plasma off.

3.3. Thickness and Deposition Rate

Figure 5 shows the thickness *h* of the coatings as a function of *t*. Films as thick as 1.6 μm were obtained with a deposition time of 15 min. As the deposition time was increased, *h* increased, reaching nearly 3.0 μm. Previous studies (XU; WANG; SANDERSON, 2010; BAZAKA; JACOB, 2009) have reported that the thickness of plasma polymerized terpinen-4-ol and linalyl acetate (PLA) thin films using low-pressure radiofrequency plasmas also increases linearly with the deposition time. However, under some deposition times, the thicknesses of the coatings produced there were around one-third of the thickness obtained in our work. It is interesting to mention that, as also shown in Fig. 5, the deposition rate, defined as *h/t*, decreased from 100 to 65 nm/min as the deposition time increased. To understand this result, it is interesting to recall that, during the deposition, the sample is exposed to large amounts of atomic oxygen and other reactive species, such as OH and O_3, resulting from interactions between the plasma and the air surrounding the samples. Such species may etch the deposited material through chemical reactions, resulting in volatile compounds such as CO and CO_2. Besides, the continuous bombardment of energetic species in the plasma may also cause the film densification (SANTOS *et al*., 2017a). Therefore, the results suggest that the higher the deposition time, the higher the influence of plasma on the ablation and densification of the growing material, which may result, for instance, in the holes observed in Figure 2.

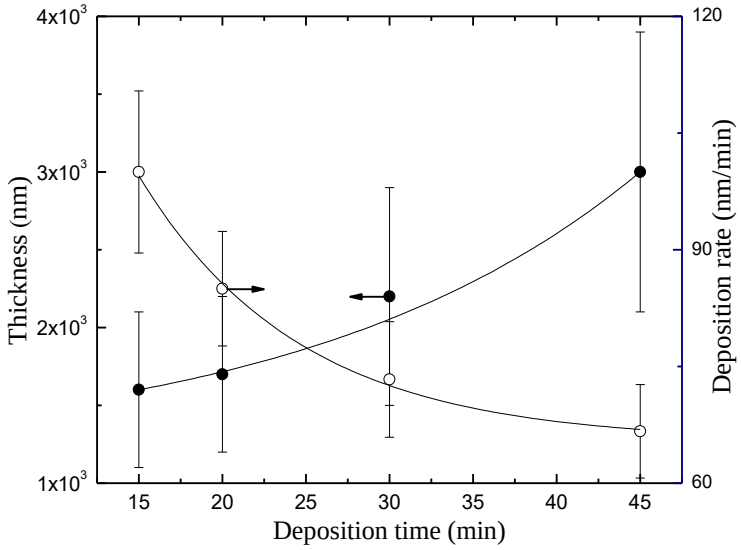

Figure 5. Thickness and deposition rate of plasma deposited films as a function of deposition time.

3.4. **Chemical Structure Analysis**

The FTIR spectrum of liquid carvacrol used as a film precursor is shown in Figure 6. On the spectrum, it is possible to note a broad band centered at 3412 cm^{-1}, ascribed to O-H stretch, and strong absorptions at 1058 and 1112 cm^{-1} assigned to the presence of O-H and C-O bond stretching of phenol groups, respectively. The strong and sharp peaks in the ranges 1519–1620 cm^{-1} and 3057–3017 cm^{-1} are attributed to aromatic C=C and C-H stretching, respectively (BOUGHENDJIOUA; DJEDDI; SERIDI, 2017; KREPKER *et al*., 2018). The peaks in the range 991–936 cm^{-1} and the peak centered at 1418 cm^{-1} indicate O-H bending vibrations overlapping with symmetric and asymmetric in-plane bending, respectively, of aromatic C-H groups. The strong band in 2959–2868 cm^{-1} indicates the C-H stretching vibration of the methyl group (BIZUNEH ADINEW, 2014). In addition, the bands at 1462 cm^{-1} and 1300 cm^{-1} also appear owing to C-H asymmetric and symmetric deformation of the methyl group, respectively. On the other hand, the strong absorption at 1177 cm^{-1} indicates the carbon skeletal vibration of C-$(CH_3)_2$ groups (JACOB *et al*., 2013). The peaks at 1363 and 1381 cm^{-1} also confirm symmetric and asymmetric deformation, respectively, of the isopropyl group.

Figure 6 also presents the spectra of films deposited under various deposition times. As one can note, the spectra of all the coatings are notably similar to that of the monomer, indicating that

the main functional groups in the monomer were preserved after the deposition. The absence of the absorption at 3017 cm^{-1} and the appearance of absorption at 1705 cm^{-1} is also noticeable on the spectra of the films, which are associated with ketone functional groups. Such absorptions may result from post-plasma oxidation of free radicals trapped during the formation of the film, as well as from tautomerization (MATIN; BHUIYAN, 2013; JACOB *et al*., 2014).

As the deposition time increase, the intensity of almost all absorption increases, which is in agreement with the increase of the film thickness with *t*, as shown in Figure 5. Furthermore, it is interesting to point out the maintenance of hydroxyl groups on the plasma deposited films. Such radicals, which are involved in the rupture of the bacteria cell membrane, are believed to be one of those responsible for the antimicrobial activity of carvacrol. In addition, when OH-containing-phenol rings penetrate the cells, they can disrupt the cytoplasmatic membrane, inhibiting the activity of several enzymes and affecting numerous mechanisms related to cell metabolism (MARINO; BERSANI; COMI, 2001; CEYLAN; FUNG, 2004).

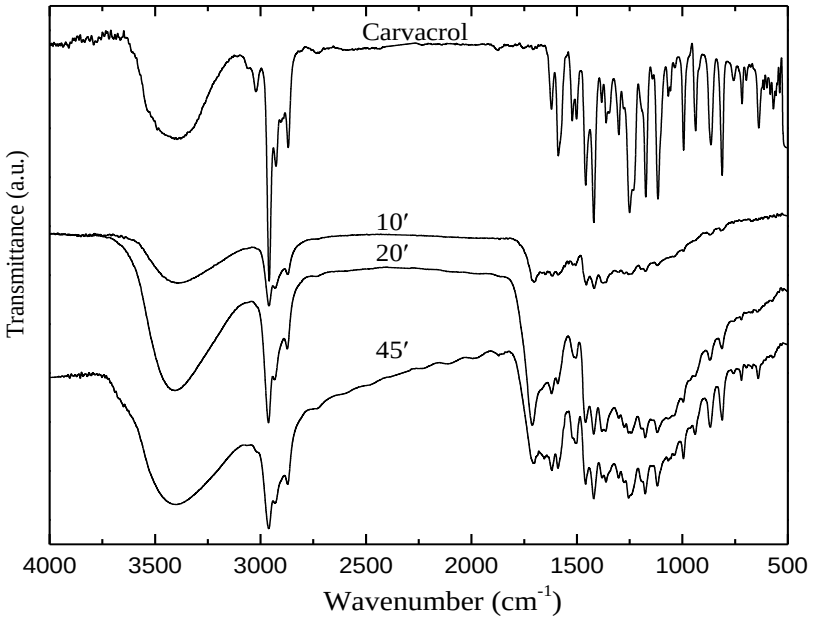

Figure 6. Fourier-transform infrared spectroscopy (FTIR) absorption spectra of liquid and plasma deposited carvacrol films grown under different deposition times.

3.5. Water Contact Angle and Surface Energy

The values of water contact angle and surface energy of the steel substrate exposed to the monomer with the plasma off and the films deposited with various deposition times are shown in

Figure 7. As can be observed, the exposure to the plasma causes the contact angle to continuously decrease from 90.2°, measured on the surface not exposed to the plasma, to 28°, after deposition for 45 min. This increment of film hydrophilicity is the result of the enhancement of oxygen-containing groups, which leads to the rise of the surface polarity, and, consequently, to the increase of surface energy, as also shown in the figure, of films fabricated at a higher deposition time (EASTON; JACOB, 2010; XU; WANG; SANDERSON, 2010). That is in agreement with the increase of the intensity of absorptions ascribed to hydroxyl groups with the increase of the deposition time, as shown in Figure 6. Another fact that contributes to the growth of the hydrophilicity is the increase of film roughness (RANGEL *et al*., 2011) with *t*, as discussed in the previous section 3.2.

Also, as can be observed in Fig. 8, of the water contact angle, the result of such film coatings are stable as the hydrophilicity conferred to the steel substrates by the deposited films is still present even 35 days after the deposition. In general, hydrophilic surfaces, as those obtained in this work, are the most suitable for many biological applications (BHATTACHARYYA *et al*., 2010; ARIMA; IWATA, 2007).

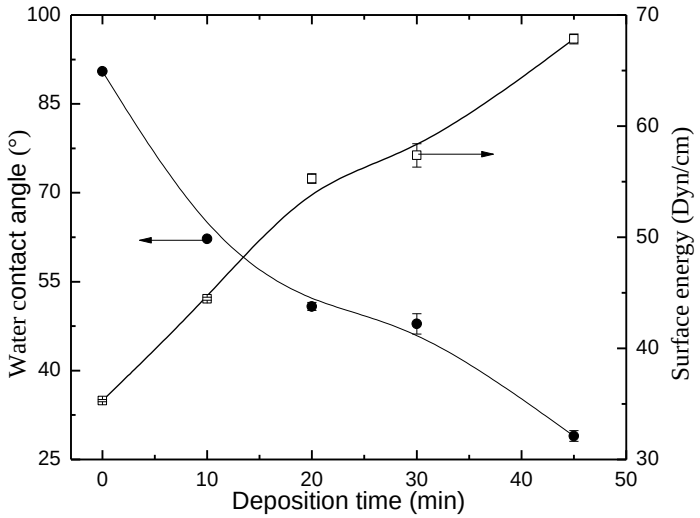

Figure 7. Water contact angle and surface energy of the plasma deposited carvacrol films as a function of deposition time. The values indicated at $t = 0$ correspond to results measured with the substrates exposed to the monomer with the plasma off.

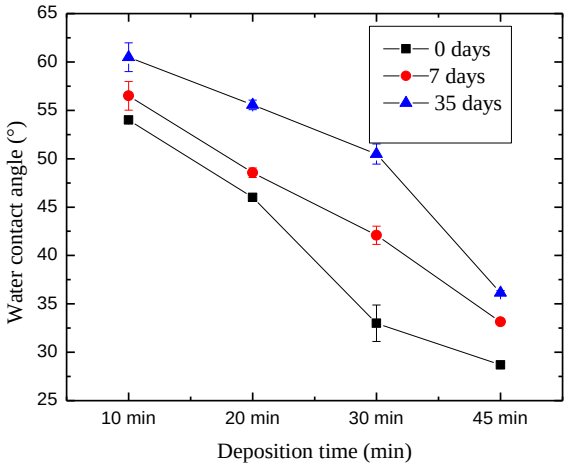

Figure 8. Water contact angles of carvacrol-derived films deposited at 0.6 W and 5 L/min gas flow rate under different deposition times, measured after aging for 0, 7, and 35 days under ambient conditions.

3.6. Biofilm Assays

Figure 9 shows SEM micrographs of *S. aureus* and *E. Coli* colonies after 24 h of incubation in the culture medium, Figure 9(**a**, **d**), as well as on steel substrates as-received, Figure 9(**b**, **e**), and coated with plasma deposited carvacrol films, Figure 9(**c**, **f**). As can be seen, for both microorganisms, the densities of colony-forming units (CFUs) attached to pristine substrates are even higher than those observed in the culture medium. Besides, it is also worth noting the formation of clusters of cells linked to each other by extracellular polymeric substances, indicating the initial stages of biofilm formation. On the other hand, in Fig. 9, it is also possible to observe that the plasma deposited carvacrol coatings completely inhibited the adhesion of *E. coli* and reduced to only a few CFU of *S. aureus* on the steel surface.

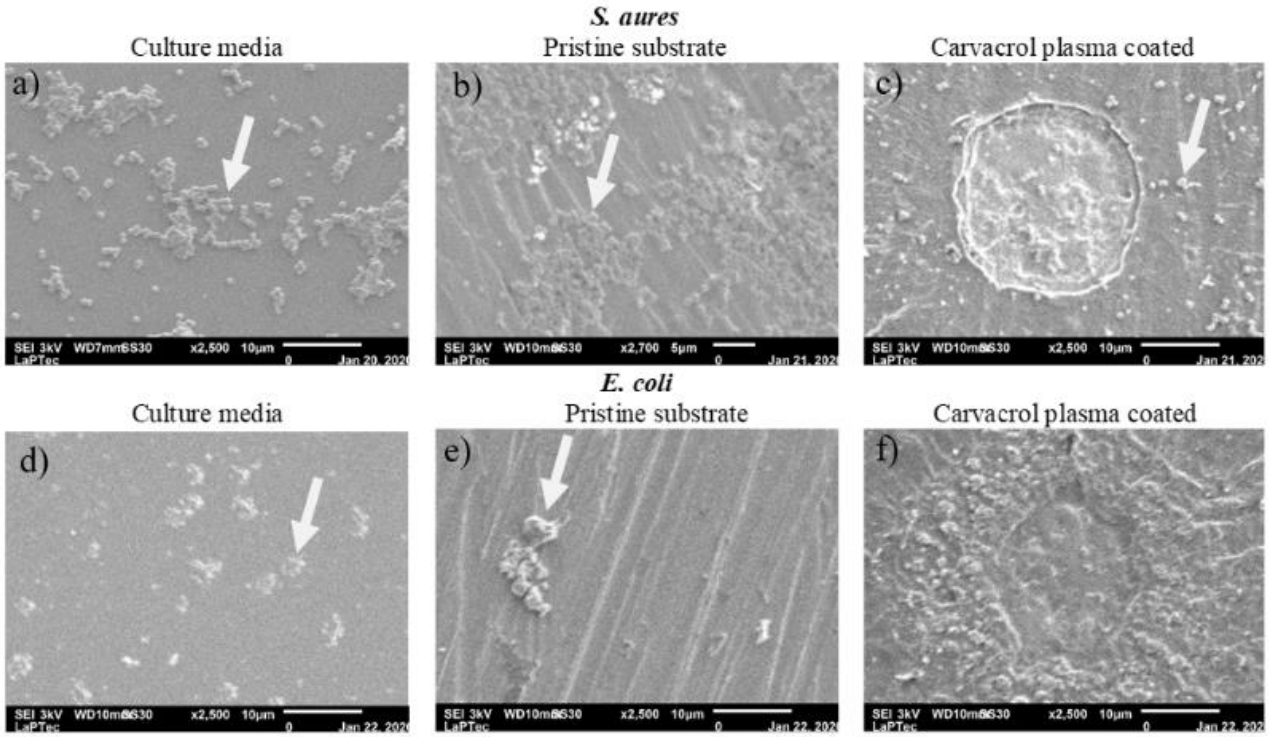

Figure 9. Scanning electron micrographs of colony-forming units (CFUs) of *S. aureus* and *E. coli* on a culture medium ((***a, d)***, respectively) as well as on stainless steel samples as-received ((***b, e)***, for *S. aureus* and *E. coli*, respectively) and coated with plasma deposited carvacrol films ((***c, f)***, for *S. aureus* and *E. coli*, respectively). The arrows indicate the bacterial colonies.

The effects of the coatings on the bacterial adhesion can be further evaluated with the help of Figure 10, which shows the results of quantifications of viability and proliferation of microorganisms on stainless steel slides as-received (a), immersed in liquid carvacrol for 45 minutes (b), and coated with a plasma deposited carvacrol film grown for 45 minutes (c). In this figure, the dotted line indicates the bacteria concentration in the initial inoculum. As can be noticed, all carvacrol-containing samples exhibit complete eradication of *E. coli* and are reduced by about six orders of magnitude the concentration of *S. aureus*. On the other hand, the pristine substrate preserved the viability of more than 90% of both bacteria. Indeed, the biofilm eradication of the coating is similar to that obtained with the immersion of the stainless-steel slides in liquid carvacrol. However, as can be concluded from the results presented in the above article 1 (Fig. 12), the coatings produced without plasma are totally degraded after 20 min under UV light/irradiation, which is a typical procedure for material sterilization. On the other hand, no

clear evidence of degradation can be observed on the plasma deposited carvacrol films even after one hour under UV irradiation. Therefore, the exposure to the plasmas results in stable coatings with bactericidal activity even after being stored in atmospheric air for more than 120 days.

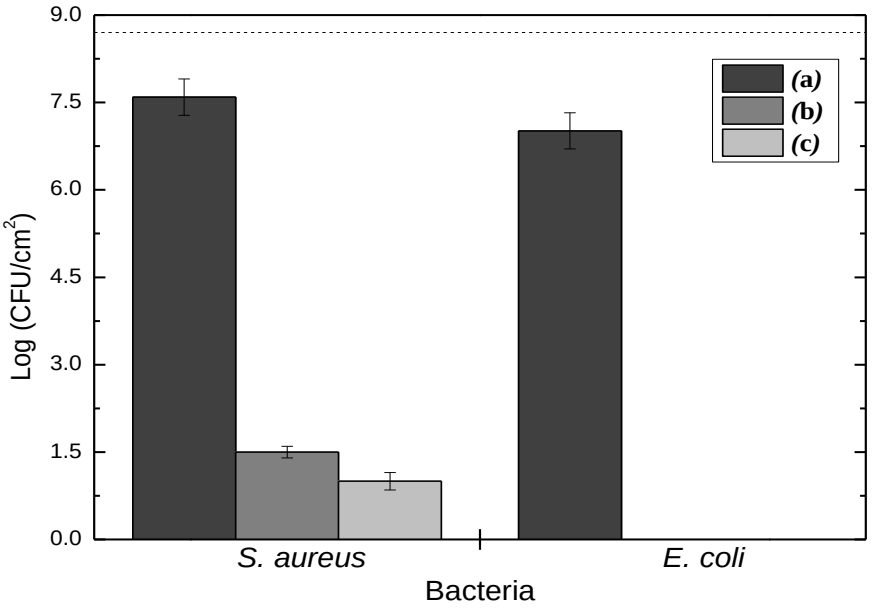

Figure 10. The concentration of *S. aureus* and *E. coli* on stainless-steel slides as-received (**a**), immersed for 45 min in liquid carvacrol (**b**), and coated with plasma deposited carvacrol for 45 min (**c**). The dotted line indicates the concentration of bacteria in the initial inoculum.

4. Conclusions

The deposition of carvacrol thin film on stainless steel substrates was successfully achieved by atmospheric pressure dielectric barrier discharge plasmas. The thickness of the films was in the range of 1, 000 to 3,000 nm with a roughness of up to 800 nm and a chemical structure similar to that of carvacrol. The obtained films are well-adhered to the substrate and stable under UV light and air exposure for prolonged periods. The coatings completely inhibited the formation of *E. coli* biofilms and reduced by six orders of magnitude the adhesion of *S. aureus* in comparison with the number of bacteria detected on the pristine substrate. The results of bactericidal activity, associated with the fact that carvacrol is a natural extract, make the films produced here good candidates for coatings to avoid the formation of biofilms on biomaterials and food packaging, for instance.

Article 3

Polymers ***2020***, 12*(11), 2692;* ***https://doi.org/10.3390/polym12112692***.

7 Thin Film Deposition by Atmospheric Pressure Dielectric Barrier Discharges Containing Eugenol: Discharge and Coating Characterizations

Tsegaye Gashaw Getnet[1,3], Milton E. Kayama[2], Elidiane C. Rangel[3], Nilson C. Cruz [3,*]

[1]Department of Chemistry, College of Science, Bahir Dar University, Bahir Dar 79, Ethiopia; [2]Laboratory of Plasma and Applications, São Paulo State University, Campus at Guaratinguetá, Guaratinguetá, SP 12516-410, Brazil; [3]Technological Plasmas Laboratory, São Paulo State University, Experimental Campus of Sorocaba, Sorocaba, SP 18087-180, Brazil**.**

*To whom correspondence should be addressed: nilson.cruz@unesp.br

Abstract: Eugenol (4-Allyl-2-methoxyphenol) is the main constituent of clove oil. In addition to being widely used as a condiment, it has been recognized as a powerful bactericide. Owing to that, eugenol has been used in several applications including odontology and as a conservative for food products. Aiming at the development of natural bactericide coatings, in this work, using an atmospheric pressure plasma in a dielectric barrier discharge (DBD) reactor eugenol was deposited on stainless steel substrate, with argon as a carrier gas. The discharge power supply was a transformer at 14.4 kV peak-to-peak voltage and 60 Hz frequency. Operating with a gas flow rate at 4 L/min, the active power was around 1.2 W. The maximum plasma electron temperature of the plasma with monomers was about 1.5 eV, estimated by visible emission spectroscopy using a local thermodynamic equilibrium approach. The study also comprehended the analysis of the film structure, aging, and thermal stability using infrared reflectance spectroscopy, and its thicknesses and roughness by profilometry. The thickness of the films was in the range of 1,000 to 2,400 nm with a roughness of up to 800 nm with good adhesion on the substrate. The FTIR result shows a stable coating with a chemical structure similar to that of the monomer. Aging analysis showed that the film does not degrade, even after exposing the film for 120 days in ambient air and 1.0 h under a high thermal UV-lamp.

Keywords: Eugenol; plasma; dielectric barrier discharge.

1. Introduction

Atmospheric dielectric barrier discharge (DBD) plasmas have drawn much attention due to low experimental cost, easy handling, and having no need for expensive vacuum systems (KHOJA; TAHIR; AMIN, 2019; LAROUSSI; LU; KEIDAR, 2017). DBD plasmas are the best

choice for a variety of industrial applications, including large-scale ozone generation, odor removal, and materials processing (PANTA *et al*., 2020a; PANTA *et al*., 2020b). In addition, the potential of non-thermal DBD plasma systems for various medical and biological applications including wound healing, tissue regeneration, blood coagulation, tooth bleaching, and cancer treatment has been demonstrated (CVRČEK; HORÁKOVÁ, 2019; KIM; CHUNG, 2016; ISEKI *et al*., 2012; TSAI *et al*., 2020; KAUSHIK *et al*., 2019; MISRA *et al*., 2019; CHA; PARK, 2014; KALGHATGI *et al*., 2011; IRANI *et al*., 2015; SAKUDO; YAGYU; ONODERA, 2019; BERNHARDT *et al*., 2019). In the midst of such applications, thin-film deposition using DBD plasmas presents several benefits compared to its vacuum counterparts in a variety of applications, such as film deposition on vacuum- or temperature-sensitive substrates and biological/living surfaces (MARTINES, 2020; KHAN *et al*., 2020). The deposition by DBD is able to tailor the physical and chemical properties of different substrates to a specific application through the modification of the deposition parameters, such as applied voltage, type, and flux of the monomer, and deposition time (RAHMAN; BHUIYAN, 2013).

Employing plasmas, it is possible to deposit films with adjustable properties on a variety of substrates, in principle, using any organic vapor, including even those non-polymerizable via conventional pathways (BAZAKA *et al*., 2010; JACOB *et al*., 2012; AHMAD; BAZAKA; JACOB, 2014) such as film precursors. For instance, the successful deposition of films using low-pressure plasmas containing natural extracts, such as eucalyptus and lavender oils (EASTON; JACOB, 2009), terpene-4-ol (JACOB *et al*., 2012), and linalyl acetate (ANDERSON *et al*., 2011) has been reported. It is interesting to point out that, a wide range of applications of those films in electronics, biomaterials, nanotechnology, and protective coatings has been investigated (BAZAKA; JACOB; BOWDEN, 2011; ADIL; AL-SHAMMARI; MURBAT, 2020). In this context, eugenol (Eu), an extract obtained from clove, is particularly interesting. Used as a condiment since ancient times, it also presents intense antimicrobial activity against free-living microorganisms. Therefore, it can be considered a very promising material to be used in the production of bactericidal coatings for food packing and other related products. However, to be of practical interest such coatings must be uniform, defect-free, and well adhered to different types of substrates. As well documented in the literature, such requirements can be perfectly met using plasma-based deposition techniques. Although several experimental studies have been conducted addressing the fundamental mechanisms and chemical phenomena of

atmospheric DBD plasmas (SATO *et al*., 2015; PEETERS; YANG; VAN DE SANDEN, 2015; SEWRAJ *et al*., 2011), there is not, as far as we know, any detailed study on the deposition of films from essential oils using DBD plasmas. In this regard, plasma diagnostic techniques such as electrical measurements and optical emission spectroscopy can be useful tools to help in understanding the underlying physical and chemical processes (PEETERS; YANG; VAN DE SANDEN, 2015; SEWRAJ *et al*., 2011; NASTUTA *et al*., 2018; STANFIELD; MENART, 2014; TSCHIERSCH; BOGACZYK; WAGNER, 2014). In this context, the present study investigated the film deposition from atmospheric DBD plasmas containing eugenol vapor. Both plasmas and coatings properties were characterized.

2. **Materials and Methods**

The plasmas used in this study have been established using the system fully described elsewhere (GETNET *et al*., 2020a; GETNET *et al*., 2020b) and shown schematically in Fig. 1. It consists of a brass cylinder (2 cm in diameter) and an aluminum disk (5.6 cm in diameter) electrodes fitted in parallel, 3 mm apart from each other, in PTFE discs. The upper brass electrode was connected to an adjustable high voltage transformer (up to 20 kV peak-to-peak, 60 Hz) while the grounded lower disc was covered by a polyethylene sheet and served as a sample holder. Argon (99.9% pure), used as a carrier gas and to help in plasma ignition, was fed through a temperature and flow rate controlled stainless steel vessel containing eugenol (4-Allyl-2-methoxyphenol, at least 98% purity of from Sigma-Aldrich). This mixture, whose flow was controlled by rotameters, was injected through an axial hole at the center of the upper electrode. The discharge area was protected from the environment by a 40 mm diameter transparent polyethylene terephthalate hollow cylinder. The peak applied voltage v_A was measured with a voltage divider while discharge current and charge were determined measuring the voltage drops across a resistor R = 57 Ω and a capacitor C = 10 nF, respectively, connected in series with the ground electrode. The signals were recorded using a 500 MS/s digital storage oscilloscope (Tektronix TDS1001C-30EDU, Tektronix China Co. Ltd., Shangai, China) to calculate the mean discharge power P, for applied voltage much larger than in the capacitor, given by:

$$P = \frac{1}{T} \int_0^Q v_A \, dq \qquad (1)$$

where Q is the charge stored in the capacitor during one period T=1/60 s^{-1} of the signal.

Chemical structure, aging, and stability of the films were characterized by infrared reflectance absorbance spectroscopy (IRRAS), using a Jasco FTIR 410 (Fourier-transform infrared, Jasco Corp., Tokyo, Japan) spectrometer co-adding 128 scans with a resolution of 4 cm^{-1}. Film thickness and roughness were measured, at least 10 times in different locations on each sample, with a surface profilometer (Veeco D150, Veeco Metrology, Tucson, AZ, USA). To evaluate the thickness, the films were deposited on stainless steel substrates partially masked with Kapton tape and the height of the step formed after removing the tape was measured with the profilometer.

The optical emission spectra of argon plasmas in the presence and the absence of eugenol was measured using an Ocean Optics spectrometer (USB4000, Ocean Insight, Rochester, NY, USA). The spectrometer was connected to a fiber optic and the light was collected from a collimating lens located 3 mm from the edge of the electrode as shown in Fig. 1. Electron temperature, T_e, was estimated using the Boltzmann plot method assuming local thermodynamic equilibrium (JIN *et al*., 2013; ŞAHIN; TANIŞLI, 2020) and using Eq. (2):

$$\ln \frac{I_{ji}\lambda_{ji}}{A_{ji}g_j} = -\frac{E_j}{kT_e} + \ln \frac{hcN_b}{4\pi Z(T)} \tag{2}$$

where I_{ji} is the intensity and λ_{ji} is the wavelength of the measured spectral line emitted in an electron transition from an exciting level with energy E_j to a lower state with energy E_i, g_j is the statistical weight of the excited level, A_{ji} is the probability of the transition between the two states responsible for the measured emission, k is the Boltzmann's constant, c the speed of light, h is the Planck's constant, N_b the total species population, and $Z(T)$ corresponds to the partition function at a temperature T.

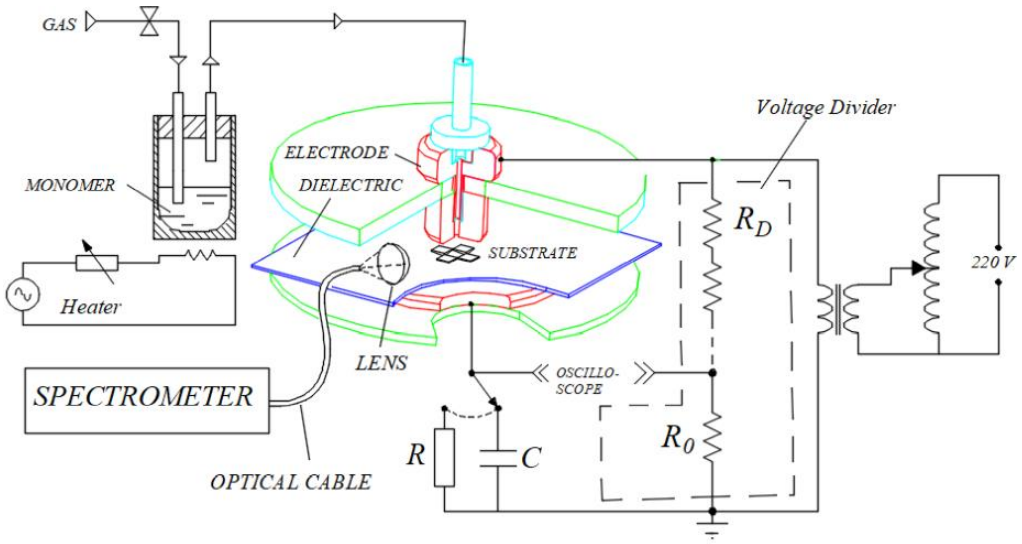

Figure 1. Schematic representation of the experimental setup used for film deposition and discharge characterization (GETNET *et al*., 2020a).

The electronic temperature has been derived from the reciprocal of the slopes of Boltzmann plots (Fig. 2) of $\ln \frac{I_{ji}\lambda_{ji}}{A_{ji}g_j}$ *versus* E_j using the data provided by the NIST atomic database (Table 1).

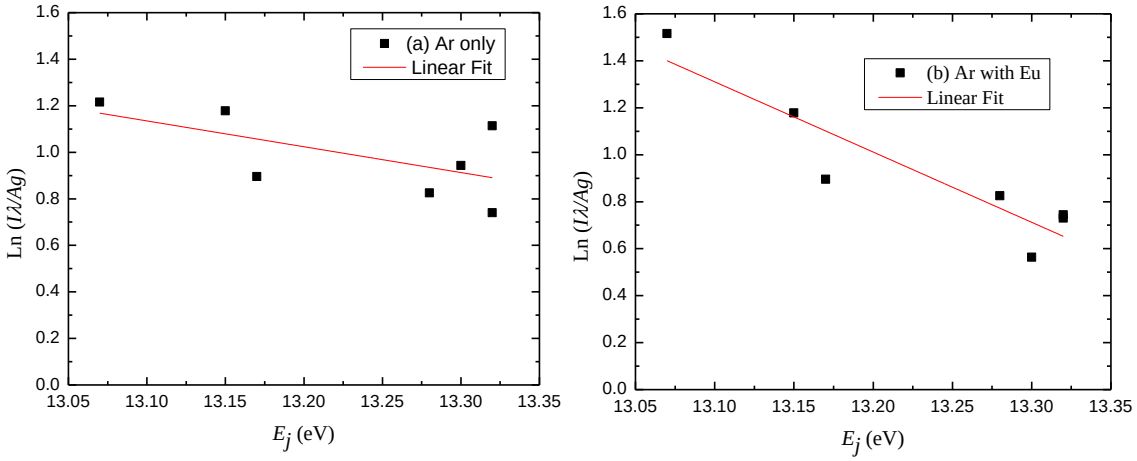

Figure 2. Boltzmann plot for argon only and argon with eugenol emission lines measured at 10.0 kV peak-peak voltage and 4 L/min gas flow rate.

Table 1. Spectroscopic data for the observed ArI lines used for the evaluation of T_e. All lines are emitted during 4p-4s transitions.

Wavelength (nm)	E_i *(eV)*	E_j *(eV)*	A_{ji} x10^7 (s^{-1})
696.54	11.54	13.32	0.63
738.39	11.62	13.30	0.84
763.50	11.54	13.17	2.45
772.37	11.54	13.15	0.51
794.82	11.72	13.28	1.86
811.53	11.54	13.07	3.31
826.45	11.82	13.32	1.54

3. Results and Discussion

3.1. Electric characteristics

3.1.1. Voltage and Current Waveforms

The electric characteristics of the DBD plasmas were evaluated by the measurement of the voltage drop (KAYAMA *et al*., 2017; XIAO *et al*., 2014; NI *et al*., 2008) on the capacitor *C* and the resistor *R* defined in Fig. 1. Figure 3 shows typical waveforms of applied voltage and current in argon discharges pure (a) and mixed with eugenol (b). As it can be observed, the discharge current curves contain several short-time spikes per each half cycle of the applied voltage, which indicates the filamentary regime of the discharges (YOKOYAMA *et al*., 1990).

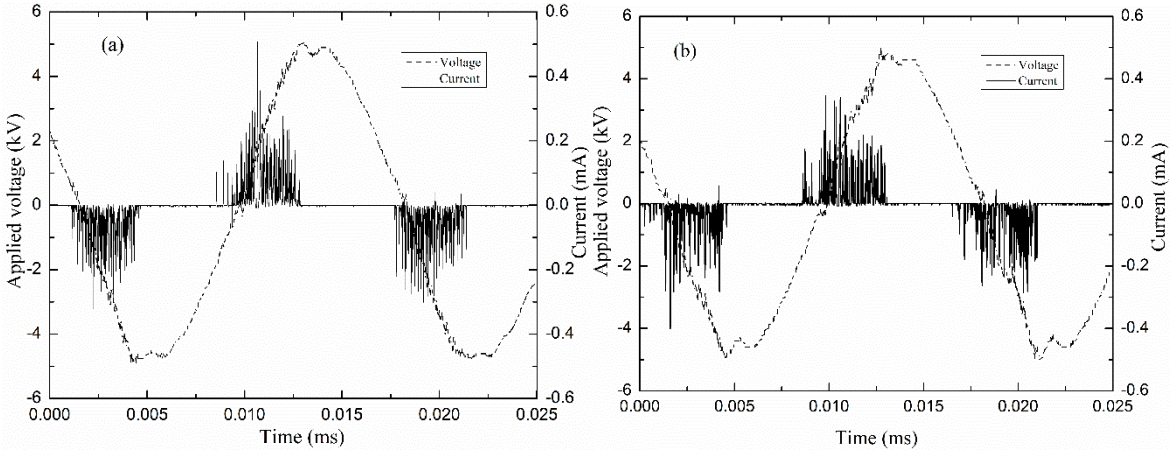

Figure 3. Typical current and voltage waveforms of discharge ignited at 10.0 *kV* peak-to-peak voltage with 4 L/min total gas flow of (a) argon and (b) mixture of argon and eugenol.

The filamentary nature of the discharges can be better observed if one considers the pictures in Figs. 4(a) and 4(b) which presents photographs of discharges established under the same conditions as those used to obtain the curves in Fig. 3(a) and 3(b), respectively. As it can be observed, the filamentary discharges cover the entire surface of the electrode without any noticeable differences between the discharges in Ar or ArEu. However, a situation completely different is observed when the stainless-steel substrate is placed on the lower electrode. As one can see in Fig. 4(c), the introduction of the substrate causes the filaments to concentrate on the substrate. This is due to the distortion of electric field lines promoted by the sharp borders of the substrate. This result is similar to the previously reported helium DBD plasma (GULATI *et al*., 2012, NASTUTA *et al*., 2018). In general, the discharge regime of the argon was not altered by the addition of the eugenol monomer and works well for polymer deposition.

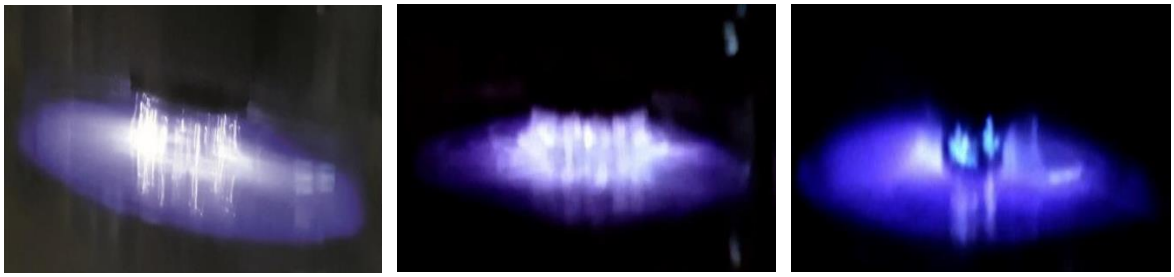

(a) (b) (c)

Figure 4. Pictures of discharges at 10.0 kV peak-to-peak voltage and 4 L/min flow rate. (a) Pure argon; (b) mixture of argon and eugenol; (c) mixture of argon and eugenol with a stainless-steel substrate on the mylar covering the lower electrode.

3.1.2. Lissajous figures and plasma power

The power of the discharge was estimated by *Q*-V plots or the Lissajous figures of both pure argon and argon mixed to eugenol (ArEu) plasmas as illustrated in figure 5. In this picture, the slopes of lines DA and CB are related to the phase when the plasma is formed in the gap and provide an approximate value of the effective capacitance (LIU *et al*., 2018). According to Eq. 1, the mean power in one cycle can be calculated from the area of the Lissajous figure (GETNET *et al*., 2020b). It can be seen in the figure that the addition of eugenol reduces the mean discharge power. This is likely due to the reduction of the plasma current as electrons may be entrapped by Eu molecules.

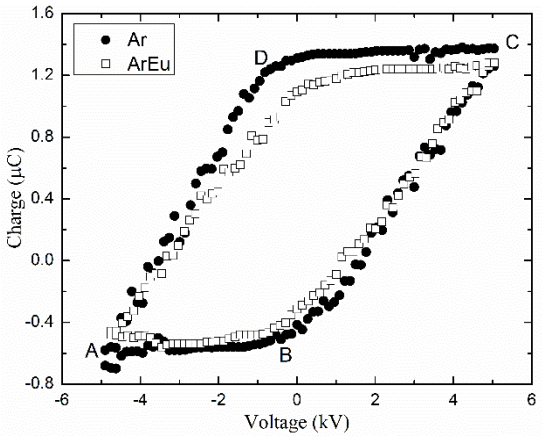

Figure 5. Lissajous figures of discharges were established in argon and argon with eugenol (ArEu) at 10.0 *kV* peak-to-peak voltage and 4 L/min gas flow rate.

Figure 6 shows the variation of the power in plasmas established in Ar and ArEu as a function of the applied voltage. In both cases, the power increased as the voltage was increased, which is in agreement with previously reported works (GETNET *et al*., 2020b; HAO *et al*., 2012; JUN-FENG *et al*., 2009).

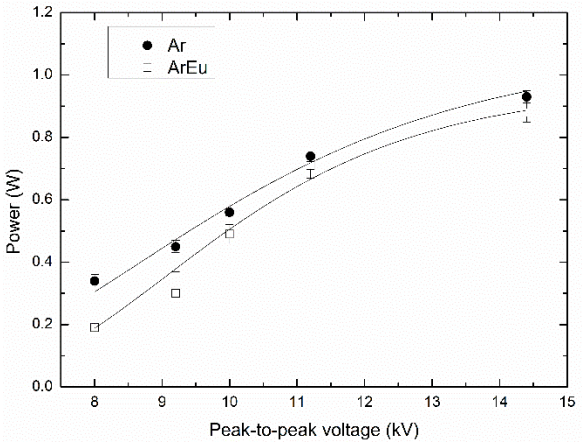

Figure 6. Mean power as a function of the applied voltage in Ar and Ar mixed with Eugenol at 4 L/min flow rate.

3.2. Optical emission spectroscopy of the discharges

Figure 7 shows typical optical emission spectra of plasmas ignited in Ar and ArEu at 10 kV peak-to-peak voltage and 1 L/min flow rate. In the spectrum of Ar discharges there can be identified four emission lines ascribed to nitrogen molecules in the range 300-415 nm and several lines of argon (ArI) in 680-880 nm. Besides, there can be observed weak emission lines at 777 and 844 nm attributed to atomic oxygen (OI), generated via reactions of metastable Ar

atoms or electrons with O_2 in the surrounding air (FALAHAT *et al.*, 2018). The presence of such lines due to the interaction of the plasma with the surrounding gas environment is also observed in helium DBD (ŞAHIN; TANIŞLI, 2020).

Additionally, the decrease in the intensity of almost all lines, especially N_2 second positive lines, when Eu was added to the gas feed can be observed. This is associated with a decrease in plasma power, as observed in Fig. 6, and the reduction in mean electron energy, and consequently, the concentration of the excited N_2 species decreases. Although Eu molecules contain hydrogen, carbon, and oxygen atoms, emission lines of species such as H, OH, and CH, indicating a low degree of monomer fragmentation was not detected. That indicates the preservation of the monomer rather than the degradation upon the plasma polymerization, which is in good agreement with the obtained Fourier-transform infrared (FTIR) spectra of polymeric films.

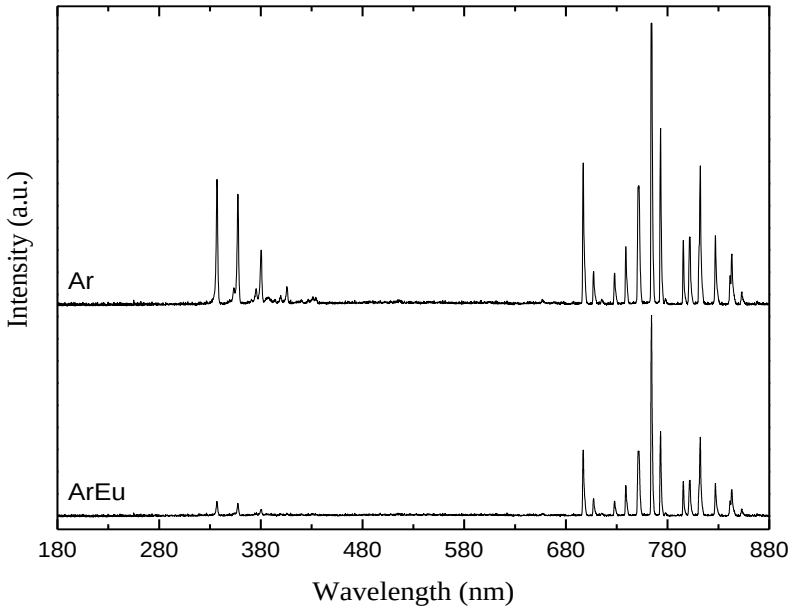

Figure 7. Emission spectra of dielectric barrier discharge in argon and a mixture of argon with eugenol (ArEu) measured at 10.0 kV peak-peak voltage and 1 L/min flow rate.

3.2.1. Effect of discharge parameters on plasma composition

Figure 8 shows the effect of plasma discharge conditions, such as applied voltage and gas flow rate, on the optical emission line intensity for discharges of Ar and ArEu. According to this result, the intensities of the lines either increases monotonically or diminishes depending on the

discharge condition, whereas the wavelength does not change. When we see these effects individually, the line intensity increases with voltage as shown in Figs. 8(a) and 8(b). This is due to the fact that the free electrons gain more energy due to the enhancement of the electric field in the gap and consequently, they increase the concentration of the excited neutral atoms and molecules. That is in agreement with the previously reported argon emission line of DBD plasma (SHRESTHA *et al*., 2017). Similarly, the intensity of ArI lines in the region of 680-880 nm increases with the gas flow rate, while the emission line of N_2 decreases as shown in Figs. 8(c) and 8(d). The possible explanation is that at a high Ar flow rate, there is a reduction in contaminant species, namely N_2, causing the rise of the density of Ar in detriment to N_2.

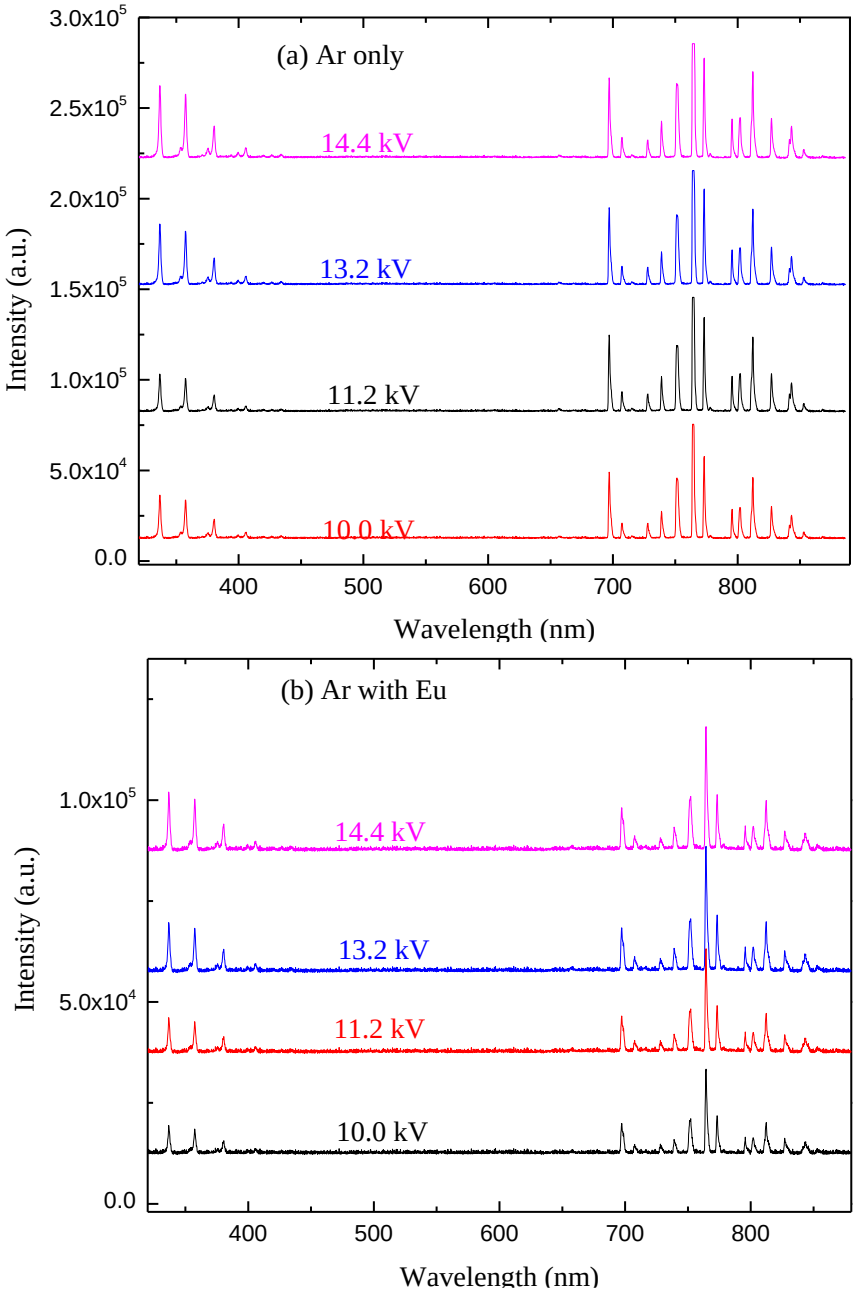
(a) Ar only
14.4 kV
13.2 kV
11.2 kV
10.0 kV
Intensity (a.u.)
Wavelength (nm)
(b) Ar with Eu
14.4 kV
13.2 kV
11.2 kV
10.0 kV
Intensity (a.u.)
Wavelength (nm)

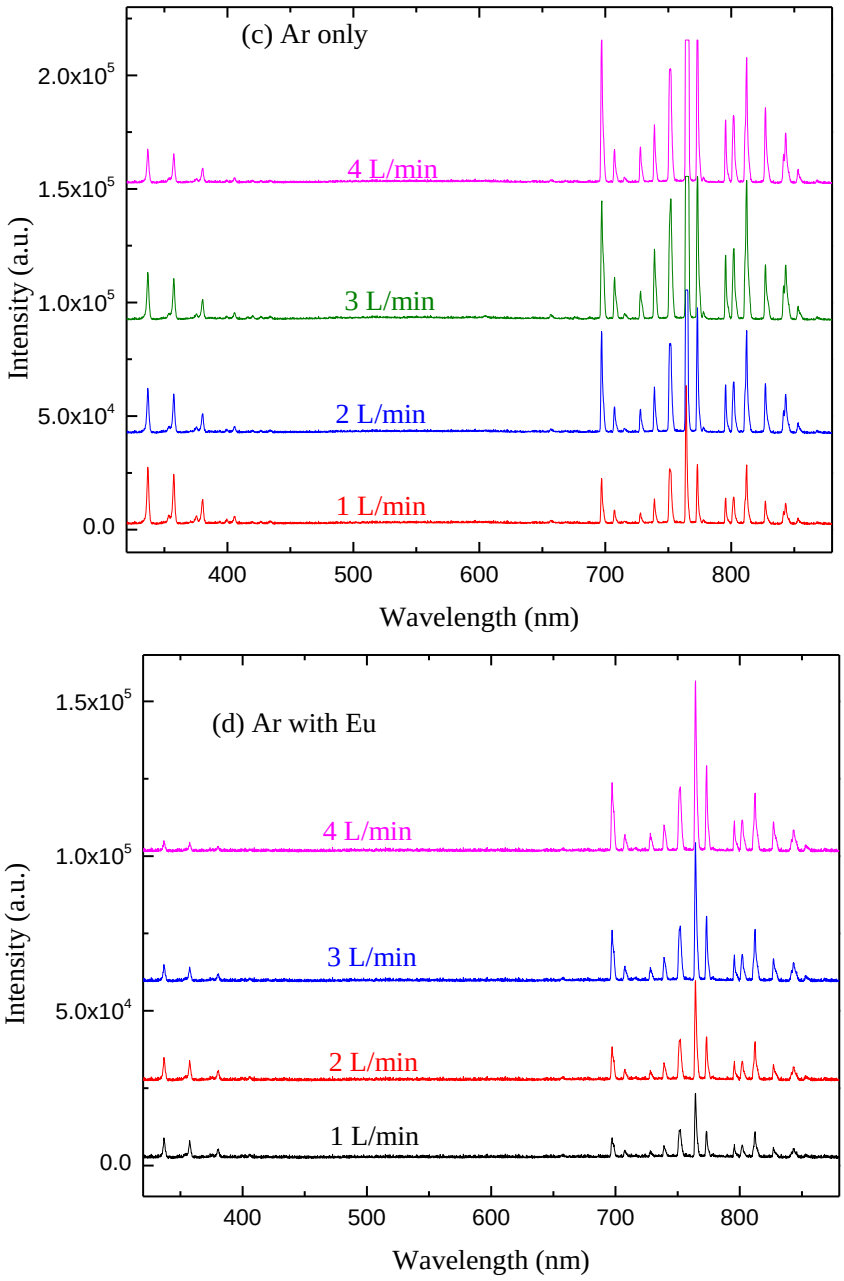

Figure 8. The optical emission lines of the argon only and argon with eugenol discharge measured by varying, respectively, (a) and (b) peak- to- peak voltage at 1 L/min gas flow rate, (c) and (d) gas flow rate at 10.0 kV peak-peak voltage.

The influence of applied voltage and gas flow rate on the relative concentration of N_2, ArI, and OI for line intensities of the discharge in both Ar and ArEu was also investigated. Using the 811 nm Ar line as a reference, the concentration of those respective species in the plasma increase with the applied voltage, at 337 and 357 nm for N_2, at 750 and 811 nm for ArI, and 844

nm for OI, as can be seen in Figure 9(a) and 9(b). This is due to the presence of energetic electrons associated with the enhancement of the electric field in the gap. As a consequence, there is an increase in the relative concentration/intensity of the excited neutral atoms and molecules (NI *et al*., 2008; N. MAZHIR *et al*., 2018). That is in agreement with the previously reported argon emission line of DBD plasma (MERTENS *et al*., 2019; SHRESTHA *et al*., 2017). Figure 8 also shows the relative argon intensity, which is indicative of plasma activity, that is, its ability to promote atoms to an excited state, and nitrogen relative concentration in the plasma.

Similarly, the relative concentration of ArI and OI lines increases with the gas flow rate, while the N_2 line decreases, as can be seen in Figure 9(c) and 9(d), as illustrated. The possible explanation is that at a high Ar flow rate there is a reduction in contaminant species, namely N_2, causing the rise of the density of Ar in detriment to N_2. It is also noticed that the concentration of N_2 decreases significantly with the flow rate for ArEu discharge compared to only Ar discharge. This is related to a more effective energy transfer of electrons to the monomer due to the high reactivity of its vinyl group in their chemical structure (MERTENS *et al*., 2019), which is in agreement with the decreasing effective discharge power (Fig. 6).

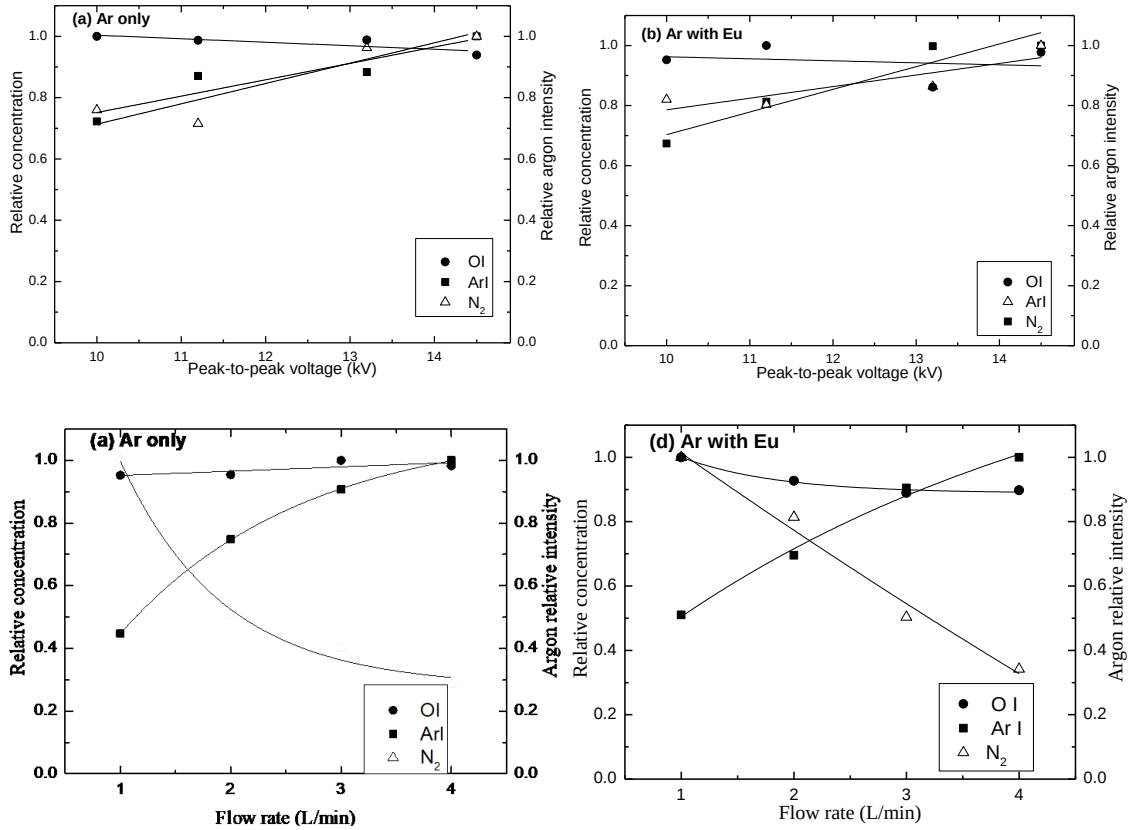

Figure 9. Variation of the relative concentration of N_2, ArI, and OI for line intensity signals (337 and 357 nm) N_2, (750 and 811 nm) ArI, and 844 nm OI with, (a, b) peak-to-peak voltage at 1 L/min gas flow rate, and (c, d) gas flow rate at 10.0 kV peak-to-peak voltage.

3.2.3. Effect of discharge parameters on electron temperature

The variation of electron temperatures was estimated in this work by using the Boltzmann plot method, according to equation 2 under Boltzmann approximation, using the neutral argon emission lines listed in Table 1, where E_j and E_i are the energies of the upper and lower levels of the radiative transitions, respectively. Figure 10 shows the effect of gas flow rate and applied voltage on electron temperature, T_e for Ar, and ArEu DBD plasma. It is clear in Fig. 10(a) that T_e decreases from 2.2 ± 0.9 to 0.9 ± 0.5 eV and 0.9 ± 0.4 to 0.4 ± 0.1 eV with the gas flow rate increases from 1 to 4 L/min for Ar and ArEu, respectively. This fact may be explained as follows. This is due to the fact that the rise of gas density in the discharge region with flow rate, which leads to the reduction of the mean energy of the electrons due to the augment of collisions with other particles (RAIZER, 1991). On the other hand, the rise of flow rate decreases the Yasuda factor given by the relation $W/(FM)$, where W is the power input, F is the flow rate and M is the molecular weight of the monomer. A low value of this factor corresponds to the lower fragmentation rate of the monomer leading to a higher chemical structure similarity of the film with the monomer (CHIPER; CHEN; STAMATE, 2009; AREFI-KHONSARI; TATOULIAN, 2008). It is in good agreement with our FTIR spectra that show preservation of the spectrum of the monomer to the films. This dependence of the electron temperature with flow rate is also observed in the DBD discharge of argon with methane plasma (JUN-FENG *et al*., 2009).

On the other hand, T_e of both Ar and ArEu rises with the applied voltage. The enhancement of the electric field increases the temperature from 2.2 ± 0.9 to 4.1 ± 1.4 eV and 0.9 ± 0.3 to 1.5 ± 0.7 eV, respectively, when a peak-to-peak voltage increases from 10.0 to 14.4 kV at a 1 L/min gas flow rate, as shown in Figure 10(b). This enhancement of the electron temperature due to the electric field has been reported in other similar experiments (GULATI *et al*., 2012; SHRESTHA *et al*., 2017), which indicates the field as the major energy source. Finally, when we compare T_e of Ar and ArEu discharges, we observe that T_e decreases significantly with the addition of monomer as a consequence of the increase in the collision frequency.

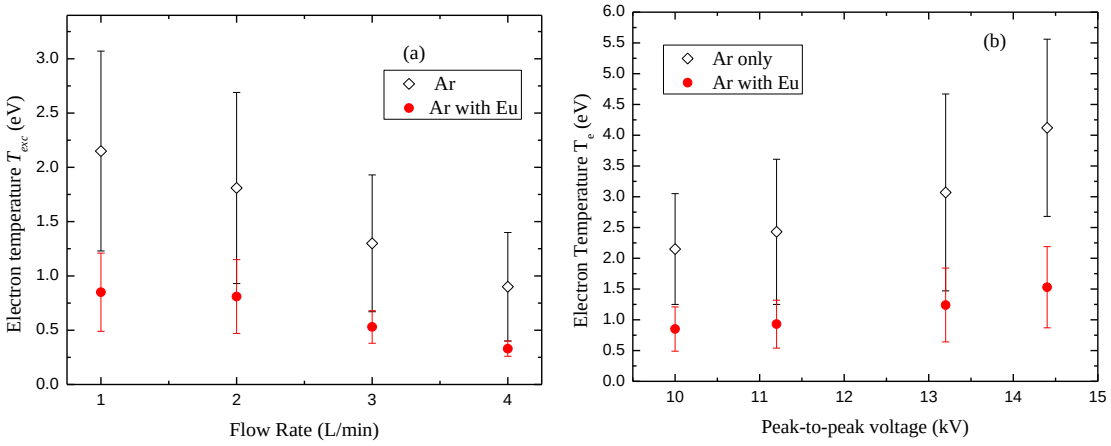

Figure 10. Relationship of electron temperature of the DBD plasma of argon and an admixture of argon with eugenol discharge with (a) gas flow rate, (b) Peak-to-peak applied voltage

3.3. **Thickness and Roughness**

Plasma polymeric thin films were successfully deposited from the eugenol monomer on the SS substrate under a different applied voltage. As mentioned in the introduction, several plasma parameters can influence the properties of the deposited thin films. Figure 11(a) shows the variation of film thickness *h* with a peak-to-peak voltage at 4 L/min gas flow rate and 30 min deposition time. The thickness of the film increases from 1.0 to 2.4 µm, with the applied voltage from 6.0 to 12.0 kV. After that, it declines to about 1.6 µm for further increases in the voltage up to 14.0 kV. The rising of the electric field enhances the fragmentation process and the concentration of active species involved in plasma polymerization reactions. As a consequence, the film becomes thicker in proportion to the field intensity. However, over a certain intensity, two competing factors occur in the polymerization process, the increase in the substrate temperature and the plasma ablation, which leads to the reduction of the film thickness. The films at higher field intensity are thinner and denser with a high degree of cross-linkage (GETNET *et al*., 2020a; SANTOS *et al*., 2017a). It should be also observed that the substrate temperature influences the adsorption of non-excited and fragmented molecules or slightly fragmented precursors during the film growing process. Such rising and decaying of the film thickness with the applied voltage are in good agreement with the absorption intensity of the functional groups shown by the FTIR spectrum

The roughness R_a of the films as a function of the applied voltage is shown in Figure 11(b). For the bare steel, the R_a value is represented by the dotted line. It clearly shows that the roughness of the film increases with applied voltage as do the uncertainty values. This behavior on the roughness and its uncertainty are proportional to the number of valleys produced by the plasma filaments in the film, which rises with the applied voltage. On the other hand, according to the scaling law, as the film thickness increases, the level of grain size and roughness also increases, until saturation (ROY; TALUKDER, 2016). This saturation occurs at high voltage with a drop in the thickness and still rises of roughness by field effect.

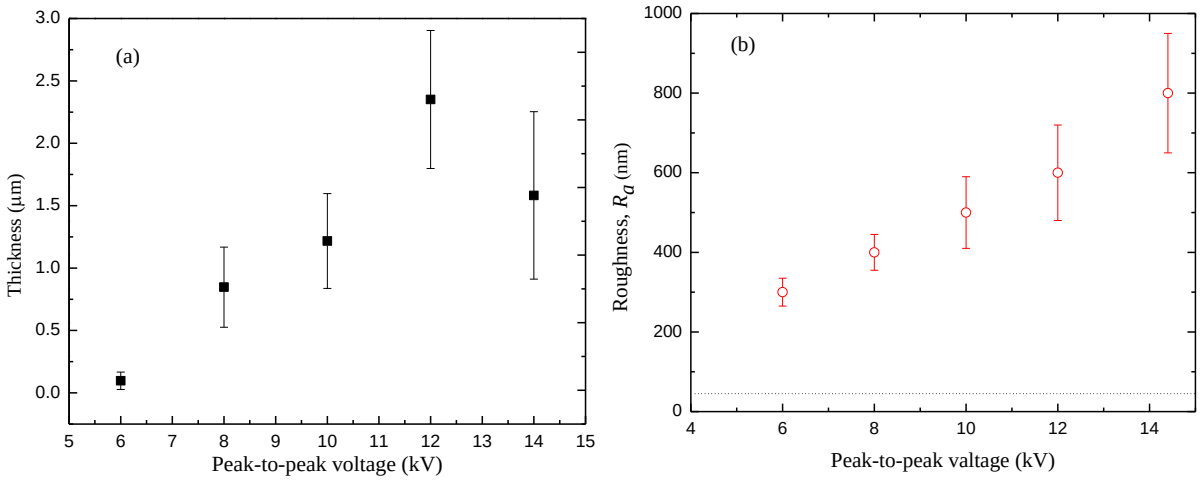

Figure 11. Variation of (a) thickness, (b) roughness of polyEugenol thin film with peak-to-peak applied voltage for a 30 min deposition time, and a 4 L/min gas in a flow rate.

3.4. **Molecular Structure**

To complete the structural study of the polymeric thin film, FTIR analysis of the monomer (Eugenol) was also carried out in addition to the film deposited under different plasma discharge conditions as shown in Figure 12.

Considering first the spectrum for the monomer eugenol, a broad peak centered at 3519 cm^{-1} corresponds to O-H stretch, indicating the presence of phenol. The absorption bands at 1234 and 1030 cm^{-1} are assigned to the stretching vibrations of C-O of the phenyl-alkyl ether (methoxy group) and phenol, respectively. The weak peaks in the range of 649-555 cm^{-1} are attributed to the C–O in-plane bending of methoxy and the peak at 1209 cm^{-1} to the O–H in-plane deformation of phenol. The peak at 1450 cm^{-1} is attributed to the asymmetric bending vibration of C-H in the methoxy group and the peak at 1363 cm^{-1} to the symmetric one. The asymmetric

stretching vibration of C-H in the methoxy group of phenyl alkyl ethers is also observed in the region of 2973-2940 cm^{-1} and its corresponding symmetric one is observed at 2841 cm^{-1}. In the same wavelength region, a peak at 2903 cm^{-1} indicates the C–H vibrational stretching of the CH_2 =C-H (vinyl) group. Additionally, two absorption bands at 995 and 916 cm^{-1} are attributed to the C–H out-of-plane bending vibration of the vinyl group. In the high wavenumber region, the weak peaks appeared at 3060 cm^{-1} and 3004 cm^{-1} which corresponds, respectively, to the C-H stretching vibrational of the aromatic skeletal and vinyl alkene group. Moreover, the weak peaks between 848 and 746 cm^{-1} are attributed to the C–H out-of-plane deformation of the 1, 2, and 4-tri-substituted benzenoid compounds.

The FTIR spectra of the monomer and the films are quite similar, except for the reduction of peak intensity in the film, particularly in the fingerprint region below 1500 cm^{-1}. This reduction means that a small quantity of monomer was polymerized and deposited. Additionally, the peaks at 2973 and 2903 cm^{-1} are assigned to asymmetric and symmetric stretching of methylene and are present only in the monomer spectra due to the loss of the vinyl group. It is interesting to point out that the vinyl double bond was broken during the plasma polymerization processes, just like conventional polymerization. Moreover, the peak at 3519 cm^{-1} shifts towards a lower frequency at 3432 cm^{-1}. That might be associated with the formation of intermolecular H-bonding caused by plasma polymer formation. On the other hand, a peak at 1705 cm^{-1} associated with ketone appeared in the film, which is absent in the spectrum of the monomer. That corresponds to the post-oxidation of the trapped free radicals confined during the formation of the film and the tautomerization as well (MATIN; BHUIYAN, 2013; JACOB *et al*., 2014).

Figure 12 also gives the spectra of films deposited for various discharge power up to 0.9 W, which corresponds to applied voltage up to 14.4 kV peak-to-peak. As can be seen, all functional groups are preserved in the film and the intensity of absorption peaks increases with the power of discharge. The partial oxidation of the film, particularly for -OH and aryl groups, leads to a slight decrease in the intensity and the bandwidth for discharges with power above 0.7 W. In general, it is interesting to mention the preservation of monomer functional groups, particularly hydroxyl and aromatics that are the key further of antimicrobial activity.

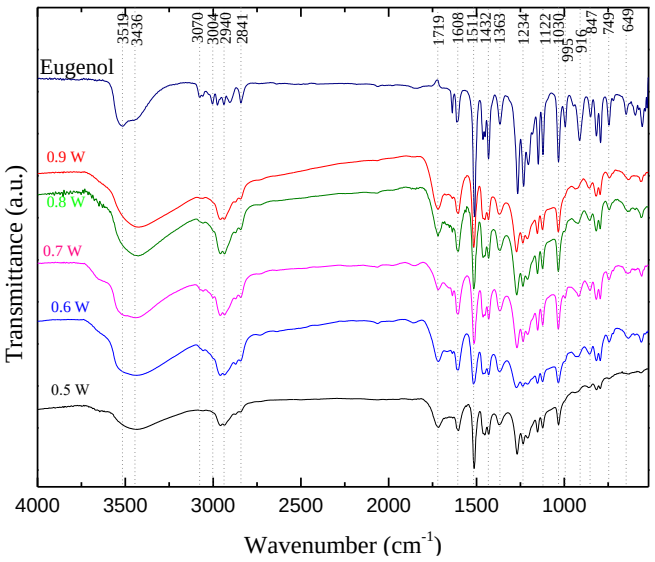

Figure 12. FTIR spectra of eugenol and polyeugenol thin films deposited with a 30 min deposition time and a 4 L/min gas flow rate by varying the plasma discharge power from 0.5 to 0.9 W.

3.5. **Stability and aging of the film**

Several medical devices often require storage for a certain period before they are used (AZIZ *et al*., 2017). Therefore films produced for biomedical applications require stability in atmospheric air for extended periods and in aqueous solutions as well. Moreover, good adhesion of the films to the substrate and the preservation of its functionality after polymerization is critical in these applications. Since the initial attachment of bacteria assay was carried out in the TSB solution, it is worth seeing the physical and chemical stability of film in this medium (CHAN *et al*., 2016).

In order to investigate these features the structure of eugenol-derived films was investigated with FTIR for attacks in Tryptone Soy Broth (TSB) solution, and by exposure to atmospheric air and a high thermal UV-lamp. The spectra of TSB before and after immersion of the films for 45 min are shown in Figure 13(a). They have a close similarity which indicates good stability of the films on the surface of the substrate without any degradation. The spectra of the film after 120 days in ambient air are shown in Fig. 13(b). Again, there is no change in the obtained spectra, which shows that the obtained films are not affected by exposure to the ambient air for this period. For UV analysis, the films were exposed to a high thermal UV-lump (at 65 °C) at a nearby 3 cm distance for 1 h, which is a typical procedure for material sterilization. The resulting

spectra are shown in Fig. 14(b) indicating that the films are unaffected by the high energy radiation. On the other hand, the IR spectra of direct coating of eugenol monomers degraded within 20 min when exposed to the same UV-lamp (Fig. 14(a)). Therefore, these tests showed that the eugenol-derived film produced in the DBD plasma is thermally stable with adhesion on a stainless steel substrate, maintaining its properties for a long period in a regular atmosphere.

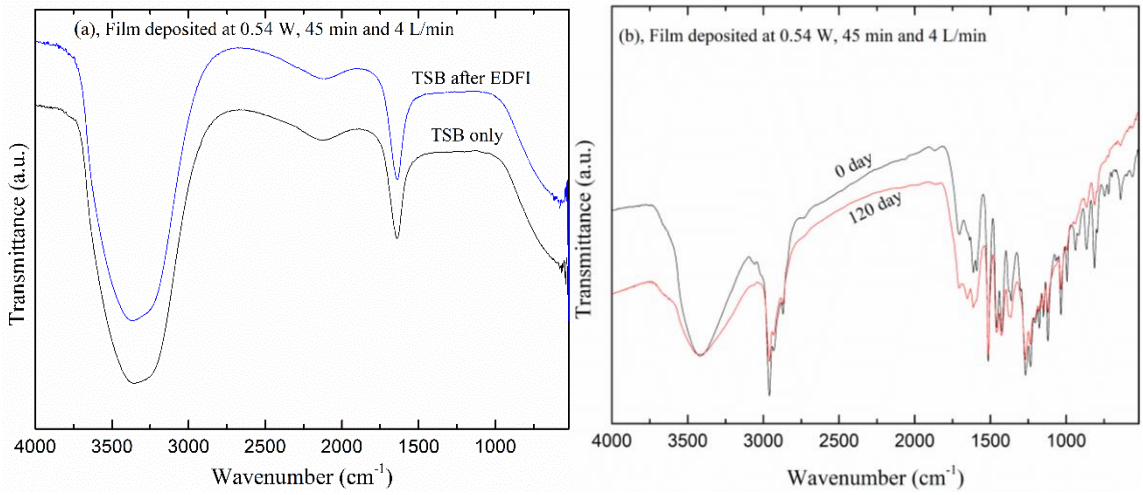

Figure 13. The FTIR spectra of (a) Tryptic Soy Broth (TSB), and (b) the film exposed to ambient air for 120 days. EDFI is eugenol-derived film immersion.

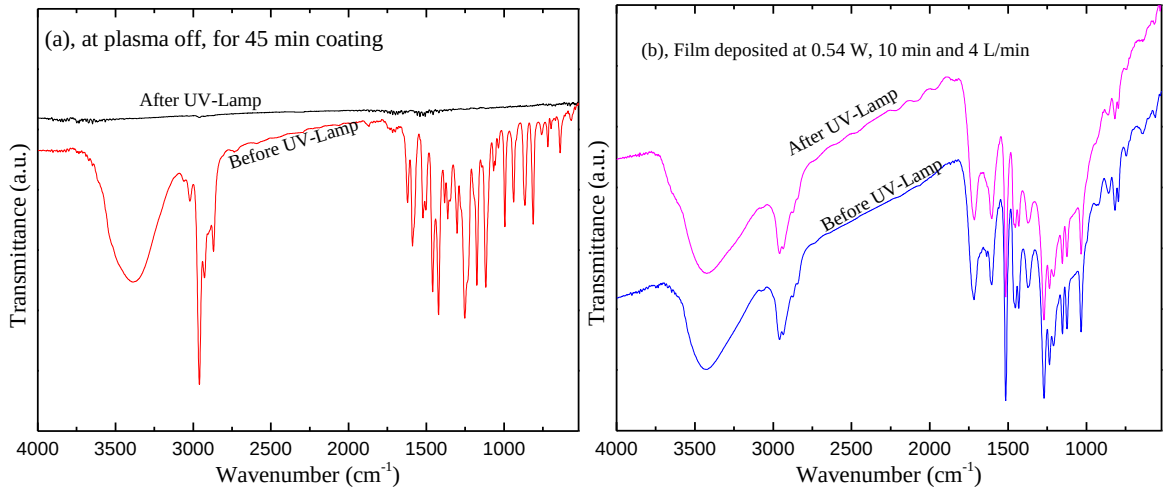

Figure 14. FTIR spectra of, (a) direct eugenol coating and (b) the eugenol-derived film-coated SS substrate, before and after exposure to high thermal UV-lamp.

4. Conclusions

In the present study, we deposited and characterized the eugenol-derived film, diagnosed the dielectric barrier discharge, and estimated the electron temperature of argon plasma in the presence and the absence of monomer eugenol, assuming local thermodynamic equilibrium. The electron temperature of the ArEu discharge was around 1.5 eV for gas flow rate 1 L/min and 14.4 kV peak-to-peak voltage. The filamentary discharge of the device was successfully used to polymerize PolyEugenol thin film on a stainless steel substrate under different discharge conditions. The obtained thin film had 2,400 nm maximum thickness and 800 nm roughness with a molecular structure similar to the monomer. They are also thermally stable, undegraded, and unaged when exposed to a high thermal UV-lamp, TSB solution, and atmospheric air for long periods of time. These results encourage the use of polyEugenol thin film coatings, for instance, for suppression of biofilm formation and corrosion protection of biomaterials.

Thin Solid Film, Under Review

8 Atmospheric Pressure Plasma Deposition of Eugenol-Derived Film on Metallic Biomaterial for Suppression of *Escherichia Coli* and *Staphylococcus Aureus* Bacterial Biofilm

Tsegaye G. Getnet[a,b], Milton E. Kayama[c], Nilson C. Cruz[a*], Elidiane C. Rangel[a], Iolanda C. S. Duarte[d], Gabriela F da Silva[d].

[a]Technological Plasmas Laboratory, São Paulo State University at Sorocaba, 18087-180, SP, Brazil,

[b]Department of Chemistry, college of science, Bahir Dar University 79, Bahir Dar, Ethiopia, [c]Laboratory of Plasma and Applications, São Paulo State University at Guaratinguetá 12516-410, SP, Brazil, [d]Laboratory of Environmental Microbiology, Federal University of São Carlos at Sorocaba 18052-780, SP, Brazil.

*Corresponding email: nilson.cruz@unesp.br.

Abstract: *Eugenol (4-Allyl-2-methoxy phenol) is widely used as a condiment and bactericidal coatings for food packing and biomaterials. We have investigated the deposition and characterization of eugenol-derived films (EDF) on stainless steel (SS) surface deposited using atmospheric pressure plasma discharge for suppression of* Escherichia coli *and* Staphylococcus aureus *bacterial adhesion and proliferation. The thickness of the deposited films was in the range of 1,000 to 2,500 nm with a roughness up to 800 nm. Infrared spectra showed that the EDF preserves the hydroxyl and aromatic groups found in liquid eugenol, which is a key feature for the antibacterial activity of the film. Scanning electron microscopy showed that the entire surface of the substrate is covered by a spherical structure approximately 10 to 20 µm in diameter. Wettability analysis showed an increase in the hydrophilicity of the stainless steel surface after the deposition. The biofilm suppression, against* E. coli *and* S. aureus *bacterial growth, revealed that these surfaces inhibited the adhesion and proliferation of these bacteria by more than 78 and 65%, respectively, while in the untreated samples the growth was more than 90% for both microbes. Therefore the eugenol thin film deposited by this method was effective for biofilm suppression with a potential application for biocompatible material coating processes.*

Keywords: dielectric barrier discharge, plasma polymer, eugenol, biofilm, contact angle.

1. Introduction

The use of biomaterial has increased significantly over the past decades as a consequence of many factors such as the increase in the number of aging population and life expectancy, changing lifestyles, and the improvements in implant technology (KUMAR *et al*., 2020; SUCI DHARMAYANTI *et al*., 2020; HOGAN *et al*., 2019). For instance, in the United State 300,000 dental implants (GAVIRIA *et al*., 2014), and up to 1 million hip and knee prosthesis (PRICE *et al*., 2018) were implanted in the last decade; in the United Kingdom, in the same period, 90,000 urinary catheters (GAGE *et al*., 2017) were implanted; and in the European Union 100,000 hip and knee prosthesis (VAZ *et al*., 2017) were implanted per country annually. However, the problems related to biocompatibility, which lead to uncontrolled biological responses such as immune system activation, protein adsorption, inflammatory reactions, and cellular adhesion, are still not fully resolved (VELNAR *et al*., 2016).

At the same time, the infections caused by bacterial colonization on medical devices and their biofilm formation represent another barrier for the permanent use of implants (HENRIKSEN *et al*., 2019; NEUBEISER *et al*., 2020; ÇAKMAK *et al*., 2019). For example, in the United States, hospital-acquired infections alone cause between 60,000 to 100,000 deaths per annum, amounting to an annual economic burden of $17 to $30 billion (GOMEZ *et al*., 2018). It is estimated that as many as 80% of these infections arise from bacterial biofilms (EDMISTON *et al*., 2015).

The biofilm formed on tooth surfaces, called dental plaque, is responsible for the majority of dental implant failure and diseases, such as periodontitis and cavities (CORDEIRO *et al*., 2018; MOSADDAD *et al*., 2019). Furthermore, once biofilm is established, it is difficult to eradicate as microbes become resistant to antibiotics (TAN *et al*., 2018; WOLFMEIER *et al*., 2018). The only solution to extirpate the colonization of biofilm-forming bacteria is to surgically remove the infected implant, which in turn causes high economic costs and extra risks of morbidity and mortality to the patients.

To overcome such problems, it is of paramount importance to modify the surface properties of the implant, such as roughness and wettability, since the initial attachment of microbes is highly determined by the features of this surface. There is an ongoing debate regarding the preferential attachment of bacteria to rougher surfaces. For example, Cordeiro

et al., (CORDEIRO *et al*., 2018) observed a reduction in colony-forming-unit (CFU) counts of bacteria adhering to rough implant surfaces (roughness around 1.26 µm), for a 90 min bacterial biofilm formation period. However, another investigator observed higher numbers of bacteria adhering to the implant surface with similar roughness, for 5 to 7 days of the biofilm formation period (ALMAGUER-FLORES *et al*., 2012). Such contradictory findings might be due to the fact that high roughness is a minor factor in the initial adhesion phase of biofilm formation though it can influence the mature biofilm (CORDEIRO *et al*., 2018). Alternatively, the adsorption of proteins may have been favored by the presence of pores on a rough surface that provides a large number of anchorage sites. It is known that this increase in protein adsorption on the implant is important to mediate the interaction of osteoblastic cells with the implanted material, accelerating osseointegratio (SHIBATA; TANIMOTO, 2015; XIE *et al*., 2017). In addition, as cited by Selvakumar *et al*., (SELVAKUMAR; BARSHILIA; RAJAM, 2010), surface roughness amplifies the wettability of the surface. It has been previously reported that increasing the roughness of the surface can lead to the rise in the hydrophilicity and bonding capacity of polymeric films (HONARVAR *et al*., 2017).

Biofunctional surface coating, such as antibiotic-releasing and silver-coating, has been developed to prevent bacterial infections on implants (KIM *et al*., 2016; AGARWAL *et al*., 2012; EBY; LUCKARIFT; JOHNSON, 2009). However, these methods are characterized by natural drawbacks of the solution-coating process such as complex and tedious procedures, lack of controllability, and leakage problems (RUHE; LOW; HAYES, 2013; CHAN *et al*., 2016). In this regard, the use of plant-derived compounds as natural antimicrobials has received close attention from researchers to overcome such limitations (BAZAKA *et al.*, 2015a; CASTRO *et al*., 2016). These natural agents have a rich source of biologically-active compounds and distinctive mechanisms to eradicate antibiotic-resistant bacteria, unlike that of the current method using synthetic antibiotics. Also, such plant-derived antibiotics are renewable, inexpensive, and environmentally friendly (HYLDGAARD; MYGIND; MEYER, 2012). However, until recently, essential oils were rarely used to produce biological-active coatings because of their complex and versatile structure (BAZAKA *et al*., 2017).

Given this situation, the concept of plasma-assisted chemical vapor deposition gained considerable interest for the conversion of bio-renewable resources into diversified structures

varying from simple polymers to advanced carbon nanostructures and also modifying the surface properties of biomaterials while preserving their bulk characteristics (AL-JUMAILI *et al*., 2017b; SANTOS *et al*., 2016a). Still, the process takes place in a dry and solvent-free environment, without the production of significant toxic byproducts. Owing to this, it has been used in many different applications, such as electrode insulation (PETER *et al*., 2018; WANG *et al*., 2017; REICHEL *et al*., 2018), diffusion barriers (HOFFMANN *et al*., 2017), corrosion protection (SANTOS *et al*., 2017b; RANGEL *et al*., 2019; RANGEL; CRUZ; RANGEL, 2020), sensor devices coating (ALEMÁN *et al*., 2018) and antimicrobial coating (GAO; HANG; CHU, 2017).

Several studies (QIAN *et al*., 2020; CAZELLI *et al*., 2017; RIBES *et al*., 2019; OLEA *et al*., 2019), have demonstrated the biocidal activity of eugenol, a natural oil extracted from cloves, against free-standing human pathogens microorganisms. In addition, the U.S. Food and Drug Administration approved the use of clove oil as a flavoring substance in the food industry, as a fragrance in the cosmetics industry, and in dentistry as a natural analgesic and antiseptic (MOHAMMADI NEJAD; ÖZGÜNEŞ; BAŞARAN, 2017; FUJISAWA *et al*., 2002). Therefore, it can be considered as a very promising material to be used in the production of bactericidal coatings for implantable and packing materials. Several experimental studies have been conducted addressing the fundamental mechanisms and chemical phenomena of atmospheric DBD plasmas (SATO *et al*., 2015; PEETERS; YANG; VAN DE SANDEN, 2015; SEWRAJ *et al*., 2011). However, we believe no studies have been conducted on the deposition of films from clove essential oil, particularly for biofilm suppression, either independently or in combination with another monomer, in both low- and atmospheric-pressure plasma discharges. In this context, the present study has focused on the development of eugenol-derived film (EDF) coating on stainless steel (SS) substrate through an atmospheric plasma discharge, aiming to inhibit bacterial adhesion and proliferation tendencies of the *E. coli* and *S. aureus* bacterial strains. These microorganisms were chosen because they are widely-spread foodborne pathogens. Also, these pathogens are well-known sources of infections in hospitals and implantable devices (KHATOON *et al*., 2018; KUMAR *et al*., 2017).

2. Materials and Methods

2.1. Sample Preparation

Before depositions, 10 mm × 10 mm SS coupons were cut using a metal cutter from a sheet of 1 mm thick SS plate. Subsequently, they were mirror-polished by different grades of waterproof sandpapers in the granulation sequence 600, 1000, and 1200 (HUACHO *et al*., 2017), and then cleaned in ultrasonic baths using detergent, distilled water, and isopropyl alcohol. Finally, the coupons were dried with a hot air blower and stored in Petri dishes until use.

2.2. Plasma Polymerization of eugenol

The system of the dielectric barrier discharge plasma reactor used for the deposition of EDF is fully described elsewhere (GETNET *et al*., 2020a; GETNET *et al*., 2020b; GETNET *et al*., 2020c; KAYAMA *et al*., 2017) and shown schematically in Fig.1. It consists of a cylindrical brass upper and an aluminum disk lower electrode separated by a polyester sheet with a 15 kV@60 Hz transformer with its primary voltage controlled by a Variac. The electrodes were assembled axially held by circular polyacetal flanges with a 3 mm discharge gap. Operating in the vertical position, a 20 kV peak-to-peak voltage was applied to the upper brass electrode.

Eugenol (4-(H_2C=$CHCH_2$) C_6H_3-2-(OCH_3) OH of at least 98% purity (Sigma-Aldrich), was dragged in an atomizer by argon (99.9% purity), at a flow of 5 L/min and 25 ^oC. A 1000× voltage divider mounted with film resistors was used to measure the applied voltage v_A and its signal was recorded by a Tektronix TDS1001C (30 MHz, 500 MS/s) oscilloscope. This device was also used to record the voltage drop on a resistor and a 10 nF capacitor, v_C. Both elements were connected alternatively in series with the lower electrode and the ground. Ultimately we estimate the mean power of the discharge using the capacitor accordingly to equation 1:

$$P = \frac{1}{T}\int_0^Q v_A dq \qquad , v_A \gg v_C \qquad (1)$$

where $q=Cv_C$ is the instantaneous charge, T the period, and Q the charge in one period. The calculation provided an averaged 12 signals in the oscilloscope and at least 1400 periods was about 0.54 ± 0.04 W, this power was used for film deposition.

The thin film deposition time was in the range of 10 to 45 minutes. Film chemical structure and aging were characterized using Fourier transform infrared spectroscopy (Jasco FT/IR-410). Scanning electron microscopy was used to characterize the surface morphology of the deposited film and their chemical composition was performed by X-ray energy dispersive spectroscopy (EDS), coupled to the SEM microscope, using a Dry SD Hyper EX-94410T1L11 detector. Also, a Veeco D150 profilometer was used to measure the film thickness and roughness. To evaluate its thickness, the films were deposited on partially masked Kapton tape SS coupons. Finally, wettability was determined by measuring the static contact angle of water and diiodomethane in a goniometer Ramé-Hart 100-00.

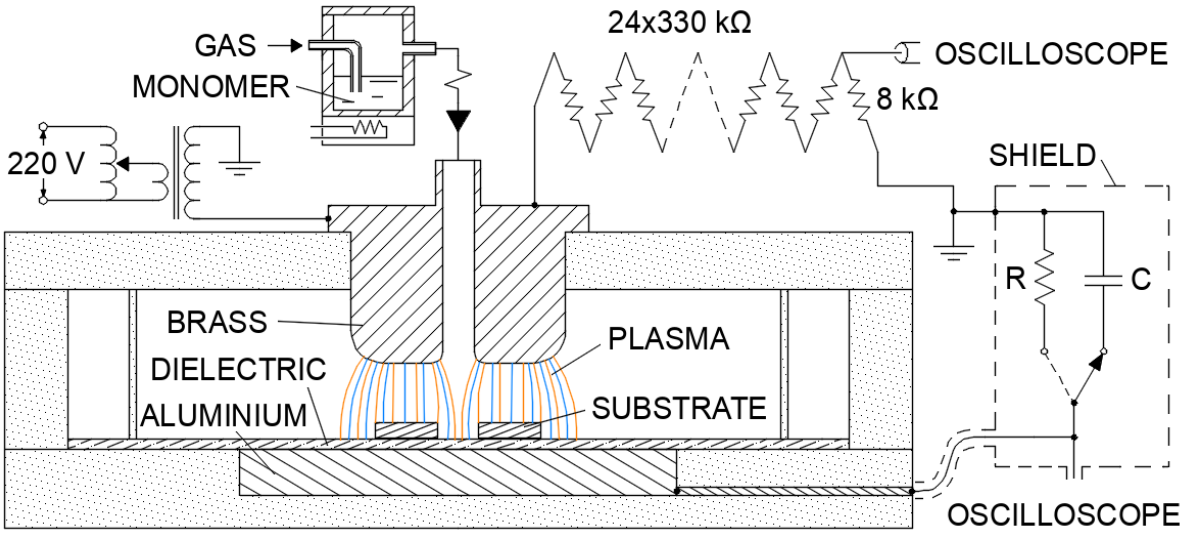

Figure 7. Schematic representation of the experimental setup used for film deposition.

2.3. Biofilm Assay

To perform biofilm assay two model bacteria were used, the *Escherichia coli* ATCC®11229 and the *Staphylococcus aureus* ATCC®6538 strains. We adopted the procedure described elsewhere in (GETNET *et al.*, 2020a), but with a slight modification. In brief, the stock strain of each microbe was spread on Tryptic Soy Agar (TSA) medium and incubated for 48 h at 37 °C. Three replicated EDF coated coupons were introduced separately in sterilized test tubes having 5 mL of Tryptone Soy Broth (TSB) medium and a 3.6-5.0 $\times 10^8$ colonies-forming unit (CFU)/mL of inoculum concentration. After that, the tubes were incubated in a static oven at 36.5 °C for 3 h, withdrawn and rinsed two times with 3 mL of saline solution (0.85%), transferred to new sterile test tubes having a new 5 mL of TSB

medium, and incubated again in a static oven at 37 °C for 24 h. After this biofilm formation phase, the substrates were transferred to a new test tube having 10 mL of saline solution and then sonicated for 30 min to release the biofilms. From such tubes, 100 µL aliquots diluted up to 10^{-6} by saline solution were seeded in TSA medium in sterile Petri dishes and incubated at 37°C for 48 h for plate counting of viability. Untreated and eugenol coated SS coupons were used as a positive and negative control, respectively. Finally, its viability was presented as the log of CFU/cm^2, by using equation 2:

$$CFU / cm^2 = \text{number of colonies} \times \text{dilution factor} \times \text{substrate area} \quad (2)$$

According to the literature, scanning electron microscopy has been the preferred method for visualizing biofilms since it provides information about the spatial structure and detects the presence of extracellular polymeric substances (EPS) (HUNG *et al*., 2013; RODRIGUES *et al*., 2013). Therefore, the attachment and biofilm formation of those bacteria were visualized by SEM images. To create contrast imaging of the adherent cells and their biofilm growth extent to the sample surface, both uncoated and EDF coated SS coupons, separately, were fixed for 3 h in Karnovsky solution (2.5% glutaraldehyde, 2% formaldehyde, 0.1 M sodium phosphate buffer; pH 7.2). Then, the Karnovsky's solution was dehydrated by washing with a phosphate buffer for 5 min and soaked with ethanol (60%, 70%, and 80%) solution for 5 min and 100% for 10 min, then aseptically air-dried. Before the SEM image examination, the samples were coated with a thin gold-palladium film for 60 seconds (GETNET *et al*., 2020a).

3. Result and Discussion

3.1. Morphology

Figure 2 shows the scanning electron micrograph image of the EDF coated SS substrate under different deposition conditions. The view of the surface area around 2.5x2.5 mm at the center of the deposition is shown in Fig. 2(a). It shows a smooth clearance at the central region surrounded by several spherical protuberances with a diameter of around 10 to 20 µm. This feature is a consequence of the geometry of the upper electrode of the discharge that has a central channel from where the gas is injected in the discharge zone. Right below the nozzle of this channel, we have the clearance with an apparent smooth surface. Around this region is the

location where the filaments have concentrated which end up producing the protuberances in the deposition.

A closer view of the surface of these two regions with magnification around x900 is given in figure 2(c) and 2(d). Fig. 2(b) is a reference showing the polished surface. The scratches seen in this figure are related to the thinnest granulation used in the polishing process. As can be seen in Fig. 2(c), the plasma polymerization process takes place in the regular form at the nozzle region producing a uniform deposition. In the discharge area, the usual random motion of the filaments on the surface tends to concentrate in specific loci. Due to the high density and temperature of the plasma in the filament, a more fragmented and ionized species will be concentrated to its close neighbor leading to nucleation of species during the deposition and the formation of clusters as shown in Fig. 2(d). The EDS analysis valley region where the filament is located shows no traces of the substrate material (Table 1, at point 3), suggesting that in this region we have either a thin filament moves around it or a wide filament with a non-uniform area in interaction with the surface, both through a dielectric layer. The analysis also shows a dominant presence of carbon and oxygen in the valleys and that all these features are insensitive to the deposition time from 10 min up to 45 min (Fig. 3). On the other hand, the clusters result from monomer polymerization derived from reactive species surrounding the filaments. Also, very similar morphological features of the EDF is observed for the film grown under different discharge conditions (Fig. 2(e) and 2(d)).

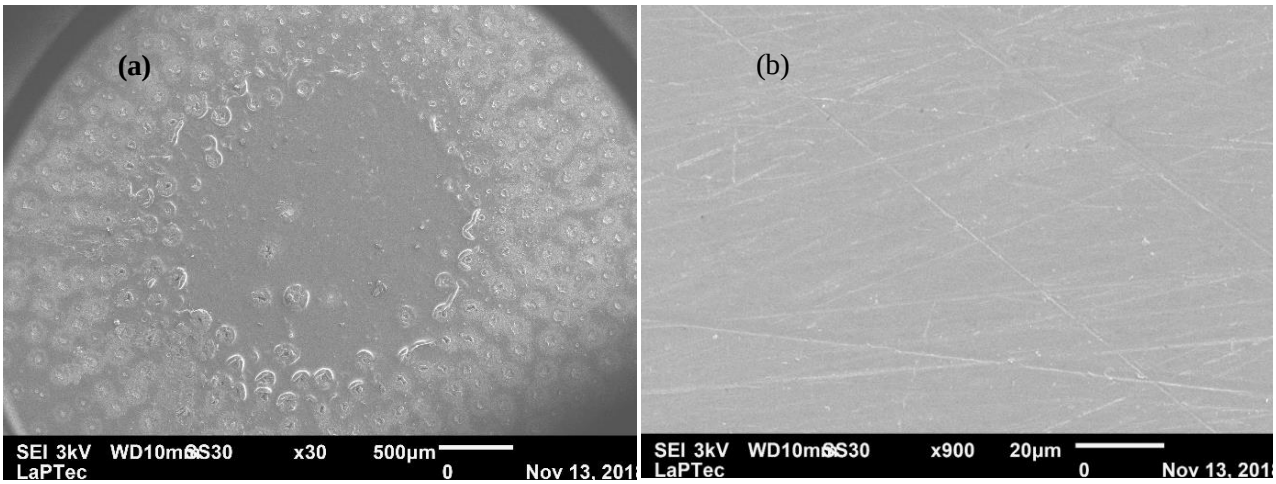

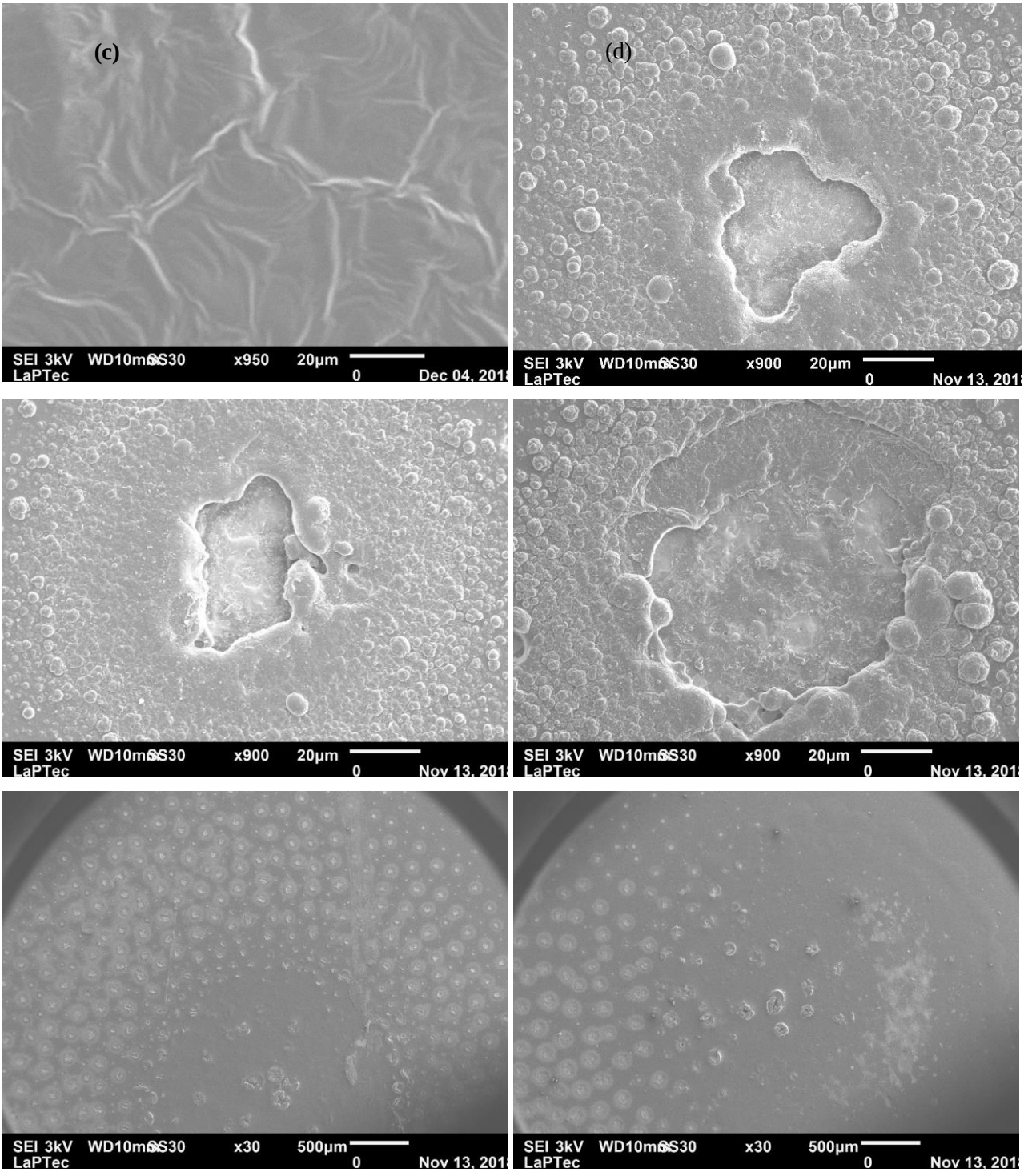

(e) (f)

Figure 2. Scanning electron microscopy (SEM) micrographs of (b) uncoated SS coupons and coated with EDF deposited for 45 min at 0.54 W of (a) 30× and (c, d) 900× magnifications at a

different point, and EDF deposited for 45 min at (e) 0.81 W and (f) 1.02 W, at a different resolution.

Table 1 shows the atomic proportions of carbon, oxygen, iron, and chromium in SS substrate as received and coated with EDF, obtained from the EDS spectra at an accelerating voltage of 5 and 10 kV, under different locations on the film-coated area. As one can note in this table, the pure SS shows 76.8% iron, 18.0% chromium, and 5.2% carbons. The film-coated SS under different discharge conditions also shows carbon and oxygen in a high proportion and iron to the smallest extent up to ~8.3% in the region of the holes and up to 1.3% concentrations from near the holes locations of the films, when the microscope operated at 10 kV. Such presence of iron in the film is caused by the penetration of the beam deeper than the film thickness, particularly at holes located in the film. It was confirmed that, when we operated the microscope at 5 kV, there was the absence of iron even at the location of the holes of the film, as shown in table 1 point 3. The remaining chromium is no longer visible in the film, except for the pure SS substrate. In general, the obtained EDS data confirmed that the whole area of the substrate was covered by the film.

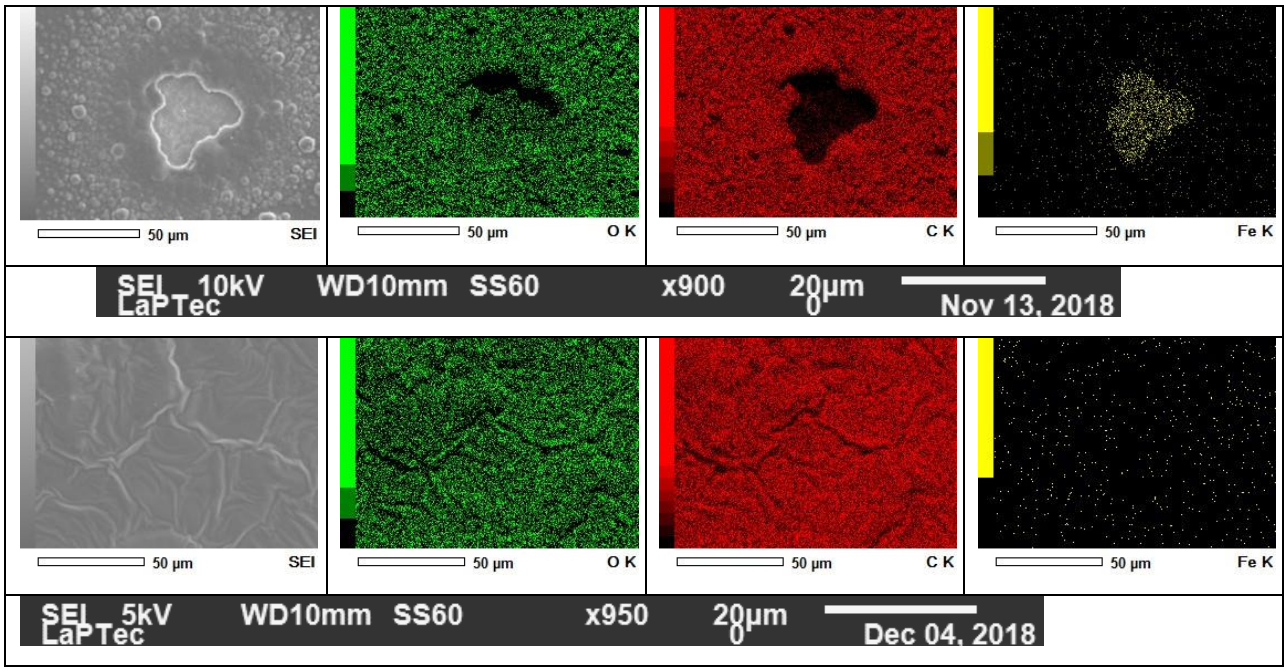

Figure 3. Elemental mapping images of iron, carbon, and oxygen of eugenol-derived film, deposited at 45 min, 5 L/min, and 0.54 W, performed by EDS at different points.

Table 1. Elemental concentration (%) of uncoated SS and coated with eugenol-derived film for 45 min deposition time and 5 L/min flow rate, at a different location in the film-coated area of the substrate.

Plasma Discharge power, at	Element	Elemental concentration (%)		
		Point 1	Point 2	Point 3
Untreated SS	Iron	76.8	-	-
	Chromium	18.0	-	-
	Carbon	5.2	-	-
1.02 W	Iron	3.5	ND	ND
	Carbon	82.6	81.9	84.9
	Oxygen	13.9	18.1	14.9
0.81 W	Iron	2.8	ND	ND
	Carbon	81.6	81.0	84.6
	Oxygen	15.6	19.0	15.1
0.54 W	Iron	5.9	1.3	-
	Carbon	79.7	80.0	-
	Oxygen	14.5	18.7	-
0.32 W	Iron	8.3	0.2	ND
	Carbon	75.6	83.4	84.7
	Oxygen	16.2	15.9	15.2

*Point 1 is at hole location, point 2 is at far from away holes location of the film (EDS at 10 kV beam energy), and point 3 is in the hole location of the film (EDS at 5 kV beam energy), ND is not detected.

3.2. Thickness and Roughness

Figure 4(a) shows the eugenol-derived film thickness *h* and the deposition rate defined by *h/t* as a function of deposition time *t*. As can be seen in this figure, with deposition time varying from 10 to 45 min the film thickness grows from 1,000 to 2,500 nm. The thickness is about the same value obtained previously with carvacrol-derived film in this same reactor (GETNET *et al.*, 2020a) and those reported using low-pressure RF discharge using terpinen-4-ol, linalyl acetate, and 1, 8-cineole (BAZAKA; JACOB, 2009; EASTON; JACOB; SHANKS, 2009). However, due

to the high concentration of active species in atmospheric discharges, the thickness of the film produced in this condition for the same deposition time is almost twice compared to the deposition in low pressure.

However, the deposition rate *h/t* decreases with the deposition time, in the opposite trend to the usual plasma deposition processes at low-pressure discharge. This behavior occurred due to the interaction of plasma species with surrounding ambient gas. Since the discharge is exposed atmospheric gas, it produces high concentrations of atomic oxygen and other reactive elements, such as OH and O_3 that can chemically etch the volatile and/or smaller molecules from the film material, like formaldehyde, CO, H_2O, CO_2, and so on (GETNET *et al*., 2020a). Besides, the continuous bombardment of energetic electrons and ions for long periods has had a significant effect on physical etching and competitive polymerization, which in turn changes the deposition rate (SANTOS *et al*., 2017b; EASTON; JACOB; SHANKS, 2009; PANKAJ *et al*., 2017). These conclusions are supported by the results of SEM images (Fig. 2(d)), which show that holes were created in the deposited film. Furthermore, an increase in the deposition time raises the substrate temperature, since the substrate is placed in the gap of the electrodes amidst the discharge during the deposition. As a consequence, the deposition rate decreases. It was observed by many investigators (MORENT *et al.*, 2009; SANTOS *et al*., 2016a; GÜRSOY; KARAMAN, 2015) that the polymer deposition rate decreases with increasing substrate temperature. The obtained result showed a similar trend with the previously reported carvacrol-derived (GETNET *et al*., 2020a), and hexamethyldisiloxane (MORENT *et al*., 2009) film deposition rate, which was deposited using an atmospheric pressure dielectric barrier discharge plasma.

Figure 4(b) shows the average roughness of the surface, R_a, of the uncoated and the coated SS substrate as a function of *t*, where $t = 0$ corresponds to the initial condition with the substrate exposed to the monomer with the plasma off. As the deposition takes place, the surface becomes rougher than the original, with R_a increasing with the deposition time. This is due to the creation of irregularities on the surface by the discharge filaments as can be seen in the SEM images in Fig. 2(b), which shows an increase of the cluster and grain size leading to the augment in the thickness of the film (Fig. 3(a)). Since the roughness is an important parameter for bacteria attachment, the kind of film produced is very suitable for biological applications.

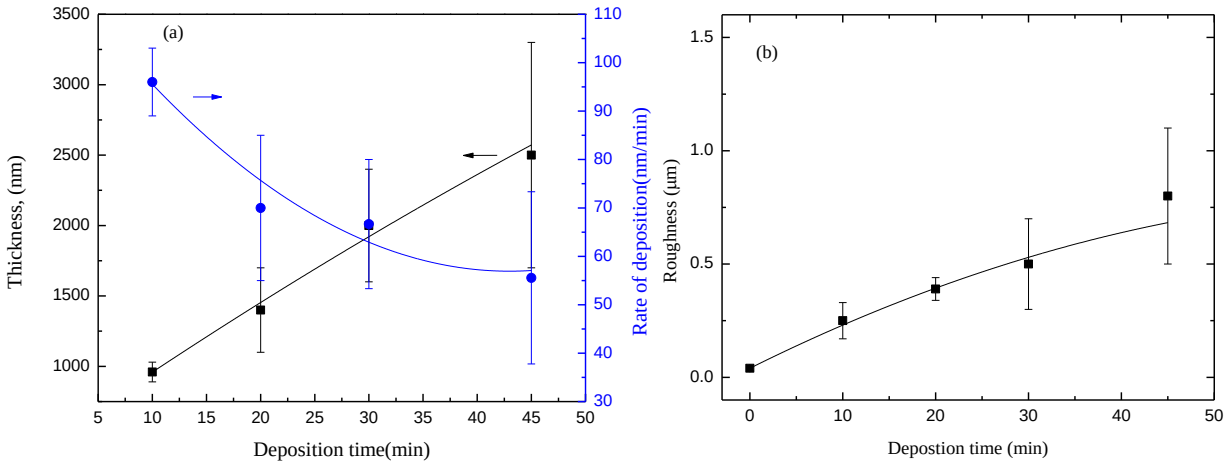

Figure **4**. (a) Thickness and deposition rate, and (b) roughness of EDF as a function of deposition time. The value at t = 0 corresponds to the roughness of the substrate exposed to the monomer with the plasma off.

3.3. Chemical structural analysis

The chemical structure of the films was analyzed by FTIR measurements and the result is shown in Fig. 5(a). On the spectrum of liquid eugenol we have: A broad band centered at 3519 cm^{-1} attributed to O-H stretch, and a strong absorption at 1234 and 1030 cm^{-1} allocated to the presence C-O bond stretching of methoxy and phenol groups, respectively; weak peaks in the range of 649-555 cm^{-1} ascribed to the C-O in-plane bending of OCH_3 and the peak at 1209 cm^{-1} to the O-H in-plane deformation of phenol; a peak at 1450 cm^{-1} accredited to the asymmetric bending vibration of C-H and a peak at 1363 cm^{-1} to the symmetric bending vibration of C-H in the methoxy group; the absorption bands in the region 2973-2940 cm^{-1} attributed to the asymmetric stretching vibration of C-H in the OCH_3 group and its symmetric vibration at 2841 cm^{-1}; in the same wavelength region, a peak at 2903 cm^{-1} indicates the C-H vibrational stretching of the CH_2 =C-H (vinyl) group and its out-of-plane bending vibration peaks appear at 995 and 916 cm^{-1}; in addition to this, two weak bands at 3060 cm^{-1} and 3004 cm^{-1} are attributed to the C-H stretching vibrational of the aryl and vinyl alkene group.

The spectra of the films deposited at 0.54 W with 30 min deposition time show the preservation of the monomer eugenol functional group. The absorption intensity varies according to the thickness of the film, in addition to shifting the band of -OH towards a lower wavenumber plus the suppression of vinyl, and the appearance of ketone functional groups. It is interesting to

mention such differentiation as follows: the shifting of -OH band from 3519 cm^{-1} to 3436 cm^{-1} is due to the formation of intramolecular H-bonding after the thin film formation; the disappearance of the peaks at 2973 and 2903 cm^{-1} associated with the vinyl group is due to their participation for the polymerization reaction such as conventional polymerization; and the appearance of a peak at 1719 cm^{-1} associated with ketone is due to the post oxidation of the trapped free radicals confined during the formation of the film and tautomerization as well (MATIN; BHUIYAN, 2013; JACOB *et al*., 2014). Similar to this work, the appearance of ketone was observed in our previously carvacrol-derived film that was deposited using DBD plasma (GETNET *et al*., 2020a).

Figure 5(a) also shows the effect of the deposition time on the chemical structure of the film, keeping the same condition of the discharge, indicating the existence of common and similar functional groups in the final products. The only variation is on peak intensity with the deposition time, i.e., for thin film, the intensities are low and rise proportionally with the deposition time. In contrast, the intensity of the IR spectra of the film decreases monotonically as we increase the gas flow rate from 1 to 3 L/min, with no changes in its functional group (Fig. 5(b)). This fact can be explained as follows: An increase in the flow rate decreases the residence time of the monomer in the effective volume of the reactor which in turn decreases the deposition rate (IQBAL *et al.*, 2019).

In general, the FTIR spectrum of all obtained films showed the preservation of hydroxyl and aromatic functional groups. This showed that the active moieties of eugenol, which is the key feature for antimicrobial activity of the monomer, were not damaged upon polymerization. Furthermore, it is worth to note the importance of the preservation of such functional groups upon deposition for the suppression of biofilm growth. Such a hydroxyl group enables the penetration of the lipopolysaccharide of the gram-negative bacteria through the cell membrane, changing the cell structure, and subsequently the leakage of intracellular constituents (NAZZARO *et al*., 2013). Previous studies have also suggested that the hydroxyl group of eugenol is the cause of the disruption of the cytoplasmic membrane of the bacterium, which increases its nonspecific permeability and affects the transport of ions and Adenosine triphosphate (ATP) (DEVI *et al*., 2010; DEVI *et al*., 2013). The presence of the aromatic group in the film is also used to enhance the delocalized electrons system of phenolic groups during proton releasing (BEN ARFA *et al*., 2006).

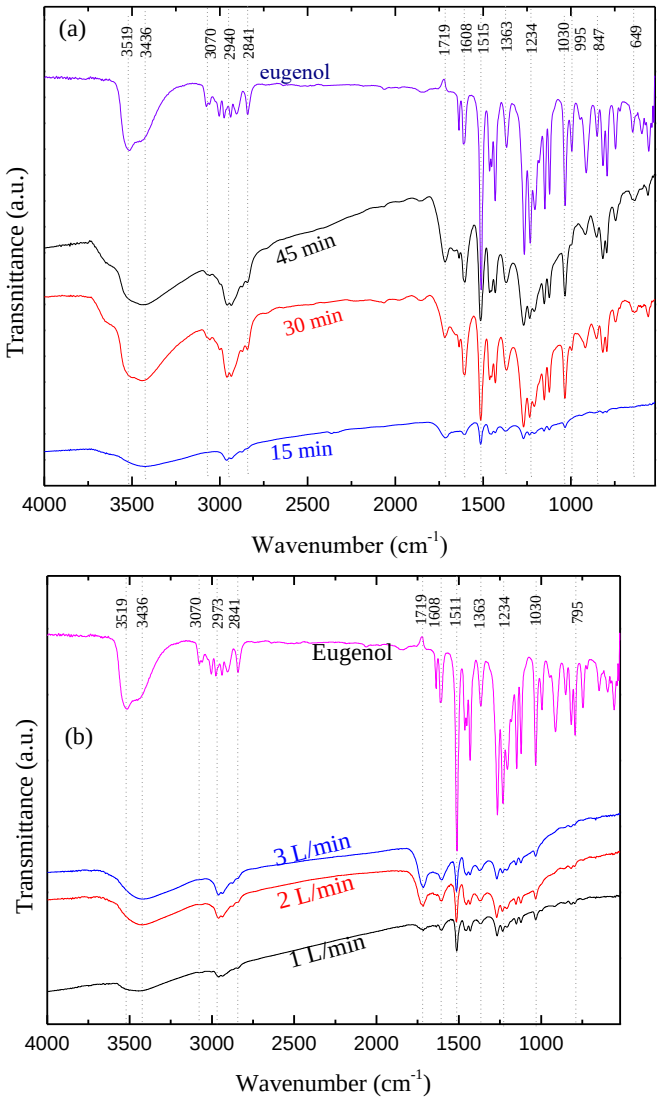

Figure 5. The FTIR spectra of the liquid eugenol and eugenol-derived films deposited at 0.54 W with (a) different deposition time at 5 L/min flow gas rate, and (b) gas flow rate for 10 min deposition time.

3.4. Contact angle and surface energy

The water contact angle (WCA) and the surface energy of the EDF were measured as a function of deposition times and the result is shown in Fig. 6(a). As can be seen in this figure, the WCA of the untreated SS is about 90° and decreases continuously to 48° for EDF deposition up to 30 min. After that, there is a rise in the contact angle to about 61° at 45 min. This continuous increase in the film hydrophilicity during the first 30 min of the deposition

time is due to the enhancement of oxygen-containing groups on the surface of the substrate, which leads to the rise of the surface polarity, and consequently, to the increase of surface energy in the deposited films (EASTON; JACOB, 2010; HONARVAR *et al.*, 2017; ÇAKMAK *et al.*, 2019). That is in agreement with the increase in the intensity of the absorptions hydroxyl group up to 30 min deposition time as described in the previous section. The rise of the angle above this deposition time indicates a reduction of hydroxyl content and an increase in hydrophobic -CH_x content in the film matrix (AL-JUMAILI *et al.*, 2017b), which indicates the production of a material that is less polar. In a similar fashion to this film, an increase in the degree of water contact angle of polyallylamine film at higher deposition time, deposited through a DBD plasma reactor, was reported previously (AZIZ *et al.*, 2017). Additionally, aging in air analysis has shown that the obtained films are stable to the adhesion up to 35 days, maintaining their hydrophilic property as well (Fig. 5(b)).

The surface energy was calculated using Young's equation given by $\gamma LV(\cos\theta) = \gamma SV - \gamma SL$ where γ represents the surface energy between the solid-vapor (SV), solid-liquid (SL) and liquid-vapor (LV) interfaces. The values of γSV and γSL were determined by measurements of the static contact angle with deionized water and diiodomethane (OWENS; WENDT, 1969). The method is ensured by EDS mapping (Fig. 3) which shows a surface chemically homogeneous and smooth (< 1 micrometer). The surface energy of the film-coated substrates is greater than that of the untreated surface and increased with deposition time up to 30 min (Fig. 5(a)). The loss of hydrophobic properties upon eugenol plasma treatment makes the films less susceptible to biofouling surface once lower bacterial adhesion is observed in surfaces with high surface energy (HURWITZ; GUILLEN; HOEK, 2010). Additionally, surfaces with such properties are more resistant against protein adsorption and cell adhesion, resulting in higher biocompatibility. Such hydrophilic surfaces, obtained in this work by only changing the deposition time, are suitable for many biological applications (BHATTACHARYYA *et al.*, 2010; ARIMA; IWATA, 2007).

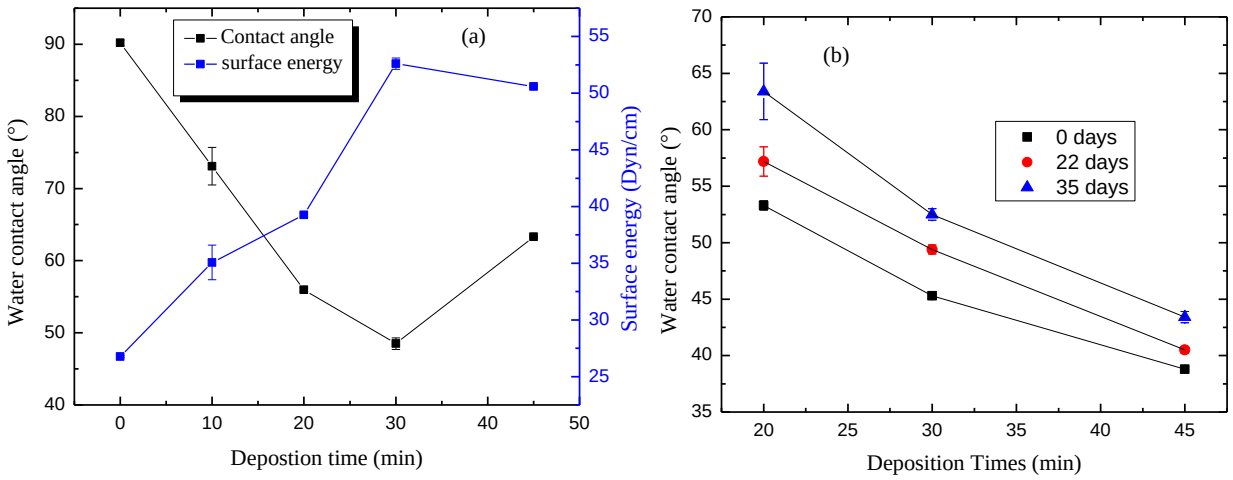

Figure 6. The wettability and surface energy of EDF (a) as a function of times, and (b) Water contact angles measured after 7 and 35 aging days under ambient conditions. The error bars result from measurements performed on three series of samples.

3.5. Biofilm assay

Figure 7 shows the SEM images of *S. aureus* and *E. coli* colonies after 24 h of incubation in the culture medium, on the pristine substrate (uncoated SS), and on coated SS with eugenol films. The population of colony-forming units (CFUs) of both microorganisms attached to the pristine substrate is higher than those observed in the culture medium. It should also be noted that the formation of interconnected cells in EPS indicates the early stages of biofilm formation (Figs. 7(**b**) and 7(**e**)). On the other hand, the EDF coated substrate showed significant suppression of the adhesion and proliferation of *E. coli*, and a reduction to a few CFU populations of *S. aureus* bacterial growth (Figs. 7(**c**) and 7(**f**)). This fact shows an intimate link among the biological activity of the surface chemistry, the topography, and a likely combination of these properties in polymeric films to prevent bacterial fouling (AL-JUMAILI *et al.*, 2017b). That is in agreement with a high concentration of oxygen-containing groups observed by EDS characterization of the film surfaces (Table 1). Previously, it has been reported that *S. aureus* cells preferentially attach to the surfaces bearing carboxylic and methyl functional groups than those containing –OH functionality (TEGOULIA; COOPER, 2002).

In addition to a significant reduction of an initial bacterial attachment, the SEM image shows a notable difference in the cell morphology, with smaller cells being present on each film-coated surface than to that of cells attached to the uncoated one and even to that of the initial

inoculum as well. This change in the morphology is largely ascribed due to the preservation of hydroxyl groups in the film structure as described above in section 3.3. The suppression of EDF against *S. aureus* bacterias is higher than those reported for polyterpenol and polygeranium thin films polymerized from terpinen-4-ol and geranium oil by low-pressure RF plasma (BAZAKA *et al*., 2011b).

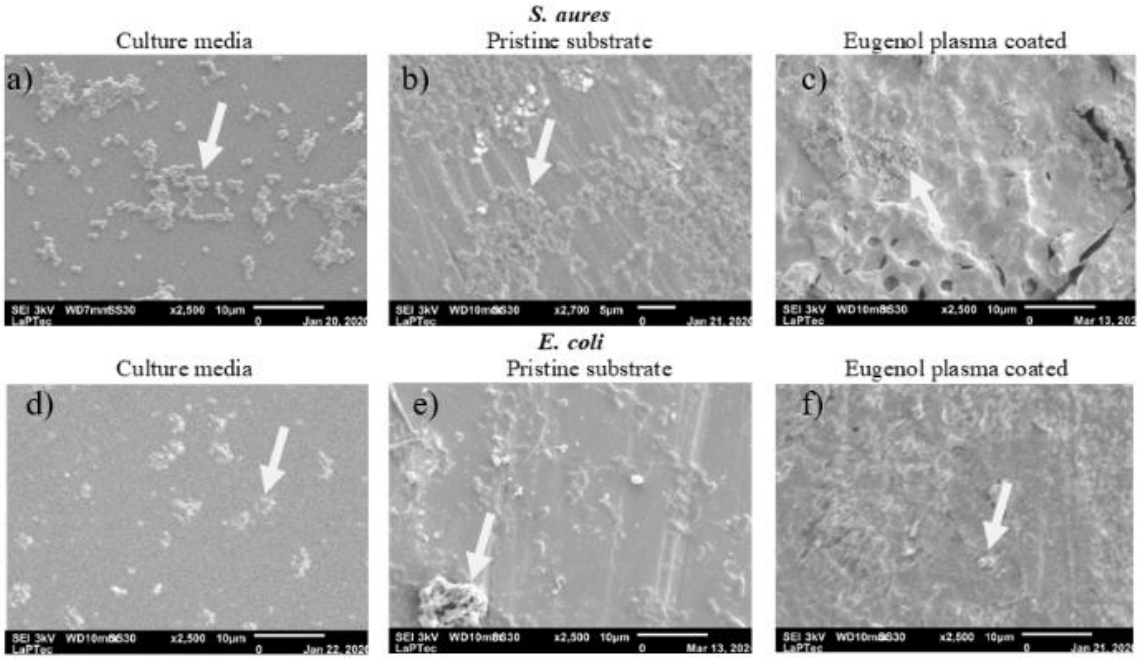

Figure 8. Scanning electron micrographs of colony-forming units (CFUs) in the culture media, on pristine (untreated SS), and coated SS with Eugenol-derived film for (a,b,c,) *S. aureus* and (d,e,f) *E. coli*. The arrows indicate the bacterial colonies.

The effects of the EDF coatings on bacterial adhesion and proliferation were further evaluated with the help of plate counting methods. Figure 8 shows the results of the quantifications of viability and proliferation of microorganisms on uncoated SS and coated with eugenol liquid and by polymerization after 45 min in the discharge. In this figure, the dotted line indicates the bacteria concentration in the initial inoculum. The pristine substrate shows the viability for both bacteria growth is more than 90%, whereas all eugenol-containing samples exhibited viability of *E. coli* growth by about 22% and for *S. aureus*, around 35%, which is consistent with the SEM images. The obtained result is in qualitative agreement for the previously reported carvacrol-derived film using the DBD reactor (GETNET *et al*., 2020a) and also through direct contact of

the bacteria with the plasma filament and indirect atmospheric cold plasma treatment of E. coli (ZIUZINA *et al*., 2015), where the reduction was about 78% of this biofilm growth.

Therefore the coated surface with the EDF improves the biofilm suppression in comparison to the uncoated SS surface. Indeed, this result is similar to that obtained with the monomer directly applied to the substrate. However, in this case, which is typically used for material sterilization, the monomer degrades after 20 min under UV-irradiation as we conclude in the previous article 3 (Fig.14 (a)). On the other hand, the plasma deposited eugenol-derived films exposed to this radiation for up to one hour does not promote any change in the properties of the film. Also, the antibacterial activity EDF lasts up to 120 days, the maximum investigated period of time (GETNET *et al*., 2020b).

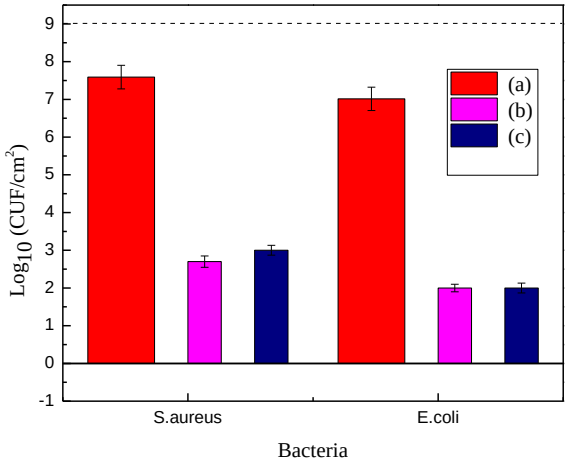

Figure 9. The concentration of *S. aureus* and *E. coli* on (a) stainless-steel coupons as-received, (b) immersed for 45 min in liquid eugenol, and (c) coated with EDF for 45 min deposition time. The dotted line indicates the concentration of bacteria in the initial inoculum.

4. Conclusions

The deposition of the eugenol-derived thin film on SS substrates was successfully achieved by atmospheric pressure dielectric barrier discharge plasma. The mean functional groups of the monomer, such as hydroxyl and aromatic, were largely preserved after polymerization. The obtained thin film had 2,500 nm maximum thickness and 800 nm roughness and did not suffer any chemical change and degradation when exposed either to UV irradiation for 1 h or to the ambient atmosphere for prolonged periods. The coatings also reduce the density of CFUs by more than 78 and 65% of *E. coli* and *S. aureus* biofilms respectively, in comparison with the

number of bacteria detected on the pristine substrate. The results of bactericidal activity, associated with the fact that eugenol is a natural agent, make the films of this compound a good alternative for coatings to avoid the formation of biofilms on biomaterials.

Article 5

Corrosion Science, Ready for Submitting

9 Biofunctional Coating of Stainless Steel Surfaces with Carvacrol- and Eugenol-Derived Film Using Atmospheric Dielectric Barrier Discharge Plasma: Aiming for Suppression of Biofilm Formation and Corrosion Protection

Tsegaye G. Getnet[a,b], Milton E. Kayama[c], Nilson C. Cruz[a*], *Elidiane C. Rangel*[a], and Iolanda C. S. Duarte[d]

[a]Technological Plasmas Laboratory, Sao Paulo State University at Sorocaba, 18087-180, SP, Brazil, [b]Department of Chemistry, college of science, Bahir Dar University, Bahir Dar 79, Ethiopia, [c]Laboratory of Plasma and Applications, São Paulo State University at Guaratinguetá 12516-410, SP, Brazil, [d]Laboratory of Environmental Microbiology, the Federal University of São Carlos at Sorocaba 18052-780, SP, Brazil.

* Corresponding email: nilson.cruz@unesp.br.

Abstract: *Owing to their excellent mechanical properties, metallic biomaterials are the most used materials as orthopedic and dental implants. However, attention must be paid when choosing the materials to be used in the implant medical device to assure the best performance of the device when in a biological environment. In addition to good biocompatibility and chemical stability, in several situations, the ideal material must also be able to inhibit implant bacterial colonization. In this context, the modification of biomaterial surfaces with natural antimicrobial compounds have the potential to address these common implant-related inconveniences. Align with this, we have investigated a biofunctional coating of carvacrol- and eugenol-derived film on stainless steel (SS) surfaces using atmospheric pressure plasma discharge to improve their electrochemical behavior and biological properties. Atomic force microscopy results showed that both CDF (carvacrol-derived film) and EDF (eugenol-derived film) coatings disappeared all the irregularities of the pristine substrate and acquired a uniform surface, free of defects and scratches. Infrared spectra results showed the deposited films largely maintaining the mimicking group of the monomer, such as hydroxyl and aromatic, which is a key feature of the film for the antibacterial and electrochemical activity. CDF exhibited a reduction in biofilm growth rate up to 44% for* P. aeruginosa *and 60% for C. albicans. Similarly, EDF film exhibited up to 36% suppression for* P. aeruginosa *and 52% for* C. albicans. *These film coatings also decrease the corrosion current density and corrosion rate up to 35% in comparison with*

uncoated SS in 3.5% (w/v) NaCl. In general, surface treatment with the present methods is a promising alternative for the SS substrate since it improved the electrochemical behavior and suppression tendencies against these microbial biofilms.
Keywords: Biofilm; Carvacrol; corrosion; Eugenol; plasma.

1. Introduction

In recent years, metallic biomaterials, such as titanium and its alloy (KULKARNI *et al*., 2014; KHORASANI *et al*., 2015; ZHANG; CHEN, 2019), cobalt-chromium alloy (AHERWAR; SINGH; PATNAIK, 2016; HASSIM *et al*., 2019; SINGH; SINGH; SIDHU, 2019), nickel-chromium alloy (FIROUZI-NERBIN; NASIRPOURI; MOSLEHIFARD, 2020; MOSLEHIFARD *et al*., 2019), and stainless steel (SS) (HASSAN; ABDEL GHANY, 2017; LONGHI *et al*., 2019), have been used as orthopedic and dental implants, and surgical instruments, because of their excellent biocompatibility, low elastic modulus, high yield strength, and corrosion resistance (LIU *et al*., 2016; ZHOU *et al*., 2005). Despite of the adequate biocompatibility and the risk of bacterial and fungal colonization, the biofilm formation on those biomaterials has posed a major challenge from both an economic and health perspective (TRAUTNER; DAROUICHE, 2004; FRANCOLINI; DONELLI, 2010). For instance, 12% of the urinary tract (DJORDJEVIC *et al*., 2013; SAMAD *et al*., 2019; TUMBARELLO *et al*., 2020; FERREIRO *et al*., 2017), and 10% of bloodstream infections (THADEN *et al*., 2017), are caused by *P. aeruginosa* biofilm formation on their surface. Similarly, a surveillance study of nosocomial bloodstream infections revealed that more than 24,000 cases in 49 USA hospitals over 7 years (1995-2002) and 2,563 patients in 16 Brazilian hospitals over 4 years (2007-2010), were caused by *Candida* species (WISPLINGHOFF *et al*., 2004; MARRA *et al*., 2011). Besides, once the bacteria is bound as a biofilm, it protects them from human immune defenses and the action of antibiotics (HOLMBERG *et al*., 2009). Often the only remedy is to remove the implanted device from the patient, which in turn causes high economic costs and extra risks of morbidity and mortality to the patients. In addition to medical problems, biofilm formation on ship hulls and heat exchangers, etc., causes equipment damage and an increase in energy consumption as well (SONG, 2016). The adverse effects of biofilms also occurred in many sectors of the industries, such as milk and food, in one or another way. It results in heavy costs for many industries in cleaning and maintenance (TARIFA; LOZANO; BRUGNONI, 2018).

At the same time, the high corrosion properties of some metallic biomaterials especially in an aggressive environment, like chloride ion, promotes wear cracks and release of particles and ions on surrounding tissues (SOUZA *et al*., 2020; ARCIOLA; CAMPOCCIA; MONTANARO, 2018), which may cause the final failure of the implanted material (MANAM *et al*., 2017). These released ions also trigger unfavorable biological responses, such as inflammatory processes and progressive bone loss. For instance, the implantation of Mg and its alloy in bone surgery (BORNAPOUR *et al*., 2013; LI *et al*., 2012), and titanium and its alloy in the dental implant (CORDEIRO *et al*., 2018), are susceptible to degradation in a corrosive environment. Because of these problems, the allowable amount of metallic biomaterials is much smaller than that for the structural materials of bridges and buildings. To overcome such drawbacks, the optimization of surface properties of metal-based biomaterials has been proposed by numerous researchers (DURDU; USTA; BERKEM, 2016). Morphological, physical, and chemical modifications are strategies indicated to achieve greater osseointegration, improved bioactivity, and implant success (RAFIEERAD *et al*., 2015; ABDAL-HAY *et al*., 2014). Hence, the development of protective and multifunctional bioactive surface coating has been designed in recent years to slow down the production of metal-ion and hydrogen bubbles and to prevent microbial colonization on the implanted material (ABDAL-HAY *et al*., 2014; FELFEL *et al*., 2015; CATS-BARIL *et al*., 2013).

Despite the broad spectrum of organic compounds available as corrosion inhibitors, the successful utilization of most corrosion inhibitors has been hindered by their toxic nature. In this regard, the green corrosion inhibitors extracted from plants have attracted the attention of numerous researchers since they are biodegradable, inexpensive, non-toxic, environmentally acceptable, readily available, and renewable (RAGHAVENDRA; BHAT, 2018; RAMEZANZADEH *et al*., 2019; OSTOVARI *et al*., 2009). It has been reported that the successful use of many of those natural products, for instance, green tea and mango leaves extracts (ALSABAGH *et al*., 2015; RAMEZANZADEH *et al*., 2019), effectively diminishes the corrosion rate of carbon steel in HCl and H_2SO_4 corrosion medium, *Hyoscyamus muticus* extract is effectively used for copper corrosion inhibitor in HNO_3 corrosion solution (FOUDA *et al*., 2015) and leaf extracts of *Chromolaena odorata* are diminished aluminum corrosion in 2 M HCl solution (OBOT; OBI-EGBEDI, 2010). In addition to protecting the implant surface against corrosive and degradation processes, plant-derived bioactive compounds, like essential oils, are

well known for antioxidant and antimicrobial activities. It has also been proven used in the field of food safety and pharmacological industry (PRAMOD; ANSARI; ALI, 2010; MARCHESE *et al*., 2017), and for biomaterials surface treatments (GETNET *et al*., 2020a; RAJARAMAN; JAINU; DHAKSHINAMOORTHY, 2016).

Although essential oils, like clove and oregano, have been documented in their wide spectrum of biological activity, including antimicrobial, antioxidant, antifungal, antiviral, anti-inflammatory, and anesthetic properties (JANG *et al*., 2008). However, applying these natural agents as a bioactive coating of biomaterials has major challenges owing to the poor water solubility, stability, and high volatility. Many initiatives have been undertaken to overcome these challenges and to expand their applications. Among those, the atmospheric pressure plasma thin film deposition technique is one of the emerging and promising technology, which enables the conversion of even highly volatile compounds to a solid thin film without losing their functional groups that are responsible for antimicrobial activity. Additionally, it produces rough, porous, and thick coatings (GETNET *et al*., 2020a) in large surface areas. Besides, the film production process takes place in a dry and solvent-free environment, without significant production of toxic byproducts. Moreover, to the best knowledge of the authors, it was not found studies on the effects of implant surface treatment with both eugenol and carvacrol essential oils, either in liquid or solid form, regarding corrosion protection, and biofilm formation, particularly against *Pseudomonas aeruginosa* bacteria and *Candida albicans* fungus. To fill this gap, for the first time, this study has been focused on a bio-functional coating of SS surface with eugenol- and carvacrol-derived film using atmospheric pressure dielectric barrier discharge plasma, to improve its surface characteristics, electrochemical behavior, and biological properties. We choose stainless steel as a substrate due to its low cost in comparison to other metals, its extensive use in many technological and biomedical applications, and consumer products.

2. Materials and method

2.1. Description of the experiment

The plasma reactor used in this study was built in the laboratory of plasma technology, LabTec, Sorocaba, Brazil, and is fully described elsewhere (GETNET *et al*., 2020a; GETNET *et al*., 2020b). It is shown schematically in Fig. 1.

Before depositions, the substrate SS with 10 mm × 10 mm and 1 mm thickness were polished and then cleaned in the sequence with ultrasonic baths using detergent, distilled water, and isopropyl alcohol. Afterward, the dried sample was placed on the dielectric (polyester) over the lower discharge electrode. The monomers, eugenol ($(CH_3)_2CHC_6H_3(CH_3)OH$) and carvacrol ($(CH_3)_2CHC_6H_3(CH_3)OH$), at least 98% purity (Sigma-Aldrich), was dragged by argon (99.9% purity) at 25 °C temperature and 5 L/min flow rate controlled vaporizer and injected in discharge region through a central hole in the upper electrode of the system. A Tektronix TDS1001C (30 MHz, 500 MS/s) oscilloscope was used to measure the applied voltage v_A on a 1000× resistive voltage divider and the voltage drop v_C on a capacitor with 10 nF-capacitance. The signals were recorded and used to calculate the discharge active power given by:

$$P = \frac{1}{T}\int_0^Q v_A dq \qquad , v_A \gg v_C \qquad (1)$$

where $q=Cv_C$ is the instantaneous charge and T the period of the signal. According to such calculations, the average power delivered during the depositions was 0.54 ± 0.04 W.

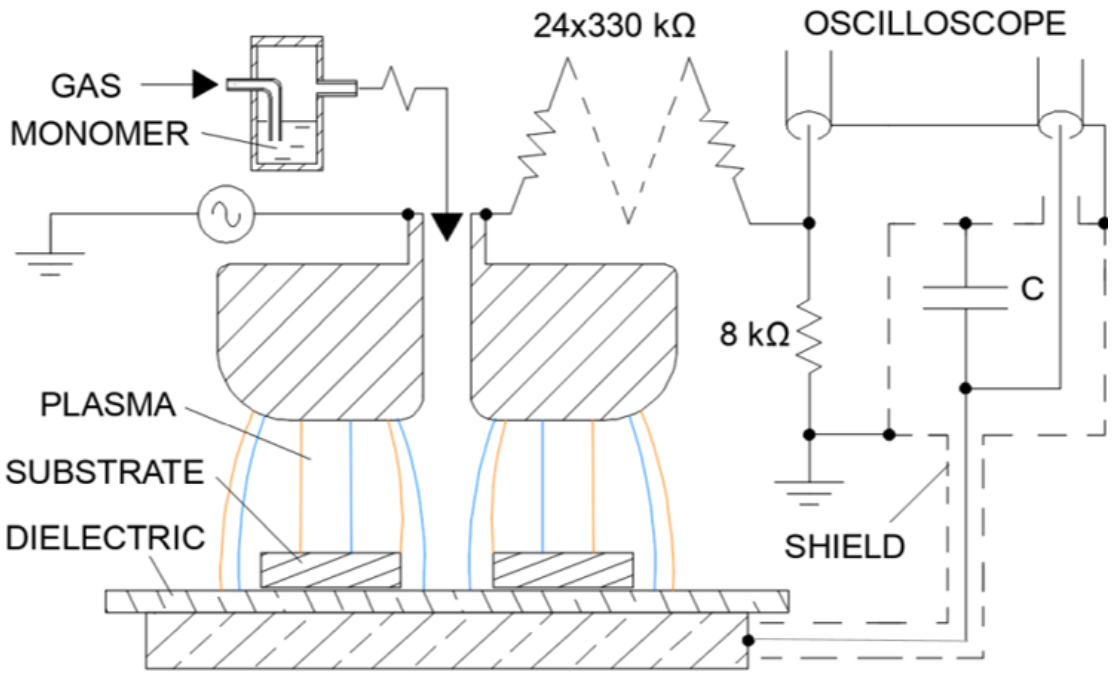

Figure 7. Schematic representation of the experimental setup.

2.2. Film structure and topography analysis

The chemical structure of the films deposited at 45 min was characterized by infrared reflectance-absorbance spectroscopy, using a Jasco FT/IR-410 spectrometer, through 128 scans with a resolution of 4 cm^{-1}. The surface topography was evaluated by atomic force microscopy (AFM), using a Shimadzu SPM 9600, in non-contact operating mode with a Zeiss stereomicroscope lens of 100X magnification systems. The 3D and 2D images were acquired over an area of 10 μm x 10 μm with 512 scan points in each direction. The root mean square (R_{MS}) roughness of the film was also determined from different AFM images using the standard deviation of the distribution of the heights found on the film surface given by Equation (2).

$$R_{MS} = \sqrt{\frac{1}{N}\sum_{i=1}^{N}(h_i - \bar{h})^2} \qquad (2)$$

where $\bar{h}$ is the mean height in the calculated region and N is the total number of points that form the AFM image.

2.3. Electrochemical behavior analysis

Electrochemical methods such as open circuit potential, potentiodynamic polarization, and electrochemical impedance spectroscopy (EIS) measurements were used in this investigation for testing the corrosion resistance of the uncoated and coated SS with carvacrol- and eugenol-derived films. All electrochemical tests were carried out using a computer-controlled potentiostat/frequency response analyzer (Autolab PGSTAT128N). To perform these tests, an electrochemical cell with three electrodes was used. The first electrode was SS (coated or uncoated) surface as a working electrode with a 0.785 cm^2 exposed area, the second one an Ag/AgCl/3M KCl (+210 mV vs SHE) as a reference electrode, and the third one, a platinum wire as the counter electrode. The electrochemical cell was filled with 100 mL of 3.5 wt.%, 0.6 M of NaCl corrosion solution, made from an analytical grade reagent of NaCl and deionized water.

Initially, the open circuit potential (E_{OC}) was monitored for 3 h to ensure a steady-state condition. Afterward, EIS measurements were performed with respect to E_{OC} in a frequency range of 100 kHz to 10 mHz at 25 °C temperature, with ±10 mV amplitude AC perturbation signal, and an acquisition rate of 10 points per decade. Right after the EIS measurements, the Tafel curve was obtained from the potentiodynamic polarization analysis which was performed by

scanning the electrode potential from -1.0 V to +1.5 V with respect to E_{OC} at a rate of 1 mV/s. Autolab PGSTAT 128N with Nova 2.1 software was used for data acquisition. Finally, the EIS data was analyzed by Zsimpwin software to determine a simulated circuit and respective parameters.

2.4. Surface bioassay of the film

The gram-negative bacteria, Pseudomonas *aeruginosa* strain ATCC®9027, and fungus, *Candida albicans* strain ATCC®10231, were used for biofilm assay. Tryptic Soy Agar (TSA) and Sabouraud Dextrose Agar (SDA) medium were used as a basal medium for the initial growth of the bacterial and fungus, respectively. Before biofilm formation, each stock microbe strain was spread and incubated for 48 h in the appropriate medium at 37 °C for bacteria and 26 °C for fungus. Subsequently, cells from this culture were also incubated in an appropriate fresh medium for 48 h, to obtain 10^8 colony-forming-unit (CFU/ mL) concentrations (GETNET *et al*., 2020a; GIAOURIS; NYCHAS, 2006; KOSTAKI *et al*., 2012). Such standardized inoculum concentration was prepared by transferring 5 drops of each well-separated colonies from the inoculated microbe, using an inoculating loop, to a separate flask containing 27 mL of sterilized saline solution (0.85%).

For biofilm assay, as described fully elsewhere (GETNET *et al*., 2020a), three replicated trials of uncoated and coated SS substrate produced on different deposition time were introduced separately in serialized test tubes containing 5 ml of Tryptone Soy Broth (TSB) and standard inoculum concentration of 6.0 x10^8 CFU/mL for P. *aeruginosa* and 0.6 ×10^8 CFU/mL for *C. albicans*. Each test tube was incubated, for the adhesion phase, in a static oven for 3 h at 37 °C for bacteria and 26 °C for the fungus. After this phase, the substrate was withdrawn, washed two times with 3 mL of saline solution, and transferred to new sterile test tubes having 5 mL of TSB medium, followed by incubation in a static oven for 24 h at their respective temperature. This is the biofilm formation phase. Afterward, the samples were withdrawn and again transferred to a new sterilized test tube containing 10 mL of saline solution and exposed to ultrasonic action for 30 minutes to release the biofilms. A dilution of 10^{-1} up to 10^{-6} in saline was made for each tube. A sample of 100 µL aliquots of each dilution was seeded in TSA medium for bacteria and SDA medium for fungus in sterile Petri dishes and incubated for 48 h. A schematic drawing of this

procedure is shown in Fig. 2. Finally, the bacteria viability was calculated by the following Equation (3), expressed as the log of CFU/cm^2:

$$CFU / cm^2 = \text{number of colonies} \times \text{dilution factor} \times \text{substrate area} \quad (3)$$

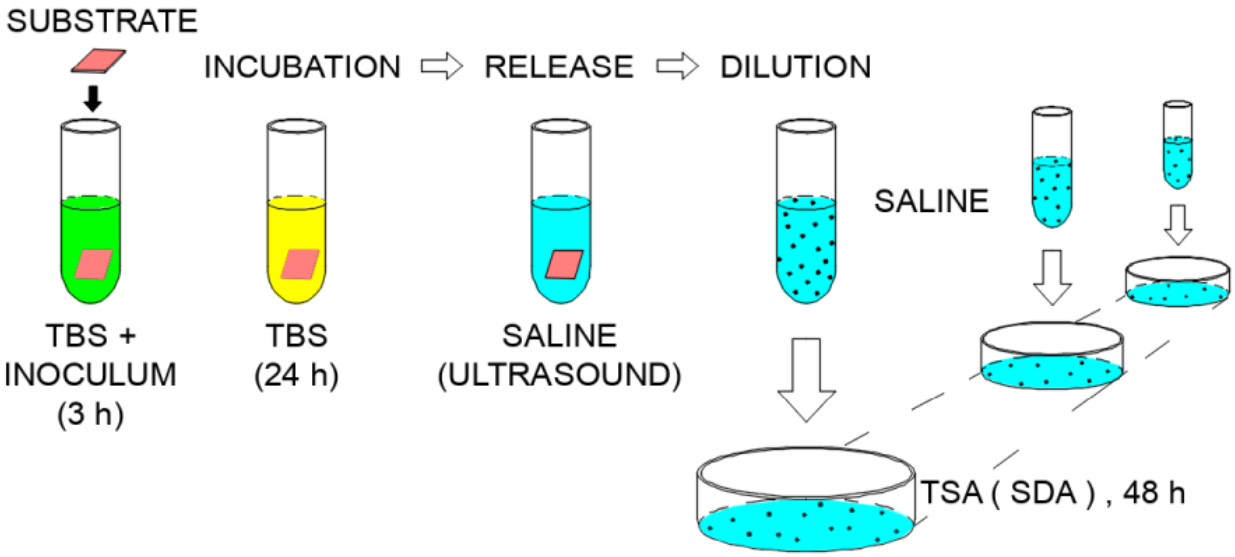

Figure 2. Experimental scheme of the biofilm assay of uncoated and coated SS substrate with CDF and EDF.

For SEM visualization of the bacterial and fungal cells attached to the surfaces of the sample and also their biofilm growth extent, uncoated and coated with CDF and EDF for 45 min deposition times, was fixed for 3 hours in Karnovsky solution (2.5% glutaraldehyde, 2% formaldehyde, 0.1 M sodium phosphate buffer; pH 7.2), followed by rinsing with phosphate buffer for 5 min, dehydration in a series of ethanol soaking (60%, 70% and 80% solution for 5 min and 100% for 10 min), and aseptically air blower. After these treatments, the thin gold-palladium coating on the samples was carried to SEM analysis, which was performed in a JEOL JSM-6010LA at an acceleration voltage of 3 kV (GETNET *et al*., 2020a; SOUZA *et al*., 2019).

3. Results and discussions

3.1. Chemical structure

The FTIR spectra analysis was used in this study to identify the functional groups that are present within the carvacrol-derived film (CDF) and eugenol-derived film (EDF). The spectra of CDF and EDF deposited on a SS surface for 45 min deposition time and 5 L/min gas flow rate is shown in Fig. 3. It shows a broad band centered at 3431 cm^{-1}, ascribed to O-H stretch, and strong absorption in the region 1234-1270 and 1030-1067 cm^{-1} assigned to the presence of C-O and O-

H bond stretching of methoxy and phenol groups, respectively. The weak peaks in the region of 649-555 cm^{-1} are attributed to the C-O in-plane bending of methoxy and the peak at 1209 cm^{-1} to the O-H in-plane deformation of phenol. The asymmetric stretching vibration of C-H in the methoxy and methyl group is also observed in the region of 2931-2963 cm^{-1} and their symmetric mode appears in the region of 2841-2874 cm^{-1} (GETNET *et al.*, 2020a; SINHA *et al.*, 2014). The asymmetric bending vibration of the C-H peak is observed in the region of 1433-1456 cm^{-1} and its symmetric corresponding mode is in 1363 -1367 cm^{-1}. Additionally, the strong absorption at 1177 cm^{-1} was observed in the CDF, which indicates the carbon skeletal vibration of the C-$(CH_3)_2$ group (JACOB *et al.*, 2013). The strong and sharp peaks in the ranges 1505 - 1620 cm^{-1} and 3057 -3017 cm^{-1} are attributed to aromatic C=C and C-H stretching, respectively. Also, the weak peaks between 848 and 746 cm^{-1} are attributed to the C-H out-of-plane deformation of the 1, 2, and 4- tri-substituted benzenoid compounds. Finally, a peak at 1705 cm^{-1} associated with ketone has appeared in the film that was not seen in the spectrum of the monomer (GETNET *et al.*, 2020a). This might be due to the post-oxidation of the trapped free radicals confined during the formation of the film and its tautomerization (JACOB *et al.*, 2014).

In general, the FTIR spectrum of all obtained films showed the presence of hydroxyl, methyl, and an aromatic group. It indicates that the functional groups of the monomers are largely retained in the structure of the film, preserving the original antimicrobial activity of the compounds (GETNET *et al.*, 2020a; BURT, 2004; NAZZARO *et al.*, 2013). It is interesting to point out the maintenance of hydroxyl and aromatic groups for biofilm suppression activity using this technique of atmospheric plasma deposition method. Such hydroxyl groups are involved in the rupture of the bacterial and fungal cells. Previous studies have also suggested that the hydroxyl group disrupts the cytoplasmic membrane of the bacterium, which increases its nonspecific permeability and affects the transport of ions and Adenosine triphosphate (ATP) (DEVI *et al.*, 2010; DEVI *et al.*, 2013). Additionally, the conjugation of OH groups with aromatic rings can penetrate the cells, disrupt the cytoplasmic membrane, inhibiting the activity of several enzymes and also, affect numerous mechanisms related to cell metabolism (EASTON; JACOB, 2010; BEN ARFA *et al.*, 2006).

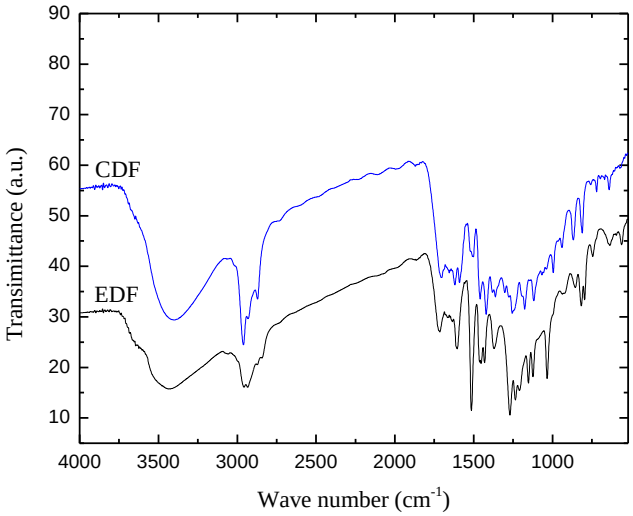

Figure 3 FTIR spectra of the film deposited for 45 min derived from carvacrol (CDF) and eugenol (EDF) monomers.

3.2. **Film Topography**

It is important to note that there is a great debate regarding the extent of bacterial adhesion on the nanometer-scale surface topography (ARAÚJO *et al.*, 2010). Although the rate of bacterial adhesion and expansion is strongly associated with the surface topography and elevated surface area (SOWA *et al.*, 2015; ROSALES-LEAL *et al.*, 2010; MARQUES *et al.*, 2015). That is why the current plasma deposited film surface topography was needed to characterize using the AFM (noncontact mode due to the softness of the film). The 2D and 3D images of the uncoated SS and coated with CDF and EDF are presented in Fig. 4 with its corresponding arithmetic average (R_a) and root-mean-square (R_{MS}) roughness. The R_a value represents the average height of the irregularities in the direction perpendicular to the sample surface, while the R_{MS} value describes the vertical distance between the highest peak and the lowest valley along the assessment length of the surface profile. On the uncoated substrate, it is found a few scratches on the surface with R_a = 37 nm and R_{MS} =48 nm as result of the polishing methods used to prepare the samples (Fig. 4(a)). With the deposition all these irregularities disappear, with CDF and EDF, acquiring a uniform surface, free of defects and scratches, and covered with spherical grains (Fig 4(b) and 4(c)). These new surface features indicate that the polymerization reactions took place on the surface of the substrate, instead of in the gas phase (AL-JUMAILI *et al.*, 2017a). The figures also show some small-clustered and surface holes in 3D and strip

intensity in 2D AFM images. That is a very common picture of what is obtained with plasma assisted deposition at atmospheric pressure discharge operating in filamentary mode, characterized by numerous peaks and valleys in the deposited films.

The R_a values of both CDF and EDF are lower than those of the untreated SS surface. They are comparably higher than the previously reported roughness of lavender oil, *lavandula angustifolia* oil, 1-isopropyl-4-methyl-1, and 4-cyclohexadiene film (WANG *et al*., 2011). The R_{MS} roughness of those films, CDF and EDF, is 43 nm and 45 nm, respectively. These high R_{MS} values are due to the fact that a thick film was produced, and in consequence, large grains and clusters were formed on the film surface (MWEMA *et al*., 2018; PANTA; SUBEDI, 2013). These R_{MS} values are also comparably higher than the previously reported in thiophene and ethylcyclohexane polymer films deposited using low-pressure RF plasma polymerization (BAZAKA; JACOB, 2009). In general, such high roughness, as obtained in the present work, has a significant effect on the surface chemical properties and performance of the films. They also provide a surface with high surface energy (FRITZ; KELLEY; FRISBIE, 2005).

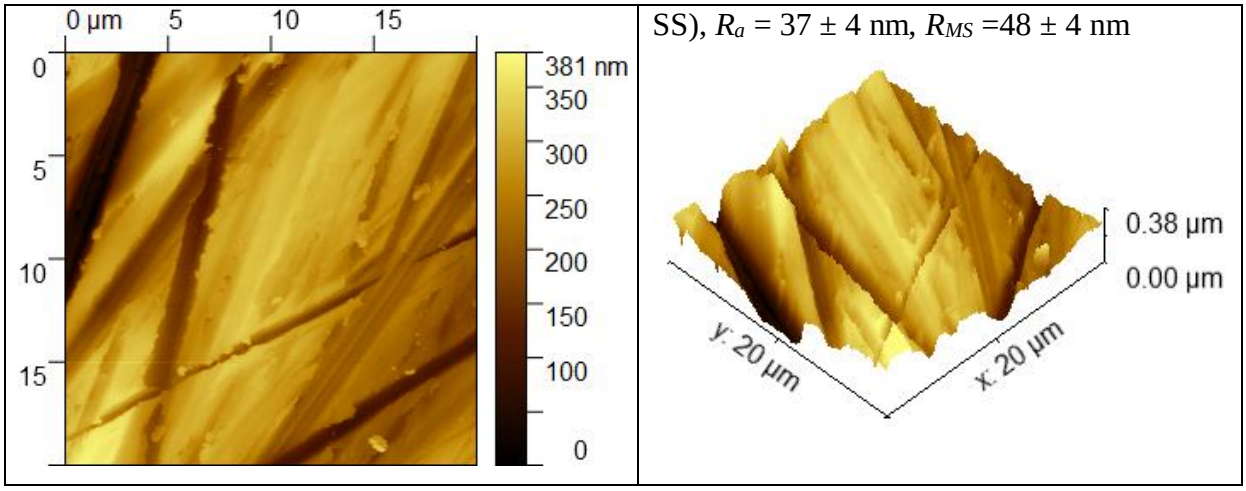

SS), R_a = 37 ± 4 nm, R_{MS} =48 ± 4 nm

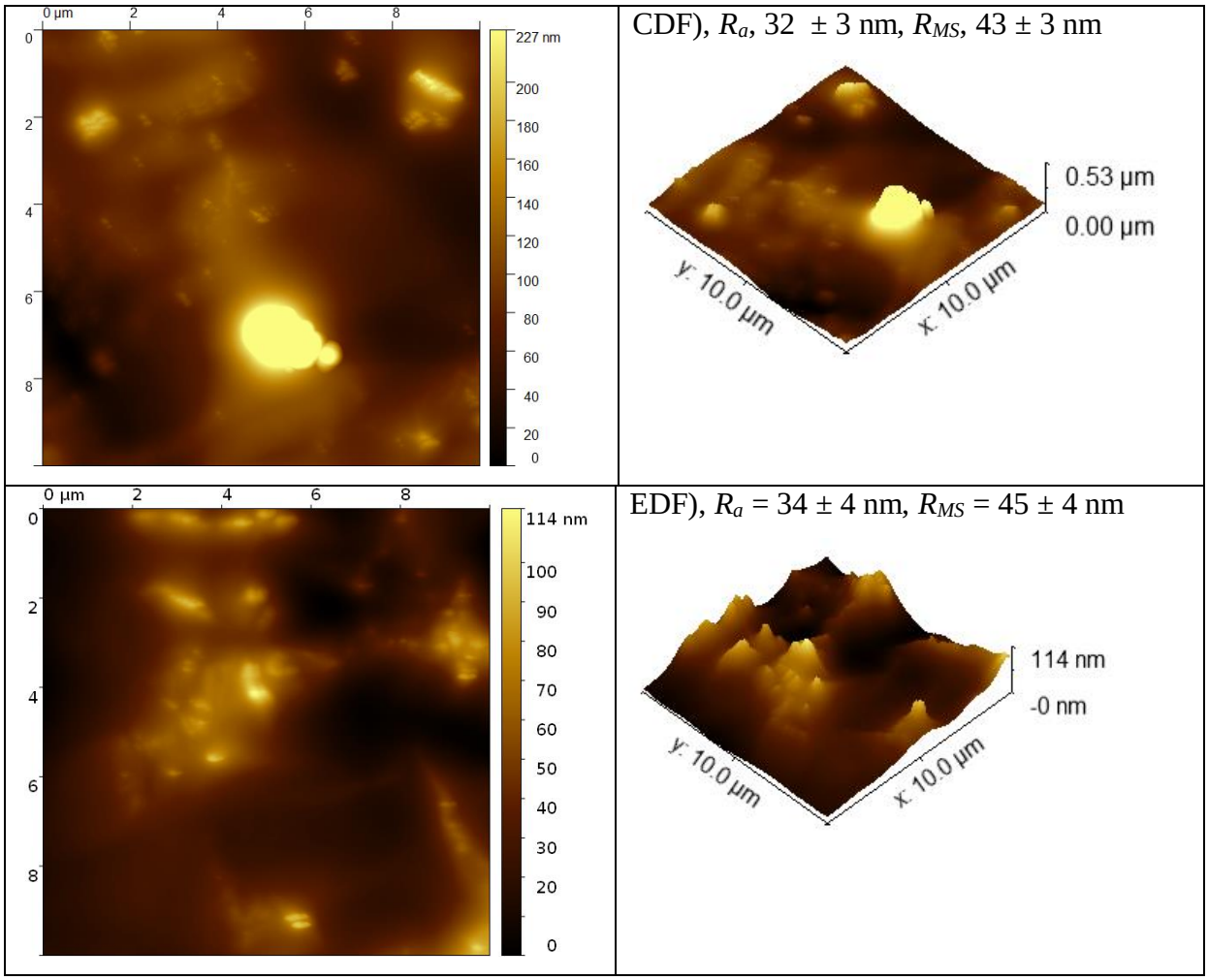

Figure 4. AFM image of stainless steel (SS), and the film deposited for 45 min derived from carvacrol (CDF) and eugenol (EDF) monomers.

3.3. Biofilm Assay

Figure 5 shows the SEM micrographs of *P. aeruginosa* and *C. albicans* colonies after 24 h of incubation in the culture medium, on the uncoated and coated substrate. The populations of colony-forming units (CFUs) attached to pristine substrates are higher than those in the culture medium for both microorganisms, as can be seen in Fig. 5(b, f). Also, there is a formation of clusters of cells, each one linked to another one by extracellular polymeric substances (EPS) on the pristine substrate, indicating an early stage of biofilm formation. On the other hand, in Fig. 5(c, g), it is possible to observe a fewer number of those microbes on CDF coated SS surfaces. It indicates that the film reduces significantly the biofilm formation due to the incorporation of the hydroxyl group in the film matrix. Likewise, a few colonies of those microbes grow on EDF

coated substrates, as shown in Fig. 5(d, h). Such inhibition of *P. aeruginosa* colonies is more effective than the previously reported results in polyterpenol and polygeranium thin films, deposited using low-pressure RF plasma (BAZAKA *et al*., 2011b; AL-JUMAILI, 2019). Furthermore, an inspection of the SEM images demonstrated notable differences in the cell morphology, on the production of EPS's, and the numbers of bacterial cells attached to the uncoated and coated substrates. This morphology change is ascribed due to the presence of a free hydroxyl group in the film structure (NAZZARO *et al* 2013), as described above in section 3.1, such hydrophilic properties of carvacrol and eugenol are enabled to penetrate the lipopolysaccharide of the bacterial cell membrane and alter the cell structure. Similarly to this study, the change in the cell morphology of *P. aeruginosa* for polyterpenes and geranium oil films has been reported (AL-JUMAILI *et al*., 2017a; BAZAKA *et al*., 2011a).

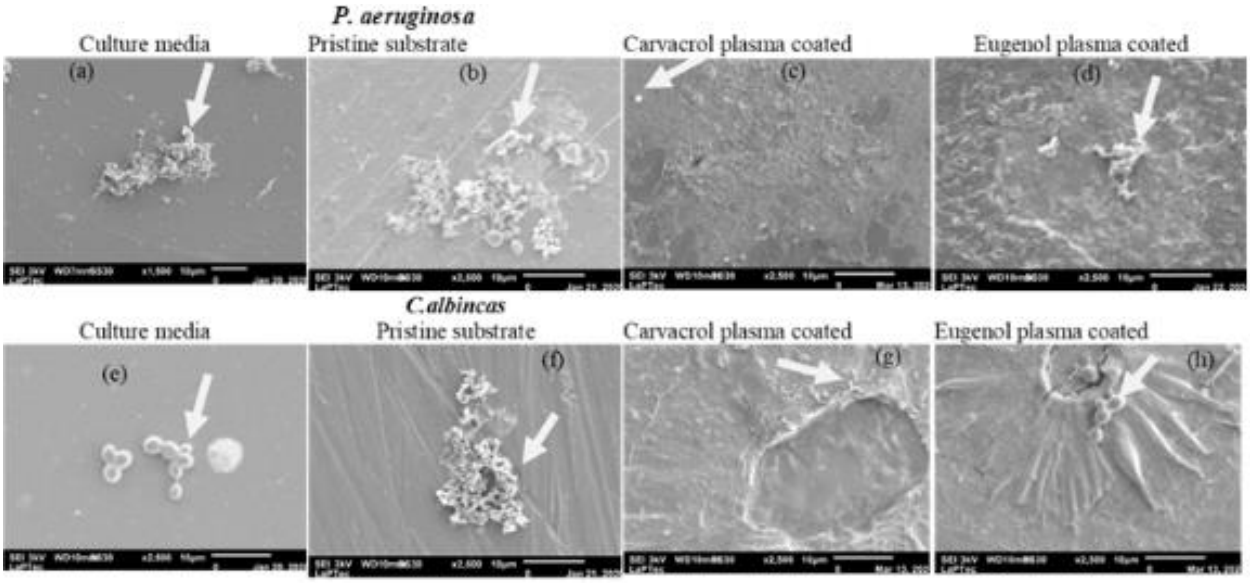

Figure 5. Scanning electron micrographs of *P. aeruginosa* and *C. albicans* colonies on (a, e) culture medium, (b, f) uncoated stainless steel, coated with (c, g) CDF and (d, h) EDF. The arrows indicate the bacterial colonies.

The proliferation of the bacteria and fungus as the action of the deposited films was evaluated by plate counting methods and the results are presented in Fig. 6. In these figures, the dotted line indicates the concentration in the initial inoculum. The samples coated with CDF exhibit a reduction in the growth rate of the biofilm in proportion with the deposition time, or equivalent form, to the thickness of the film, at a rate of 32 to 44% for *P. aeruginosa* and 45 to 60% for *C. albicans* (Fig. 6A). This biofilm suppression is associated with the preservation of the

mean functional groups of the monomers in the film structure, such as hydroxyl and aromatic, as indicated by the FTIR analysis. The reduction in the population was also observed for samples with EDF at a rate of 30 to 36% for *P. aeruginosa* and 44 to 52% for *C. albicans*, also proportionally to the thickness of the film and again due to the rise of the hydroxyl group in the coated samples (GETNET *et al*., 2020a; GETNET *et al*., 2020c). On the other hand, the pristine substrate showed viability by more than 81% for *P. aeruginosa* and 77% for *C. albicans*. Therefore both CDF and EDF significantly prevent the attachment of these particular bacteria and fungus on the surface of SS.

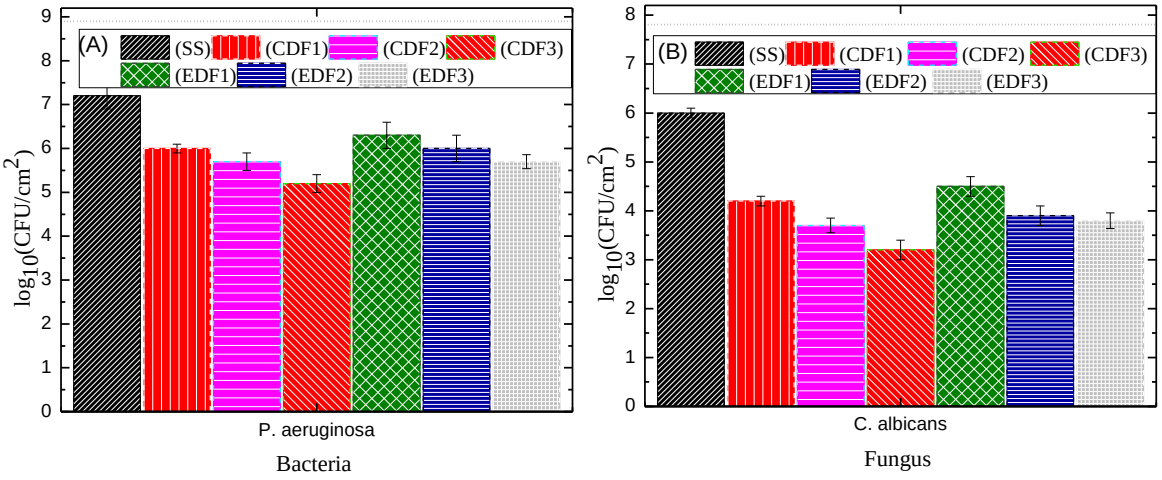

Figure 6**.** The concentration of *P. aerginosa (*A) and *C. albicans (*B*)* on uncoated (SS), and coated with deposition time of (CDF1) 20 min, (CDF2) 30 min, (CDF3) 45 min for carvacrol film, and (EDF1) 20 min, (EDF2) 30 min, (EDF3) 45 min for the eugenol-derived film. The dotted line indicates the concentration of *P. aerginosa* and *C. albicans* in the initial inoculum.

3.4. Corrosion Behavior

3.4.1. Potentiodynamic Polarization Measurements

The variation of open circuit potential E_{OC} with immersion time t is shown in Fig. 7(A) for films with 45 min deposition time. The coating of the substrate with CDF and EDF leads to a fast stabilization of E_{OC} with a higher time average potential for the former and lower for the latter. For uncoated substrate this average potential is intermediary and E_{OC} decreases continuously from about 800 mV to -90 mV until at t= 5,000 s, maintaining a steady-state value around -100 mV until the end of the test at t=10,800 s. For CDF, due to the formation of oxide film on the surface of the substrate, that takes place at different sites, leads to a reduction of potential in the

negative direction. As a result, a sequence of fast pulses is observed from the beginning of the E_{OC} measurement up to t= 3,000 s. After that, it remains with a constant positive value of around 100 mV, indicating achieving a steady-state condition for EIS analysis. In addition, the potential of both CDF and untreated SS started with a positive value, indicating the diffusion of the electrolyte into the active sites of metal (TABATABAEI MAJD *et al.*, 2019), as can be seen in the Nyquist plot in Fig.8(A). On the other hand, for EDF, there is a fast formation of the oxide film in the electrochemical cells, which increase the E_{OC} drastically from about -2,500 to -1000 mV at t= 900 s, and then, maintaining this variation until the end of the test time, this indicates that the corrosion resistance of SS increases with time and eventually reaches a relatively stable value. At the end of the measurement, the potential of all treated substrates relative to the untreated one is positive, indicating a decrease in anodic dissolution current (KHALAF; ABD EL-LATEEF, 2017).

The potentiodynamic polarization curves of SS (uncoated and coated), in 3.5 wt.% NaCl solution is presented in Fig.7(B). The corrosion potential E_{Corr}, current density $j_{Corr,}$ and other electrochemical parameters, determined by the tangent method from Tafel plots (EL-SAYED; SHAKER; ABD EL-LATEEF, 2010), are presented in Table 1. The CDF coating decreases the j_{corr} in comparison to the uncoated SS substrate by 36% and rises E_{corr} in a positive direction by about 194 mV. Similarly, the EDF coated decreases the j_{corr} by 25%, and again, rises E_{corr} in the positive direction by 103 mV. This reduction in current density upon film coating shows clearly the effectiveness of the deposited films on the steel surface for corrosion protection (HUANG *et al.*, 2019; TABATABAEI MAJD *et al.*, 2019). Also, the positive shift of E_{corr} confirmed that both film coatings exhibited the retardation of anodic reaction (KHALAF; ABD EL-LATEEF, 2017; ALSABAGH *et al.*, 2015). This retardation of anodic reaction has occurred in both film coating corrosion processes is due to the adsorption of metal surfaces by the film structures, which is mainly associated with the presence of polar functional groups with O atoms conjugated to aromatic pi electrons in the reaction center. As a consequence, it provides a dense barrier to protect metal structures from corrosive attack/species.

The table also shows the polarization resistance R_p calculated according to:

$$R_p = \frac{\beta_a \beta_c}{2.33 i_{corr} (\beta_a + \beta_c)} \quad (4)$$

where βa and βc are anodic and cathodic Tafel slopes, respectively.

As shown in the Table, the coatings increase the R_P *of* bare steel by two and three times for EDF and CDF, respectively. Despite the rise of the slopes, there is a significant reduction of the current density, rising polarization resistance, and reducing the corrosion rate of the bare steel by 30-35%. The protection of SS to the corrosion using these monomers is higher than those reported of vinyltrimethoxysilane and henna extract thin-film coating (MOTALEBI *et al*., 2012; TALEBIAN e*t al*., 2019). However, they did not show efficient inhibition against pit nucleation, as indicated by the reduction of pitting potential with the coating. In general, both EDF and EDF are acting as an anodic type inhibitor to the SS substrate in 3.5 wt.% NaCl and retard majorly anodic corrosion reactions.

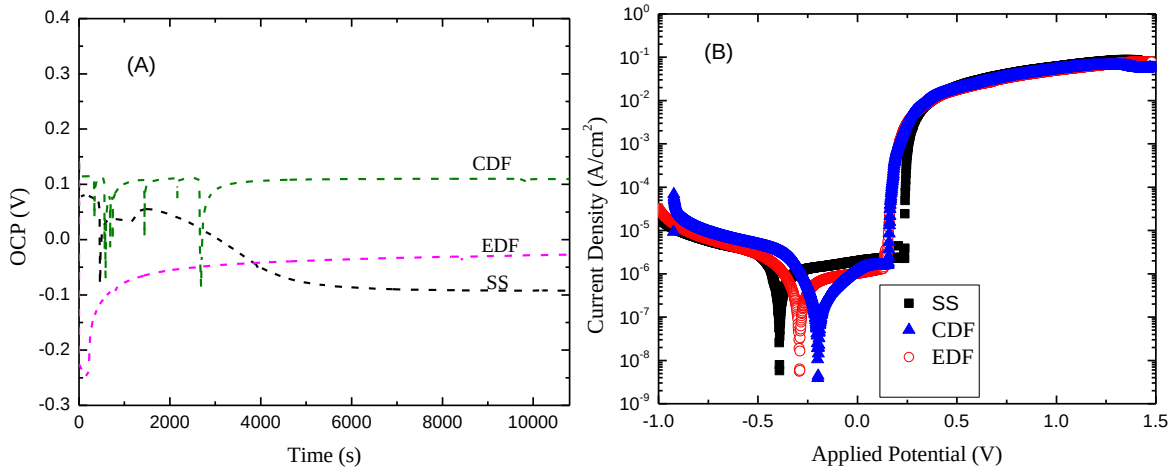

Figure 7. (A) The open-circuit potential as a function of the time and (B) potentiodynamic polarization curves of uncoated (SS) and coated with carvacrol (CDF) and eugenol films (EDF) for 45 min deposition time**.**

Table 1. Corrosion (E_{corr}), pitting (E_{pit}) potentials, and other polarization parameters of coated and uncoated bare steel derive from Tafel plots.

Sample	E_{corr}	E_{pit}	I_{cor}	β_a	β_c	R_p	Corr. Rate
	mV	mV	nA/cm^2	mV/dec	mV/dec	kΩcm^2	nm/year
Bare steel	-393	236	48	17	7	58	132
Eugenol film Coated	-290	131	36	22	23	138	91
Carvacrol film coated	-199	54	31	27	16	184	83

3.4.2. Electrochemical Property of the Film

Figure 8 shows the Nyquist and Bode plots of uncoated and coated SS in 3.5% NaCl. As can be observed from the Nyquist plot (Fig. 8(A)), the uncoated SS contains a capacitive loop at the intermediate frequency and a straight line in the low-frequency region. The first is associated with the capacitive effect and the latter is associated with the Warburg effect (MARTINS *et al.*, 2012). The appearance of Warburg impedance is a result of the diffusion of corrosion product from the SS surface to the bulk solution, and also, dissolved oxygen to the electrode surface (AMIN; KHALED, 2010). Also, as can be noted from this figure, both CDF and EDF coatings show a significant change in the capacitive loop diameter, which gives the largest semicircle diameter in the Nyquist plot, representing a greatly improved performance in terms of enhanced corrosion resistance in comparison with uncoated one. Additionally, the Warburg response line of the SS surface was vanished for the EDF and significantly diminished for the CDF coating, which indicates the inhibitive effect of these films for controlling the diffusion process.

According to Zhao *et al.*, (2011), the semicircle at the intermediate frequencies indicates that the coating could be treated as a barrier to a corrosive medium. Similarly, Montemor *et al.* (2006), have claimed that the semicircle having a large diameter can be characterized by a capacitive response. In agreement with these reports, both film coatings have increased the diameter of capacitive lopes, indicating an inhibiting effect of the film for the improvement of corrosion resistance.

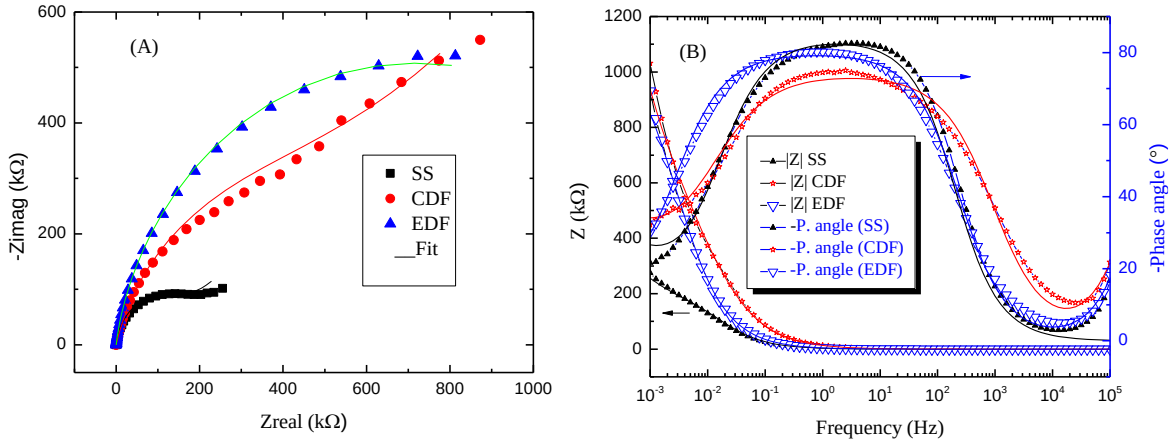

Figure 8. Nyquist (**A**) and Bode (B) plots of uncoated (SS), and the film-coated for 45 min deposition time derived from carvacrol (CDF) and eugenol (EDF) monomers. (Scattered: experimental data; lines: fitting data).

Impedance experiments were undertaken to explore the characteristics and kinetics of electrochemical processes occurring at the metal/electrolyte interface with and without coating. The impedance responses of both uncoated and coated SS, measured at E_{CO} after 3 h immersion, as a function of frequency, is presented as the Bode plot in Fig. 8(B). As can be noted from this figure, the impedance of the SS substrate is close to zero at a higher frequency in the range from 100,000 to 1 Hz, which corresponds to the solution resistance, and as a consequence, it does not oppose the flow of current. After that, the impedance is grown linearly up to 250 kΩ with decreasing frequency. This corresponds to the impedance of the metallic oxide layer film, like chromium oxide, that formed on the SS surface, which acts as a dielectric barrier between the metal surface and the corrosion solution. The coatings raise the impedance in a very significant manner. For both CDF and EDF it starts with 1 MΩ at 10^{-3} Hz and higher frequency follows a similar tendency of reduction to zero as observed in uncoated SS. Such a significant amount of impedance enhancement showed that these films have better performance in this corrosive environment, as well as the capacitive behavior (BAI *et al*., 2016).

The capacitive effect introduced by the deposition can be also seen by the phase angle measurement shown in Figure 8(B), under the restricted range of frequency between 0.1 Hz and 100 kHz. As one note from the Bode plot, in all samples we have a maximum phase angle around -80º, in the range of frequency between 10^2 to 10^{-1} Hz, except for CDF where the phase decreased to around -75º. This similarity indicates the resilience of the films against the action of the corrosive solution (SANTOS *et al*., 2017b). Also, the absence of the second concavity in the coated substrate, suggests greater stability of the coatings to the action of the solution, since the second concavity is a result of electrolyte-metal interactions, non-porous, compact layers are expected in such cases. Additionally, at the high-frequency region, around 10^5 Hz, the phase angle curves of both film-coated substrates rises from 20° to 25° remaining higher than the phase of bare steel, that is less than 10°, as a consequence of the dielectric feature of the film on the substrate (SANTOS *et al*., 2017b). It also shows that deposited film effectively adsorbs on the alloy surface. The active resistance of the film promotes a phase angle of about -80º that is close to the ideal capacitive behavior (LIU *et al*., 2003; GALVÁN *et al*., 2016).

To further understand the electrochemical properties of both CDF and EDF coatings, the EIS data were fitted using an appropriate equivalent electric circuits with an association of passive elements (Fig. 9), such as the solution resistance R_S, the pore resistance of coating R_P, the

charge-transfer resistance R_C, the coating capacitance C_C, the double-layer capacitance C_D, and the Warburg impedance *W*. The fitting process was run until Chi-square (χ^2) reached values in the order of 10^{-2} to 10^{-3} and the final values of the parameters are in Table 2. The value of R_S, the high-frequency intercept with the real axis in the Nyquist plots, remains about the same order of magnitude once the distance of the working electrode to the reference electrode is fixed as the concentration of the solution as well (MORETO *et al*., 2014).

The coating promotes the effective protection of the substrate from the corrosion solution with an increase in R_C by about six times the value of the uncoated one. There is a reduction in the density of charged species next to the surface and in consequence one effective augment on the shielding length of SS substrate to the electric field. This represents a reduction in the capacitance, with C_D changing from 55 µF of SS to 42 µF for EDF and 22 µF for CDF. The diffusion of the byproducts of the corrosion to the bulk solution and/or of the dissolved oxygen to the surface of the electrode, represented by the Warburg impedance, is present only for SS and CDF coating, the latter with lower impedance value. It indicates a negligible amount of water and electrolyte penetrates through the CDF coating to the metal surface until the coating replenishes or self-heals to form a new dielectric barrier layer on the metal surface. This process appears in the form of a sequence of sharp peaks in the negative direction in OCP before 1 h immersion time (Fig. 7(A)). In contrast, EDF controls the diffusion process and in consequence, vanishing the W of SS substrate. This control is attributed to the presence of methoxy groups, in addition to hydroxyl, which enhances the adsorption on the SS surface and produces a dense and homogeneous film across the substrate.

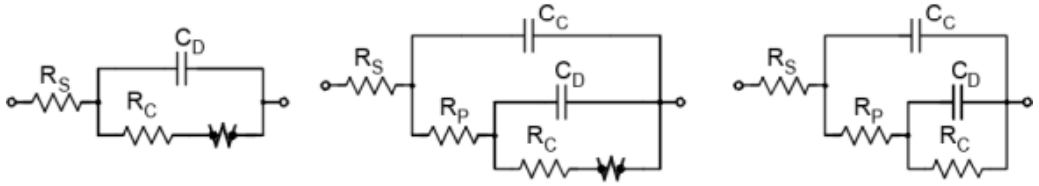

SS CDF EDF

Figure 9. The electrical equivalent circuit used to fit the EIS data of uncoated stainless steel (SS), and the film-coated for 45 min derived from carvacrol (CDF), and eugenol monomers (EDF).

Table 2. Fitting results of EIS parameters for uncoated and coated bare steel.

Sample	R_S, Ω	R_P, kΩ	R_C, kΩ	C_C, nF	Q_D, µF	W, µMho*s^1/2	R_T, kΩ
Bare steel	23	-	162	-	55	95	162
EDF Coated	16	35	915	41	42	-	950
CDF coated	18	37	594	23	17	20	631

4. Conclusion

The deposition of carvacrol- and eugenol-derived film on stainless steel substrates was successfully achieved through an atmospheric pressure discharge barrier discharge plasma reactor. The infrared spectra result revealed the preservation of mimicking the functional group of the monomers, hydroxyl and aromatic, in the film matrix. They are the key futures for the antibacterial and electrochemical activity of these films deposited through the DBD plasma reactor. Atomic force microscopy results showed a few scratches on the surface of the uncoated substrate, and the disappearance of these irregularities upon EDF and EDF coating and acquired a uniform surface, free of defects and scratches. This new surface feature indicates the film deposition takes place on the surface of the substrate. CDF coatings showed the capability to reduce the microbial adhesion and biofilm formation of *P. aeruginosa* around four orders of magnitude and *C. albicans* by five orders in comparison with the number of microbes detected on the pristine substrate. Similarly, eugenol film was reduced by three orders of *P. aeruginosa* and four orders of *C. albicans*. The obtained films also act as anodic inhibitors and reduce the corrosion rate of the bare steel by 30- 35%. In general, thus bactericidal activity and corrosion protection results are associated with the preservation of monomer functional groups, which make them a good alternative for coatings, for instance, to avoid the formation of biofilms and corrosion on biomaterials.

10 General Conclusions

Biofilm is a three-dimensional polymeric matrix and it is produced by a community of bacteria and fungi. It can be formed on diverse natural or artificial surfaces. Recently, the interest in developing an effective antibacterial coating of biomaterials has increased because of substantial concerns about the microbial-resistance towards synthetics antibiotics following the biofilm formation on IMDs. Interestingly, antimicrobial surface coating before implanting, particularly coatings from natural essential oils, has shown great potential as active biomaterials in hospitals, clinics, and implants. These materials offer promising features, such as biocompatibility, biodegradability, physical stability, cost-effectiveness, and environmentally friendly. Hence, in the present work, both carvacrol- and eugenol-derived films were deposited on the surface of the stainless steel substrate, through dielectric barrier discharge plasma reactors under different deposition conditions, aiming for the reduction of biofilm formation and proliferation, as well as corrosion protection. In addition, the spectroscopic and electrical characterization of argon only, and an admixture of argon with the monomer in DBD plasmas were analyzed. The electron temperature and the main power of the discharge were also investigated as a function of gas flow rate and applied voltage. The electron temperature and the mean plasma power increased with the applied voltage.

Thin films derived from both carvacrol and eugenol monomers were successfully deposited on a stainless steel surface through dielectric barrier discharge plasma reactors under different plasma discharge conditions. Depending on plasma deposition conditions, thicker films up to 3 µm thickness, which lasts for a long period when exposed to atmospheric air, are stable and chemically bonded to the surface of the substrate, were obtained. The SEM images confirmed that the surface property of the stainless steel substrate was changed after coating with these films. Each film was deposited uniformly on the surface of the substrate by round structures in a spherical shape roughly 10 to 20 µm in diameter. Also, the AFM result showed the absence of any signals of detachment, cracks, or uncoated regions in the inspected area of the substrate, which signs the polymerization reactions occurred essentially on the surface of the substrate, instead of in the gas phase.

The EDS result showed that the hydrocarbon materials, such as carbon and oxygen, were deposited in both films. Carbon was identified to be the main element and it had contributed up to 87 and 85% of the total atomic concentration for film fabricated from carvacrol and eugenol

monomer, respectively. And, oxygen was identified as the second most abundant element in the films, estimated to be around 15 and 19% of the entire films fabricated for those monomers, respectively. No impurities were identified from any of the deposited films. The water contact angle of the pristine substrate was decreased significantly after treatment and varied depending on the deposition conditions. This decrease in the water contact angle upon film coating demonstrated the increase in hydrophilicity (hydroxyl group), which is responsible for the antimicrobial activates, on the pristine substrate.

Both carvacrol and eugenol-derived film coating had the potential to reduce the microbial adhesion and biofilm formation of the tested human pathogens, *E. coli, S. aureus*, *P. aeruginosa,* and C. *albicans*. Interestingly, films deposited from carvacrol showed complete inhibition of *E. coli and a* significant decrease in the density of CFUs by 90, 32 to 44, and 45 to 60%, respectively, against *S. aureus, P. aeruginosa,* and C. *alibicans* biofilm formation. Likewise, eugenol-plasma-derived film reduced the density of CFUs by more than 78, 65, 30 to 36, and 44 to 52% against those microbes, respectively. In contrast, the pristine substrate showed the viability of *E. coli and S. aureus* at more than 90% and around 80% of *P. aeruginosa* and C. *alibicans* biofilm formation.

SEM imaging, similar to viability assay, showed that a much higher number of cells of the tested microorganisms were adhered to pristine substrates compared to the culture medium. On the other hand, the redaction of biofilm growth and the CFU population were observed on the surfaces of each film-coated substrate. The results showed that surface coating with monomer derived film was effective in inhibiting biofilm formation. The film coating substrate and immersion of the stainless-steel substrate in both liquid monomers showed a similar effect in suppressing biofilm caused by *E. coli and S. aureus* bacteria. However, the coatings produced without plasma were degraded after 20 min under UV-irradiation, which is a typical procedure for material sterilization. On the other hand, no clear evidence of degradation was observed on the plasma deposited from carvacrol and eugenol films even after one hour under the same UV irradiation.

Bothe carvacrol- and eugenol-derived films were increased at least 10 times the corrosion resistance of the SS surface in 3.5% (w/v) NaCl solution. In general, this finding emphasizes that the bactericidal activity associated with carvacrol and eugenol, make the films produced here good candidates for coatings to avoid the formation of biofilms on biomaterials and food

packaging, for instance. The EIS and potentiodynamic polarization results also encouraged the use of carvacrol and eugenol-derived film coating for corrosion protection of biomaterials and food packaging materials. Furthermore, this research contributes to the knowledge of developing a polymeric thin film from carvacrol and eugenol essential oil using atmospheric pressure plasma-enhanced chemical vapor deposition.

5.1. **Recommendations for Future Work**

In this study, both carvacrol- and eugenol-derived film coating on stainless steel surfaces showed promising results in suppressing biofilm-forming pathogenic microorganisms and increasing corrosion resistance. However, such thin film deposition was tested on one substrate, stainless steel. Therefore, further investigation is needed to deposit such film on other substrates, such as ceramics, polymers, and other metallic surfaces, under different plasma discharge conditions for various types of applications. More importantly, evaluating the biocompatibility of the film (both carvacrol and eugenol) needs further study. This will enhance the chance of commercializing carvacrol and eugenol films for successful antibacterial coatings on implantable devices.

11 References

ABDAL-HAY, A. *et al*. Enhanced Biocorrosion Resistance of Surface Modified Magnesium Alloys Using Inorganic/Organic Composite Layer for Biomedical Applications. **Ceramics International**, v. 40, n. 1 PART B, p. 2237-2247, 2014.

ADIL, B. H.; AL-SHAMMARI, A. M.; MURBAT, H. H. Breast Cancer Treatment Using Cold Atmospheric Plasma Generated by the FE-DBD Scheme. **Clinical Plasma Medicine**, v. 19-20, n. May, p. 100103, 2020.

ABDI, S. *et al*. Decontamination of Red Pepper Using Cold Atmospheric Pressure Plasma as an Alternative Technique. **Applied Food Biotechnology**, v. 6, n. 4, p. 247-254, 2019.

AGARWAL, A. *et al*. Polymeric Multilayers That Localize the Release of Chlorhexidine from Biologic Wound Dressings. **Biomaterials**, v. 33, n. 28, p. 6783-6792, 2012.

AHERWAR, A.; SINGH, A. K.; PATNAIK, A. Cobalt-based alloy: A better choice biomaterial for hip implants. **Trends in Biomaterials and Artificial Organs**, v, 30, n. 1, p. 50-55, 2016.

AHMAD, J.; BAZAKA, K.; JACOB, M. Optical and Surface Characterization of Radio Frequency Plasma Polymerized 1-Isopropyl-4-Methyl-1,4-Cyclohexadiene Thin Films. **Electronics**, v. 3, n. 2, p. 266-281, 2014.

AL-JUMAILI, A. *et al*. The Electrical Properties of Plasma-Deposited Thin Films Derived from Pelargonium Graveolens. **Electronics**, v. 6, n. 4, p. 86, 2017a.

AL-JUMAILI, A. *et al*. Review on the antimicrobial properties of carbon nanostructures**.** **Materials**, v. 10, n. 9, p. 1066, 2017b.

AL-JUMAILI, A. *et al*. Plasma Treatment of Polymeric Membranes. **In Non-Thermal Plasma Technology for Polymeric Materials**, p. 211-240, 2019.

AL-JUMAILI, A. Fabrication and Characterization of Antibacterial Surfaces Derived from *Geranium* Essential Oil Using PECVD. **Ph.D. diss., James Cook University**, 2019.

AL-JUMAILI, A.; BAZAKA, K.; JACOB, M. Retention of Antibacterial Activity in *Geranium* Plasma Polymer Thin Films. **Nanomaterials**, v. 7, n. 9, p. 270, 2017.

ALEMÁN, C. *et al*. Plasma Surface Modification of Polymers for Sensor Applications. **Journal of Materials Chemistry B**, v. 6, n. 41, p. 6515-6533, 2018.

ALMAGUER-FLORES, A. *et al*. Influence of Topography and Hydrophilicity on Initial Oral Biofilm Formation on Microstructured Titanium Surfaces in Vitro. **Clinical Oral Implants**

Research, v. 23, n. 3, p. 301-307, 2012.

ALSABAGH, A. M. *et al*. Utilization of Green Tea as an Environmentally Friendly Corrosion Inhibitor for Carbon Steel in Acidic Medium. **International Journal of Electrochemical Science**, v. 10, p. 1855-1872, 2015.

ALVES, C. *et al.* Nitriding of Titanium Disks and Industrial Dental Implants Using Hollow Cathode Discharge. **Surface and Coatings Technology**, v. 200, n. 11, p. 3657-3663, 2005.

ALVES, S. M.; ALBANO, W.; DE OLIVEIRA, A. J. Improvement of Coating Adhesion on Cemented Carbide Tools by Plasma Etching. **Journal of the Brazilian Society of Mechanical Sciences and Engineering**, v. 39, n. 3, p. 845-856, 2017.

AMBRICO, P. F. *et al*. On the Air Atmospheric Pressure Plasma Treatment Effect on the Physiology, Germination, and Seedlings of Basil Seeds. **Journal of Physics D: Applied Physics**, v. 53, n. 10, p. 104001, 2020.

AMIN, M. A.; KHALED, K. F. Copper Corrosion Inhibition in O_2-Saturated H_2SO_4 Solutions. **Corrosion Science**, v. 52, n. 4, p. 1194-1204, 2010.

ANDERSON, L. J. *et al*. Effect of a Plasma Polymerised Linalyl Acetate Dielectric on the Optical and Morphological Properties of an N-Type Organic Semiconductor. **Applied Physics A: Materials Science and Processing**, v. 105, n. 1, p. 95-102, 2011.

ANTONIA NOSTRO; TERESA PAPALIA. Antimicrobial Activity of Carvacrol: Current Progress and Future Prospectives. **Recent Patents on Anti-Infective Drug Discovery**, v. 7, n. 1, p. 28-35, 2012.

ARAÚJO, E. A. *et al.* Control of microbial adhesion as a strategy for food and bioprocess technology. **Food and Bioprocess Technology**, v, 3, n, 3, p. 321-332, 2010.

ARCIOLA, C. R.; CAMPOCCIA, D.; MONTANARO, L. Implant Infections: Adhesion, Biofilm Formation, and Immune Evasion. **Nature Reviews Microbiology**, v. 16, n. 7, p. 397-409, 2018.

AREFI-KHONSARI, F.; TATOULIAN, M. Plasma Processing of Polymers by a Low-Frequency Discharge with Asymmetrical Configuration of Electrodes. **Advanced plasma technology**, p. 137-174, 2008.

ARIMA, Y.; IWATA, H. Effect of Wettability and Surface Functional Groups on Protein Adsorption and Cell Adhesion Using Well-Defined Mixed Self-Assembled Monolayers.

Biomaterials, v. 28, n. 20, p. 3074-3082, 2007.

ARJUNAN, K. P.; SHARMA, V. K.; PTASINSKA, S. Effects of Atmospheric Pressure Plasmas on Isolated and Cellular DNA-a Review. **International Journal of Molecular Sciences**, v. 16, n. 2, p. 2971-3016, 2015.

ASHPIS, D. E.; LAUN, M. C.; GRIEBELER, E. L. Progress toward Accurate Measurements of Power Consumptions of DBD Plasma Actuators. **50th AIAA Aerospace Sciences Meeting Including the New Horizons Forum and Aerospace Exposition**, n. January, p. 1-24, 2012.

AZIZ, G. *et al*. Plasma Parameters Effects on the Properties, Aging, and Stability Behaviors of Allylamine Plasma Coated Ultra-High Molecular Weight Polyethylene (UHMWPE) Films. **Applied Surface Science**, v. 409, p. 381-395, 2017.

AGARWAL, A.; SINGH, K. P.; JAIN, A. Medical significance and management of staphylococcal biofilm. **FEMS Immunology and Medical Microbiology**, v. 58, n.2, p. 147-160, 2010.

ACHINGER, S. G.; AYUS, J. C. When the source of inflammation is hiding in plain sight: Failed kidney transplants, clotted arteriovenous grafts, and central venous catheters. **Seminars in Dialysis**, v. 32, n. 1, p. 15-21, 2019.

AGRAWAL, N. K. *et al*. Plasma Irradiation of Polymers: Surface to Biological Mitigation. **Radiation Effects in Polymeric Materials. Spring**er, Cham. p. 319-350, 2019.

AHMAD, A. *et al*. Proton Translocating ATPase Medium ted Fungicidal Activity of Eugenol and Thymol. **Fitoterapia**, v. 81, n. 8, p. 1157-1162, 2010.

AL-AMIERY, A. A. *et al.* The Use of Umbelliferone in the Synthesis of New Heterocyclic Compounds. **Molecules**, v. 16, n. 8, p. 6833- 6843, 2011.

ANTONIJEVIĆ, M. M. *et al.* The Influence of Chloride Ions and Benzotriazole on the Corrosion Behavior of Cu37Zn Brass in Alkaline Medium. **Electrochimica Acta**, v. 50, n. 18, p. 3693-3701, 2005.

ASRI, R. I. M. *et al.* Corrosion and surface modification on biocompatible metals: A review. **Materials Science and Engineering C**, v. 77, p. 1261-1274, 2017.

BARRÈRE, F. *et al*. Advanced biomaterials for skeletal tissue regeneration: Instructive and smart functions**. Materials Science and Engineering R: Reports**, v. *59*, n. 1-6, p. 38-71, 2008.

MEARS, S. C.; KATES, S. L. A Guide to Improving the Care of Patients with Fragility Fractures, Edition 2. **Geriatric Orthopaedic Surgery & Rehabilitation**, v. 6, n. 2, p. 58-120, 2015.

PRASAD, K. *et al.* Metallic Biomaterials: Current Challenges and Opportunities. **Materials**, v. 10, n. 8, 2017.

SU, Y. *et al.* Bioinspired Surface Functionalization of Metallic Biomaterials. **Journal of the Mechanical Behavior of Biomedical Materials**, v. 77, p. 90-105, 2018.

VAITHILINGAM, J. *et al*. Functionalisation of Ti6Al4V Components Fabricated Using Selective Laser Melting with a Bioactive Compound. **Materials Science and Engineering C**, v. 46, p. 52-61, 2015.

BAI, Y. *et al.* Characterization, Corrosion Behavior, Cellular Response, and in Vivo Bone Tissue Compatibility of Titanium-Niobium Alloy with Low Young's Modulus. **Materials Science and Engineering C**, v. 59, p. 565-576, 2016.

BAJPAI, V. K.; SHARMA, A.; BAEK, K. H. Antibacterial Mode of Action of the Essential Oil Obtained from Chamaecyparis Obtusa Sawdust on the Membrane Integrity of Selected Foodborne Pathogens. **Food Technology and Biotechnology**, v. 52, n. 1, p. 109-118, 2014.

BAMPIDIS, V. *et al*. Safety, and Efficacy of an Essential Oil of *Origanum Vulgare* Ssp. Hirtum (Link) Leetsw. for All Poultry Species. **EFSA Journal**, v. 17, n. 4, 2019.

BARBOUN, P. M.; C. HICKS, J. Unconventional Catalytic Approaches to Ammonia Synthesis. **Annual Review of Chemical and Biomolecular Engineering**, v. 11, n. 10, p. 503-521, 2020.

BARTLETT, J. G. Treatment of Infections Associated with Surgical Implants. **Infectious Diseases in Clinical Practice**, v. 12, n. 4, p. 258-259, 2004.

BASSOLÉ, I. H. N.; JULIANI, H. R. Essential Oils in Combination and Their Antimicrobial Properties. **Molecules**, v. 17, n. 4, p. 3989-4006, 2012.

BAZAKA, K. *et al*. Plasma-Enhanced Synthesis of Bioactive Polymeric Coatings from Monoterpene Alcohols: A Combined Experimental and Theoretical Study. **Biomacromolecules**, v. 11, n. 8, p. 2016-2026, 2010.

BAZAKA, K. *et al*. Plasma-assisted surface modification of organic biopolymers to prevent bacterial attachment. **Acta Biomaterialia**, v, 7, n. 5, p. 2015-2028, 2011a.

BAZAKA, K. *et al*. The Effect of Polyterpenol Thin Film Surfaces on Bacterial Viability and Adhesion. **Polymers**, v. 3, n. 1, p. 388-404, 2011b.

BAZAKA, K. *et al*. Plasma Assisted Surface Modification of Organic Biopolymers. **Acta Biomaterialia**, p. 1-32, 2015a.

BAZAKA, K. *et al*. Anti-Bacterial Surfaces: Natural Agents, Mechanisms of Action, and Plasma Surface Modification. **RSC Advances**, v. 5, n. 60, p. 48739-48759, 2015b.

BAZAKA, K. *et al*. Plasma-potentiated small molecules-possible alternative to antibiotics. **Nano Futures**, v. 1, n. 2, p. 025002, 2017.

BAZAKA, K.; JACOB, M. V. Synthesis of Radio Frequency Plasma Polymerized Non-Synthetic Terpinen-4-Ol Thin Films. **Materials Letters**, v. 63, n. 19, p. 1594-1597, 2009.

BAZAKA, K.; JACOB, M. V.; BOWDEN, B. F. Optical and Chemical Properties of Polyterpenol Thin Films Deposited via Plasma-Enhanced Chemical Vapor Deposition. **Journal of Materials Research**, v. 26, n. 8, p. 1018-1025, 2011.

BEN ARFA, A. *et al*. Antimicrobial Activity of Carvacrol Related to Its Chemical Structure. **Letters in Applied Microbiology**, v. 43, n. 2, p. 149-154, 2006.

BERNHARDT, T. *et al*. Plasma Medicine: Applications of Cold Atmospheric Pressure Plasma in Dermatology. **Oxidative Medicine and Cellular Longevity**, v. 2019, p. 10-13, 2019.

BHATTACHARYYA, D. *et al*. Surface Chemistry and Polymer Film Thickness Effects on Endothelial Cell Adhesion and Proliferation. **Journal of Biomedical Materials Research - Part A**, v. 94, n. 2, p. 640-648, 2010.

BIZUNEH ADINEW. GC-MS and FT-IR Analysis of Constituents of Essential Oil from Cinnamon Bark Growing in South-West of Ethiopia. **International Journal of Herbal Medicine**, v. 1, n. 6, p. 22-31, 2014.

BORCIA, G.; ANDERSON, C. A.; BROWN, N. M. D. Dielectric Barrier Discharge for Surface Treatment: Application to Selected Polymers in Film and Fibre Form. **Plasma Sources Science and Technology**, v. 13, n. 3, p. 335, 2003.

BORMASHENKO, E. *et al*. Physical Mechanisms of Interaction of Cold Plasma with Polymer Surfaces. **Journal of Colloid and Interface Science**, v. 448, p. 175-179, 2015.

BORNAPOUR, M. *et al*. Biocompatibility and Biodegradability of Mg-Sr Alloys: The Formation of Sr-Substituted Hydroxyapatite. **Acta Biomaterialia**, v. 9, n. 2, p. 5319-5330, 2013.

BOSE, S.; ROBERTSON, S. F.; BANDYOPADHYAY, A. Surface modification of

biomaterials and biomedical devices using additive manufacturing. **Acta Biomaterialia**, v. 66, p. 6-22, 2018.

BOUGHENDJIOUA, H.; DJEDDI, S.; SERIDI, R. A Complementary Analysis of Thyme Essential Oil by Fourier Transformed Infrared Spectroscopy. v. 1, n. 1, p. 29-32, 2017.

BOURKE, P. *et al*. Microbiological interactions with cold plasma. **Journal of Applied Microbiology**, v. 123, n. 2, p. 308-324, 2017.

BRANDENBURG, R. Dielectric barrier discharges: Progress on plasma sources and the understanding of regimes and single filaments. **Plasma Sources Science and Technology**, v. *26, n.* 5, p. 053001, 2017.

BURT, S. Essential oils: Their antibacterial properties and potential applications in foods - A review. **International Journal of Food Microbiology**, v. *94*, n. 3, p. 223-253, 2004.

BARRETO, L. S. *et al*. Evaluation of the Anticorrosion Performance of Peel Garlic Extract as a Corrosion Inhibitor for Astm 1020 Carbon Steel in Acidic Solution. **Revista Materia**, v. 22. n.3, 2017.

BELIBEL, R. *et al*. Effect of Chemical Heterogeneity of Biodegradable Polymers on Surface Energy: A Static Contact Angle Analysis of Polyester Model Films. **Materials Science and Engineering C**, v. 59, p. 998-1006, 2016.

BENNIS, S. *et al*. Surface Alteration of Saccharomyces Cerevisiae Induced by Thymol and Eugenol. **Letters in Applied Microbiology**, v. 38, n. 6, p. 454-8, 2004.

BERMAN, J.; KRYSAN, D. J. Drug Resistance and Tolerance in Fungi. **Nature Reviews Microbiology**, p. 1-13, 2020.

BERRÍOS-TORRES, S. I. *et al.* Activity of Commonly Used Antimicrobial Prophylaxis Regimens against Pathogens Causing Coronary Artery Bypass Graft and Arthroplasty Surgical Site Infections in the United States, 2006-2009. **Infection Control & Hospital Epidemiology**, v. 35, n. 3, p. 231-239, 2014.

BI, S. *et al*. Spectroscopic Study on the Interaction of Eugenol with Salmon Sperm DNA in Vitro. **Journal of Luminescence**, v. 132, n. 9, p. 2355-2360, 2012.

BOSE, S. *et al*. Additive manufacturing of biomaterials. **Progress in Materials Science**, v.93, p. 45-111, 2018.

BRAGA, P. C. *et al.* Eugenol, and Thymol, Alone or in Combination, Induce Morphological Alterations in the Envelope of *Candida Albicans*. **Fitoterapia**, v. 78, n. 6, p. 396-

400, 2007.

BREZNICKY, J.; NOVAK, M. The Most Common Etiological Agents of Prosthetic Joint Infections in Orthopaedics. **Medicinski Glasnik**, v. 16, n. 2, p. 2962-6894, 2019.

ÇAKMAK, K. *et al*. Plasma Polymerized Linalool (PpLin): An Antimicrobial and Biocompatible Coating. **Turkish Journal of Chemistry**, v. 43, n. 2, p. 687-704, 2019.

CAO, X. *et al*. Design and Characteristics of a Laminar Plasma Torch for Materials Processing. **Plasma Chemistry and Plasma Processing**, v. 36, n. 2, p. 693-710, 2016.

CASTELL, R.; IGLESIAS, E. J.; RUIZ-CAMACHO, J. Glow discharge plasma properties of gases of environmental interest. **Brazilian Journal of Physics**, v. *34*, n. 4b, p. 1734-1737, 2004.

CASTRO, D. O. *et al*. Effect of Different Carboxylic Acids in Cyclodextrin Functionalization of Cellulose Nanocrystals for Prolonged Release of Carvacrol. **Materials Science and Engineering C**, v. 69, p. 1018-1025, 2016.

CATS-BARIL, W. *et al*. International Consensus on Periprosthetic Joint Infection: Description of the Consensus Process. **Clinical Orthopaedics and Related Research**, v. 471, n. 12, p. 4065-4075, 2013.

CEYLAN, E.; FUNG, D. Y. C. Antimicrobial activity of spices 1. **Journal of Rapid Methods and Automation in Microbiology**, v. 12, n. 1, p. 1-55, 2004.

CHA, S.; PARK, Y. S. Plasma in Dentistry. **Clinical Plasma Medicine**, v. 2, n. 1, p. 4-10, 2014.

CHAN, Y. W. *et al*. Plasma Polymerized Carvone as an Antibacterial and Biocompatible Coating. **Materials Science and Engineering C**, v. 68, p. 861-871, 2016.

CHANG, Y.; MCLANDSBOROUGH, L.; MCCLEMENTS, D. J. Physicochemical Properties and Antimicrobial Efficacy of Carvacrol Nanoemulsions Formed by Spontaneous Emulsification. **Journal of Agricultural and Food Chemistry**, v. 61, n. 37, p. 8906-8913, 2013.

CHEN, X. *et al*. Plasma-Induced PAA-ZnO Coated PVDF Membrane for Oily Wastewater Treatment: Preparation, Optimization, and Characterization through Taguchi OA Design and Synchrotron-Based X-Ray Analysis. **Journal of Membrane Science**, v. 582, p. 70-82, 2019.

CHIPER, a S.; CHEN, W.; STAMATE, E. Diagnostics of DBD Plasma Produced Inside a Closed Package. **Ispc-19**, p. 26-31, 2009.

CHIRUMAMILLA, V. R. *et al*. Experimental Investigation on the Effect of a Microsecond

Pulse and a Nanosecond Pulse on No Removal Using a Pulsed DBD with Catalytic Materials**. Plasma Chemistry and Plasma Processing**, v. *3*, *n.* 2, p. 487-510, 2016.

CHNG, T. L. *et al*. Electric Field Evolution in a Diffuse Ionization Wave Nanosecond Pulse Discharge in Atmospheric Pressure Air. **Plasma Sources Science and Technology**, v. 28, n. 9, p. 09LT02, 2019.

CORBELLA, C.; GROSSE-KREUL, S.; VON KEUDELL, A. Exploring the Structure of the Modified Top Layer of Polypropylene during Plasma Treatment. **Plasma Processes and Polymers**, v. 12, n. 6, p. 564-573, 2015.

CORDEIRO, J. M. *et al*. Synthesis of Biofunctional Coating for a TiZr Alloy: Surface, Electrochemical, and Biological Characterizations. **Applied Surface Science**, v. 452, p. 268-278, 2018.

CRISTANI, M. *et al*. Interaction of Four Monoterpenes Contained in Essential Oils with Model Membranes: Implications for Their Antibacterial Activity. **Journal of Agricultural and Food Chemistry**, v. 55, n. 15, p. 6300-6308, 2007.

CUI, F. Z.; LUO, Z. S. Biomaterials Modification by Ion-Beam Processing. **Surface and Coatings Technology**, v. 112, n. 3, p. 278-285, 1999.

CVRČEK, L.; HORÁKOVÁ, M. Plasma Modified Polymeric Materials for Implant Applications. In Non-Thermal Plasma Technology for Polymeric Materials. **Elsevier**, p. 367-407, 2019.

CAZELLI, D. S. P. *et al.* The Relationship between the Antimicrobial Activity of Eugenol and the LPETG Peptide Structure and Associated Analysis for Docking Purposes. **Chemical Papers**, v. 71, n. 10, p. 1877–1886, 2017

CAZZOLA, M. *et al.* Grafting of the Peppermint Essential Oil to a Chemically Treated Ti6Al4V Alloy to Counteract the Bacterial Adhesion. **Surface and Coatings Technology**, v. 378, n. September 2019.

CELLS, Y. Molecules Effect of Clove and Thyme Essential Oils on *Candida* Biofilm Formation and the Oil Distribution In. p. 1-12, 2019.

CHANG, T. *et al*. The Golden Alloy Cu5Zn5Al1Sn: Patina Evolution in Chloride-Containing Atmospheres. **Corrosion Science**, v. 133, p. 190-203, 2018.

CHENG, G. *et al.* Antimicrobial drugs in fighting against antimicrobial resistance. **Frontiers in Microbiology**, v.7, p. 470, 2016.

CÓRDOVA-ALCÁNTARA, I. M. *et al*. Biofilm Characterization of Fusarium Solani Keratitis Isolate: Increased Resistance to Antifungals and UV Light. **Journal of Microbiology**, v. 57, n. 6, p. 485-497, 2019.

DAS, B. *et al*. Eugenol Provokes ROS-Medium ted Membrane Damage-Associated Antibacterial Activity against Clinically Isolated Multidrug-Resistant *Staphylococcus Aureus* Strains. **Infectious Diseases: Research and Treatment**, v. 9, p. IDRT-S31741, 2016.

DAS GHATAK, P. *et al*. A Surfactant Polymer Dressing Potentiates Antimicrobial Efficacy in Biofilm Disruption. **Scientific Reports**, v. 8, n. 1, p. 873, 2018.

DI PASQUA, R. *et al*. Membrane Toxicity of Antimicrobial Compounds from Essential Oils. **Journal of Agricultural and Food Chemistry**, v. 55, n. 12, p. 4863-4870, 2007.

DÍAZ DE RIENZO, M. A. *et al*. *Pseudomonas Aeruginosa* Biofilm Disruption Using Microbial Surfactants. **Journal of Applied Microbiology**, v. 120, n. 4, p. 868-876, 2016.

DONELIAN, A. *et al*. Comparison of extraction of patchouli (*Pogostemon cablin*) essential oil with supercritical CO_2 and by steam distillation. **Journal of Supercritical Fluids**, v. 48, n. 1, p. 15-20, 2009.

DOUGLAS, L. J. *Candida* biofilms and their role in infection**. Trends in Microbiology**, v. 11, n. 1, p.30-36, 2003.

DEVI, K. P. *et al*. Eugenol (an Essential Oil of Clove) Acts as an Antibacterial Agent against *Salmonella Typhi* by Disrupting the Cellular Membrane. **Journal of Ethnopharmacology**, v. 130, n. 1, p. 107-115, 2010.

DEVI, K. P. *et al*. Eugenol Alters the Integrity of Cell Membrane and Acts against the Nosocomial Pathogen *Proteus Mirabilis*. **Archives of Pharmacal Research**, v. 36, n. 3, p. 282-292, 2013.

DJORDJEVIC, Z. *et al*. Nosocomial Urinary Tract Infections Caused by *Pseudomonas Aeruginosa* and *Acinetobacter Species*: Sensitivity to Antibiotics and Risk Factors. **American Journal of Infection Control**, v. 41, n. 12, p. 1182-1187, 2013.

DONNELLY, V. M.; KORNBLIT, A. Plasma Etching: Yesterday, Today, and Tomorrow. **Journal of Vacuum Science & Technology A: Vacuum, Surfaces, and Films**, v. 31, n. 5, p. 050825, 2013.

DORIA, A. C. O. C. *et al.* Sterilization of *candida albicans* biofilms grown on polymers by atmospheric plasma: From plasma devices to biofilm analysis. In: **Biofilms**

Characterization, Applications, and Recent Advances. Hauppauge, NY: Nova Science Publications, 2016.

DURDU, S.; USTA, M.; BERKEM, A. S. Bioactive Coatings on Ti6Al4V Alloy Formed by Plasma Electrolytic Oxidation. **Surface and Coatings Technology**, v. 301, p. 85-93, 2016.

DURRANT, S. F. a-C:O:H: PECVD of a-C:O:H films. In: **Handbook of Thin Film Process Technology: 98/2 Recipes for Optical Materials**. p. 384, 2018.

EAFUS (Everything Added to Foods in the United States). A Food Additive Database. Centre for Food Safety, and Applied Nutrition; U.S. Food, and Drug Administration: Washington, DC, USA, 2006; No. 0202.

EASTON, C. D.; JACOB, M. V. Optical Characterisation of Radio Frequency Plasma Polymerised *Lavandula Angustifolia* Essential Oil Thin Films. **Thin Solid Films**, v. 517, n. 15, p. 4402-4407, 2009.

EASTON, C. D.; JACOB, M. V. Solubility and Adhesion Characteristics of Plasma Polymerized Thin Films Derived from *Lavandula Angustifolia* Essential Oil. **Journal of Applied Polymer Science**, v. 115, n. 1, p. 404-415, 2010.

EASTON, C. D.; JACOB, M. V.; SHANKS, R. A. Fabrication and Characterisation of Polymer Thin-Films Derived from Cineole Using Radio Frequency Plasma Polymerisation. **Polymer**, v. 50, n. 15, p. 3465-3469, 2009.

EBY, D. M.; LUCKARIFT, H. R.; JOHNSON, G. R. Hybrid Antimicrobial Enzyme and Silver Nanoparticle Coatings for Medical Instruments. **ACS Applied Materials and Interfaces**, v. 1, n. 7, p. 1553-1560, 2009.

EDMISTON, C. E. *et al.* Clinical and Microbiological Aspects of Biofilm-Associated Surgical Site Infections. **Advances in Experimental Medicine and Biology**, p. 47-67, 2015.

EL-SAYED, A. R.; SHAKER, A. M.; ABD EL-LATEEF, H. M. Corrosion Inhibition of Tin, Indium, and Tin-Indium Alloys by Adenine or Adenosine in Hydrochloric Acid Solution. **Corrosion Science**, v. 52, n. 1, p. 72-81, 2010.

ELIAZ, N. Corrosion of Metallic Biomaterials: A Review. **Materials**, v. 12, n. 3, 2019.

ELTIT, F.; WANG, Q.; WANG, R. Mechanisms of Adverse Local Tissue Reactions to Hip Implants. **Frontiers in Bioengineering and Biotechnology**, v. 7, n. JUL, p. 1-17, 2019.

ESSID, R. *et al.* Combined Effect of Thymus Capitatus and Cinnamomum Verum Essential Oils with Conventional Drugs against *Candida Albicans* Biofilm Formation and

Elucidation of the Molecular Mechanism of Action. **Industrial Crops and Products**, v. 140, p. 111720, 2019.

FAN, N. S. *et al*. Deciphering the Toxic Effects of Antibiotics on Denitrification: Process Performance, Microbial Community, and Antibiotic Resistance Genes. **Journal of Environmental Management**, v. 262, p. 110375, 2020.

FALEIRO M.L. The Mode of Antibacterial Action of Essential Oils. **Science against microbial pathogens: communicating current research and technological advances**, v. 3, n. 3, p. 1143-1156, 2011.

FILGUEIRAS, C. T.; VANETTI, M. C. D. Effect of Eugenol on Growth and Listeriolysin O Production by Listeria Monocytogenes. **Brazilian Archives of Biology and Technology**, v. 49, n. 3, p. 405-409, 2006.

FOUDA, A. S.; DIAB, M. A.; FATHY, S. Role of Some Organic Compounds as Corrosion Inhibitors for 316l Stainless Steel in 1 M HCl. **International Journal of Electrochemical Science**, v. 12, p. 347-362, 2017.

FALAHAT, A. *et al*. Optical Characteristics of an RF DBD Plasma Jet in Various Ar / O_2 Mixtures. **Pramana - Journal of Physics**, v. 90, n. 2, p. 1-11, 2018.

FELFEL, R. M. *et al*. Accelerated in Vitro Degradation Properties of Polylactic Acid/Phosphate Glass Fibre Composites. **Journal of Materials Science**, v. 50, n. 11, p. 3942-3955, 2015.

FERREIRO, J. L. L. *et al*. *Pseudomonas Aeruginosa* Urinary Tract Infections in Hospitalized Patients: Mortality and Prognostic Factors. **PLoS ONE**, v. 12, n. 5, p. e0178178, 2017.

FIEBRANDT, M.; LACKMANN, J. W.; STAPELMANN, K. From patent to a product? 50 years of low-pressure plasma sterilization. **Plasma Processes and Polymers**, v. 15, n. 12, p. 1800139, 2018.

FIROUZI-NERBIN, H.; NASIRPOURI, F.; MOSLEHIFARD, E. Pulse Electrodeposition and Corrosion Properties of Nanocrystalline Nickel-Chromium Alloy Coatings on Copper Substrate. **Journal of Alloys and Compounds**, v. *822*, p. 153712, 2020.

FOUDA, A. S. *et al*. Electrochemical Study on the Effectively of *Hyoscyamus Muticus* Extract as a Green Inhibitor for Corrosion of Copper in 1 MHNO_3. **Journal of Materials and Environmental Science**, v. 6, p. 1519-1531, 2015.

FRANCOLINI, I.; DONELLI, G. Prevention and Control of Biofilm-Based Medical-Device-Related Infections. **FEMS Immunology and Medical Microbiology**, v. 59, n. 3, p. 227-238, 2010.

FRIDMAN, G. *et al*. Blood coagulation and living tissue sterilization by floating-electrode dielectric barrier discharge in air. **Plasma Chemistry and plasma processing,** v. *26*, n. 4, p. 425-442, 2008.

FRIEDRICH, J. Mechanisms of plasma polymerization - Reviewed from a chemical point of view**. Plasma Processes and Polymers**, v. *8, n.* 9, 783-802, 2011.

FRIEDRICH, J. The Plasma Chemistry of Polymer Surfaces: Advanced Techniques for Surface Design. **John Wiley & Sons,** 2012.

FRITZ, S. E.; KELLEY, T. W.; FRISBIE, C. D. Effect of Dielectric Roughness on Performance of Pentacene TFTs and Restoration of Performance with a Polymeric Smoothing Layer. **Journal of Physical Chemistry B**, v. 109, n. 21, p. 10574-10577, 2005.

FUJISAWA, S. *et al*. Antioxidant and Prooxidant Action of Eugenol-Related Compounds and Their Cytotoxicity. **Toxicology**, v. 177, n. 1, p. 39–54, 2002

GAGE, H. *et al*. Community Prevalence of Long-Term Urinary Catheters Use in England. **Neurourology and Urodynamics**, v. 36, n. 2, p. 293-296, 2017.

GALLUCCI, M. N. *et al.* Antimicrobial Combined Action of Terpenes against the Food-Borne Microorganisms *Escherichia Coli*, *Staphylococcus Aureus* and *Bacillus Cereus*. **Flavour and Fragrance Journal**, v. 24, n. 6, p. 348-354, 2009.

GALMIZ, O. *et al*. Study of Surface Dielectric Barrier Discharge Generated Using Liquid Electrodes in Different Gases. **Journal of Physics D: Applied Physics**, v. 49, n. 6, p. 065201, 2015.

GALVÁN, J. C. *et al.* In Vitro Corrosion Behaviour of Surgical 316LVM Stainless Steel Modified by Si+ Ion Implantation - An Electrochemical Impedance Spectroscopy Study. **Journal of Alloys and Compounds**, v. 676, p. 414-427, 2016.

GAN, J. A.; BERNDT, C. C. Plasma surface modification of metallic biomaterials. **Woodhead Publishing**, p. 103-157, 2015.

GANJIAN, M. *et al*. Reactive Ion Etching for Fabrication of Biofunctional Titanium Nanostructures. **Scientific Reports**, v. 9, n. 1, p. 1-20, 2019.

GAO, A.; HANG, R.; CHU, P. K. Recent Advances in Anti-Infection Surfaces Fabricated

on Biomedical Implants by Plasma-Based Technology. **Surface and Coatings Technology**, v. 312, p. 2-6, 2017.

GAVIRIA, L. *et al*. Current Trends in Dental Implants. **Journal of the Korean Association of Oral and Maxillofacial Surgeons**, v. 40, n. 2, p. 50-60, 2014.

GETNET, T. G. *et al*. Atmospheric Pressure Plasma Chemical Vapor Deposition of Carvacrol Thin Films on Stainless Steel to Reduce the Formation of *E. Coli* and *S. Aureus* Biofilms. **Materials**, v. 13, n. 14, p. 3166, 2020a.

GETNET, T. G. *et al*. Plasma polymer deposition of neutral agent carvacrol on a metallic surface by using dielectric barrier discharge plasma in ambient air. **Springer International Publishing,** 2020b. v. 308 LNICST.

GETNET, T. G. *et al*. Thin Film Deposition by Atmospheric Pressure Dielectric Barrier Discharges Containing Eugenol : Discharge and Coating Characterizations, **Polymer, v**. 66, p. 1–16, 2020c.

GHERARDI, N. *et al*. Transition from Glow Silent Discharge to Micro-Discharges in Nitrogen Gas. **Plasma Sources Science and Technology**, v. 9, n. 3, p. 340, 2000.

GIAOURIS, E. D.; NYCHAS, G. J. E. The Adherence of *Salmonella Enteritidis* PT4 to Stainless Steel: The Importance of the Air-Liquid Interface and Nutrient Availability. **Food Microbiology**, v. 23, n. 8, p. 747-752, 2006.

GOMEZ, I. J. *et al*. Nitrogen-Doped Carbon Nanodots for Bioimaging and Delivery of Paclitaxel. **Journal of Materials Chemistry B**, v. 6, n. 35, p. 5540-5548, 2018.

GONÇALVES, T. Caracterização de Filmes Finos Obtidos Por Deposição de Vapor Químico Assistido a Plasma (PECVD) e Deposição e Implantação Iônica Por Imersão Em Plasma (PIIID). **Aleph**, p. 147, 2012.

GOULTER, R. M.; GENTLE, I. R.; DYKES, G. A. Issues in Determining Factors Influencing Bacterial Attachment: A Review Using the Attachment of *Escherichia Coli* to Abiotic Surfaces as an Example. **Letters in Applied Microbiology**, v. 49, n. 1, p. 1-7, 2009.

GRUNDMANN, S.; TROPEA, C. Experimental Damping of Boundary-Layer Oscillations Using DBD Plasma Actuators. **International Journal of Heat and Fluid Flow**, v. 30, n. 3, p. 394-402, 2009.

GULATI, P. *et al*. Diagnostic of Plasma Discharge Parameters in Helium Filled Dielectric Barrier Discharge. **Journal of Theoretical and Applied Physics**, v. 6, n. 1, p. 35, 2012.

GÜRSOY, M.; KARAMAN, M. Effect of Substrate Temperature on Initiated Plasma Enhanced Chemical Vapor Deposition of PHEMA Thin Films. **Physica Status Solidi (C) Current Topics in Solid State Physics**, v. 12, n. 7, p. 1006-1010, 2015.

GOMEZ-CARRETERO, S.; NYBOM, R.; RICHTER-DAHLFORS, A. Electroenhanced Antimicrobial Coating Based on Conjugated Polymers with Covalently Coupled Silver Nanoparticles Prevents *Staphylococcus Aureus* Biofilm Formation. **Advanced Healthcare Materials**, v. 6, n. 20, p. 1700435, 2017.

HARB, S. V. *et al.* Advanced organic nanocomposite coatings for effective corrosion protection. In: **Corrosion Protection at the Nanoscale**, p. 315-343, 2020.

HIROMOTO, S. Corrosion of Metallic Biomaterials. **Metals for Biomedical Devices**, p. 99-121, 2010.

HAERTEL, B. *et al*. Non-Thermal Atmospheric-Pressure Plasma Possible Application in Wound Healing. **Biomolecules and Therapeutics**, v. 22, n. 6, p. 477, 2014.

HAN, L. *et al*. Atmospheric Cold Plasma Interactions with Modified Atmosphere Packaging Inducer Gases for Safe Food Preservation. **Innovative Food Science and Emerging Technologies**, v. 38, p. 384-392, 2016.

HAO, Z. *et al*. Optical and Electric Diagnostics of DBD Plasma Jet in Atmospheric Pressure Argon. **Proceedings of 2012 IEEE International Conference on Condition Monitoring and Diagnosis, CMD 2012**, p. 1187-1190, 2012.

HASSAN, N.; ABDEL GHANY, N. A. Corrosion of Biomaterials: Anodic Treatment and Evaluation of 316L Stainless Steel in Simulated Body Fluid. **Corrosion Engineering Science and Technology**, v. *52, n.* 4, p. 267-275, 2017.

HASSIM, M. H. *et al.* Mechanical and Wear Behaviour of Nanostructure TiO2-Ag Coating on Cobalt-Chromium Alloys by Air Plasma Spray and High-Velocity Oxy-Fuel. **Journal of Materials Research and Technology**, v. 8, n. 2, p. 2290-2299, 2019.

HEGEMANN, D. *et al*. Energy Conversion Efficiency in Plasma Polymerization-A Comparison of Low- and Atmospheric-Pressure Processes. **Plasma Processes and Polymers**, v. *13, n.* 8, 834-842, 2016.

HENRIKSEN, T. H. *et al*. Association between Antimicrobial Resistance among Enterobacteriaceae and Burden of Environmental Bacteria in Hospital Acquired Infections: Analysis of Clinical Studies and National Reports. **Heliyon**, v. 5, n. 7, p. e02054, 2019.

HERTWIG, C.; MENESES, N.; MATHYS, A. Cold atmospheric pressure plasma and low energy electron beam as alternative non-thermal decontamination technologies for dry food surfaces: A review. **Trends in Food Science and Technology**, v. *77*, p. 131-142, 2018.

HOFFMAN, L. R. *et al*. Aminoglycoside Antibiotics Induce Bacterial Biofilm Formation. **Nature**, v. 436, n. 7054, p. 1171-1175, 2005.

HOFFMANN, L. *et al*. Gas Diffusion Barriers Prepared by Spatial Atmospheric Pressure Plasma Enhanced ALD. **ACS Applied Materials and Interfaces**, v. 9, n. 4, p. 4171-4176, 2017.

HOGAN, S. *et al*. A Novel Medical Device Coating Prevents *Staphylococcus Aureus* Biofilm Formation on Medical Device Surfaces. **FEMS Microbiology Letters**, v. 366, n. 9, p. 107, 2019.

HOLMBERG, A. *et al*. Biofilm Formation by Propionibacterium Acnes Is a Characteristic of Invasive Isolates. **Clinical Microbiology and Infection**, v. 15, n. 8, p. 787-795, 2009.

HONARVAR, Z. *et al*. Application of Cold Plasma to Develop Carboxymethyl Cellulose-Coated Polypropylene Films Containing Essential Oil. **Carbohydrate Polymers**, v. 176, p. 1-10, 2017.

HONG, D. *et al*. Measurement of Ozone Production in Non-Thermal Plasma Actuator Using Surface Dielectric Barrier Discharge. **Plasma Chemistry and Plasma Processing**, v. 34, n. 4, p. 887-897, 2014.

HU, J. *et al*. Inductively Coupled Plasma Etching of Bulk Molybdenum. **Proceedings of the IEEE International Conference on Micro Electro Mechanical Systems (MEMS)**, p. 267-270, 2012.

HUACHO, P. M. M. *et al*. Analyses of Biofilm on Implant Abutment Surfaces Coating with Diamond-like Carbon and Biocompatibility. **Brazilian Dental Journal**, v. 28, n. 3, p. 317-323, 2017.

HUANG, Q. *et al*. Corrosion Behavior of ZnO-Reinforced Coating on Aluminum Alloy Prepared by Plasma Electrolytic Oxidation. **Surface and Coatings Technology**, v. 374, p. 1015-1023, 2019.

HUNG, C. *et al*. *Escherichia Coli* Biofilms Have an Organized and Complex Extracellular Matrix Structure. **mBio**, v. 4, n. 5, p. e00645-13, 2013.

HURWITZ, G.; GUILLEN, G. R.; HOEK, E. M. V. Probing Polyamide Membrane Surface Charge, Zeta Potential, Wettability, and Hydrophilicity with Contact Angle

Measurements. **Journal of Membrane Science**, v. 349, n. 2, p. 349-357, 2010.

HYLDGAARD, M.; MYGIND, T.; MEYER, R. L. Essential Oils in Food Preservation: Mode of Action, Synergies, and Interactions with Food Matrix Components. **Frontiers in Microbiology**, v. 3, p. 12, 2012.

IQBAL, M. *et al*. Controlled Surface Wettability by Plasma Polymer Surface Modification. **Surfaces**, v. 2, n. 2, p. 349-371, 2019.

IRANI, S. *et al*. Induction of Growth Arrest in Colorectal Cancer Cells by Cold Plasma and Gold Nanoparticles. **Archives of Medical Science**, v. 11, n. 6, p. 1286, 2015.

ISEKI, S. *et al*. Selective Killing of Ovarian Cancer Cells through Induction of Apoptosis by Nonequilibrium Atmospheric Pressure Plasma. **Applied Physics Letters**, v. 100, n. 11, p. 113702, 2012.

IGE, O. O.; UMORU, L. E.; ARIBO, S. Natural Products: A Minefield of Biomaterials. **ISRN Materials Science**, v. 2012, p. 1-20, 2012.

IÑIGO, M.; DEL POZO, J. L. Fungal biofilms: From bench to bedside. **Revista espanola de quimioterapia : publicacion oficial de la Sociedad Espanola de Quimioterapia**, v. 31, n. 1, p. 35, 2018.

JAGANATHAN, S. K.; SUPRIYANTO, E**.** Antiproliferative and Molecular Mechanism of Eugenol-Induced Apoptosis in Cancer Cells. **Molecules**, v. 17, n. 6, p. 6290-6304, 2012.

JACOB, M. V. *et al*. Electron-Blocking Hole-Transport Polyterpenol Thin Films. **Chemical Physics Letters**, v. 528, p. 26-28, 2012.

JACOB, M. V. *et al*. Plasma Polymerised Thin Films for Flexible Electronic Applications. **Thin Solid Films**, v. 546, p. 167-170, 2013.

JACOB, M. V. *et al*. RF Plasma Polymerised Thin Films from Natural Resources. **International Journal of Modern Physics: Conference Series**, v. 32, p. 1460319, 2014.

JANG, M. H. e*t al*. Inhibition of Cholinesterase and Amyloid-β; Aggregation by Resveratrol Oligomers from Vitis Amurensis. **Phytotherapy Research**, v. 22, n. 4, p. 544-549, 2008.

JARAFAR, H. *et al*. Analysis of Cylindrical Monopole Plasma Antenna Design. **ISAP 2018 - 2018 International Symposium on Antennas and Propagation**, p 1-2, 2019.

JIN, Y. *et al*. Atmospheric Pressure Plasma Jet in Ar and O_2/Ar Mixtures: Properties and High Performance for Surface Cleaning. **Plasma Science and Technology**, v. 15, n. 12, p. 1203-

1208, 2013.

JUN-FENG, Z. *et al*. Diagnosis of Methane Plasma Generated in an Atmospheric Pressure DBD Micro-Jet by Optical Emission Spectroscopy. **Chinese Physics Letters**, v. 26, n. 3, p. 035203, 2009.

KAKIUCHI, H.; OHMI, H.; YASUTAKE, K. Atmospheric-Pressure Low-Temperature Plasma Processes for Thin Film Deposition. **Journal of Vacuum Science & Technology A: Vacuum, Surfaces, and Films**, v. 23, n. 3, p. 030801, 2014.

KALGHATGI, S. *et al.* Effects of Non-Thermal Plasma on Mammalian Cells. **PLoS ONE**, v. 6, n. 1, p. 1-11, 2011.

KAYAMA, M. E. *et al*. Characteristics of Needle-Disk Electrodes Atmospheric Pressure Discharges Applied to Modify PET Wettability. **IEEE Transactions on Plasma Science**, v. 45, n. 5, p. 843-848, 2017.

KANAZAWA, S. *et al.* Stable Glow Plasma at Atmospheric Pressure. **Journal of Physics D: Applied Physics**, v. 21, n. 5, p. 838-840, 1988.

KANAZAWA, S. *et al.* Glow Plasma Treatment at Atmospheric Pressure for Surface Modification and Film Deposition. **Nuclear Inst. and Methods in Physics Research, B**, v. 37-38, n. C, p. 842-845, 1989.

KAYAMA, M. E. *et al*. Characteristics of Needle-Disk Electrodes Atmospheric Pressure Discharges Applied to Modify PET Wettability. **IEEE Transactions on Plasma Science**, v. 45, n. 5, p. 843-848, 2017.

KAUSHIK, N. K. *et al*. Plasma, and Nanomaterials: Fabrication and Biomedical Applications. **Nanomaterials**, v. 9, n. 1, p. 1-19, 2019.

KHAN, T. M. *et al*. A New Strategy of Using Dielectric Barrier Discharge Plasma in Tubular Geometry for Surface Coating and Extension to Biomedical Application. **Review of Scientific Instruments**, v. 91, n. 7, 2020

KHOJA, A. H.; TAHIR, M.; AMIN, N. A. S. Recent Developments in Non-Thermal Catalytic DBD Plasma Reactor for Dry Reforming of Methane. **Energy Conversion and Management**, v. 183, n. September 2018, p. 529-560, 2019.

KHALAF, M.; ABD EL-LATEEF, H. Impact of Porosity and Thickness of Nano-TiO_2 Films on the Corrosion Protection Performance of C-Steel in H_2SO_4. **International Journal of Applied Ceramic Technology**, v. 14, n. 2, p. 145-161, 2017.

KHATOON, Z. *et al*. Bacterial Biofilm Formation on Implantable Devices and Approaches to its Treatment and Prevention. **Heliyon**, v. 4, n. 12, p. e01067, 2018.

KHELIFA, F. *et al*. Free-Radical-Induced Grafting from Plasma Polymer Surfaces. **Chemical Reviews**, v. 116, n. 6, p. 3975-4005, 2016.

KHORASANI, A. M. *et al*. Titanium in biomedical applications-properties and fabrication: A review. **Journal of Biomaterials and Tissue Engineering**, v. 5, n. 8, p. 593-619, 2015.

KHUN, N. W.; LIU, E.; ZENG, X. T. Corrosion Behavior of Nitrogen-Doped Diamond-like Carbon Thin Films in NaCl Solutions. **Corrosion Science**, v. 51, n. 9, p. 2158-2164, 2009.

KIM, C. H. *et al*. Induction of Cell Growth Arrest by Atmospheric Non-Thermal Plasma in Colorectal Cancer Cells. **Journal of Biotechnology**, v. 150, n. 4, p. 530-538, 2010.

KIM, J. E.; LEE, D. U.; MIN, S. C. Microbial Decontamination of Red Pepper Powder by Cold Plasma. **Food Microbiology**, v. 38, p. 128-136, 2014.

KIM, S. *et al*. Mussel-Inspired Approach to Constructing Robust Multilayered Alginate Films for Antibacterial Applications. **Advanced Functional Materials**, v. 26, n. 23, p. 4099-4105, 2016.

KIM, S. J.; CHUNG, T. H. Cold Atmospheric Plasma Jet-Generated RONS and Their Selective Effects on Normal and Carcinoma Cells. **Scientific Reports**, v. 6, p. 20332, 2016.

KOGELHEIDE, F. *et al*. Characterisation of Volume and Surface Dielectric Barrier Discharges in N_2–O_2 Mixtures Using Optical Emission Spectroscopy. **Plasma Processes and Polymers**, 17, n. 6, p. 1900126, 2020.

KOSTAKI, M. *et al*. Differential Biofilm Formation and Chemical Disinfection Resistance of Sessile Cells of Listeria Monocytogenes Strains under Monospecies and Dual-Species (with Salmonella Enterica) Conditions. **Applied and Environmental Microbiology**, v. 78, n. 8, p. 2586-2595, 2012.

KREPKER, M. *et al*. Antimicrobial Carvacrol-Containing Polypropylene Films: Composition, Structure and Function. **Polymers**, v. 10, n. 1, p. 79, 2018.

KÜHN, S. *et al*. Non-Thermal Atmospheric Pressure HF Plasma Source: Generation of Nitric Oxide and Ozone for Bio-Medical Applications. **Plasma Sources Science and Technology**, v. 19, n. 1, p. 015013, 2010.

KULAWIK, P.; KUMAR TIWARI, B. Recent advancements in the application of non-

thermal plasma technology for the seafood industry. **critical Reviews in Food Science and Nutrition**, v. 59, n. 19, p. 3199-3210, 2019.

KULKARNI, M. *et al*. Biomaterial Surface Modification of Titanium and Titanium Alloys for Medical Applications. **Nanomedicine**, v. 111, p. 111, 2014.

KUMAR, A. *et al*. Biofilms: Survival and Defense Strategy for Pathogens. **International Journal of Medical Microbiology**, v. 307, n. 8, p. 481-489, 2017.

KUMAR, A. *et al*. Tailoring Terpenoid Plasma Polymer Properties by Controlling the Substrate Temperature during PECVD. **Journal of Applied Polymer Science**, v. 135, n. 5, p. 45771, 2018.

KUMAR, S. *et al*. Nanotechnology-based biomaterials for orthopaedic applications: Recent advances and future prospects**. Materials Science and Engineering C**, v. 106, p. 110154, 2020.

KUO, S. P. *et al*. Characteristic Study of a Portable Arc Microwave Plasma Torch. **IEEE Transactions on Plasma Science**, v. 34, n. 6, p. 2537-2544, 2006.

KUO, S. Y. *et al*. Effects of RF Power on the Structural, Optical and Electrical Properties of Al-Doped Zinc Oxide Films. **Microelectronics Reliability**, v. 50, n. 5, p. 730-733, 2010.

KYZEK, S. *et al*. Cold Atmospheric Pressure Plasma Can Induce Adaptive Response in Pea Seeds. **Plasma Chemistry and Plasma Processing**, v. 39, n. 2, p. 475-486, 2019.

KAMATOU, G. P.; VERMAAK, I.; VILJOEN, A. M. Eugenol From the remote Maluku Islands to the international market place: A review of a remarkable and versatile molecule. **Molecules**, v. 17, n. 6, p. 6953-6981, 2012.

KANG, C. *et al*. *Pseudomonas Aeruginosa* Bacteremia: Risk Factors for Mortality and Influence of Delayed Receipt of Effective Antimicrobial Therapy on Clinical Outcome. **Clinical Infectious Diseases**, v. 37, n. 6, p. 745-751, 2003.

KHALID, M. *et al*. Identification of Oral Cavity Biofilm Forming Bacteria and Determination of Their Growth Inhibition by *Acacia Arabica*, Tamarix Aphylla L. and Melia Azedarach L. Medicinal Plants. **Archives of Oral Biology**, v. 81, p. 175-185, 2017.

KHALIL, A. A. *et al*. Essential oil eugenol: Sources, extraction techniques, and nutraceutical perspectives. **RSC Advances**, v. *7*, n. 52, p. 32669-32681, 2017.

KHAN, H. A.; BAIG, F. K.; MEHBOOB, R. Nosocomial infections: Epidemiology, prevention, control, and surveillance Asian Pacific**. Journal of Tropical Biomedicine**, v. *7*, n. 5,

478-482, 2017.

KOŽUHA, S. *et al*. Comparison of the Corrosion Behavior and Surface Morphology of Niti Alloy and Stainless Steels in Sodium Chloride Solution. **Journal of Mining and Metallurgy, Section B: Metallurgy**, v. *52*, n. 1, p. 53-61, 2016.

KYLIAN, O. *et al*. Plasma Polymers: From Thin Films to Nanocolumnar Coatings. **Thin Solid Films**, v. 630, p. 86-91, 2017.

LAXMINARAYAN, R. *et al.* Antibiotic resistance-the need for global solutions. **Lancet Infectious Diseases**, v. 13, n. 12, p. 1057-1098, 2013.

LIU, F. *et al*. Inhibition of Biofilm Formation and Exopolysaccharide Synthesis of *Enterococcus Faecalis* by Phenyllactic Acid. **Food Microbiology**, v. 86, p. 103344, 2020.

LV, F. *et al*. In Vitro Antimicrobial Effects and Mechanism of Action of Selected Plant Essential Oil Combinations against Four Food-Related Microorganisms. **Food Research International**, v. 44, n. 9, p. 3057-3064, 2011.

LAMBERT, R. J. W. *et al*. A Study of the Minimum Inhibitory Concentration and Mode of Action of Oregano Essential Oil, Thymol and Carvacrol. **Journal of Applied Microbiology**, v. 91, n. 3, p. 453-462, 2001.

LANCIOTTI, R. *et al*. Application of Hexanal, (E)-2-Hexenal, and Hexyl Acetate to Improve the Safety of Fresh-Sliced Apples. **Journal of Agricultural and Food Chemistry**, v. 51, n. 10, p. 2958-2963, 2003.

LANGMUIR, I. Oscillations in Ionized Gases. **Proceedings of the National Academy of Sciences**, v. 14, n. 8, p. 627, 1928.

LAROUSSI, M.; LU, X.; KEIDAR, M. Perspective: The Physics, Diagnostics, and Applications of Atmospheric Pressure Low-Temperature Plasma Sources Used in Plasma Medicine. **Journal of Applied Physics**, v. 122, n. 2, 2017.

LEE, K. H. *et al*. Evaluation of Cold Plasma Treatments for Improved Microbial and Physicochemical Qualities of Brown Rice. **LWT-Food Science and Technology**, v. 73, p. 442-447, 2016.

LI, M. *et al*. Surface Characteristics and Corrosion Behaviour of WE43 Magnesium Alloy Coated by SiC Film. **Applied Surface Science**, v. 258, n. 7, p. 3074-3081, 2012.

LIGOT, S. *et al*. Correlation between Mechanical Properties and Cross-Linking Degree of Ethyl Lactate Plasma Polymer Films. **Plasma Processes and Polymers**, v. 12, n. 6, p. 508-518,

2015.

LIU, C. *et al.* An Electrochemical Impedance Spectroscopy Study of the Corrosion Behavior of PVD Coated Steels in 0.5 N NaCl Aqueous Solution: Part II. EIS Interpretation of Corrosion Behaviour. **Corrosion Science**, v. 45, n. 6, p. 1257-1273, 2003.

LIU, S. Y. *et al*. Nonoxidative Conversion of Methane in a Dielectric Barrier Discharge Reactor: Prediction of Reaction Performance Based on Neural Network Model. **Journal of Physical Chemistry C**, v. 118, n. 20, p. 10686-10693, 2014a.

LIU, X. *et al*. Surface Modification by Allylamine Plasma Polymerization Promotes Osteogenic Differentiation of Human Adipose-Derived Stem Cells. **ACS Applied Materials and Interfaces**, v. 6, n. 12, p. 9733-9741, 2014b.

LIU, Y. *et al*. Ti-Cu-Zr-Fe-Sn-Si-Sc Bulk Metallic Glasses with Good Mechanical Properties for Biomedical Applications. **Journal of Alloys and Compounds**, v. 679, p. 341-349, 2016.

LIU, Y. *et al.* Atmospheric-Pressure Diffuse Dielectric Barrier Discharges in Ar/O_2 gas Mixture Using 200 KHz/13.56 MHz Dual Frequency Excitation. **Journal of Physics D: Applied Physics**, v. 51, n. 11, 2018.

LONGHI, M. *et al*. Obtainment and Characterization of a Silicon Alkoxides-Based Coating Applied to a Substrate of Stainless Steel 316L for Use in Biomaterials. **Materials Research**, v. 22, n. 3, p. e20180514, 2019.

LU, T.; QIAO, Y.; LIU, X. Surface modification of biomaterials using plasma immersion ion implantation and deposition. **interface Focus**, v. *2*, n. 3, p. 325-336, 2012.

LYTLE, S. *et al*. Analysis and Modelling of Microwave Plasma Hydrogen Production Utilizing Water Vapor and Tungsten Electrodes. **International Journal of Hydrogen Energy**, v. 44, n. 47, p. 25319-25334, 2019.

MACGREGOR, M.; VASILEV, K. Perspective on Plasma Polymers for Applied Biomaterials Nanoengineering and the Recent Rise of Oxazolines. **Materials**, v. 12, n. 1, p. 191, 2019.

MACKINDER, M. A. *et al*. Magnetic Field Enhanced Cold Plasma Sterilization. **Clinical Plasma Medicine**, p. 100092, 2020.

MALIK, M. A. *et al*. Ozone-Free Nitric Oxide Production Using an Atmospheric Pressure Surface Discharge - A Way to Minimize Nitrogen Dioxide Co-Production. **Chemical**

Engineering Journal, v. 283, p. 631-638, 2016.

MANAM, N. S. *et al*. Study of corrosion in biocompatible metals for implants: A review. **Journal of Alloys and Compounds**, v. 701, p. 698-715, 2017.

MANCINI, S. D. *et al*. Solid-State Hydrolysis of Postconsumer Polyethylene Terephthalate after Plasma Treatment. **Journal of Applied Polymer Science**, 2013.

MARCHESE, A. *et al*. Critical Reviews in Microbiology Antimicrobial Activity of Eugenol and Essential Oils Containing Eugenol : A Mechanistic Viewpoint. v. 7828, 2017.

MARINO, M.; BERSANI, C.; COMI, G. Impedance Measurements to Study the Antimicrobial Activity of Essential Oils from *Lamiaceae* and Compositae. **International Journal of Food Microbiology**, v. 67, p. 187-195, 2001.

MARQUES, I. da S. V. *et al*. Electrochemical Behavior of Bioactive Coatings on Cp-Ti Surface for Dental Application. **Corrosion Science**, v. 100, p. 133-146, 2015.

MARTINS, J. I. *et al*. Polypyrrole Coating Doped with Dihydrogenophosphate Ion to Protect Aluminium against Corrosion in Sodium Chloride Medium. **Journal of the Brazilian Chemical Society**, v. 23, n. 3, p. 377-384, 2012.

MASSINES, F. *et al*. Experimental and Theoretical Study of a Glow Discharge at Atmospheric Pressure Controlled by Dielectric Barrier. **Journal of Applied Physics**, v. 83, n. 6, p. 2950-2957, 1998.

MASTELIĆ, J. *et al*. Comparative Study on the Antioxidant and Biological Activities of Carvacrol, Thymol, and Eugenol Derivatives. **Journal of Agricultural and Food Chemistry**, v. 56, n. 11, p. 3989-3996, 2008.

MATIN, R.; BHUIYAN, A. H. Infrared and Ultraviolet-Visible Spectroscopic Analyses of Plasma Polymerized 2,6 Diethylaniline Thin Films. **Thin Solid Films**, v. 534, n. 1, p. 100-106, 2013.

MARTINES, E. Special Issue "Plasma Technology for Biomedical Applications." **Applied Sciences (Switzerland)**, v. 10, n. 4, p. 1-6, 2020.

MISRA, N. N. *et al.* Cold Plasma for Effective Fungal and Mycotoxin Control in Foods: Mechanisms, Inactivation Effects, and Applications. **Comprehensive Reviews in Food Science and Food Safety**, v. 18, n. 1, p. 106-120, 2019.

MEMAR, M. Y. *et al*. Carvacrol and thymol: Strong antimicrobial agents against resistant isolates. **Reviews in Medical Microbiology**, v. 28, n. 2. p. 63-68, 2017.

MERTENS, J. *et al.* Atmospheric Pressure Plasma Polymerization of Organics: Effect of the Presence and Position of Double Bonds on Polymerization Mechanisms, Plasma Stability and Coating Chemistry. **Thin Solid Films**, v. 671, p. 64-76, 2019.

MESA, A. *et al*. Anodized/etched and dis treated Ti surfaces to promote bone formation. **Transactions of the Annual Meeting of the Society for Biomaterials and the Annual International Biomaterials Symposium**, 2019.

MICHELMORE, A. *et al*. Where physics meets chemistry: Thin film deposition from reactive plasmas. **Frontiers of Chemical Science and Engineering**, v. *10*, n. 4, p. 441-458, 2016.

MINATI, L. *et al*. Plasma Assisted Surface Treatments of Biomaterials. **Biophysical Chemistry**, v. 31, n. 5, p. 050825, 2017.

MOKHTAR, M. Experimental Study of Cold Atmospheric Plasma for Plasma Medicine Research and Applications. **Dissertation**, p. 1-159, 2018.

MONTEMOR, M. F. *et al*. Modification of Bis-Silane Solutions with Rare-Earth Cations for Improved Corrosion Protection of Galvanized Steel Substrates. **Progress in Organic Coatings**, v. 57, n. 1, p. 67-77, 2006.

MORENT, R. *et al.* Plasma-Polymerization of HMDSO Using an Atmospheric Pressure Dielectric Barrier Discharge. **Plasma Processes and Polymers**, v. 6, n. SUPPL. 1, p. 537-542, 2009.

MORETO, J. A. *et al*. SVET, SKP and EIS Study of the Corrosion Behaviour of High Strength Al and Al-Li Alloys Used in Aircraft Fabrication. **Corrosion Science**, v. 84, p. 30-41, 2014.

MOSADDAD, S. A. *et al*. Oral Microbial Biofilms: An Update. **European Journal of Clinical Microbiology and Infectious Diseases**, v. 38, n. 11, p. 2005-2019, 2019.

MOSLEHIFARD, E. *et al.* Corrosion Behavior of a Nickel-Base Dental Casting Alloy in Artificial Saliva Studied by Weight Loss and Polarization Techniques. **Frontiers in Dentistry**, v. 16, n. 1, p. 13, 2019.

MOTALEBI, A. *et al*. Improvement of Corrosion Performance of 316L Stainless Steel via PVTMS/Henna Thin Film. **Progress in Natural Science: Materials International**, v. 22, n. 5, p. 392-400, 2012.

MONZILLO, V. *et al*. Chlorhexidine-Silver Sulfadiazine-Impregnated Central Venous

Catheters: In Vitro Antibacterial Activity and Impact on Bacterial Adhesion. **New Microbiologica**, v. 35, n. 2, p. 175-182, 2012.

MUÑOZ-BONILLA, A.; FERNÁNDEZ-GARCÍA, M. Polymeric Materials with Antimicrobial Activity. **Progress in Polymer Science (Oxford)**, v. 37, n. 2, p. 281-339, 2012.

MWEMA, F. M. *et al*. Atomic Force Microscopy Analysis of Surface Topography of Pure Thin Aluminum Films. **Materials Research Express**, v. 5, n. 4, 2018.

MACGREGOR, M. *et al.* Preserving the Reactivity of Coatings Plasma Deposited from Oxazoline Precursors - An in Depth Study. **Plasma Processes and Polymers**, v. 16, n. 2, p. 1-12, 2019.

MANAKHOV, A. *et al*. The Robust Bio-Immobilization Based on Pulsed Plasma Polymerization of Cyclopropylamine and Glutaraldehyde Coupling Chemistry. **Applied Surface Science**, v. 360, p. 28-36, 2016.

MAJEED, H. *et al*. Bactericidal Action Mechanism of Negatively Charged Food Grade Clove Oil Nanoemulsions. **Food Chemistry**, v. 197, p. 75- 83, 2016.

MAKHLOUF, A. S. H.; HERRERA, V.; MUÑOZ, E. Chapter 6 -Corrosion and protection of the metallic structures in the petroleum industry due to corrosion and the techniques for protection. **Elsevier Ltd**, p. 107-122, 2018.

MANION, C. R.; WIDDER, R. M. Essentials of Essential Oils. **American Journal of Health-System Pharmacy**, v. *74*, n. 9, p. e153-e162, 2017.

MARRA, A. R. *et al.* Nosocomial Bloodstream Infections in Brazilian Hospitals: Analysis of 2,563 Cases from a Prospective Nationwide Surveillance Study. **Journal of Clinical Microbiology**, v. 49, n. 5, p. 1866-1871, 2011.

MARTINS, K. B. *et al.* In Vitro Effects of Antimicrobial Agents on Planktonic and Biofilm Forms of *Staphylococcus Saprophyticusisolated* from Patients with Urinary Tract Infections. **Frontiers in Microbiology**, v. 10, p. 40, 2019.

MILADI, H. *et al.* Synergistic Effect of Eugenol, Carvacrol, Thymol, p-Cymene, and γ-Terpinene on Inhibition of Drug Resistance and Biofilm Formation of Oral Bacteria. **Microbial Pathogenesis**, v. 112, p. 156-163, 2017.

MITTAL, M. *et al*. Phytochemical evaluation and pharmacological activity of *Syzygium aromaticum*: A comprehensive review**. International Journal of Pharmacy and Pharmaceutical Sciences**, v. 6, n. 8, p. 67-72, 2014.

MOHAMMADI, M. *et al.* Study the Antibacterial and Antibiofilm Activity of Carum copticum against Antibiotic-Resistant Bacteria in Planktonic and Biofilm Forms. **Microbial Pathogenesis**, v. 129, p. 99-105, 2019.

MOHAMMADI NEJAD, S.; ÖZGÜNEŞ, H.; BAŞARAN, N. Pharmacological and Toxicological Properties of Eugenol. **Turkish Journal of Pharmaceutical Sciences**, v. 14, n. 2, p. 201-206, 2017.

MORAN, E. *et al.* Guiding Empirical Antibiotic Therapy in Orthopaedics: The Microbiology of Prosthetic Joint Infection Managed by Debridement, Irrigation, and Prosthesis Retention. **Journal of Infection**, v. 55, n. 1, p. 1-7, 2007.

MURUVE, N. G. G. *et al*. Peptide-Based Biocoatings for Corrosion Protection of Stainless Steel Biomaterial in a Chloride Solution. **Materials Science and Engineering C**, v. 698, p. 695-700, 2016.

MUSA, A. Y. *et al.* A Comparative Study of the Corrosion Inhibition of Mild Steel in Sulphuric Acid by 4,4-Dimethyloxazolidine-2-Thione. **Corrosion Science**, v. 51, n. 10, p. 2393-2399, 2009.

NASERI, R. *et al.* A Comparison of Axial Fatigue Strength of Coarse and Ultrafine Grain Commercially Pure Titanium Produced by ECAP. **Archives of Civil and Mechanical Engineering**, v. 18, n. 3, p. 755-767, 2018.

NOBILE, C. J.; JOHNSON, A. D. *Candida Albicans* Biofilms, and Human Disease. **Annual Review of Microbiology**, v. 69, p. 71-92, 2015.

N. MAZHIR, S. *et al*. Measurement of Plasma Electron Temperature and Density by Using Different Applied Voltages and Working Pressures in a Magnetron Sputtering System. **International Journal of Engineering & Technology**, v. 7, n. 3, p. 1177, 2018.

NAPARTOVICH, A. P. Overview of Atmospheric Pressure Discharges Producing Nonthermal Plasma. **Plasmas and Polymers**, v. 6, n. 2, p. 1-14, 2001.

NASTUTA, A. V. *et al.* Diagnosis of a Short-Pulse Dielectric Barrier Discharge at Atmospheric Pressure in Helium with Hydrogen-Methane Admixtures. **Physics of Plasmas**, v. 25, n. 4, 2018.

NAZZARO, F. *et al*. Effect of essential oils on pathogenic bacteria. **Pharmaceuticals**, v. 6, n. 12, p. 1451-1474, 2013.

NEUBEISER, A. *et al*. Mortality Attributable to Hospital Acquired Infections with

Multidrug-Resistant Bacteria in a Large Group of German Hospitals. **Journal of Infection and Public Health**, v. 13, n. 2, p. 204-210, 2020.

NI, T. L. *et al*. Cold Microplasma Plume Produced by a Compact and Flexible Generator at Atmospheric Pressure. **Applied Physics Letters**, v. 92, n. 24, p. 241503, 2008.

NIU, Q. *et al*. Effects of Flue Gas Components on the Oxidation of Gaseous Hg by Dielectric Barrier Discharge Plasma. **Fuel**, v. 150, p. 619-624, 2015.

NOSTRO, A. *et al*. Susceptibility of Methicillin-Resistant *Staphylococci* to Oregano Essential Oil, Carvacrol and Thymol. **FEMS Microbiology Letters**, v. 230, n. 2, p. 191-195, 2004.

OBOT, I. B.; OBI-EGBEDI, N. O. An Interesting and Efficient Green Corrosion Inhibitor for Aluminium from Extracts of *Chlomolaena Odorata L*. in Acidic Solution. **Journal of Applied Electrochemistry**, v. 40, n. 11, p. 1977-1984, 2010.

OLEA, A. F. *et al*. Antifungal Activity of Eugenol Derivatives against Botrytis Cinerea. **Molecules**, v. 24, n. 7, 2019.

OSTOVARI, A. *et al*. Corrosion Inhibition of Mild Steel in 1 M HCl Solution by Henna Extract: A Comparative Study of the Inhibition by Henna and Its Constituents (Lawsone, Gallic Acid, α-d-Glucose, and Tannic Acid). **Corrosion Science**, v. 51, n. 9, p. 1935-1949, 2009.

OSTRIKOV, K. Reactive Plasmas as a Versatile Nanofabrication Tool. **Reviews of Modern Physics**, v. 77, n. 2, p. 489, 2005.

OWENS, D. K.; WENDT, R. C. Estimation of the Surface Free Energy of Polymers. **Journal of Applied Polymer Science**, v. 13, n. 8, p. 1741-1747, 1969.

OTERO REY, E. *et al*. *Candidiasis* Oral En El Paciente Mayor. **Avances en Odontoestomatologia**, v. *31*, n. 3, p. 135-148, 2015.

PANKAJ, S. K. *et al*. Effects of Cold Plasma on Surface, Thermal and Antimicrobial Release Properties of Chitosan Film. **Journal of Renewable Materials**, v. 5, n. 1, p. 14-20, 2017.

PAHARIK, A. E.; HORSWILL, A. R. The *Staphylococcal* Biofilm: Adhesins, Regulation, and Host Response. **Microbiology Spectrum**, p. 529-566, 2016.

PATEL, N. R.; GOHIL, P. P. International Journal of Emerging Technology and Advanced Engineering A Review on Biomaterials: Scope, Applications & Human Anatomy Significance. **International Journal of Emerging Technology and Advancing Engineering**, v.

2, n. 4, p. 91-101, 2012.

PATHAK, P. *Candida albicans* Biofilm: Risks, Complications, and Preventive Strategies. In: Implication of Quorum Sensing and Biofilm Formation in Medicine, Agriculture, and Food Industry. **Springer, Singapore**, p. 121-128, 2019.

PERUGINI BIASI-GARBIN, R. *et al*. Effect of Eugenol against *Streptococcus agalactiae* and *Synergistic* Interaction with Biologically Produced Silver Nanoparticles. **Evidence-based Complementary and Alternative Medicine**, v. 2015, p. 1-8, 2015.

PETROVIĆ MIHAJLOVIĆ, M. B. *et al*. Imidazole Based Compounds as Copper Corrosion Inhibitors in Seawater. **Journal of Molecular Liquids**, v. 225, p. 127-136, 2017.

POLYAKOV, A. V. *et al.* Impact Toughness of Ultrafine-Grained Commercially Pure Titanium for Medical Application. **Advanced Engineering Materials**, v. 20, n. 5, p. 1700863, 2018.

PANTA, G.; SUBEDI, D. Electrical Characterization of Aluminum (Al) Thin Films Measured by Using Four-Point Probe Method. **Kathmandu University Journal of Science, Engineering and Technology**, v. 8, n. 2, p. 31-36, 2013.

PANTA, G. P. *et al.* An Experimental Study of Co-Axial Dielectric Barrier Discharge for Ozone Generation An Experimental Study of Co-Axial Dielectric Barrier Discharge. **Journal of Nepal Physical Society**, v. 6, n. 1, p. 84-89, 2020b.

PANTA, G. P. *et al.* Ozonizer Design by Using Double Dielectric Barrier Discharge for Ozone Generation. **The African Review of Physics**, n. 6250, p. 43-55, 2020a.

PARK, H. W.; CHA, W. B.; UHM, S. Highly efficient thermal plasma scrubber technology for the treatment of perfluoro compounds (PFCs). **Applied Chemistry for Engineering**, 2018.

PEETERS, F. J. J.; YANG, R.; VAN DE SANDEN, M. C. M. The Relation between the Production Efficiency of Nitrogen Atoms and the Electrical Characteristics of a Dielectric Barrier Discharge. **Plasma Sources Science and Technology**, v. 24, n. 4, 2015.

PENG, C. *et al*. Antibacterial TiCu/TiCuN Multilayer Films with Good Corrosion Resistance Deposited by Axial Magnetic Field-Enhanced Arc Ion Plating. **ACS Applied Materials and Interfaces**, v. 11, n. 1, p. 125-136, 2019.

PETER, S. *et al*. ECR Plasma Deposited A-SiCN:H as Insulating Layer in Piezoceramic Modules. **Vacuum**, v. 155, p. 118-126, 2018.

PIAVIS, W.; TURN, S.; ALI MOUSAVI, S. M. Non-Thermal Gliding-Arc Plasma Reforming of Dodecane and Hydro processed Renewable Diesel. **International Journal of Hydrogen Energy**, v. 40, n. 39, p. 13295-13305, 2015.

PRAMOD, K.; ANSARI, S. H.; ALI, J. Eugenol: A natural compound with versatile pharmacological actions**. Natural Product Communications**, v. 5, n. 12, p. 1000501236, 2010.

PRICE, A. J. *et al*. Knee replacement. **Lancet**, 2018.

PULIYALIL, H.; CVELBAR, U. Selective Plasma Etching of Polymeric Substrates for Advanced Applications. **Nanomaterials**, v. 6, n. 6, p. 108, 2016.

QIAN, M. *et al*. Stark broadening measurement of the electron density in an atmospheric pressure argon plasma jet with double-power electrodes. **Journal of Applied Physics**, v. 107, n. 6, p. 063303, 2010.

QIAN, W. *et al.* Antimicrobial Activity of Eugenol against Carbapenem-Resistant *Klebsiella Pneumoniae* and its Effect on Biofilms. **Microbial Pathogenesis**, v. 139, p. 103924, 2020.

RAFIEERAD, A. R. *et al*. Surface Characterization and Corrosion Behavior of Calcium Phosphate-Base Composite Layer on Titanium and its Alloys via Plasma Electrolytic Oxidation: A Review Paper. **Materials Science and Engineering C**, v. 57, p. 397-413, 2015.

RAGHAVENDRA, N.; BHAT, J. I. Unripe Arecanut Seed Extract as a Natural Corrosion Inhibitor for Mild Steel (Ms) in Acid and Alkali Medium. **Research Journal of Chemistry and Environment**, v. 62, n. 3, p. 351-358, 2018.

RAHMAN, M. J.; BHUIYAN, A. H. Structural and Optical Properties of Plasma Polymerized O-Methoxyaniline Thin Films. **Thin Solid Films**, v. 534, p. 132-136, 2013.

RAIZER, 55. Yuri P. **Gas Discharge Physics.** New York: Springer, p. 19, 1991.

RAJARAMAN, S. K.; JAINU, M.; DHAKSHINAMOORTHY, G. *Ocimum Basilicum L.* Essential Oil Coated Biomaterial Surfaces Prevent Bacterial Adhesion and Biofilm Growth. **Asian Journal of Pharmaceutical and Clinical Research**, v. 9, n. 3, 2016.

RAJASEKARAN, P. *et al.* Filamentary and Homogeneous Modes of Dielectric Barrier Discharge (DBD) in Air: Investigation through Plasma Characterization and Simulation of Surface Irradiation. **Plasma Processes and Polymers**, v. 7, n. 8, p. 665-675, 2010.

RAMEZANZADEH, M. *et al*. Corrosion Inhibition of Mild Steel in 1 M HCl Solution by Ethanolic Extract of Eco-Friendly *Mangifera Indica* (Mango) Leaves Electrochemical,

Molecular Dynamics, Monte Carlo and Ab Initio Study. **Applied Surface Science**, v. 463, p. 1058-1077, 2019.

RANGEL, E. C. *et al*. Treatment of PVC Using an Alternative Low Energy Ion Bombardment Procedure. **Applied Surface Science**, v. 258, n. 5, p. 1854-1861, 2011.

RANGEL, R. C. C. *et al*. Barrier and Mechanical Properties of Carbon Steel Coated with SiO_x/$SiOxCyH_z$ Gradual Films Prepared by PECVD. **Surface and Coatings Technology**, v. 378, n. October, p. 124996, 2019.

RANGEL, R. C. C.; CRUZ, N. C.; RANGEL, E. C. Role of the Plasma Activation Degree on Densification of Organosilicon Films. **Materials**, v. 13, n. 1, p. 25, 2020.

RAVENSDALE, J. T.; COOREY, R.; DYKES, G. A. Integration of Emerging Biomedical Technologies in Meat Processing to Improve Meat Safety and Quality. **Comprehensive Reviews in Food Science and Food Safety**, v. 17, n. 3, p. 615-632, 2018.

REICHEL, C. *et al*. Insulating and Passivating Plasma-Enhanced Atomic Layer Deposited Aluminum Oxide Thin Films for Silicon Solar Cells. **Thin Solid Films**, v. 656, p. 53-60, 2018.

RIBEIRO-SANTOS, R. *et al*. Use of Essential Oils in Active Food Packaging: Recent Advances and Future Trends. **Trends in Food Science and Technology**, v. 61, p. 132-140, 2017.

RODRIGUES, D. *et al*. Effect of Magnetic Hyperthermia on the Structure of Biofilm and Cellular Viability of a Food Spoilage Bacterium. **Biofouling**, v. 29, n. 10, p. 1225-1232, 2013.

ROSALES-LEAL, J. I. *et al*. Effect of Roughness, Wettability and Morphology of Engineered Titanium Surfaces on Osteoblast-like Cell Adhesion. **Colloids and Surfaces A: Physicochemical and Engineering Aspects**, v. 365, n. 3, p. 222-229, 2010.

ROY, N.; TALUKDER, M. Electrical and Spectroscopic Diagnostics of Atmospheric Pressure DBD Plasma Jet. **Journal of Bangladesh Academy of Sciences**, v. 40, n. 1, p. 23-36, 2016.

RUHE, Z. C.; LOW, D. A.; HAYES, C. S. Bacterial contact-dependent Growth Inhibition. **Trends in Microbiology**, v. 21, n. 5, p. 230-237, 2013.

RYAN, T. P.; STALDER, K. R.; WOLOSZKO, J. Overview of plasma technology used in medicine. **Energy-based Treatment of Tissue and Assessment VII**, v. 8584, p. 85840, 2013.

RAJA, A. S. *et al*. Corrosion Control by Aminoacetic Acid (Glycine) an Overview. **International Journal of Innovative Research in Science, Engineering and Technology**, v. 3,

n. 4, p. 11455-11467, 2014.

RAMRITU, P. *et al*. A Systematic Review Comparing the Relative Effectiveness of Antimicrobial-Coated Catheters in Intensive Care Units. **American Journal of Infection Control**, v. 36, n. 2, p. 104-117, 2008.

RIBES, S. *et al*. Enhancing the Antimicrobial Activity of Eugenol, Carvacrol, and Vanillin Immobilised on Silica Support against *Escherichia Coli* or *Zygosaccharomyces Rouxii* in Fruit Juices by Their Binary Combinations. **LWT**, v. 113, p. 08326, 2019.

RAMAGE, G. *et al*. Denture Stomatitis: A Role for *Candida* Biofilms. **Oral Surgery, Oral Medicine, Oral Pathology, Oral Radiology, and Endodontology**, v. 98, n. 1, p. 53-59, 2004.

RAMAGE, G.; MARTÍNEZ, J. P.; LÓPEZ-RIBOT, J. L. *Candida* biofilms on implanted biomaterials: A clinically significant problem. **FEMS Yeast Research**, **v.** *6*, *n.* 7, p. 979-986, 2006.

RAO, P. V.; GAN, S. H. Cinnamon: A Multifaceted Medicinal Plant1. Rao, P. V. & Gan, S. H. Cinnamon: A Multifaceted Medicinal Plant. Evidence-Based Complement. Altern. Med. 2014, (2014). **Evidence-based Complementary and Alternative Medicine**, p. 2014, 2014.

REVIE, R. W.; UHLIG, H. H. Corrosion, and Corrosion Control: An Introduction to Corrosion Science and Engineering: **Fourth Edition**, 2008.

RODRÍGUEZ-CERDEIRA, C. *et al.* Biofilms and vulvovaginal candidiasis. **Colloids and Surfaces B. Biointerfaces**, v. *174*, p. 110-125, 2019.

RUBINI, D. *et al.* Essential Oils from Unexplored Aromatic Plants Quench Biofilm Formation and Virulence of Methicillin-Resistant *Staphylococcus Aureus*. **Microbial Pathogenesis**, n. 122, p. 162-173, 2018.

SAHAL, G. *et al*. Antifungal and Biofilm Inhibitory Effect of *Cymbopogon Citratus* (Lemongrass) Essential Oil on Biofilm Forming by *Candida Tropicalis* Isolates; an in Vitro Study. **Journal of Ethnopharmacology**, v. 246, n. August 2019, p. 112188, 2020.

Şahin, N.; Tanışlı, M. Electron temperature estimation of helium plasma via line intensity ratio at atmospheric pressure. **Eur. Phys. J. Plus., v**. 1*35*, n. 8, p. 1-10, 2020.

SAKUDO, A.; YAGYU, Y.; ONODERA, T. Disinfection and Sterilization Using Plasma Technology: Fundamentals and Future Perspectives for Biological Applications. **International Journal of Molecular Sciences**, v. 20, n. 20, p. 1-17, 2019.

SHAO, Y. *et al*. Eugenol-Chitosan Nanoemulsions by Ultrasound-Medium ted Emulsification: Formulation, Characterization, and Antimicrobial Activity. **Carbohydrate Polymers**, v. 193, p. 144-152, 2018.

SILVER, S.; PHUNG, L. T.; SILVER, G. Silver as biocides in burn and wound dressings and bacterial resistance to silver compounds. **Journal of Industrial Microbiology and Biotechnology**, v. *33*, n. 7, p. 627-634, 2006.

SONG, F. Effects of Substrate Stiffness on Bacterial Biofilm Formation Recommended Citation. n. May 2016.

SHINTANI, D. *et al*. Electrochemical Behavior of Various Kinds of Stainless Steels in a High-Temperature and High-Pressure Methanol Solution. **Corrosion**, v. 64, n. 7, p. 607-612, 2008.

SINGH, S. *et al*. Understanding the Mechanism of Bacterial Biofilms Resistance to Antimicrobial Agents. **The Open Microbiology Journal**, v. 11, p. 53, 2017.

SOKOVIĆ, M.; VAN GRIENSVEN, L. J. L. D. Antimicrobial Activity of Essential Oils and their Components against the Three Major Pathogens of the Cultivated Button Mushroom, *Agaricus Bisporus*. **European Journal of Plant Pathology**, v. 116, n. 3, p. 211-224, 2006.

SUETENS, C. *et al*. Prevalence of Healthcare-Associated Infections, Estimated Incidence, and Composite Antimicrobial Resistance Index in Acute Care Hospitals and Long-Term Care Facilities: Results from Two European Point Prevalence Surveys, 2016 to 2017. **Eurosurveillance**, v. 23, n. 46, p. 1800516, 2018.

SULEYMAN, G.; ALANGADEN, G. J. Nosocomial Fungal Infections: Epidemiology, Infection Control, and Prevention. **Infectious Disease Clinics of North America**, 2016.

SURYALETHA, K. *et al.* Decoding the Proteomic Changes Involved in the Biofilm Formation of *Enterococcus Faecalis* SK460 to Elucidate Potential Biofilm Determinants. **BMC Microbiology**, v. *19*, n. 1, p. 146, 2019.

SABOOHI, S. *et al*. Synthesis of Highly Functionalised Plasma Polymer Films from Protonated Precursor Ions: Via the Plasma α-γ Transition. **Physical Chemistry Chemical Physics**, v. 19, n. 7, p. 5637-5646, 2017.

SAJIB, S. A. *et al*. Plasma Activated Water: The next Generation Eco-Friendly Stimulant for Enhancing Plant Seed Germination, Vigor and Increased Enzyme Activity, a Study on Black Gram (*Vigna Mungo L.*). **Plasma Chemistry and Plasma Processing**, v. 40, n. 1, p. 119-143,

2020.

SAMAD, A. *et al*. Assessment of Biofilm Formation by *Pseudomonas Aeruginosa* and Hydrodynamic Evaluation of Microtiter Plate Assay. **Journal of the Pakistan Medical Association**, v. 59, n. 5, p. 666-671, 2019.

SANTOS, M. *et al.* Mechanically Robust Plasma-Activated Interfaces Optimized for Vascular Stent Applications. **ACS Applied Materials and Interfaces**, v. 8, n. 15, p. 9635-9650, 2016a.

SANTOS, M. R. E. *et al*. Recent Developments in Antimicrobial Polymers: A Review. **Materials**, v. 9, n. 7, 2016b.

SANTOS, N. M. *et al.* Effect of the Plasma Excitation Power on the Properties of $SiO_xC_yH_z$ Films Deposited on AISI 304 Steel. **Surface and Coatings Technology**, v. 311, p. 127-137, 2017a.

SANTOS, N. M. *et al.* Effect of the Plasma Excitation Power on the Properties of SiOxCyHz Films Deposited on AISI 304 Steel. **Surface and Coatings Technology**, v. 311, p. 127-137, 2017b.

SARANGAPANI, C. *et al.* Recent Advances in the Application of Cold Plasma Technology in Foods. **Annual Review of Food Science and Technology**, v. 9, p. 609-629, 2018.

SASUJIT, K.; DUSSADEE, N.; TIPPAYAWONG, N. Overview of tar reduction in biomass-derived producer gas using non-thermal plasma discharge. **Maejo International Journal of Science and Technology**, v. 13, n. 1, p. 42-61, 2019.

SATO, M. *et al.* Multifactorial Effects of Operating Conditions of Dielectric-Barrier-Discharge Plasma Actuator on Laminar-Separated-Flow Control. **AIAA Journal**, v. 53, n. 9, p. 2544-2559, 2015.

SELVAKUMAR, N.; BARSHILIA, H. C.; RAJAM, K. S. Effect of Substrate Roughness on the Apparent Surface Free Energy of Sputter Deposited Superhydrophobic Polytetrafluoroethylene Coatings: A Comparison of Experimental Data with Different Theoretical Models. **Journal of Applied Physics**, v. 108, n. 1, p. 013505, 2010.

SEWRAJ, N. *et al*. Electric and Spectroscopic Analysis of a Pure Nitrogen Mono-Filamentary Dielectric Barrier Discharge (MF-DBD) at 760 Torr. **Journal of Physics D: Applied Physics**, v. 44, n. 14, 2011.

SHARIFI-RAD, M. *et al*. Carvacrol and human health: A comprehensive review**.** **Phytotherapy Research**, v. 32, n. 9, p. 1675-1687, 2018.

SHIBATA, Y.; TANIMOTO, Y. A review of improved fixation methods for dental implants. Part I: Surface optimization for rapid osseointegration. **Journal of Prosthodontic Research**, v. 59, n. 1, p. 20-30, 2015.

SHRESTHA, R. *et al*. Generation and Diagnostics of Atmospheric Pressure Dielectric Barrier Discharge in Argon/Air. **Indian Journal of Pure and Applied Physics**, v. 55, n. 2, p. 155-162, 2017.

SIKKEMA, J.; DE BONT, J. A. M.; POOLMAN, B. Mechanisms of membrane toxicity of hydrocarbons. **Microbiological Reviews**, v. 59, n. 2, p. 201-222, 1995.

SIMENI SIMENI, M. *et al*. Electric Field Measurements in a Nanosecond Pulse Discharge in Atmospheric Air. **Journal of Physics D: Applied Physics**, v. 50, n. 18, p. 184002, 2017.

SINGH, B.; SINGH, G.; SIDHU, B. S. In Vitro Investigation of Nb–Ta Alloy Coating Deposited on CoCr Alloy for Biomedical Implants. **Surface and Coatings Technology**, v. 377, p. 124932, 2019.

SINHA, L. *et al*. FT-IR, FT-Raman and UV Spectroscopic Investigation, Electronic Properties, Electric Moments, and NBO Analysis of Anethole Using Quantum Chemical Calculations. **Spectrochimica Acta Part A: Molecular and Biomolecular Spectroscopy**, v. 133, p. 165-177, 2014.

SONG, L. *et al*. Inductively coupled plasma etching of bulk tungsten for MEMS applications. **In: Proceedings of the IEEE International Conference on Micro Electro Mechanical Systems (MEMS),** 2014.

SOUZA, J. G. S. *et al.* Citric Acid Reduces Oral Biofilm and Influences the Electrochemical Behavior of Titanium: An in Situ and in Vitro Study. **Journal of Periodontology**, v. 90, n. 12, p. 149-158, 2019.

SOUZA, J. G. S. *et al*. Titanium Particles and Ions Favor Dysbiosis in Oral Biofilms. **Journal of Periodontal Research**, v. 55, n. 2, p. 258-266, 2020.

SOWA, M. *et al*. Bioactivity of Coatings Formed on Ti-13Nb-13Zr Alloy Using Plasma Electrolytic Oxidation. **Materials Science and Engineering C**, v. 49, p. 159-173, 2015.

STANFIELD, S. A.; MENART, J. A. Spectroscopic Investigation of a Dielectric Barrier Discharge. **AIAA Journal**, v. 52, n. 5, p. 991-997, 2014.

STRYCZEWSKA, H. D. *et al*. Power Systems of Plasma Reactors for Non-Thermal Plasma Generation. **Journal of Advanced Oxidation Technologies**, v. 16, n. 1, p. 52-62, 2013.

SUBLET, A. *et al*. Atmospheric and Sub-Atmospheric Dielectric Barrier Discharges in Helium and Nitrogen. **Plasma Sources Science and Technology**, v. 15, n. 4, p. 627, 2006.

SUCI DHARMAYANTI, A. W. *et al.* Implant surface modification strategies through antibacterial and bioactive components. **Elsevier Inc**, p. 647-673, 2020.

SUNTRES, Z. E.; COCCIMIGLIO, J.; ALIPOUR, M. The Bioactivity and Toxicological Actions of Carvacrol. **Critical Reviews in Food Science and Nutrition**, v. 55, n. 3, p. 304-18, 2015.

SZABO, P. S. *et al*. Experimental and simulated solar wind sputtering of lunar analogue material. **In: EGU General Assembly Conference Abstracts**, p. 8680, 2018.

TABATABAEI MAJD, M. *et al*. Development of a High-Performance Corrosion Protective Functional Nano-Film Based on Poly Acrylic Acid-Neodymium Nitrate on Mild Steel Surface. **Journal of the Taiwan Institute of Chemical Engineers**, v. 96, p. 610-626, 2019.

TALEBIAN, M. *et al*. Pitting Corrosion Inhibition of 304 Stainless Steel in NaCl Solution by Three Newly Synthesized Carboxylic Schiff Bases. **Corrosion Science**, v. 160, p. 108130, 2019.

TAN, L. *et al*. Rapid Biofilm Eradication on Bone Implants Using Red Phosphorus and Near-Infrared Light. **Advanced Materials**, v. 30, n. 31, p. 1-10, 2018.

TANAKA, H. *et al.* State of the Art in Medical Applications Using Non-Thermal Atmospheric Pressure Plasma. **Reviews of Modern Plasma Physics**, v. 1, n. 1, p. 3, 2017.

TANG, J. F. *et al*. Experimental Investigation on a Multicathode Dielectric-Barrier Discharge: Effects of Airflows. **IEEE Transactions on Plasma Science**, v. 47, n. 5, p. 1944-1949, 2019.

TARIFA, M. C.; LOZANO, J. E.; BRUGNONI, L. I. Disinfection Efficacy over Yeast Biofilms of Juice Processing Industries. **Food Research International**, v. 105, p. 473-481, 2018.

TEGOULIA, V. A.; COOPER, S. L. *Staphylococcus Aureus* Adhesion to Self-Assembled Monolayers: Effect of Surface Chemistry and Fibrinogen Presence. **Colloids and Surfaces B: Biointerfaces**, v. 24, n. 3-4, p. 217-228, 2002.

THADEN, J. T. *et al*. Results from a 13-Year Prospective Cohort Study Show Increased

Mortality Associated with Bloodstream Infections Caused by *Pseudomonas Aeruginosa* Compared to Other Bacteria. **Antimicrobial Agents and Chemotherapy**, v. 61, n. 6, p. e02671-16, 2017.

THESIS, M. P.; AKTER, T. Study of Electron Acoustic Solitary Waves In A Two Temperature Plasma System With Kappa Distributed Electrons Study of Electron Acoustic Solitary Waves. **A Two Temperature Plasma System**, p. 2012-2013, 2017.

THIRY, D. *et al.* Plasma diagnostics for the low-pressure plasma polymerization process: A critical review. **Thin Solid Films**, v. 606, p. 19-44, 2016.

TRAUTNER, B. W.; DAROUICHE, R. O. Role of Biofilm in Catheter-Associated Urinary Tract Infection. **American Journal of Infection Control**, v. 32, n. 3, p. 177-183, 2004.

TREJBAL, J. *et al*. Utilization of surface-modified polymer and glass micro-fibers as reinforcement in cement composites. **In Key Engineering Materials**, v. 760, p. 225-230, 2018.

TSAI, T. C. *et al.* Copper Film Deposition Using a Helium Dielectric Barrier Discharge Jet. **Plasma Processes and Polymers**, n. December 2019, p. 1-11, 2020.

TSCHIERSCH, R.; BOGACZYK, M.; WAGNER, H. E. Systematic Investigation of the Barrier Discharge Operation in Helium, Nitrogen, and Mixtures: Discharge Development, Formation, and Decay of Surface Charges. **Journal of Physics D: Applied Physics**, v. 47, n. 36, 2014.

TUMBARELLO, M. *et al*. Characterisation and Risk Factor Profiling of *Pseudomonas Aeruginosa* Urinary Tract Infections: Pinpointing Those Likely to Be Caused by Multidrug-Resistant Strains. **International Journal of Antimicrobial Agents**, p. 105900, 2020.

TANWAR, J. *et al.* Multidrug resistance: An emerging crisis. **Interdisciplinary Perspectives on Infectious Diseases**, v. 2014, 2014.

TASIC, Z. Z. *et al.* The Influence of Synergistic Effects of 5-Methyl-1H-Benzotriazole and Potassium Sorbate as Well as 5-Methyl-1H-Benzotriazole and Gelatin on the Copper Corrosion in Sulphuric Acid Solution. **Journal of Molecular Liquids**, v. 219, p. 463-473, 2016.

TORNERO, E. *et al*. Prosthetic Joint Infections Due to *Staphylococcus Aureus* and Coagulase-Negative *Staphylococci*. **International Journal of Artificial Organs**, v. 34, n. 10, p. 884- 892, 2012.

TORZEWSKA, A.; BEDNARSKA, K.; RÓŻALSKI, A. Influence of Various Uropathogens on Crystallization of Urine Mineral Components Caused by Proteus Mirabilis.

Research in Microbiology, v. *170*, n. 2, p. 80-85, 2019.

TSUI, C.; KONG, E. F.; JABRA-RIZK, M. A. Pathogenesis of *Candida albicans* biofilm. **Pathogens and Disease**, v. *74*, n. 4, p. ftw018, 2016.

TUMBARELLO, M. *et al.* Biofilm production by *Candida* Species and Inadequate Antifungal Therapy as Predictors of Mortality for Patients with Candidemia. **Journal of Clinical Microbiology**, v. 45, n. 6, p. 1843-1850, 2007.

UMOREN, S. A.; SOLOMON, M. M. Synergistic corrosion inhibition effect of metal cations and mixtures of organic compounds: A Review. **Journal of Environmental Chemical Engineering**, v. *5*, n. 1, p. 246-273, 2017.

U, W. E. N. I. A. N. D. *et al.* Storage Stability and Antibacterial Activity against *Escherichia Coli* O157:H7 of Carvacrol in Edible Apple Films Made by Two Different Casting Methods. **Journal of Agricultural and Food Chemistry**, v. 56, n. 9, p. 3082-3088, 2008.

ULTEE, A.; BENNIK, M. H. J.; MOEZELAAR, R. The Phenolic Hydroxyl Group of Carvacrol Is Essential for Action against the Food-Borne Pathogen *Bacillus Cereus*. **Applied and Environmental Microbiology**, v. 68, n. 4, p. 1561-1568, 2002.

VALERO, M.; FRANCÉS, E. Synergistic Bactericidal Effect of Carvacrol, Cinnamaldehyde or Thymol and Refrigeration to Inhibit *Bacillus Cereus* in Carrot Broth. **Food Microbiology**, v. 23, n. 1, p. 68-73, 2006.

VALIEV, R. Z.; PARFENOV, E. V.; PARFENOVA, L. V. Developing nanostructured metals for manufacturing of medical implants with improved design and biofunctionality. **Materials Transactions**, v. 60, n. 7, p. 1356-1366, 2019.

VANDENBOSSCHE, M.; HEGEMANN, D. Recent approaches to reduce aging phenomena in oxygen- and nitrogen-containing plasma polymer films: An overview. **Current Opinion in Solid State and Materials Science**, v. 22, n. 1, p. 26-36, 2018.

VASILEV, K. *et al*. Antibacterial Surfaces for Biomedical Devices. Expert Rev Med Devices 6-553-567.Pdf. **Expert Rev Med Devices**, v. 6, n. Sep, p. 1-20, 2009.

VAZ, S. *et al.* Bone scan usefulness in patients with painful hip or knee prosthesis: 10 situations that can cause pain, other than loosening and infection. **European Journal of Orthopaedic Surgery and Traumatology**, v. 27, n. 2, p. 147-156, 2017.

VELNAR, T. *et al*. Biomaterials, and Host versus Graft Response: A Short Review. **Bosnian Journal of Basic Medical Sciences**, v. 16, n. 2, p. 82-90, 2016.

VINCIGUERRA, V. *et al*. Chemical Characterization and Antifungal Activity of *Origanum Vulgare*, Thymus Vulgaris Essential Oils and Carvacrol against Malassezia Furfur. **Natural Product Research**, v. 33, n. 22, p. 3273-3277, 2019.

VON KEUDELL, A.; CORBELLA, C. Review Article: Unraveling Synergistic Effects in Plasma-Surface Processes by Means of Beam Experiments. **Journal of Vacuum Science & Technology A: Vacuum, Surfaces, and Films**, v. 35, n. 5, p. 050801, 2017.

VAHIDGOLPAYEGANI, A. *et al*. Production methods and characterization of porous Mg and Mg alloys for biomedical applications. In: **Metallic Foam Bone: Processing, Modification and Characterization, and Properties**. p. 25-82. 2017.

VAN ACKER, H.; VAN DIJCK, P.; COENYE, T. Molecular Mechanisms of Antimicrobial Tolerance and Resistance in Bacterial and Fungal Biofilms. **Trends in Microbiology**, v. 22, n. 6, p. 326-333, 2014.

VERMA, C. *et al*. Substituents effect on corrosion inhibition performance of organic compounds in aggressive ionic solutions: A review. **Journal of Molecular Liquids**, v. *251*, p. 100-118, 2018.

WANG, C. *et al*. Antifungal Activity of Eugenol against *Botrytis Cinerea*. **Tropical Plant Pathology**, v. 35, n. 3, p. 137-143, 2010.

WANG, Y. *et al.* Interfacial Structures, Surface Tensions, and Contact Angles of Diiodomethane on Fluorinated Polymers. **Journal of Physical Chemistry C**, v. 118, n. 19, p. 10143-10152, 2014.

WOUTHUYZEN-BAKKER, M. *et al*. Clinical Outcome and Risk Factors for Failure in Late Acute Prosthetic Joint Infections Treated with Debridement and Implant Retention. **Journal of Infection**, v. 78, n. 1, p. 40-47, 2019.

WALTON, S. G.; GREENE, J. E. Plasmas in Deposition Processes. In: **Handbook of Deposition Technologies for Films and Coatings**. p. 32-92, 2010.

WANG, Q. *et al*. Effects of Air Dielectric Barrier Discharge Plasma Treatment Time on Surface Properties of PBO Fiber. **Applied Surface Science**, v. 258, n. 1, p. 513-520, 2011.

WANG, R. *et al.* Thin Insulating Film Deposition on Copper by Atmospheric-Pressure Plasmas. **Plasma Processes and Polymers**, v. 14, n. 7, p. 1-9, 2017.

WANG, T. *et al*. Effect of Reactor Structure in DBD for Nonthermal Plasma Processing of NO in N_2 at Ambient Temperature. **Plasma Chemistry and Plasma Processing**, v. 32, n. 6, p.

1189-1201, 2012.

WANG, W. *et al*. Superhydrophobic Coatings with Edible Materials. **ACS Applied Materials and Interfaces**, v. 8, n. 29, p. 18664-18668, 2016a.

WANG, W. L. *et al*. Electrical and Optical Characteristics of the Radio Frequency Surface Dielectric Barrier Discharge Plasma Actuation. **Chinese Physics B**, v. 25, n. 4, 2016b.

WANG, Y. *et al*. Low-temperature catalytic CO_2 dry reforming of methane on Ni-based catalysts: A review. **Fuel Processing Technology**, v. 169, p. 199-206, 2018.

WEBER, F. J.; DE BONT, J. A. M. Adaptation mechanisms of microorganisms to the toxic effects of organic solvents on membranes Biochimica Biophysica. **Acta - Reviews on Biomembranes**, v. 1286, n. 3, p. 225-245, 1996.

WISPLINGHOFF, H. *et al*. Nosocomial Bloodstream Infections in US Hospitals: Analysis of 24,179 Cases from a Prospective Nationwide Surveillance Study. **Clinical Infectious Diseases**, v. 39, n. 3, p. 309-317, 2004.

WOLFMEIER, H. *et al*. New Perspectives in Biofilm Eradication. **ACS Infectious Diseases**, v. 4, n. 2, p. 93-106, 2018.

XIAO, D. *et al*. Characteristics of Atmospheric-Pressure Non-Thermal N_2 and N_2/O_2 Gas Mixture Plasma Jet. **Journal of Applied Physics**, v. 115, n. 3, p. 033303, 2014.

XIE, Y. *et al*. Nano Modified SLA Process for Titanium Implants. **Materials Letters**, v. 186, p. 38-41, 2017.

XU, Q. F.; WANG, J. N.; SANDERSON, K. D. Organic-Inorganic Composite Nanocoatings with Superhydrophobicity, Good Transparency, and Thermal Stability. **ACS Nano**, v. 4, n. 4, p. 2201-2209, 2010.

YANG, H. *et al*. Effects of Atmospheric Pressure Cold Plasma on Human Hepatocarcinoma Cell and Its 5-Fluorouracil Resistant Cell Line. **Physics of Plasmas**, v. 22, n. 12, p. 122006, 2015.

YASUDA, H.; WANG, C. R. Plasma Polymerization Investigated by The Substrate Temperature Dependence. **Journal of polymer science. Part A-1, Polymer chemistry**, v. 23, n. 1, p. 87-106, 1985.

YASUDA, H.; IRIYAMA, Y. Plasma Polymerization. In: **Comprehensive Polymer Science and Supplements**, 1989

YOKOYAMA, T. *et al.* The Mechanism of the Stabilisation of Glow Plasma at

Atmospheric Pressure. **Journal of Physics D: Applied Physics**, v. 23, n. 8, p. 1125-1128, 1990.

YU, G. *et al*. The Interaction between Volume Discharges and Surface Discharges in Spot-Line White-Eye Hexagonal Superlattice Pattern in Dielectric Barrier Discharge. **Physics of Plasmas**, v. 26, n. 2, p. 023507, 2019.

YURTCAN, M. T.; KHANGHAH, M. F. Characterization of Polymeric Thin Films from Cinnamaldehyde Essential Oil Compounds by Using Radio Frequency-Plasma Enhanced Chemical Vapor Characterization of Plasma Polymerized Polyaniline. **Thin Films**. n. April 2014, 2019.

YAQUB KHAN, M.; MOHD YAQUB, K.; MIN-HUA, C. A Review on Role of Biomaterials in Biomedical Field. **International Journal of Bio-Pharma Research**,v. 8, n. 9, p. 2788–2793, 2019.

ZAIDI, S. F. *et al.* Diverse pharmacological properties of Cinnamomum cassia: A revie**w. Pakistan Journal of Pharmaceutical Sciences**, v. 28, n. 4, 2015.

ZHANG, W. *et al*. Effect of Machining-Induced Surface Residual Stress on Initiation of Stress Corrosion Cracking in 316 Austenitic Stainless Steel. **Corrosion Science**, v. 108, p. 173-184, 2016.

ZHANG, L. C.; CHEN, L. Y. A Review on Biomedical Titanium Alloys: Recent Progress and Prospect Advanced Engineering. **Materials**, v. 21, n. 4, p. 1801215, 2019.

Zhao, G.; Feng, J. J.; Xu, J. J.; Chen, H. Y. Direct electrochemistry and electrocatalysis of heme proteins immobilized on self-assembled ZrO_2 film. **Electrochem. Commun**. v. 7, p. 724-729, 2005.

ZILLE, A.; SOUTO, A. P.; OLIVEIRA, F. R. Plasma treatments. In: MILAŠIUS, R. (Ed.). **Textile Strategy for Innovative Higher Education**. p. 1102-1106, 2019.

ZAHORANOVÁ, A. *et al*. Effect of Cold Atmospheric Pressure Plasma on Maize Seeds: Enhancement of Seedlings Growth and Surface Microorganisms Inactivation. **Plasma Chemistry and Plasma Processing**, v. 38, n. 5, p. 969-988, 2018.

ZHOU, R. *et al.* Plasma-Enabled Catalyst-Free Conversion of Ethanol to Hydrogen Gas and Carbon Dots near Room Temperature. **Chemical Engineering Journal**, v. 382, p. 122745, 2020.

ZHOU, Y. *et al.* Investigation of Discharge Characteristics of DBD Plasma Produced with Multi-Needle to Plate Electrodes in Water by Optical Emission Spectroscopy. **Vacuum**, v. 162,

n. January, p. 121-127, 2019.

ZHOU, Y. L. *et al.* Corrosion Resistance and Biocompatibility of Ti-Ta Alloys for Biomedical Applications. **Materials Science and Engineering A**, v. 398, n. 1-2, p. 28-36, 2005.

ZIUZINA, D. *et al*. Cold Plasma Inactivation of Bacterial Biofilms and Reduction of Quorum Sensing Regulated Virulence Factors. **PLoS ONE**, v. 10, n. 9, p. e0138209, 2015. `